GENERALIZED CONTINUUM MODELING OF SCALE-DEPENDENT CRYSTALLINE PLASTICITY

A Dissertation
Presented to
The Academic Faculty

By

Jason R. Mayeur

In Partial Fulfillment
of the Requirements for the Degree
Doctor of Philosophy in the
George W. Woodruff School of Mechanical Engineering

Georgia Institute of Technology

December 2010

GENERALIZED CONTINUUM MODELING OF SCALE-DEPENDENT CRYSTALLINE PLASTICITY

Approved by:

Dr. David L. McDowell, Advisor
George W. Woodruff School of
Mechanical Engineering
Georgia Institute of Technology

Dr. Naresh N. Thadhani
School of Materials Science
and Engineering
Georgia Institute of Technology

Dr. Richard W. Neu
George W. Woodruff School of
Mechanical Engineering
Georgia Institute of Technology

Dr. Douglas J. Bammann
Bagley College of Engineering
Mechanical Engineering Dept.
Mississippi State University

Dr. Jianmin Qu
George W. Woodruff School of
Mechanical Engineering
Georgia Institute of Technology

Date Approved: 12/9/2010

ACKNOWLEDGEMENTS

Anytime one achieves something significant in life, there are many people that contribute to the accomplishment along the way. At this time, I'd like to offer an acknowledgement of the various people that have helped me either directly or indirectly during the completion of my PhD. First and foremost, I'd like to thank my entire family for all of the love and support that they have provided throughout the years. Even though they may not have completely understood all of the ups and downs of the process, they were always there offering encouragement when I needed it the most. In particular, I'd like to thank my parents, John and Melinda, my sister and brother-in-law, Kacie and Brent Miller, and my precious little niece, Cecilia Reid Miller. She has only been with us for about eight months now, but she has already managed to steal all of our hearts. I would also like to acknowledge my grandparents, the late Muriel Moseley, Nancy Moseley, the late Frank Mayeur, and Janie Rhea Hall. Pops, I wish you were here to celebrate this accomplishment with me and I think about you often. Special thanks are reserved for my fiancé, Leslie Lewis. She has made substantial sacrifices during the final stages of my PhD, during which, I essentially took up residence in my office. I am grateful that she had the patience to put up with me through all of the odd hours and my far too often singular focus on my research. I love you.

I would to thank my advisor, Dr. David McDowell, for his support and advice throughout the course of this work. This dissertation has benefitted greatly from the high standards of achievement that he demands from his students, and also from his depth of knowledge in a wide range of topics related to the mechanics of materials. I am appreciative of my reading committee, which is comprised of Dr. Richard Neu, Dr. Jianmin Qu, Dr. Naresh Thadhani, and Dr. Douglas Bammann for their invaluable contributions and comments which helped shape the final form of the dissertation. I am especially indebted to Dr. Bammann, whom I first met during his visit to Georgia Tech in the Fall of 2002 while he was on leave from Sandia National Laboratories. The mentoring that he provided during the summers I spent at Sandia as a participant in the Engineering Sciences Summer Institute greatly influenced my philosophical view of mechanics and contributed substantially in shaping who I am as a researcher.

Throughout the years, there have been many friends and colleagues that have contributed to my experience at Georgia Tech. Some have helped with technical matters, others have provided a much needed distraction from work, and some have done a little bit of both. I have seen a lot of faces come and go during my time here, but I'd like to call attention to a few who have had a prominent impact. In no particular order, I'd like to acknowledge Dr. Douglas Spearot, Dr. Ali Gordon, Dr. Mahesh Shenoy, Dr. John Clayton, Benjamin Dempsey, Dr. Timothy Ferguson, Dr. James Shepherd, Dr. Rajesh Prasannavenkatesan, Dr. Craig Przybyla, Dr. Laurent Capolungo, Dr. Ryan Austin, Dr. Darby Luscher, Dr. Arash Yavari, Dr. Jonathan Zimmerman, Dr. Ambarish Kulkarni, Robert Matthews, Nima Salajegheh, Garritt Tucker, and all of the "young guns" currently residing in MRDC 3338. Of the previous acknowledgements, I'd like to single out Dr. Ryan Austin and Dr. Darby Luscher. My research has benefited enormously from countless hours and emails spent discussing various aspects of mechanics with them both, and more importantly, my life has been more enjoyable as a result of their friendship.

A hearty tip of the cap also goes out to the notably non-technical distractions provided by the members of the Shalimar Crew and other assorted unsavory characters, i.e., Dr. Matthew Kontz, Brent Hull, Mike Curry, Peter Barros, Dr. Allison Lange, Dr. Nick Borer, and Dr. Kyle Webber. I'd also like to acknowledge Joseph Ceremuga for the hospitality and friendship that he has provided throughout the years, especially during my summers in Livermore.

TABLE OF CONTENTS

LIST OF TABLES

LIST OF FIGURES

SUMMARY

The use of metallic material systems (e.g. pure metals, alloys, metal matrix composites) in a wide range of engineering applications from medical devices to electronic components to automobiles continues to motivate the development of improved constitutive models to meet increased performance demands while minimizing cost. Emerging technologies often incorporate materials in which the dominant microstructural features have characteristic dimensions reaching into the submicron and nanometer regime. Metals comprised of such fine microstructures often exhibit unique and size-dependent mechanical response, and classical approaches to constitutive model development at engineering (continuum) scales, being local in nature, are inadequate for describing such behavior. Therefore, traditional modeling frameworks must be augmented and/or reformulated to account for such phenomena. Crystal plasticity constitutive models have proven quite capable of capturing first-order microstructural effects such as grain orientation (elastic/plastic anisotropy), grain morphology, phase distribution, etc. on the deformation behavior of both single and polycrystals, yet suffer from the same limitations as other local continuum theories with regard to capturing scale-dependent mechanical response. This research is focused on the development, numerical implementation, and application of a generalized (nonlocal) theory of single crystal plasticity capable of describing the scale-dependent mechanical response of both single and polycrystalline metals that arises as a result of heterogeneous deformation.

This research developed a dislocation-based theory of micropolar single crystal plasticity. The majority of nonlocal crystal plasticity theories are predicated on the connection between gradients of slip and geometrically necessary dislocations. Due to the diversity of existing nonlocal crystal plasticity theories, a review, summary, and comparison of representative model classes is presented in Chapter 2 from a unified dislocation-based perspective. The discussion of the continuum crystal plasticity theories is prefaced by a brief review of discrete dislocation plasticity, which facilitates the comparison of certain model aspects and also serves as a reference for latter segments of the research which make connection to this constitutive description. Chapter 2 has utility not only as a literature review, but also as a synthesis and analysis of competing and alternative nonlocal crystal plasticity modeling strategies from a common

viewpoint. The micropolar theory of single crystal plasticity is presented in Chapter 3. Two different types of flow criteria are considered - the so-called single and multicriterion theories, and several variations of the dislocation-based strength models appropriate for each theory are presented and discussed.

The numerical implementation of the two-dimensional version of the constitutive theory is given in Chapter 4. A user element subroutine for the implicit commercial finite element code Abaqus/Standard is developed and validated through the solution of initial-boundary value problems with closed-form solutions. Convergent behavior of the subroutine is also demonstrated for an initial-boundary value problem exhibiting strain localization. In Chapter 5, the models are employed to solve several standard initial-boundary value problems for heterogeneously deforming single crystals including simple shearing of a semi-infinite constrained thin film, pure bending of thin films, and simple shearing of a metal matrix composite with elastic inclusions. The simulation results are compared to those obtained from the solution of equivalent boundary value problems using discrete dislocation dynamics and alternative generalized crystal plasticity theories. Comparison and calibration with respect to the former provides guidance in the specification of non-traditional material parameters that arise in the model formulation and demonstrates its effectiveness at capturing the heterogeneous deformation fields and size-dependent mechanical behavior predicted by a finer scale constitutive description.

Finally, in Chapter 6, the models are applied to simulate the deformation behavior of small polycrystalline ensembles. Several grain boundary constitutive descriptions are explored and the response characteristics are analyzed with respect to experimental observations as well as results obtained from discrete dislocation dynamics and alternative nonlocal crystal plasticity theories. Particular attention is focused on how the various grain boundary descriptions serve to either locally concentrate or diffuse deformation heterogeneity as a function of grain size.

CHAPTER 1

INTRODUCTION

1.1 Motivation

The use of metallic material systems (e.g. pure metals, alloys, metal matrix composites) in a wide range of engineering applications from medical devices to electronic components to automobiles continues to motivate the development of improved constitutive models to meet increased performance demands while minimizing cost. Emerging technologies often incorporate materials in which the dominant microstructural features have characteristic dimensions reaching into the submicron and nanometer regime. Metals comprised of such fine microstructures often exhibit unique and size-dependent mechanical response, with the relationship that "smaller is stronger". Representative examples of the "smaller is stronger" phenomena have been experimentally observed with respect to the yield strength of polycrystals [1, 2], indentation of single crystals [3], bending of thin films [4], torsion of thin rods [5], and tension of passivated thin films [6, 7]. The ability to model and predict variations in the mechanical response due to changes in microstructure is crucial to the advancement and optimization of metallic material systems. Classical models of crystal plasticity [8-10] have proven quite capable of describing the influence of first-order microstructural effects such as grain orientation (elastic/plastic anisotropy), grain morphology, phase distribution, etc. on the mechanical response of both single and polycrystalline metals, yet suffer from the same limitations as other local continuum theories with regard to modeling scale-dependent behavior. Therefore, the classical theory must be augmented or reformulated to account for these higher-order effects.

To address the shortcomings of the classical (local) theory, generalized (nonlocal) crystal plasticity theories that appeal to the notion of geometrically necessary dislocations (GNDs) [11] have been developed on multiple conceptual fronts. The term nonlocal is used here in the broad sense as defined by Bazant and Jirasek [12] and is meant to imply "weak nonlocality". Weakly nonlocal constitutive models

incorporate additional gradient dependence in the formulation and are to be contrasted against the "strong nonlocality" synonymous with nonlocal integral formulations. From this point forward in this research, when a model is referred to as nonlocal, it is to be understood that weak nonlocality is implied. As noted by Kuroda and Tvergaard [13], there are three main subclasses of nonlocal single crystal plasticity models: (i) low-order theories (ii) non-work-conjugate higher-order theories and (iii) work-conjugate higher-order theories. The distinction between the low-order and higher-order theories is that the former's governing partial differential equations are of the same order as the classical theory, whereas the latter are of a higher-order. Low-order theories do not admit the application of non-standard boundary conditions and only incorporate nonlocality via enhanced constitutive relations, while the higher-order theories do admit non-standard boundary conditions as well as nonlocal constitutive relations. In higher-order theories, the continuum is assumed to have additional degrees-of-freedom, and the difference between the non-work-conjugate and work-conjugate theories, as one might infer, is that the additional degrees-of-freedom do not contribute to the power of internal forces in the former, whereas they do in the latter.

The vast majority of generalized single crystal plasticity models are formulated such that the explicit calculation of slip gradients is required (cf. [14-20]. While certain slip gradient-based approaches do possess some attractive features such as being able to apply boundary conditions on slip at the slip system level [15, 17], there are also certain practical and philosophical limitations as compared to the classical theory. From a practical standpoint, the numerical implementation of slip gradient-based approaches requires either modified [21, 22] or higher-order [23-25] finite element (FE) interpolation schemes as compared standard C^0-continuous methods. Furthermore, if the slip system shears or GND densities are taken as continuum degrees-of-freedom, the FE matrix bandwidth for a given discretization of an initial-boundary value problem will be significantly larger for the nonlocal theory as compared to the classical one, as the number of additional degrees-of-freedom scales with the number of slip systems. In addition to the steep increase in computational burden associated with the slip gradient-based approaches, there are also, in our opinion, some philosophical disadvantages to the slip gradient theories that treat the slip system shearing rates as power-conjugate generalized velocities [18]. In these approaches, it is now common practice to incorporate "energetic" and "dissipative" decompositions of the thermodynamic *stresses*, and to include the plastic strain gradients directly in the free energy function (not as internal state

variables). In contrast, a more traditional approach would introduce elastic (energetic) and plastic (dissipative) decompositions of the thermodynamic *strains*, and the free energy would then only depend on the elastic parts and possibly a set of internal state variables reflecting energy storage due to irreversible changes in microstructure.

It is with these issues in mind that we are motivated to pursue an alternative (to the slip gradient-based approaches) formulation of generalized single crystal plasticity. Specifically, we seek to develop a model of generalized single crystal plasticity that:

- ◊ Maintains the standard approach of elastic-plastic thermodynamics
- ◊ Avoids treating the slip system shears as generalized displacements
- ◊ Admits higher-order (non-standard) boundary conditions
- ◊ Offers a simpler and more efficient numerical implementation as compared to the slip gradient-based approaches

Examples of alternative models of generalized single crystal plasticity are the full second gradient theories of Smyshlyaev and Fleck [26] and Shu and Fleck [27], the couple-stress theory of Kim and Oh [28], the micromorphic theories of Naghdi and Srinivasa [29, 30] and Le and Stumpf [31, 32], and the micropolar theory of Forest et al. [33-35]. The full second gradient and couple stress models require the use of higher-order interpolation functions [25] in numerical implementations, whereas the micromorphic and micropolar models may be implemented using standard C^0-continuous interpolation functions since the higher-order kinematics (additional degrees-of-freedom) are independent of the displacement field. Based on these considerations and motivated by the prior works of Clayton et al. [36] and Forest and collaborators [34, 35, 37-41], this research is focused on the development and application of micropolar models of single crystal plasticity.

1.2 Scope of the work

This research is concerned with the development of models of micropolar single crystal plasticity as an alternative to the more common slip gradient-based models of generalized single crystal plasticity. A micropolar [42] or Cosserat [43] continuum is type of work-conjugate higher-order continuum which possesses extra rotational degrees-of-freedom. Early works in phenomenological micropolar elastoplasticity are due to Besdo [44], Lippmann [45], and Sawczuk [46], while more recent representative contributions in this vein are due to de Borst [47], Steinmann [48], Grammenoudis and Tsakmakis [49], and Neff [50]. Most relevant to this research are the works of Forest et al. [33-35, 38] which present phenomenological models of micropolar single crystal plasticity. Building upon these previous works, the current research is undertaken with three main objectives:

- ◊ Develop physically-based models of micropolar single crystal elasto-viscoplasticity.
- ◊ Implement the constitutive models in a finite element code.
- ◊ Apply the models to simulate the scale-dependent mechanical response of single and polycrystalline metals, benchmark against discrete dislocation simulations, and conduct parametric studies to shed light on more appropriate forms of constitutive relations within the micropolar crystal plasticity construct.

These research objectives are achieved as outlined in the remainder of this thesis which is structured as follows. Chapter 2 introduces background material relevant to the development of scale-dependent models of continuum single crystal plasticity. The chapter begins with a review of discrete dislocation plasticity. Topics covered in the review will facilitate the comparison of certain concepts that arise in the scale-dependent continuum theories, and also serve as a reference for latter segments of the research where discrete dislocation simulation results are compared to those obtained from the developed micropolar theories. Classical single crystal plasticity theory is then reviewed prior to discussing representative developments of generalized single crystal plasticity, and attention is focused on dislocation-based constitutive models. This material is intended to provide appropriate depth and perspective for the

micropolar model of single crystal plasticity that is presented in Chapter 3. Chapter 2 has utility not only as a literature review, but also as a synthesis and analysis of competing and alternative nonlocal crystal plasticity modeling strategies from a common viewpoint. Both theoretical and computational aspects of the models are discussed.

The micropolar theory of single crystal plasticity is presented in Chapter 3. Two distinct viscoplastic modeling frameworks - the so-called single and multicriterion theories are introduced. The previous works of Forest et al. [34, 35] based on a multicriterion framework and containing a phenomenological strength model are extended to incorporate a dislocation-based strength models. This is an important contribution as it enables one to establish clear connections between micropolar single crystal plasticity and various aspects of slip gradient-based generalized crystal plasticity models, and also provides a more physically-based description of scale-dependent strengthening behavior. Additionally, a new single criterion formulation is presented with an analogous, but simplified strength model. The development of the single criterion model is motivated by related earlier works in phenomenological macroscopic micropolar elastoplasticity, and represents the first attempt to embed a single criterion flow rule within a micropolar single crystal plasticity framework. Several variations of dislocation-based strength models appropriate for each theory are presented and discussed.

Chapter 4 presents the numerical implementation of the two-dimensional version of the constitutive theory given in Chapter 3 appropriate for plane strain and plane stress problems. A user element (UEL) subroutine has been developed for the implicit commercial FE code Abaqus/Standard [51]. The element has three degrees-of-freedom per node (two displacements and one rotation), and a rate-tangent method [52] appropriate for a micropolar elasto-viscoplastic material has been presented for the constitutive update. Element performance is validated through the solution of elastic initial-boundary value problems with closed-form solutions, and the convergent behavior is also demonstrated for an elastic-plastic initial-boundary value problem exhibiting strain localization.

The constitutive models are employed in Chapter 5 to solve several standard initial-boundary value problems for heterogeneously deforming single crystals including: simple shearing of a constrained thin film, pure bending of thin films, and simple shearing of a metal matrix composite with elastic inclusions. First, the general performance of the constitutive models is demonstrated via solution of the

constrained shear problem in order to gain an understanding of how the non-classical inelastic material constants affect the mechanical response and the resulting deformation fields. This information is then used to guide calibration of the micropolar models to results of equivalent initial-boundary value problems solved using discrete dislocation dynamics. The deformation behavior predicted by the calibrated micropolar models is then compared to results obtained from both discrete dislocation dynamics simulations as well as alternative generalized crystal plasticity theories. Comparison and calibration with respect to the former provides guidance in the specification of non-traditional material intrinsic length scale parameters, and demonstrates the developed models' effectiveness at capturing the heterogeneous deformation fields and size-dependent mechanical behavior predicted by a finer scale constitutive description.

In Chapter 6 the models are applied to simulate the deformation behavior of small polycrystalline ensembles. Two different polycrystal representations are considered: a traditional model in which the micropolar crystal plasticity constitutive description is applied to each grain up to a sharp grain boundary interface, and a core-mantle model in which the polycrystal is divided into grain interior (core) and mantle (grain boundary) regions. The grain cores are modeled as viscoplastic single crystals and the grain boundary mantle is modeled as an elastic micropolar phase. Direct numerical simulations are performed for a range of grain sizes using both polycrystal representations in order to evaluate the aggregate mechanical response, and the scale-dependent deformation behavior is subsequently analyzed. Particular attention is focused on how the different polycrystal descriptions serve to either locally concentrate or diffuse deformation heterogeneity as a function of grain size, and also on the scaling behavior of the flow stress with respect to grain size.

Chapter 7 provides a summary of the work, acknowledges the original contributions, and suggests potential avenues for future work. The unique contributions of this dissertation as summarized as follows:

Constitutive Model Development

- Two new physically-based theories of micropolar single crystal plasticity have been developed.
  - A multicriterion flow theory with a dislocation-based strength model has been proposed as an extension of the phenomenological strength model of Forest et al. [34]. The replacement of the

phenomenological strength model with a dislocation-based model is a necessary step for relating the current developments to existing physically-based models, and also for making direct comparisons to finer scale simulations, i.e., discrete dislocation dynamics.

- A novel single criterion flow theory with a dislocation-based strength model has also been proposed. Single criterion flow rules are commonly used in other types of higher-order nonlocal crystal plasticity theories, and are advantageous because they significantly reduce the number of non-standard material constants as compared to multicriterion theories.

- Several variations of the dislocation-based strength models have been proposed and their performance has been evaluated via direct numerical simulation. It has been demonstrated that some of the strength models do not produce deformation behavior consistent with observations from finer scale (e.g., discrete dislocation) simulations.

❖ The relationship between the developed models and the more common slip gradient-based theories has been established.

- A focused effort has been made to relate the models to the prominent and highly cited model due to Gurtin [17], which is a significant contribution since the proposed models offer a simpler numerical implementation than the former. This has important implications in the practical application of the model in future 3-D numerical simulations.

Numerical Simulations

❖ A numerical implementation of the model has been developed and incorporated into the commercial finite element code Abaqus/Standard as a user element subroutine.

❖ The numerical implementation has been validated through the solution of boundary value problems with known analytical solutions, and the convergence behavior for an inelastic problem featuring strain localization has been studied and the mesh regularization properties have been demonstrated.

❖ The role of the model length scale parameters has been clearly defined in terms of their effect on the mechanical response and the development of heterogeneous deformation fields. This understanding is critical to ascribing physical significance to the nonlocal material parameters.

❖ The viability of the models has been established through a comparison to discrete dislocation dynamics simulations of equivalent initial-boundary value problems. This not only demonstrates that the models are capable of capturing the physics of lower length scale deformation processes in meaningful way, but also suggests they could be incorporated as part of a multiscale modeling framework.

- A pathway and methodology for calibrating the micropolar model parameters to discrete dislocation dynamics simulations has been established. Knowledge of how the nonlocal material parameters relate to various aspects of the finer scale simulations lends confidence that the calibrated values are physically meaningful.

CHAPTER 2

SCALE-DEPENDENT SINGLE CRYSTAL PLASTICITY

2.1 Introduction

This chapter presents background material relevant to the development of scale-dependent models of single crystal plasticity. The generalized or nonlocal continuum, as discussed in the introduction, has been advanced on several conceptual fronts, and it is covered herein how these different philosophies have been applied to constitutive modeling of metallic single crystals. This material will provide appropriate depth and perspective for the micropolar model of single crystal plasticity that is introduced in Chapter 3 and is the focus of this research. The following discussion is undertaken within the context of small deformations since the micropolar theory is developed within a geometrically linear setting. The small deformation assumption also simplifies comparison of various nonlocal single crystal plasticity theories. With regard to constitutive model development, attention is focused on dislocation-based strength evolution equations. In addition to the various nonlocal single crystal plasticity theories presented in Sections 2.4.3-2.4.5, a few supplemental topics are included to facilitate the review. The list of supplemental topics include: discrete dislocation dynamics (Section 2.2), the classical theory of single crystal plasticity (Section 2.3), and the geometrically necessary dislocation density tensor (Sections 2.4.1-2.4.2). Although these topics are not necessarily essential to this research, they are included for completeness and ease of reference.

2.2 Discrete Dislocation Dynamics

Discrete dislocation dynamics is a constitutive description of crystalline plasticity which explicitly models the motion and evolution of individual dislocations. In this formalism, dislocations are treated as line singularities embedded in an elastic continuum, and the description of plastic deformation follows

directly from their nucleation, glide, obstruction, and interaction. Discrete dislocation dynamics simulation frameworks of various levels of sophistication have been developed and employed by several research groups [53-59]. All of the methodologies are based on the same fundamental steps of computing the migration of dislocations due to the forces acting upon them, but differ in the different numerical algorithms used to discretize the continuum and dislocation lines, treat dislocation interactions, the computation of long-range forces, etc. The two-dimensional discrete dislocation dynamics simulation methodology of Needleman and Van der Giessen [57] is outlined here in part for simplicity and clarity of presentation, and also because comparisons are made to results obtained using their model later in the research. The model is developed for small deformations and elastically isotropic materials.

The mechanical initial-boundary value problem in discrete dislocation dynamics is solved as a three step process. First, the stress field within the body is determined based on current position of the dislocations. The Peach-Koehler force acting on each dislocation is then determined, and finally used to evolve the dislocation's positions based on a set of constitutive relations describing the glide, nucleation, trapping, and annihilation processes. The stress field in the body is obtained through a superposition procedure which takes advantage of analytical solutions for the dislocation stress fields in an infinite continuum and then calculates a corrective stress field on a domain without dislocations to account for the actual boundary conditions applied to the finite body. A schematic representation of the field decomposition is given in Figure 2.1. Consider a linear elastic body of volume R which consists of a matrix phase denoted R^M which may contain dislocations and an elastic inclusion phase denoted $R^\Diamond$ that is dislocation free such that $R = R^M \cup R^\Diamond$. Individual dislocations, indicated by an index i, are treated as line defects in the elastic matrix and are characterized by their Burgers vector, $\mathbf{b}^i$, and the unit vector normal to the slip plane, $\mathbf{n}^i$. At a given material point, $\mathbf{x} \in R$, in the interior of the body, the displacement field is expressed as an additive superposition of the displacements caused by the N dislocations in an infinite medium of the homogeneous matrix material and the corrective displacements required to correct for the actual boundary conditions on the finite body and also the presence of inclusions, i.e.,

$$\mathbf{u} = \tilde{\mathbf{u}} + \breve{\mathbf{u}} \tag{2.1}$$

where $\mathbf{u}$ is the actual displacement field. The dislocation displacement field is indicated by $(\breve{\bullet})$ and the corrective field by $(\breve{\bullet})$. The strain, ε, and stress, $\boldsymbol{\sigma}$, fields are also expressed in terms of the dislocation and corrective fields, respectively, as

$$\varepsilon = \tfrac{1}{2}(\mathbf{u}\vec{\nabla} + \vec{\nabla}\mathbf{u}) = \tilde{\varepsilon} + \breve{\varepsilon} \tag{2.2}$$

$$\boldsymbol{\sigma} = \tilde{\boldsymbol{\sigma}} + \breve{\boldsymbol{\sigma}} \tag{2.3}$$

The balance of linear and angular momentum expressed in terms of the total fields for a body in static equilibrium in the absence of body forces are given as

$$\left.\begin{array}{l} \vec{\nabla}\cdot\boldsymbol{\sigma} = \mathbf{0} \\ \\ \boldsymbol{\sigma} = \boldsymbol{\sigma}^{T} \end{array}\right\} \quad \forall \mathbf{x} \in R \tag{2.4}$$

Standard displacement and traction boundary conditions can be applied to the body, i.e.,

$$\mathbf{u} = \mathbf{u}^{*} \qquad \forall \mathbf{x} \in \partial R_{u} \tag{2.5}$$

$$\mathbf{T} = \hat{\mathbf{n}}\cdot\boldsymbol{\sigma} = \mathbf{T}^{*} \qquad \forall \mathbf{x} \in \partial R_{\sigma} \tag{2.6}$$

where $\mathbf{u}^{*}$ and $\mathbf{T}^{*}$ are the applied displacements and tractions, respectively, on complimentary portions of the external boundary such that $\partial R = \partial R_{u} \cup \partial R_{\sigma}$ and $\partial R_{u} \cap \partial R_{\sigma} = \varnothing$. The total dislocation fields are given as the sum of the individual dislocation fields as

$$\tilde{\mathbf{u}} = \sum_{i} \tilde{\mathbf{u}}^{i}, \quad \tilde{\varepsilon} = \sum_{i} \tilde{\varepsilon}^{i}, \quad \tilde{\boldsymbol{\sigma}} = \sum_{i} \tilde{\boldsymbol{\sigma}}^{i} \tag{2.7}$$

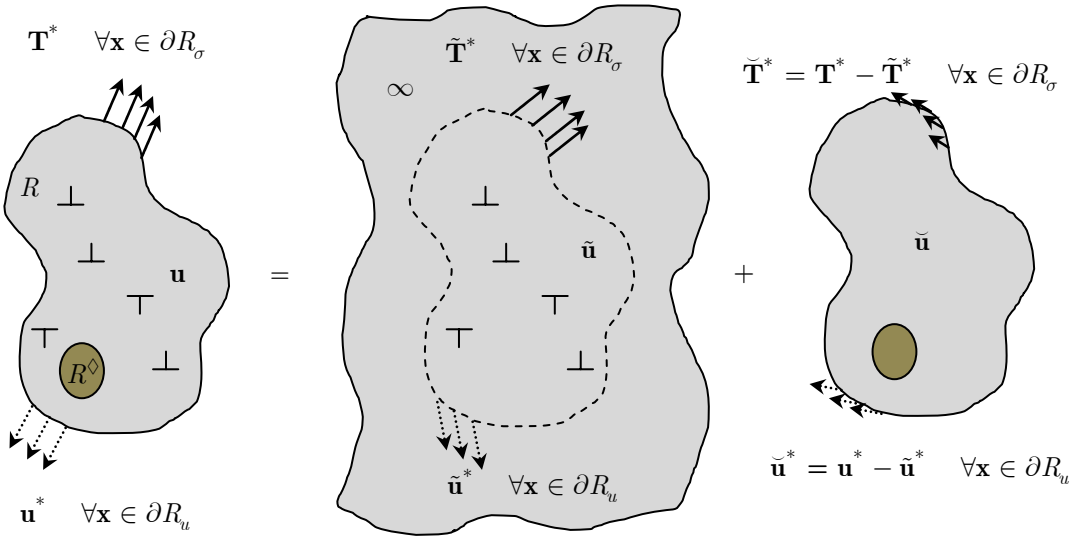

Figure 2.1: Decomposition of the total fields for a discrete dislocation dynamics problem into the dislocation ($\tilde{\bullet}$) and corrective ($\breve{\bullet}$) components. Gray matrix phase (R^M) and brown elastic dislocation-free inclusion phase ($R^\diamond$).

The ($\tilde{\bullet}$) fields are determined for an infinite homogeneous (inclusion-free) matrix material based on the current dislocation configuration (see Figure 2.1) and the governing equations for this sub-problem are given as

$$\left.\begin{array}{l} \vec{\nabla} \cdot \tilde{\boldsymbol{\sigma}} = \mathbf{0} \\ \\ \tilde{\boldsymbol{\sigma}} = \tilde{\boldsymbol{\sigma}}^T \end{array}\right\} \quad \forall \mathbf{x} \in R = R^M \cup R^\diamond \tag{2.8}$$

$$\tilde{\boldsymbol{\sigma}} = \mathbb{C} : \tilde{\boldsymbol{\varepsilon}} \qquad \forall \mathbf{x} \in R \tag{2.9}$$

$$\mathbf{u} = \tilde{\mathbf{u}}^* \qquad \forall \mathbf{x} \in \partial R_u \tag{2.10}$$

$$\mathbf{T} = \hat{\mathbf{n}} \cdot \tilde{\boldsymbol{\sigma}} = \tilde{\mathbf{T}}^* \qquad \forall \mathbf{x} \in \partial R_\sigma \tag{2.11}$$

where $\mathbb{C}$ is the 4th rank tensor of elastic moduli for the matrix material. Solving for the dislocation fields is simplified by the fact that analytical solutions exist for dislocations embedded in an elastically isotropic infinite medium. The dislocation displacement, $\tilde{\mathbf{u}}^*$, and traction fields, $\tilde{\mathbf{T}}^*$, are those that result on the

actual surface of the body due to the presence of dislocations. The governing equations for the corrective fields are then given as

$$\left.\begin{array}{l} \vec{\nabla}\cdot\breve{\boldsymbol{\sigma}} = \mathbf{0} \\ \\ \breve{\boldsymbol{\sigma}} = \breve{\boldsymbol{\sigma}}^{T} \end{array}\right\} \quad \forall \mathbf{x} \in R = R^{M} \cup R^{\Diamond} \tag{2.12}$$

$$\mathbf{u} = \breve{\mathbf{u}}^{*} = \mathbf{u}^{*} - \tilde{\mathbf{u}}^{*} \qquad \forall \mathbf{x} \in \partial R_{u} \tag{2.13}$$

$$\mathbf{T} = \hat{\mathbf{n}}\cdot\breve{\boldsymbol{\sigma}} = \breve{\mathbf{T}}^{*} = \mathbf{T}^{*} - \tilde{\mathbf{T}}^{*} \qquad \forall \mathbf{x} \in \partial R_{\sigma} \tag{2.14}$$

$$\begin{array}{ll} \breve{\boldsymbol{\sigma}} = \mathbb{C} : \breve{\boldsymbol{\varepsilon}} & \forall \mathbf{x} \in R^{M} \\ \\ \breve{\boldsymbol{\sigma}} = \mathbb{C}^{\Diamond} : \breve{\boldsymbol{\varepsilon}} + (\mathbb{C}^{\Diamond} - \mathbb{C}) : \tilde{\boldsymbol{\varepsilon}} & \forall \mathbf{x} \in R^{\Diamond} \end{array} \tag{2.15}$$

where $\mathbb{C}^{\Diamond}$ is the 4th rank elasticity tensor for the elastic inclusions. It is noted that the corrective stress field for the inclusions contains a term (2nd term in Eq. $(2.15)_2$) that is due to the dislocation strain fields and the difference in elastic properties between the matrix and inclusion phases. Given that the dislocation displacement fields remain continuous on ∂R_{u} and along the interface between the matrix and inclusion, Eqs. (2.12)-(2.14) constitute a well-posed linear elastic boundary value problem that can be solved using the finite element procedure outlined in Lubarda et al. [60]. Once the stress fields are known, the glide component of the Peach-Koehler force is computed according to

$$\mathbf{f}^{i} = \mathbf{n}^{i}\cdot\left(\tilde{\boldsymbol{\sigma}} + \sum_{j\neq i}\boldsymbol{\sigma}^{j}\right)\cdot\mathbf{b}^{i} \tag{2.16}$$

where the first term inside the parenthesis is the stress due to external loading and the second term accounts for the stress fields produced by all of the individual dislocations (excluding the one under consideration).

The dislocation configuration is then updated through an appropriate set of constitutive relations. Dislocation generation is accommodated by activation from point sources which are randomly distributed with source density, ϱ_{src}, throughout the matrix material. A source is activated when the source strength, τ_{nuc}, is exceeded by the shear stress acting at the source over a time period of t_{nuc}. Nucleation consists of

the creation of a dipole where the oppositely signed dislocations are placed at a distance, l_{nuc}, apart (each dislocation is placed at a distance of $l_{nuc} / 2$ on either side of the source) to balance the critical source stress. This critical distance is defined as

$$l_{nuc} = \frac{\mu}{2\pi(1-\nu)} \frac{b}{\tau_{nuc}} \tag{2.17}$$

The dislocation glide velocity, $\overline{\mathbf{v}}^i$, is assumed to be linearly related to the Peach-Koehler force according to

$$\overline{\mathbf{v}}^i = B^{-1}\mathbf{f}^i \tag{2.18}$$

where B is a drag coefficient. A glide dislocation may become trapped at point obstacles which are characterized by an obstacle strength, τ_{obs}, and will remain pinned until the resolved shear stress acting on the lead dislocation exceeds the obstacle strength. Mutual annihilation of dislocations is specified to occur when two oppositely signed dislocations are separated by a distance less than or equal to the critical annihilation distance, y_c. Additional constitutive assumptions specifying the initial state of the simulated crystal are required such as: the slip plane spacing, the initial dislocation density, the spatial distribution of dislocation sources and obstacles, and the statistical distribution of source and obstacle strengths.

Discrete dislocation dynamics simulations are widely used to study the scale-dependent mechanical behavior of crystalline materials, and they are capable of capturing both statistical and nonlocal aspects of the deformation. The statistical aspects emerge due to the initial dislocation and source configurations, whereas the nonlocality arises due to long-range dislocation forces. Although the length and time scales currently capable of being simulated are somewhat limited by the *n*-body nature of the problem and the time discretization required to accurately capture the transients of dislocation motion, discrete dislocation models are a useful tool for benchmarking and calibrating nonlocal crystal plasticity models.

2.3 Classical Single Crystal Plasticity

2.3.1 Kinematics

The traditional theory of single crystal plasticity is based on three fundamental assumptions: (i) a two-term decomposition of the total deformation into elastic and plastic parts (ii) the plastic deformation is given as the sum of individual slips (shears) on a discrete number of active slip systems and (iii) the lattice deformation is equal to the elastic material deformation. The usual two-term multiplicative decomposition of the deformation gradient, $\mathbf{F}$, into elastic, $\mathbf{F}^{\mathrm{e}} = \mathbf{I} + \mathbf{H}^{\mathrm{e}}$, and plastic, $\mathbf{F}^{\mathrm{p}} = \mathbf{I} + \mathbf{H}^{\mathrm{p}}$, parts in a geometrically linear ($\left\|\mathbf{H}^{\mathrm{e}}\right\|, \left\|\mathbf{H}^{\mathrm{p}}\right\| \ll 1$) setting leads to the approximation

$$\mathbf{F} = \mathbf{I} + \mathbf{H} = \mathbf{F}^{\mathrm{e}} \cdot \mathbf{F}^{\mathrm{p}} \approx \mathbf{I} + \mathbf{H}^{\mathrm{e}} + \mathbf{H}^{\mathrm{p}} \tag{2.19}$$

where $\mathbf{H} = \mathbf{u}\overset{\leftarrow}{\nabla}$, $\mathbf{H}^{\mathrm{e}}$ and $\mathbf{H}^{\mathrm{p}}$ are the total, elastic and plastic distortions, respectively. As shown in Figure 2.2, a material vector, $d\mathbf{X}$, is transformed under a given deformation into the vector $d\mathbf{x}$ according to

$$d\mathbf{x} = \mathbf{F} \cdot d\mathbf{X} = d\mathbf{X} + (\boldsymbol{\varepsilon} + \boldsymbol{\omega}) \cdot d\mathbf{X} = d\mathbf{X} + (\mathbf{H}^{\mathrm{e}} + \mathbf{H}^{\mathrm{p}}) \cdot d\mathbf{X} \tag{2.20}$$

where the additive decomposition of the total distortion into the infinitesimal strain, $\boldsymbol{\varepsilon} = \mathrm{sym}(\mathbf{H})$, and linear rotation, $\boldsymbol{\omega} = \mathrm{skw}(\mathbf{H})$, tensors has been stated in Eq. $(2.20)_2$. According to (iii), it is assumed that the lattice deformation is equal to the elastic material deformation, $\mathbf{H}^{\mathrm{e}}$, which implies that during deformation an arbitrary lattice vector, $\mathbf{D}^{\alpha}$, is transformed according to

$$\mathbf{d}^{\alpha} = \mathbf{F}^{\mathrm{e}} \cdot \mathbf{D}^{\alpha} = \mathbf{D}^{\alpha} + \mathbf{H}^{\mathrm{e}} \cdot \mathbf{D}^{\alpha} \tag{2.21}$$

where $\mathbf{d}^{\alpha}$ is the deformed lattice vector. As in Eq. $(2.20)_2$ the elastic distortion can be additively decomposed into strain and rotation components, i.e., $\mathbf{H}^{\mathrm{e}} = \boldsymbol{\varepsilon}^{\mathrm{e}} + \boldsymbol{\omega}^{\mathrm{e}}$, such that the lattice rotation is given by $\boldsymbol{\omega}^{\mathrm{e}}$. Any rigid body rotations are encompassed in $\mathbf{H}^{\mathrm{e}}$ via $\boldsymbol{\omega}^{\mathrm{e}}$ so that lattice vectors follow material

vectors under such motions, accordingly, the intermediate configuration defined by $\mathbf{F}^{\mathrm{p}}$ in Figure 2.2 is isoclinic. The temporal evolution of the plastic distortion due to dislocation glide is given as [10]

$$\dot{\mathbf{H}}^{\mathrm{p}} = \sum_{\alpha} \dot{\gamma}^{\alpha} \mathbf{s}^{\alpha} \otimes \mathbf{n}^{\alpha} \tag{2.22}$$

where $\dot{\gamma}^{\alpha}$, $\mathbf{s}^{\alpha}$, and $\mathbf{n}^{\alpha}$ are the (signed) slip system shearing rate and unit vectors in the shearing and slip plane normal directions, respectively, for the α^{th} slip system.

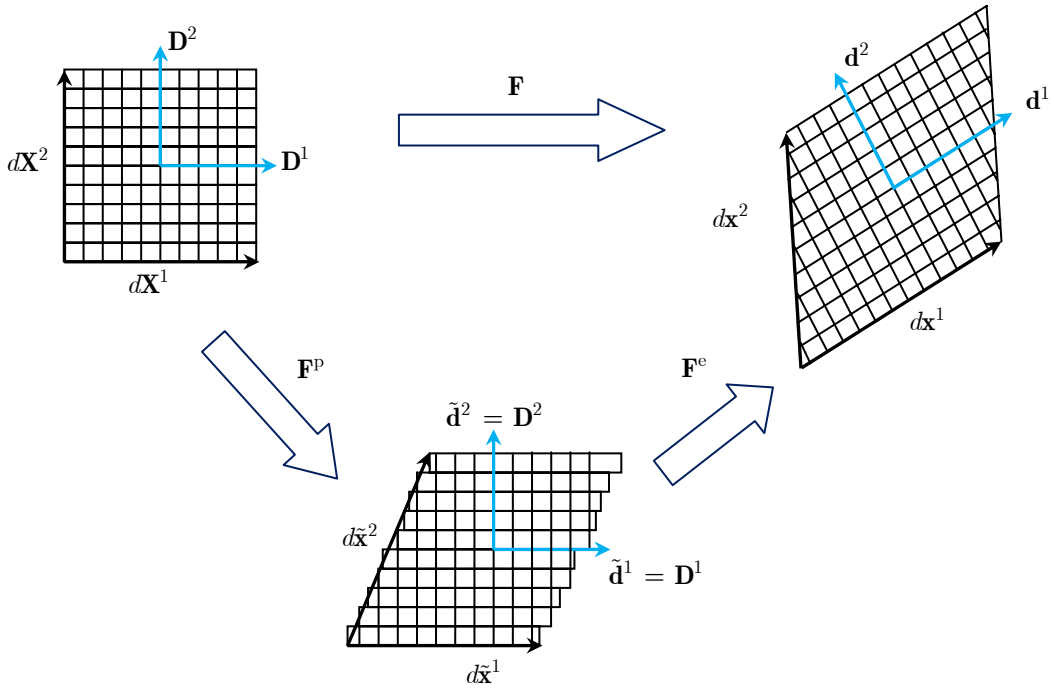

Figure 2.2: Elastic-plastic kinematics for the classical theory of single crystal plasticity.

2.3.2 Balance Laws and Thermodynamics

The classical balances of linear and angular momentum for a nonpolar body in static equilibrium and in the absence of body forces are stated as

$$\left.\begin{array}{l} \vec{\nabla}\cdot\boldsymbol{\sigma}=\mathbf{0} \\ \\ \boldsymbol{\sigma}=\boldsymbol{\sigma}^{T} \end{array}\right\} \quad \forall \mathbf{x}\in R \tag{2.23}$$

where $\boldsymbol{\sigma}$ is the Cauchy stress. The boundary value problem admits the usual natural and essential boundary conditions, respectively, on appropriate parts of the external surface, ∂R, i.e.,

$$\mathbf{T}=\hat{\mathbf{n}}\cdot\boldsymbol{\sigma}=\mathbf{T}^{*} \qquad \forall \mathbf{x}\in \partial R_{\sigma} \tag{2.24}$$

$$\mathbf{u}=\mathbf{u}^{*} \qquad \forall \mathbf{x}\in \partial R_{u} \tag{2.25}$$

where $\mathbf{T}$ is the traction vector, $\mathbf{T}^{*}$ is the applied traction, $\hat{\mathbf{n}}$ is the unit normal to the bounding surface, ∂R_{σ}, where tractions are applied, and $\mathbf{u}^{*}$ are the prescribed tractions and displacements on the complementary portion of the boundary, ∂R_{u}, and $\partial R=\partial R_{\sigma}\cup\partial R_{u}$.

A set of constitutive relations is proposed within a thermodynamic setting considering isothermal processes and neglecting other forms of energy production. The 2nd Law inequality under these conditions states that the deformation power must be greater than or equal to the rate of change in the free energy of the system, i.e.,

$$\mathfrak{p}_{I}\geq\rho\dot{\psi} \qquad \forall \mathbf{x}\in R \tag{2.26}$$

where, $\mathfrak{p}_{I}=\boldsymbol{\sigma}:\dot{\boldsymbol{\varepsilon}}$, is the deformation power, ρ is the mass density, and is the ψ is the Helmholtz free energy. Assuming that the free energy depends on the elastic strains and a set of scalar strain-like internal state variables (ISVs), ζ_{I}^{α}, for each slip system, i.e., $\psi=\hat{\psi}(\boldsymbol{\varepsilon}^{\mathrm{e}},\zeta_{I}^{\alpha})$, where the subscript signifies the I^{th} ISV, $I=1, 2, \ldots, N$ it can be shown via standard thermodynamic arguments [61] that the state laws are given by

$$\boldsymbol{\sigma}=\rho\frac{\partial\psi}{\partial\boldsymbol{\varepsilon}^{\mathrm{e}}} \quad , \quad \chi_{I}^{\alpha}=\rho\frac{\partial\psi}{\partial\zeta_{I}^{\alpha}} \tag{2.27}$$

where χ_I^α are the thermodynamic forces work-conjugate to the thermodynamic displacements, ζ_I^α, and the reduced dissipation inequality is given as

$$\mathfrak{d} = \boldsymbol{\sigma} : \dot{\boldsymbol{\varepsilon}}^{\mathrm{p}} - \sum_\alpha \sum_I \chi_I^\alpha \dot{\zeta}_I^\alpha \geq 0 \tag{2.28}$$

The ζ_I^α, reflect microstructural evolution that leads to energy storage in addition to that embodied by the recoverable elastic strains, $\boldsymbol{\varepsilon}^{\mathrm{e}}$.

2.3.3 Constitutive Equations

The plastic strain evolution equation for an associative theory of single crystal plasticity may be cast in a general form as

$$\dot{\boldsymbol{\varepsilon}}^{\mathrm{p}} = \sum_\alpha \dot{\lambda}^\alpha \frac{\partial F^\alpha}{\partial \boldsymbol{\sigma}} = \sum_\alpha \dot{\lambda}^\alpha \mathbf{N}^\alpha \tag{2.29}$$

where $\dot{\lambda}^\alpha$, F^α, and $\mathbf{N}^\alpha$ are the plastic parameter, yield function (also the flow potential in the associated flow case), and plastic flow direction for the α^{th} slip system, respectively. Since $\dot{\boldsymbol{\varepsilon}}^{\mathrm{p}} = \mathrm{sym}(\dot{\mathbf{H}}^{\mathrm{p}})$, it can be asserted with the aid of Eq. (2.22) that

$$F^\alpha = \left| \tau^\alpha - \tau_b^\alpha \right| - r^\alpha \tag{2.30}$$

$$\tau^\alpha = \mathbf{n}^\alpha \cdot \boldsymbol{\sigma} \cdot \mathbf{s}^\alpha = \boldsymbol{\sigma} : \mathbf{P}^\alpha \tag{2.31}$$

$$\mathbf{N}^\alpha = \mathbf{P}^\alpha \,\mathrm{sgn}\left(\tau^\alpha - \tau_b^\alpha \right) \tag{2.32}$$

$$\dot{\gamma}^\alpha = \dot{\lambda}^\alpha \,\mathrm{sgn}(\tau^\alpha - \tau_b^\alpha) \tag{2.33}$$

where τ^α is the resolved shear stress, τ_b^α is the slip system back stress, r^α is a slip threshold stress defining the elastic domain in stress space, and $\mathbf{P}^\alpha = \mathrm{sym}(\mathbf{s}^\alpha \otimes \mathbf{n}^\alpha)$ is the Schmid tensor. The expression in Eq. $(2.31)_2$ may be written in this form due to the symmetry of the Cauchy stress tensor and

elucidates the plastic flow direction as the derivative of a flow potential. A rate-dependent formulation is adopted and the plastic parameter is given by the power law overstress function as

$$\dot{\lambda}^{\alpha} = \dot{\gamma}_0 \left(\left\langle F^{\alpha} \right\rangle \Big/ g^{\alpha} \right)^m \qquad \left\langle x \right\rangle = \begin{cases} x & \forall x \geq 0 \\ 0 & \forall x < 0 \end{cases} \tag{2.34}$$

where $\dot{\gamma}_0$ is a reference shearing rate, g^{α} is a drag stress, and m is the inverse strain rate sensitivity exponent. The threshold stress is given by the Taylor relation, i.e.,

$$r^{\alpha} = r_0^{\alpha} + \mu c_1 b \sqrt{\sum\nolimits_{\beta} h^{\alpha\beta} \varrho^{\beta}} \tag{2.35}$$

where r_0^{α} is the intrinsic lattice resistance to slip, c_1 is a material constant related to the dislocation configuration, μ is the shear modulus, b is the magnitude of the Burgers vector, $h^{\alpha\beta}$ is an slip system interaction matrix, and ϱ^{β} is the total dislocation density on slip system β. The dislocation density evolution equation is taken to be of the Kocks-Mecking [62] form as a competition between storage due to dislocation trapping and annihilation due to dynamic recovery, i.e.,

$$\dot{\varrho}^{\alpha} = \frac{1}{b} \left(\frac{1}{l^{\alpha}} - 2 y_c \varrho^{\alpha} \right) \left| \dot{\gamma}^{\alpha} \right| \tag{2.36}$$

where l^{α} is the mean free path for mobile dislocations and y_c is the capture radius for the annihilation of oppositely signed dislocations. The mean free path for dislocations is defined as

$$l^{\alpha} = \frac{K}{\sqrt{\sum\nolimits_{\beta} a^{\alpha\beta} \varrho^{\beta}}} \tag{2.37}$$

where K is material parameter and $a^{\alpha\beta}$ is an interaction matrix defining the potency of dislocations on slip system β for trapping dislocations on slip system α [63]. A typical phenomenological description of back stress evolution used in classical crystal plasticity models is an appropriate adaptation of the

Armstrong-Frederick [64] law for each slip system with the assumption of self-hardening due to dislocations of like sign on the same system, i.e.,

$$\dot{\tau}_b^\alpha = B\dot{\gamma}^\alpha - C\tau_b^\alpha \mid \dot{\gamma}^\alpha \mid \tag{2.38}$$

where B and C are direct hardening and dynamic recovery coefficients, respectively. Equation (2.38) can be transformed into a dislocation-based one by postulating a relationship between the back stress and a signed dislocation density, $\varrho_\pm^\alpha$, that is interpreted as a phenomenological geometrically necessary dislocation density, i.e.,

$$\tau_b^\alpha = \mu c_2 b \sqrt{\mid \varrho_\pm^\alpha \mid} \operatorname{sgn}(\varrho_\pm^\alpha) \tag{2.39}$$

where c_2 is a dislocation configuration-dependent material constant. Equations (2.38) and (2.39) are connected through the signed dislocation density evolution equation which is specified as

$$\dot{\varrho}_\pm^\alpha = \left[c_3 \sqrt{\mid \varrho_\pm^\alpha \mid} \operatorname{sgn}(\tau^\alpha - \tau_b^\alpha) - c_4 \varrho_\pm^\alpha \right] \mid \dot{\gamma}^\alpha \mid \tag{2.40}$$

where c_3 and c_4 are material constants defining the accumulation and annihilation rates, respectively, of the signed dislocation density. Time differentiation of Eq. (2.39), insertion of Eq (2.40), and then comparing the resulting expression to Eq. (2.38) leads to the interpretation of the phenomenological constants in terms of the dislocation-based ones as

$$B = \frac{c_2 c_3 \mu b}{2} \quad , \quad C = \frac{c_4}{2} \tag{2.41}$$

While the signed dislocation density, $\varrho_\pm^\alpha$, can be thought of as a type of geometrically necessary dislocation density, it should not be confused with *the* geometrically necessary dislocation density that is required to maintain compatibility of the total deformation field, as discussed in Section 2.4.2.

It is assumed that two scalar ISVs are needed to describe the energy storage due to microstructure evolution; one each for the total and signed dislocation densities, i.e.,

$$\zeta_1^\alpha = c_1 b\sqrt{\textstyle\sum_\beta h^{\alpha\beta}\varrho^\beta} \tag{2.42}$$

$$\zeta_2^\alpha = c_2 b\sqrt{|\ \varrho_\pm^\alpha\ |}\,\mathrm{sgn}(\varrho_\pm^\alpha) \tag{2.43}$$

The variable ζ_1^α is defined as the short-range elastic strain field on slip system α produced by dislocations on all other slip systems, and ζ_2^α is the pseudo long-range strain field produced by dislocation pileups lying on slip system α. Introducing a free energy function with quadratic dependence on its arguments, i.e.,

$$\psi_v = \tfrac{1}{2}\boldsymbol{\varepsilon}^{\mathrm{e}} : \mathbb{C} : \boldsymbol{\varepsilon}^{\mathrm{e}} + \tfrac{1}{2}\sum_\alpha\sum_\beta(\zeta_1^\alpha E_1^{\alpha\beta}\zeta_1^\beta + \zeta_2^\alpha E_2^{\alpha\beta}\zeta_2^\beta) \tag{2.44}$$

where, $\psi_v = \rho\psi$, is the free energy per unit volume, $\mathbb{C}$ is the 4[th] rank tensor of elastic moduli, and $E_I^{\alpha\beta}$ $I = 1,2$ are symmetric positive-definite matrices of material moduli with units of force/length^2. Inserting Eq. (2.44) into Eq. (2.27) leads to explicit state laws, i.e.,

$$\boldsymbol{\sigma} = \mathbb{C} : \boldsymbol{\varepsilon}^e \quad , \quad \chi_1^\alpha = \sum_\beta E_1^{\alpha\beta}\zeta_1^\beta \quad , \quad \chi_2^\alpha = \sum_\beta E_2^{\alpha\beta}\zeta_2^\beta \tag{2.45}$$

Assuming that $E_1^{\alpha\beta} = E_2^{\alpha\beta} = \mu\delta^{\alpha\beta}$, it is seen that $\chi_1^\alpha = r^\alpha$ and $\chi_2^\alpha = \tau_b^\alpha$. Considering Eqs.(2.42), (2.43), (2.36), and (2.31) the reduced dissipation inequality for the single ISV constitutive model may be expressed as

$$\mathfrak{d} = \sum_\alpha\left(\tau^\alpha - \frac{c_2 c_3 b}{2}\tau_b^\alpha\right)\dot{\gamma}^\alpha - \sum_\alpha\sum_\beta\left(r^\alpha H^{\alpha\beta} - \frac{c_4}{2}\tau_b^\alpha\zeta_2^\alpha\delta^{\alpha\beta}\right)\left|\dot{\gamma}^\beta\right| \geq 0 \tag{2.46}$$

where $H^{\alpha\beta}$ is defined as

$$H^{\alpha\beta} = \frac{c_1}{2}\frac{h^{\alpha\beta}}{\sqrt{\sum_\delta h^{\alpha\delta}\varrho^\delta}}\left(\frac{1}{K}\sqrt{\textstyle\sum_\xi a^{\beta\xi}\varrho^\xi} - 2y_c\varrho^\beta\right) \tag{2.47}$$

The first term in Eq. (2.46) is the rate of energy dissipated by plastic deformation, and the second term is the rate of energy stored due to microstructural evolution.

Physically, the product term $r^{\alpha}\zeta_1^{\alpha}$ is the energy stored due to the short-range interactions of dislocations lying in slip plane α and can be related to the self-energy of the dislocation configuration. To elucidate this fact, consider the expression for the self-energy per unit length, $E_d \,/\, l_d$, of a dislocation as expressed in dislocation theory [65], i.e.,

$$E_d \,/\, l_d = c_5 \mu b^2 \tag{2.48}$$

where c_5 is a numerical constant that depends on the dislocation configuration and character. The total line length, l_d, of dislocations in a given volume, V, is given as

$$l_d = \varrho V \tag{2.49}$$

where $\varrho = \sum_{\alpha} \varrho^{\alpha}$. Therefore, the dislocation energy per unit volume of material may be expressed as

$$E_d \,/\, V = c_5 \mu b^2 \varrho \tag{2.50}$$

Now consider the energy per unit volume stored due to microstructural rearrangement, ψ_v^m, (the second term in Eq. (2.44)), i.e.,

$$\psi_v^m \equiv \sum_{\alpha} r^{\alpha}\zeta_1^{\alpha} = \mu c_1^2 b^2 \sum_{\alpha}\sum_{\beta} h^{\alpha\beta}\varrho^{\beta} \tag{2.51}$$

The two expressions given in Eqs. (2.50) and (2.51) are equivalent if the constant c_5 is specified such that

$$c_5 = c_1^2 \frac{\sum_{\alpha}\sum_{\beta} h^{\alpha\beta}\varrho^{\beta}}{\sum_{\delta}\varrho^{\delta}} \tag{2.52}$$

Equation (2.52) shows that the constant c_5 is function of the current microstructural state via the dislocation density. On the other hand, the product $\tau_b^{\alpha}\zeta_2^{\alpha}$ is the energy stored due to long-range effects on slip system α, i.e., those due to dislocation pileup effects.

2.4 Generalized Single Crystal Plasticity

There are a variety of ways in which generalized theories of crystal plasticity can be constructed, and this is reflected by the diversity of the models that can be found in the literature. Accordingly, it is beneficial to introduce a classification system as in Kuroda and Tvergaard [66] which delineates broadly between three classes of models: low-order theories, non-work-conjugate theories, and work-conjugate theories. Low-order theories incorporate nonlocality into the constitutive response while maintaining the classical structure of the mechanical balance equations and do not admit non-standard boundary conditions. Such models are incapable of predicting size-dependent mechanical behavior for a homogeneous material subjected to uniform remote boundary conditions. Non-work-conjugate theories are defined as those that maintain the classical structure of the mechanical balance laws, but include additional non-mechanical balance equations. The class of work-conjugate continua is comprised of models with non-standard expressions of deformation power and mechanical balance laws; examples include second or n^{th} gradient models and generalized micromorphic models with the distinction that grade-n theories incorporate higher-order derivatives of the usual displacement degrees-of-freedom, whereas the latter introduce additional micro degrees-of-freedom that are independent of the displacement field.

Classical single crystal plasticity is extended to account for scale effects by appealing to the concept of geometrically necessary dislocations (GNDs) [11]. From a purely kinematic point of view, the origins of the connection between heterogeneous states of deformation, deformation incompatibility, and geometrically necessary dislocations can be traced back to the early works of Kondo[67], Bilby et al. [68], and Kröner [69], amongst others, whereas the connection between GNDs and lattice curvature can be traced back to the work of Nye [70]. According to Ashby [11], GNDs lead to increases of both isotropic and kinematic hardening by further reducing the mean free path of mobile dislocations and by virtue of the long-range nature of their associated stress fields; however, there are many models that neglect GND effects on kinematic hardening. Disregarding this aspect of material strengthening is questionable as the long-range and directional nature of the internal stress fields induced by GNDs is unequivocal and deemed critically important by many; Mughrabi [71] noted that the inclusion of GND-enhanced isotropic hardening

by itself is insufficient to properly model scale-dependent mechanical behavior. While most nonlocal theories have been applied to boundary value problems involving forward uniaxial loading, thereby making the two hardening contributions difficult to distinguish, an appropriate coupling of GNDs to back stresses is imperative to capturing material behavior during load reversal. Kinematic hardening due to the presence of GNDs has been incorporated into crystal plasticity models in a number of ways [17, 72-74], but with the commonality that the back stresses are related to *gradients* in the GND density. Representative generalized crystal plasticity models within the three previously described classes are the low-order theories due to [19, 21, 22, 75], the non-work-conjugate theories due to [14, 73, 76-79] and the work-conjugate theories due to [17, 25, 28, 29, 31, 34, 36, 80, 81].

The GND density tensor used in nonlocal crystal plasticity theories can be derived from the mathematical compatibility requirements of deformation measures; however, it is instructive to first examine the GND density tensor from the discrete dislocation perspective. The presentation and discussion of Section 2.4.1 follows closely to the seminal 1999 contribution of Arsenlis and Parks [82].

2.4.1 The Discrete Geometrically Necessary Dislocation Density Tensor

In 1953, Nye [70] introduced a tensorial measure of the dislocated state of the lattice [70]. Nye's tensor, like the usual dislocation density familiar to metallurgists and materials scientists, must be evaluated over a reference volume of material and is a function of the Burgers and line tangent vectors of all of the dislocations contained within the volume. Considering a single straight (constant line tangent vector) dislocation which extends across a volume of characteristic length, l, which is perpendicular to and pierces opposing faces of the cube, Nye's tensor, $\boldsymbol{\alpha}$, is defined as

$$\boldsymbol{\alpha} = \varrho\, \mathbf{b} \otimes \boldsymbol{\xi} \tag{2.53}$$

where $\varrho = 1 / l^2$, $\mathbf{b}$ is the Burgers vector of the dislocation, and $\boldsymbol{\xi}$ is the unit tangent vector directed along the dislocation line in the right-hand screw sense. If a volume of material containing an ensemble of dislocations is considered, then Nye's tensor is defined by the line integral over *all* dislocation segments within the volume as

$$\boldsymbol{\alpha} = \frac{1}{V}\sum_{i}\int_{\Gamma} \mathbf{b}^{i} \otimes \boldsymbol{\xi}^{i} dl^{i} \tag{2.54}$$

It is seen that Eq. (2.53) is just a special case of the more general definition given in Eq. (2.54). From this definition it becomes clear that Nye's dislocation density tensor is an aggregate measure for all dislocations contained within the volume; and that as pointed out by Arsenlis and Parks [82], the inverse problem of determining the exact dislocation distribution for a volume of material given the components of $\boldsymbol{\alpha}$ does not have a unique solution. In fact, as shown by Kröner [83], the scalar dislocation density (total line length per unit volume) and Nye's dislocation density tensor are just two different invariants of various statistical moments of the dislocation distribution in a given volume. Furthermore, if each dislocation segment can be treated individually as having a constant Burgers vector, the definition of Nye's tensor given in Eq. (2.54) can be expressed as

$$\boldsymbol{\alpha} = \frac{1}{V}\sum_{i} \mathbf{b}^{i} \otimes \int_{\Gamma} \boldsymbol{\xi}^{i} dl^{i} \tag{2.55}$$

As a consequence of being expressed in this form, the integrated properties of Nye's tensor are revealed. For example, consider the generally curved dislocation threading the reference volume shown in Figure 2.3, and applying Eq. (2.55) to evaluate Nye's tensor over this volume yields

$$\boldsymbol{\alpha} = \frac{1}{V}\mathbf{b} \otimes (\mathbf{r}^{+} - \mathbf{r}^{-}) \tag{2.56}$$

where $\mathbf{r}^{+}$ and $\mathbf{r}^{-}$ are the coordinate positions of the beginning and end points of the dislocation segments on the boundaries of the volume, as defined by the direction of integration in Eq. (2.55). Equation (2.56) shows that the Burgers vector and the two threading points are all that is needed to calculate an individual dislocation segment's contribution to Nye's tensor, and that the actual path of the segment has no consequence on the calculation. This reinforces the earlier comment that given the components of Nye's tensor over the volume (the straight red dash-dotted line in Figure 2.3), the total dislocation distribution (the generally curved path between the two end points) cannot be uniquely determined. Making use of Eq.

(2.56), Eq. (2.55) may be expressed for a population of dislocation segments in terms of the *average* tangent vector, $\overline{\boldsymbol{\xi}}^i$, and the secant length, $\overline{l}^i$, as

$$\boldsymbol{\alpha} = \frac{1}{V}\sum_i \overline{l}^i \mathbf{b}^i \otimes \overline{\boldsymbol{\xi}}^i \tag{2.57}$$

where

$$\overline{\boldsymbol{\xi}}^i = \frac{\mathbf{r}^{i+} - \mathbf{r}^{i-}}{\left\|\mathbf{r}^{i+} - \mathbf{r}^{i-}\right\|} \quad , \quad \overline{l}^i = \left\|\mathbf{r}^{i+} - \mathbf{r}^{i-}\right\| \tag{2.58}$$

Introducing a scalar measure of the discrete GND density for a given segment as

$$\varrho_{GD}^i = \frac{\overline{l}^i}{V}, \tag{2.59}$$

Nye's tensor can also be written in the form

$$\boldsymbol{\alpha} = \sum_i \varrho_{GD}^i \mathbf{b}^i \otimes \overline{\boldsymbol{\xi}}^i \tag{2.60}$$

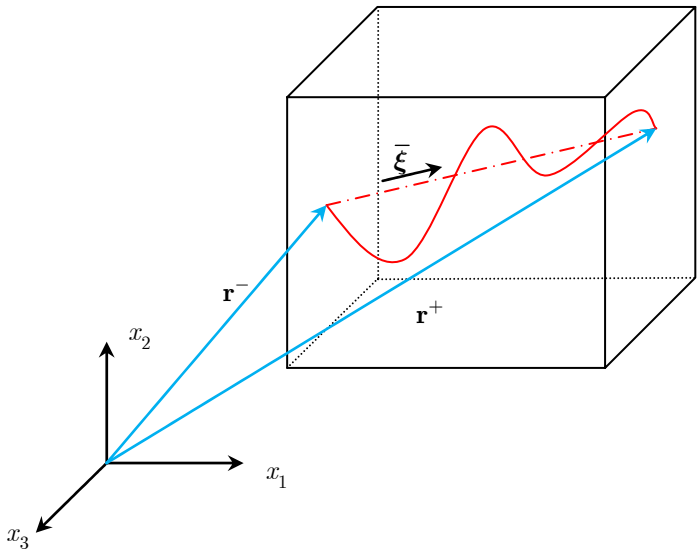

Figure 2.3: Demonstration of the geometrically necessary dislocation density (dash-dot straight red line) associated with the arbitrarily curved (solid red line) dislocation.

A natural measure of the discrete SSD density for each segment can then be defined as

$$\varrho^i_{SD} = \varrho^i - \varrho^i_{GD} \tag{2.61}$$

where the total dislocation density for each segment is defined in the usual manner as

$$\varrho^i = \frac{1}{V}\sum_i \int_\Gamma dl^i \tag{2.62}$$

Considering Eq. (2.61) and the dislocation segment shown in Figure 2.3, it is clear that the discrete SSD and GND densities cannot be thought of as belonging to separate dislocation populations - *a dislocation is neither geometrically necessary or statistically stored* - rather they are two different statistical moments of the total dislocation distribution within the volume under consideration.

The lattice-geometric consequences of Nye's tensor are illustrated by considering a single face of the reference volume. The integral over the enclosed area of the inner product of Nye's tensor with the plane normal gives the net Burgers vector, $\mathbf{B}$, of all dislocations piercing the plane, i.e.,

$$\mathbf{B} = \int_{\partial R} \boldsymbol{\alpha} \cdot \hat{\mathbf{n}} dA \tag{2.63}$$

Evaluating the surface integral in Eq. (2.63) over all of the surfaces of the reference volume and making use of the divergence theorem, the previous result leads directly to the conservation equation for Nye's tensor as

$$\boldsymbol{\alpha} \cdot \bar{\nabla} = \mathbf{0} \quad \forall \mathbf{x} \in V \tag{2.64}$$

which is interpreted as a statement of conservation of Burgers vector that implies that dislocations cannot terminate within the interior of a crystal. Finally, a representation of Nye's tensor for the special case of a dislocation population consisting entirely of straight, pure edge and screw segments with constant Burgers vector (e.g., fcc) is given in Eq. (2.65). This representation of the dislocated state of a crystal is employed in some discrete dislocation dynamics frameworks [53] and is often encountered in discussions of continuum measures of the GND density tensor. For a given slip system defined by the right-handed triad of vectors $(\mathbf{s}^\beta, \mathbf{n}^\beta, \mathbf{t}^\beta)$ where $\mathbf{t}^\beta$ is a unit vector defined as $\mathbf{t}^\beta = \mathbf{s}^\beta \times \mathbf{n}^\beta$ Nye's tensor is given for this special case as

$$\boldsymbol{\alpha} = b \sum_\beta \left(\varrho_\perp^\beta - \varrho_\top^\beta \right) \mathbf{s}^\beta \otimes \mathbf{t}^\beta + \left(\varrho_\odot^\beta - \varrho_\otimes^\beta \right) \mathbf{s}^\beta \otimes \mathbf{s}^\beta \tag{2.65}$$

where, $\varrho_\perp^\beta$, $\varrho_\top^\beta$ are the positive and negative edge densities and $\varrho_\odot^\beta$, $\varrho_\otimes^\beta$ are the positive and negative screw densities, respectively. For more general crystal structures (e.g., hcp), the Burgers vector is not constant and cannot be pulled outside of the summation. It is emphasized that the dislocation densities in Eq. (2.65) refer to the β^{th} slip system and not to the individual dislocation segments as in the previous developments of this section. In other words, each slip system density can be thought of as being the cumulative individual segment density lying within that system over the given volume.

2.4.2 Deformation Compatibility and the Continuum GND Density Tensor

Compatibility, i.e., the mathematical requirement for a single-valued global displacement field, on a standard continuum, is ensured if $\mathbf{H} \times \overset{\leftarrow}{\nabla} = \mathbf{u}\overset{\leftarrow}{\nabla} \times \overset{\leftarrow}{\nabla} = \mathbf{0}$. Therefore, a continuum measure of the deformation incompatibility is the continuous analog to the discrete GND density tensor, $\boldsymbol{\alpha}$, which was introduced in the Section 2.4.1 and is defined in this context as

$$\boldsymbol{\alpha} \equiv -\mathbf{H}^{\mathrm{e}} \times \overset{\leftarrow}{\nabla} = \mathbf{H}^{\mathrm{p}} \times \overset{\leftarrow}{\nabla} \tag{2.66}$$

The following reciprocal relationships between the GND density tensor and the lattice (elastic material) deformation can be established [82], i.e.,

$$\boldsymbol{\alpha} = -\boldsymbol{\kappa}^{T} + \mathrm{tr}(\boldsymbol{\kappa})\mathbf{1} - \boldsymbol{\varepsilon}^{\mathrm{e}} \times \overset{\leftarrow}{\nabla} \tag{2.67}$$

$$\boldsymbol{\kappa} = -\boldsymbol{\alpha}^{T} + \tfrac{1}{2}\mathrm{tr}(\boldsymbol{\alpha})\mathbf{1} - (\boldsymbol{\varepsilon}^{\mathrm{e}} \times \overset{\leftarrow}{\nabla})^{T} \tag{2.68}$$

where the lattice torsion-curvature is defined as

$$\boldsymbol{\kappa} = \boldsymbol{\phi}\overset{\leftarrow}{\nabla} \tag{2.69}$$

The lattice rotation (axial) vector, $\boldsymbol{\phi}$, is related to the lattice linear rotation tensor in the usual manner via the alternating tensor, $\boldsymbol{\epsilon}$, i.e., $\boldsymbol{\phi} = -1/2\,\boldsymbol{\epsilon} : \boldsymbol{\omega}^{e}$. The original relationships between the continuum GND density tensor and lattice torsion-curvature derived by Nye [70] neglected the elastic strain terms in Eqs. (2.67) and (2.68). Researchers frequently use the original expressions (neglecting the elastic strain term) to convert experimentally measured lattice orientations into GND densities cf. [84-88]. Expressed in terms of the plastic distortion (see Eq. (2.22)), the continuum GND density tensor is written as

$$\boldsymbol{\alpha} = b\sum_{\alpha}\left(\varrho_{G,\perp}^{\alpha}\mathbf{s}^{\alpha} \otimes \mathbf{t}^{\alpha} + \varrho_{G,\odot}^{\alpha}\mathbf{s}^{\alpha} \otimes \mathbf{s}^{\alpha}\right) \tag{2.70}$$

where the edge, $\varrho_{G,\perp}^{\alpha}$, and screw, $\varrho_{G,\odot}^{\alpha}$, GND densities are defined as gradients of slip projected in the respective glide directions for pure edge and screw dislocations, i.e.,

$$\varrho^{\alpha}_{G,\perp} = -\frac{1}{b}\vec{\nabla}\gamma^{\alpha}\cdot\mathbf{s}^{\alpha} \quad , \quad \varrho^{\alpha}_{G,\odot} = \frac{1}{b}\vec{\nabla}\gamma^{\alpha}\cdot\mathbf{t}^{\alpha} \tag{2.71}$$

Comparing Eqs. (2.70) and (2.71) to Eq. (2.65) leads to the following connection between the polarity of the discrete dislocation densities and the continuum gradients of slip, i.e.,

$$\varrho^{\alpha}_{G,\perp} = -\frac{1}{b}\vec{\nabla}\gamma^{\alpha}\cdot\mathbf{s}^{\alpha} = \varrho^{\alpha}_{\perp} - \varrho^{\alpha}_{\top} \tag{2.72}$$

$$\varrho^{\alpha}_{G,\odot} = \frac{1}{b}\vec{\nabla}\gamma^{\alpha}\cdot\mathbf{t}^{\alpha} = \varrho^{\alpha}_{\odot} - \varrho^{\alpha}_{\otimes} \tag{2.73}$$

The relationships in Eq. (2.71) and (2.73) may be used to incorporate nonlocality into the slip system hardening description, and are central to the slip gradient-based extensions of the classical theory.

2.4.3 Low-Order Theories

The distinguishing feature of low-order theories is that the classical structure of mechanical balance laws remains intact and no additional non-mechanical balance laws are introduced. The model enhancements are restricted to the material hardening description. Specifically, the constitutive equations are modified to account for the additional strain-hardening due to GNDs, and in most cases both isotropic and kinematic contributions are accounted for. To extend the model presented in Section 2.3 to incorporate isotropic hardening due to GNDs, for example, the total dislocation density on each slip system is written as the sum of SSDs and GNDs, i.e.,

$$\varrho^{\alpha} = \varrho^{\alpha}_{S} + \varrho^{\alpha}_{G} \tag{2.74}$$

Here, the total GND density is given in terms of the edge and screw GND densities as

$$\varrho^{\alpha}_{G} = \sqrt{\left(\varrho^{\alpha}_{G,\perp}\right)^2 + \left(\varrho^{\alpha}_{G,\odot}\right)^2} \tag{2.75}$$

Taking the time derivative of Eq.(2.75) and making use of the rate version of Eq. (2.71) yields the total GND density evolution equation, i.e.,

$$\dot{\varrho}_G^\alpha = \frac{1}{b\varrho_G^\alpha}\Big[\varrho_{G,\perp}^\alpha\left(-\vec{\nabla}\dot{\gamma}^\alpha\cdot\mathbf{s}^\alpha\right)+\varrho_{G,\odot}^\alpha\left(\vec{\nabla}\dot{\gamma}^\alpha\cdot\mathbf{t}^\alpha\right)\Big] \tag{2.76}$$

The SSD evolution equation is assumed to have the same functional form as in the classical theory (see Eq. (2.36)) such that

$$\dot{\varrho}_S^\alpha = \frac{1}{b}\left(\frac{1}{l^\alpha}-2y_c\varrho_S^\alpha\right)\left|\dot{\gamma}^\alpha\right| \tag{2.77}$$

where the mean free path, l^α, may be defined in one of two ways, i.e.,

$$l_1^\alpha = \frac{K}{\sqrt{\sum_\beta a^{\alpha\beta}\varrho_S^\beta}} \quad \text{or} \quad l_2^\alpha = \frac{K}{\sqrt{\sum_\beta a^{\alpha\beta}(\varrho_S^\beta+\varrho_G^\beta)}} \tag{2.78}$$

In the first definition, Eq. $(2.78)_1$, the mean free path is a function of only the SSD density, whereas in the second it is a function of the total density. Similarly, the slip threshold stress maybe defined in terms of the SSD or total densities as

$$r_1^\alpha = r_0^\alpha + \mu c_1 b\sqrt{\sum_\beta h^{\alpha\beta}\varrho_S^\beta} \quad \text{or} \quad r_2^\alpha = r_0^\alpha + \mu c_1 b\sqrt{\sum_\beta h^{\alpha\beta}(\varrho_S^\beta+\varrho_G^\beta)} \tag{2.79}$$

The particular choices that one makes regarding the definitions of the mean free path and the threshold stress are constitutive assumptions, and to date there has been no definitive answer as to which, if either, description is more appropriate. Clearly, if the combination (l_1^α, r_1^α) is chosen, then the isotropic hardening description remains classical, whereas any of the other combinations will include a nonlocal contribution.

In generalized crystal plasticity theories, the typical phenomenological back stress contribution used in many classical theories that is given in Eqs. (2.39)-(2.40) is often replaced by a more physical description that is derived considering the pseudo long-range internal stress fields generated by the GNDs [14, 72, 73, 89]. In these works, the back stress contribution at a material point is determined from a first-order (linear) approximation of the GND density distribution about the point in question which is assumed to be valid within a cylinder of radius R. The GND density linearization is used in conjunction with the analytical solutions for the stress fields produced by edge and screw dislocations to determine the total back

stress contribution via integration. The calculated internal stress fields are approximate since they are determined considering only the cylindrical region of influence defined by R, and also because the analytical stress field solutions are derived assuming an elastically isotropic infinite medium and a state of plane strain. The individual back stress components due to edge, $\tau^{\alpha}_{b,\perp}$, and screw $\tau^{\alpha}_{b,\odot}$, GND densities are considered separately such that the total back stress tensor, $\boldsymbol{\sigma}_b$, is expressed as

$$\boldsymbol{\sigma}_b = \sum_{\alpha} -(\tau^{\alpha}_{b,\perp} + \tau^{\alpha}_{b,\odot})(\mathbf{s}^{\alpha} \otimes \mathbf{n}^{\alpha} + \mathbf{n}^{\alpha} \otimes \mathbf{s}^{\alpha}) \tag{2.80}$$

and the resolved slip system back stress is given by

$$\tau^{\alpha}_{b} = \boldsymbol{\sigma}_b : (\mathbf{s}^{\alpha} \otimes \mathbf{n}^{\alpha}) \tag{2.81}$$

The edge and screw-related back stress components, respectively, are given as [14]

$$\tau^{\alpha}_{b,\perp} = -\frac{\mu b R^2}{8(1-\nu)} \sum_{\beta} d^{\alpha\beta}_{\perp} (\vec{\nabla} \varrho^{\beta}_{G} \cdot \mathbf{s}^{\alpha}) \tag{2.82}$$

$$\tau^{\alpha}_{b,\odot} = \frac{\mu b R^2}{4} \sum_{\beta} d^{\alpha\beta}_{\odot} (\vec{\nabla} \varrho^{\beta}_{G} \cdot \mathbf{t}^{\alpha}) \tag{2.83}$$

where ν is Poisson's ratio and $d^{\alpha\beta}_{\perp}$ and $d^{\alpha\beta}_{\odot}$ are matrices defining the relative shear stress contributions on the α^{th} system due to gradients of GND densities on the β^{th} slip system. These matrices are defined as

$$d^{\alpha\beta}_{\perp} = \begin{cases} 1 & \text{for } \alpha = \beta = 1,2,\ldots 12 \\ 0 & \text{otherwise} \end{cases} \tag{2.84}$$

$$d^{\alpha\beta}_{\odot} = \begin{cases} -1 & \text{for } (\alpha,\beta) = (4,13),(6,18),(8,17),(9,15),(10,16),(11,14) \\ 1 & \text{for } (\alpha,\beta) = (1,16),(2,17),(3,18),(5,14),(7,13),(12,15) \\ 0 & \text{otherwise} \end{cases} \tag{2.85}$$

The preceding developments are referred to as a "self-internal formulation" of the nonlocal back stress, and it is noted that further studies [72, 89] have sought to improve upon this approximation. However, Eqs. (2.82) and (2.83) suffice in highlighting the key features of this and related GND-induced back stress

formulations; namely, that the back stress is a function of *gradients* in GND densities (or second gradients of slip via Eq. (2.71)) and the intrinsic material length scale is given by the cut-off radius, R, which determines the region of influence of the pseudo long-range effects. It is to be understood here that pseudo refers to the fact that the calculation of the back stresses has been truncated.

To proceed with the thermodynamic analysis, certain decisions must be made regarding which versions of Eqs (2.78) and (2.79) will be employed. Rather than considering all of the possible combinations, a description of isotropic hardening based on $l^\alpha = l_2^\alpha$ and $r^\alpha = r_2^\alpha$ is pursued. Three ISVs are introduced to capture the stored energy due to microstructural rearrangement, i.e.,

$$\zeta_1^\alpha = c_1 b\sqrt{\textstyle\sum_\beta h^{\alpha\beta}(\varrho_S^\beta + \varrho_G^\beta)} \tag{2.86}$$

$$\zeta_2^\alpha = \frac{bR^2}{8(1-\nu)}\sum_\beta d_\perp^{\alpha\beta}(\vec{\nabla}\varrho_{G,\perp}^\beta \cdot \mathbf{s}^\alpha) \tag{2.87}$$

$$\zeta_3^\alpha = \frac{bR^2}{4}\sum_\beta d_\odot^{\alpha\beta}(\vec{\nabla}\varrho_{G,\odot}^\beta \cdot \mathbf{t}^\alpha) \tag{2.88}$$

where ζ_1^α is the elastic strain due to short-range dislocation interactions and ζ_2^α and ζ_3^α are the elastic strains due to the long-range dislocation interactions of edge and screw populations, respectively. The free energy is assumed to have the same functional form as Eq. (2.44), i.e.,

$$\psi_v = \tfrac{1}{2}\boldsymbol{\varepsilon}^{\mathrm{e}} : \mathbb{C} : \boldsymbol{\varepsilon}^{\mathrm{e}} + \tfrac{1}{2}\mu\sum_\alpha\Big[(\zeta_1^\alpha)^2 + (\zeta_2^\alpha)^2 + (\zeta_3^\alpha)^2\Big] \tag{2.89}$$

and the state laws are given as

$$\begin{aligned} \boldsymbol{\sigma} &= \mathbb{C} : \boldsymbol{\varepsilon}^{\mathrm{e}} & \chi_1^\alpha &= r^\alpha = \mu\zeta_1^\alpha \\ \chi_2^\alpha &= -\tau_{b,\perp}^\alpha = \mu\zeta_2^\alpha & \chi_3^\alpha &= \tau_{b,\odot}^\alpha = \mu\zeta_3^\alpha \end{aligned} \quad , \tag{2.90}$$

The dissipation inequality for the proposed constitutive description then follows as

$$\mathfrak{d} = \sum_{\alpha} \tau^{\alpha} \dot{\gamma}^{\alpha} - \sum_{\alpha} \sum_{\beta} (r^{\alpha} H_1^{\alpha\beta} \left| \dot{\gamma}^{\beta} \right| + r^{\alpha} \mathbf{H}_2^{\alpha\beta} \cdot \vec{\nabla} \dot{\gamma}^{\beta}) \cdots$$
$$- \sum_{\alpha} \sum_{\beta} (\tau_{b,\perp}^{\alpha} \mathbf{H}_3^{\alpha\beta} + \tau_{b,\odot}^{\alpha} \mathbf{H}_4^{\alpha\beta}) : \vec{\nabla} (\vec{\nabla} \dot{\gamma}^{\beta}) \geq 0 \tag{2.91}$$

where the matrices $H_1^{\alpha\beta}$, $\mathbf{H}_2^{\alpha\beta}$, $\mathbf{H}_3^{\alpha\beta}$, and $\mathbf{H}_4^{\alpha\beta}$ are defined as

$$H_1^{\alpha\beta} = \frac{c_1}{2} \frac{h^{\alpha\beta}}{\sqrt{\sum_{\delta} h^{\alpha\delta} (\varrho_S^{\delta} + \varrho_G^{\delta})}} \left(\frac{1}{K} \sqrt{\sum_{\xi} a^{\beta\xi} (\varrho_S^{\xi} + \varrho_G^{\xi})} - 2 y_c \varrho_S^{\beta} \right) \tag{2.92}$$

$$\mathbf{H}_2^{\alpha\beta} = \frac{c_1}{2} \frac{h^{\alpha\beta}}{\sqrt{\sum_{\delta} h^{\alpha\delta} (\varrho_S^{\delta} + \varrho_G^{\delta})}} \frac{-\varrho_{G,\perp}^{\beta} \mathbf{s}^{\beta} + \varrho_{G,\odot}^{\beta} \mathbf{t}^{\beta}}{\varrho_G^{\beta}} \tag{2.93}$$

$$\mathbf{H}_3^{\alpha\beta} = \frac{R^2}{8(1-\nu)} d_{\perp}^{\alpha\beta} \mathbf{s}^{\beta} \otimes \mathbf{s}^{\beta} \tag{2.94}$$

$$\mathbf{H}_4^{\alpha\beta} = \frac{R^2}{4} d_{\odot}^{\alpha\beta} \mathbf{t}^{\beta} \otimes \mathbf{t}^{\beta} \tag{2.95}$$

It is shown in Eq. (2.91) that there are contributions from both first- and second-order slip gradients to the energy storage rate due to microstructural evolution. The first-order gradient contribution is the result of the GND-enhanced isotropic hardening, whereas the second-order gradient effects are the result of the long-range GND stress fields.

2.4.4 Non-Work-Conjugate Theories: The Dislocation Sub-Problem

Higher-order theories, in addition to nonlocal constitutive response, also involve supplemental balance equations that must be satisfied as part of the initial-boundary value problem. The non-work-conjugate theories are a subset of higher-order theories in which the additional conservation equation(s) are of a kinematical nature (not mechanical) and, therefore, do not involve higher-order stress measures. Within the context of crystal plasticity, this is typically achieved by introducing dislocation density conservation equations that admit dislocation density and density-flux boundary conditions. Among these types of models, there are those which *augment* the standard mechanical initial-boundary value problem with a weak form implementation of Eq. (2.71) as in Evers et al. [14, 73], and those which *couple* the

mechanical problem with the dislocation sub-problem via the well-known Orowan relation [74, 78, 79, 90]. Orowan's relation is the kinematical relationship between the slip system shearing rate and the mobile dislocations lying in that system and is given as

$$\dot{\gamma}^{\alpha} = \varrho^{\alpha}\mathbf{b}^{\alpha} \cdot \overline{\mathbf{v}}^{\alpha} \tag{2.96}$$

where $\overline{\mathbf{v}}^{\alpha}$ is continuum dislocation glide velocity in slip direction. This relation provides a natural link between theories of single crystal plasticity which include $\dot{\gamma}^{\alpha}$ as a fundamental ingredient and the evolution and flux of dislocation density. No distinction is made here between the mobile and immobile population dislocation densities, but it is seen from Eq. (2.96) that only mobile segments, i.e., those with nonzero velocity contribute to the slip system shearing rate.

A related but unique coupled approach has also been introduced and developed by Acharya and co-workers in a series of papers [76, 91-99]. Their theories of field dislocation mechanics [76] and the coarse-grained version, phenomenological field dislocation mechanics [95], are different from the other coupled approaches in that they capture the long-range internal stress fields due to dislocations exactly, whereas the formerly mentioned coupled models incorporate approximate versions of these fields which are functionally similar to Eq. (2.82). The field dislocation mechanics model is able to capture the exact internal dislocation stress fields, in essence, because it explicitly includes the elastic deformation fields produced by the dislocations as part of an orthogonal decomposition of the total elastic deformation. This aspect of the theory is closely related to the superposition principle employed in the discrete dislocation dynamics framework discussed in Section 2.2 in which the strains produced by dislocations and external loading are treated separately. In fact, the omission of these dislocation-induced elastic strain fields results in the introduction of a non-equilibrated internal stress field that is manifested by including a back stress in the slip rate evolution equation (see Eqs. (2.30), (2.33), and (2.34)) without including the additional kinematic degrees-of-freedom that are associated with it. This deficiency has led some [36, 73, 100-102] to argue in favor of expanding the usual two-term decomposition of the total deformation given in Eq. (2.19) to include another elastic term which accounts for the internal stress fields that remain when external tractions are removed from the material element. While this assumption is different from the orthogonal

decomposition of the elastic deformation employed by Acharya [76], it is intended address the same shortcoming of the classical ISV-type approach to kinematic hardening.

Finally, the models of Ashmawi and Zikry [103-106] are mentioned as another augmented-type of approach which is distinct from those which employ the weak form of the GND density conservation equation. They introduce evolution equations for mobile and immobile dislocation densities, similar in spirit to the kinetic relations used by Walgraef and Aifrantis [107] to study dislocation pattern formation, and then develop a set of constitutive rules and a numerical scheme for "passing" mobile dislocation density from one material point to another. As a result no explicit dislocation boundary conditions are required in their formulation. Oddly, the mobile dislocation density is not explicitly coupled to the slip system shearing rate via Orowan's relation, and is linked to the mechanical problem only through its participation in the mobile/immobile dislocation density evolution equations their contribution to the slip resistance.

A few of the representative approaches to the dislocation sub-problem are subsequently introduced and compared. Specifically, the models of Evers et al. [14], Arsenlis et al. [78] and Yefimov and Van der Giessen [74] are discussed, and to simplify the presentation attention is focused on 2-D versions of the models such that only conservation equations for the edge dislocation density are considered. In the works of Evers et al. [14], Geers [89], and Gerken and Dawson [73] the dislocation sub-problem consists of a weak form of Eq. $(2.71)_1$ which is obtained by multiplying the equation by a virtual edge GND density, $\delta\varrho^{\alpha}_{G,\perp}$, and integrating over a volume, i.e.,

$$\int_R \left(\dot{\varrho}^{\alpha}_{G,\perp} + \tfrac{1}{b} \vec{\nabla} \dot{\gamma}^{\alpha} \cdot \mathbf{s}^{\alpha} \right) \delta\varrho^{\alpha}_{G,\perp} dV = 0 \tag{2.97}$$

where the rate form of the equation has been used to facilitate comparison with the other theories. Integrating by parts to transfer the gradients from the slip rate to the GND density yields the following

$$\int_R \left[\dot{\varrho}^{\alpha}_{G,\perp} \delta\varrho^{\alpha}_{G,\perp} - \tfrac{1}{b} \dot{\gamma}^{\alpha} \mathbf{s}^{\alpha} \cdot \vec{\nabla}(\delta\varrho^{\alpha}_{G,\perp}) \right] dV = -\tfrac{1}{b} \int_{\partial R} \dot{\gamma}^{\alpha} \mathbf{s}^{\alpha} \cdot \hat{\mathbf{n}} \delta\varrho^{\alpha}_{G,\perp} dA \tag{2.98}$$

The surface integral term in Eq. (2.98) clearly shows that natural boundary conditions are admitted in terms of the slip rate and essential boundary conditions in terms of the edge GND densities.. While it is possible

to apply arbitrary boundary conditions of either type, two types of extreme conditions have typically been employed in practice. These limiting cases are the so-called microhard (microrigid, microclamped) and microfree conditions and are given, respectively, as

$$\dot{\gamma}^{\alpha}\mathbf{s}^{\alpha}\cdot\hat{\mathbf{n}}=0 \quad \forall\mathbf{x}\in\partial R_{\dot{\gamma}} \tag{2.99}$$

$$\varrho^{\alpha}_{G,\perp}=0 \quad \forall\mathbf{x}\in\partial R_{\varrho} \tag{2.100}$$

where the microhard condition (Eq. (2.99)) represents a boundary that is impenetrable to slip and the microfree condition (Eq. (2.100)) describes a boundary that is a perfect sink for GNDs, i.e., a free surface. The remaining treatment of the dislocation substructure evolution and the slip system hardening description is handled exactly as in the low-order theories discussed in Section 2.4.3, such that all of the previous analysis can be directly applied here. The key components which seem to be missing from such formulations are (i) a coupling of the dislocation density to the slip rate equation via Orowan's relation and (ii) the total density conservation equation. Equation (2.98) is the GND density balance equation and only accounts for the conservation of the total amount of local Burgers vector (GNDs). The total dislocation density conservation equation, if included, states that the rate of increase of total dislocation density within a given volume is equal to the net increase in density produced by generation and annihilation by interior sources/sinks minus the net outflux of density through the boundaries.

The model of Arsenlis et al. [78], on the other hand, addresses the two missing components of the previous approach enumerated in the preceding paragraph, but does not handle the GND density conservation equation in a transparent manner. Their model also differs from the previous model in that it employs a signed dislocation density basis to describe the dislocated state of the crystal, and this approach has the distinct advantage that the GND and SSD densities may be unambiguously defined. In the 2-D case, this leads to the introduction of two edge dislocation densities (positive/negative) for each slip system, $\varrho^{\alpha}_{\perp}$ and $\varrho^{\alpha}_{\top}$, respectively. Therefore, the total, GND, and SSD dislocation densities are defined as

$$\varrho^{\alpha}=\varrho^{\alpha}_{\perp}+\varrho^{\alpha}_{\top} \tag{2.101}$$

$$\varrho^{\alpha}_{G}=\left|\varrho^{\alpha}_{\perp}-\varrho^{\alpha}_{\top}\right| \tag{2.102}$$

$$\varrho_S^\alpha = \varrho^\alpha - \varrho_G^\alpha = \varrho_\perp^\alpha + \varrho_\top^\alpha - \left|\varrho_\perp^\alpha - \varrho_\top^\alpha\right| \tag{2.103}$$

The evolution equation for each species on each slip system, $\varrho_\perp^\alpha$ and $\varrho_\top^\alpha$, can be written in general form as

$$\dot{\varrho}_i^\alpha = \dot{\varrho}_i^{\alpha^+} + \dot{\varrho}_i^{\alpha^-} + \dot{\varrho}_i^{\alpha^{flux}} \qquad i = \perp, \top \tag{2.104}$$

where $\dot{\varrho}_i^{\alpha^+}$ and $\dot{\varrho}_i^{\alpha^-}$ are the volumetric generation (multiplication and nucleation) and annihilation terms, respectively, and $\dot{\varrho}_i^{\alpha^{flux}}$ gives the rate of change of density due to dislocation flux. The generation and annihilation terms are constitutively specified and have functional forms similar to those given in Eq. (2.36) , while the flux terms are given as

$$\begin{aligned} \dot{\varrho}_\perp^{\alpha^{flux}} &= -\vec{\nabla}\cdot\left(\varrho_\perp^\alpha \overline{v}_\perp^\alpha \mathbf{s}^\alpha\right) = -\vec{\nabla}\left(\varrho_\perp^\alpha \overline{v}_\perp^\alpha\right)\cdot \mathbf{s}^\alpha \\ \dot{\varrho}_\top^{\alpha^{flux}} &= \vec{\nabla}\cdot\left(\varrho_\top^\alpha \overline{v}_\top^\alpha \mathbf{s}^\alpha\right) = \vec{\nabla}\left(\varrho_\top^\alpha \overline{v}_\top^\alpha\right)\cdot \mathbf{s}^\alpha \end{aligned} \tag{2.105}$$

Here, $\overline{v}_\perp^\alpha$ and $\overline{v}_\top^\alpha$ are the signed scalar dislocation glide velocities and Eq. (2.105) represents the volumetric loss of dislocation density due to net outward flux of the dislocation species. Neglecting for the moment the generation and annihilation source terms, the weak form of Eq. (2.104) for each species is obtained by multiplying by the appropriate virtual dislocation density ($\delta\varrho_\perp^\alpha$ or $\delta\varrho_\top^\alpha$)and integrating over a volume as

$$\begin{aligned} \int_R \left[\dot{\varrho}_\perp^\alpha + \vec{\nabla}\left(\varrho_\perp^\alpha \overline{v}_\perp^\alpha\right)\cdot \mathbf{s}^\alpha\right]\delta\varrho_\perp^\alpha dV = 0 \\ \int_R \left[\dot{\varrho}_\top^\alpha - \vec{\nabla}\left(\varrho_\top^\alpha \overline{v}_\top^\alpha\right)\cdot \mathbf{s}^\alpha\right]\delta\varrho_\top^\alpha dV = 0 \end{aligned} \tag{2.106}$$

Integrating by parts and applying the divergence theorem yields the relations

$$\begin{aligned} \int_R \left[\dot{\varrho}_\perp^\alpha \delta\varrho_\perp^\alpha - \varrho_\perp^\alpha \overline{v}_\perp^\alpha \mathbf{s}^\alpha \cdot \vec{\nabla}\left(\delta\varrho_\perp^\alpha\right)\right] dV = -\int_{\partial R} \varrho_\perp^\alpha \overline{v}_\perp^\alpha \mathbf{s}^\alpha \cdot \hat{\mathbf{n}}\delta\varrho_\perp^\alpha dA \\ \int_R \left[\dot{\varrho}_\top^\alpha \delta\varrho_\top^\alpha + \varrho_\top^\alpha \overline{v}_\top^\alpha \mathbf{s}^\alpha \cdot \vec{\nabla}\left(\delta\varrho_\top^\alpha\right)\right] dV = \int_{\partial R} \varrho_\top^\alpha \overline{v}_\top^\alpha \mathbf{s}^\alpha \cdot \hat{\mathbf{n}}\delta\varrho_\top^\alpha dA \end{aligned} \tag{2.107}$$

As before in the case of the GND density conservation equation, it is seen that analogous microhard (natural) and microfree (essential) boundary conditions are admitted as extreme cases, respectively, as

$$\left.\begin{array}{l} \varrho_{\perp}^{\alpha}\overline{v}_{\perp}^{\alpha}\mathbf{s}^{\alpha}\cdot\hat{\mathbf{n}}=0 \\ \\ \varrho_{\top}^{\alpha}\overline{v}_{\top}^{\alpha}\mathbf{s}^{\alpha}\cdot\hat{\mathbf{n}}=0 \end{array}\right\} \quad \forall\mathbf{x}\in\partial R_{\varrho\overline{v}} \tag{2.108}$$

$$\left.\begin{array}{l} \varrho_{\perp}^{\alpha}=0 \\ \\ \varrho_{\top}^{\alpha}=0 \end{array}\right\} \quad \forall\mathbf{x}\in\partial R_{\varrho} \tag{2.109}$$

While the relations given in Eqs. (2.98)-(2.100) are similar to those given in Eqs. (2.107)-(2.109), it is emphasized that they have been obtained from two different dislocation conservation equations; the former from a statement of GND density (net Burgers vector) conservation and the latter from a statement of total dislocation density conservation. Furthermore, had the source terms been included in the weak form of Eq. (2.104) there would have been additional terms in this Eq. (2.107) accounting for this contribution. Ideally, a complete formulation of the dislocation sub-problem should include both conservation equations. Considering the 2-D dislocation density basis employed, the dislocation and mechanical problems are related by the appropriate form of Orowan's relation, i.e.,

$$\dot{\gamma}^{\alpha}=\varrho_{\perp}^{\alpha}\mathbf{b}_{\perp}^{\alpha}\cdot\overline{\mathbf{v}}_{\perp}^{\alpha}+\varrho_{\top}^{\alpha}\mathbf{b}_{\top}^{\alpha}\cdot\overline{\mathbf{v}}_{\top}^{\alpha}=b(\varrho_{\perp}^{\alpha}\overline{v}_{\perp}^{\alpha}+\varrho_{\top}^{\alpha}\overline{v}_{\top}^{\alpha}) \tag{2.110}$$

since $\mathbf{b}_{\perp}^{\alpha}=b\mathbf{s}^{\alpha}=-\mathbf{b}_{\top}^{\alpha}$, $\overline{\mathbf{v}}_{\perp}^{\alpha}=\overline{v}_{\perp}^{\alpha}\mathbf{s}^{\alpha}$, and $\overline{\mathbf{v}}_{\top}^{\alpha}=-\overline{v}_{\top}^{\alpha}\mathbf{s}^{\alpha}$. The scalar dislocation velocities are specified as constitutive functions and contain a slip resistance contribution that is a function of the total dislocation density akin to Eq. (2.35) and a back stress contribution that is a function of the gradients in GND density which is similar to Eq. (2.82). However, instead of using the analytical stress fields and GND density linearization as described Section 2.4.3, the back stress is assumed to be given as follows

$$\tau_{b}^{\alpha}=\frac{c_{6}\mu b}{\varrho^{\alpha}}\vec{\nabla}\varrho_{G,\perp}^{\alpha}\cdot\mathbf{s}^{\alpha} \tag{2.111}$$

where c_6 is a numerical constant. This approximate functional form of the back stress has been derived by Groma et al. [108] by coarse-graining the internal stress fields produced by 2-D ensemble of edge dislocations. Comparing Eq. (2.111) to Eq. (2.82) and taking account of the fact that $d_{\perp}^{\alpha\alpha} = 1$, it is seen that the two expressions are equivalent if $c_6 \,/\, \varrho^{\alpha} = R^2 \,/\, 8(1-\nu)$. This is brought to attention to point out that the intrinsic material length scale appearing in the back stress derived from the semi-analytical approach is constant and defined by R, whereas the one derived from coarse-graining of dislocation ensembles evolves with deformation. The model of Arsenlis et al. [78] does not appear to explicitly incorporate the GND density balance equation although it does allow for polar densities to develop, for example, through the specification of microhard boundary conditions of the type given in Eq. (2.108).

A non-work-conjugate theory which features both dislocation conservation equations and couples the dislocation sub-problem to the mechanical problem via Orowan's relation are those due to Yefimov and Van der Giessen [74] and Limkumnerd and Van der Giessen [90]. The dislocation density balance equations in their model are stated as

$$\frac{\partial \varrho^{\alpha}}{\partial t} + \vec{\nabla} \cdot (\varrho_{G,\perp}^{\alpha} \overline{\mathbf{v}}^{\alpha}) = f^{\alpha} \tag{2.112}$$

$$\frac{\partial \varrho_{G,\perp}^{\alpha}}{\partial t} + \vec{\nabla} \cdot (\varrho^{\alpha} \overline{\mathbf{v}}^{\alpha}) = 0 \tag{2.113}$$

where Eq. (2.112) is the total dislocation density balance equation and Eq. (2.113) is the GND balance equation. The function f^{α} embodies the source/sink terms describing the volumetric generation and annihilation rates. It can easily be shown that Eq. (2.107) of Arsenlis et al. [78] is identical to Eq. (2.112). Adding the rate equations given in Eq. (2.104), including the generation and annihilation terms, leads to the following

$$\dot{\varrho}_{\perp}^{\alpha} + \dot{\varrho}_{\top}^{\alpha} + \vec{\nabla}(\dot{\varrho}_{\perp}^{\alpha} \overline{v}_{\perp}^{\alpha} - \dot{\varrho}_{\top}^{\alpha} \overline{v}_{\top}^{\alpha}) \cdot \mathbf{s}^{\alpha} = \varrho_{\perp}^{\alpha^{+}} + \varrho_{\perp}^{\alpha^{-}} + \varrho_{\top}^{\alpha^{+}} + \varrho_{\top}^{\alpha^{-}} \tag{2.114}$$

Recognizing that $\overline{v}_{\perp}^{\alpha} = \overline{v}_{\top}^{\alpha}$ and pulling the slip vector $\mathbf{s}^{\alpha}$ inside the parenthesis on the second term on the LHS of Eq. (2.114) clearly asserts the equivalence between the two expressions where

$f^\alpha = \varrho_\perp^{\alpha^+} + \varrho_\perp^{\alpha^-} + \varrho_\top^{\alpha^+} + \varrho_\top^{\alpha^-}$. Similarly, equivalence between Eq. (2.113) and the rate form of Eq. (2.72) is established by moving the unit slip vector outside of the parenthesis in Eq. (2.113) and utilizing Eq. (2.96) such that

$$\frac{\partial \varrho_{G,\perp}^\alpha}{\partial t} + \vec{\nabla}(\varrho^\alpha \overline{v}^\alpha) \cdot \mathbf{s}^\alpha = \frac{\partial \varrho_{G,\perp}^\alpha}{\partial t} + \frac{1}{b}\vec{\nabla}\dot{\gamma}^\alpha \cdot \mathbf{s}^\alpha = 0\,, \tag{2.115}$$

which is identical to the rate form of Eq. (2.72). The weak forms of the two balance equations (neglecting the source term for convenience) are obtained as before by multiplying by virtual dislocation densities and integrating over the volume such that the following two expressions are obtained, i.e.,

$$\int_R \Big[\dot{\varrho}^\alpha \delta\varrho^\alpha - \varrho_{G,\perp}^\alpha \overline{\mathbf{v}}^\alpha \cdot \vec{\nabla}(\delta\varrho^\alpha) \Big] dV = -\int_{\partial R} \Big[\varrho_{G,\perp}^\alpha \overline{\mathbf{v}}^\alpha \cdot \hat{\mathbf{n}} \delta\varrho^\alpha \Big] dA \tag{2.116}$$

$$\int_R \Big[\dot{\varrho}_{G,\perp}^\alpha \delta\varrho_{G,\perp}^\alpha - \varrho^\alpha \overline{\mathbf{v}}^\alpha \cdot \vec{\nabla}(\delta\varrho_{G,\perp}^\alpha) \Big] dV = -\int_{\partial R} \Big[\varrho^\alpha \overline{\mathbf{v}}^\alpha \cdot \hat{\mathbf{n}} \delta\varrho_{G,\perp}^\alpha \Big] dA \tag{2.117}$$

Inspection of Eq. (2.116) reveals that the total dislocation density conservation equation admits natural boundary conditions with respect to the GND density flux and essential boundary conditions with respect to the total density, whereas Eq. (2.117) reveals that the GND density conservation equation admits natural boundary conditions with respect to the total dislocation density flux and essential boundary conditions with respect to the GND densities. The coupled mechanical-dislocation initial-boundary value problem is completed by employing Orowan's relation and prescribing constitutive equations for f^α and also the dislocation stress-velocity relationship, i.e., the functional form for $\overline{\mathbf{v}}^\alpha$ are required. It is noted that these modeling frameworks provide a transparent connection to the discrete dislocation dynamics models discussed in Section 2.2, and that all of the so-called material length scales have a direct and physical connection to unit dislocation processes. Additionally, the higher-order boundary conditions required for the dislocation sub-problem have a clear physical interpretation in terms of dislocation density and density-flux and again are analogous to the boundary conditions employed in discrete dislocation dynamics models of plasticity.

2.4.5 Work-Conjugate Theories

Work-conjugate theories of higher-order generalized crystal plasticity are characterized by the inclusion of non-standard power-conjugate degrees-of-freedom at each continuum point. These theories are sometimes referred to as "continua with microstructure" or alternatively as "generalized micromorphic continua". The usage of microstructure here is not to be confused with an actual material microstructure (e.g., grains, porosity, multiple phases, inclusions, etc.), but instead refers to the fact that each continuum point is imbued with micro degrees-of-freedom in addition to the usual displacement field. Therefore, the deformation power, the mechanical balance laws, and the required boundary conditions for such theories are non-classical. This is contrasted with the non-work-conjugate higher-order theories discussed in the previous section in which the standard mechanical balance laws apply, and the additional balance laws and boundary conditions are restricted to the dislocation sub-problem. There are two sub-classes of work-conjugate theories: (i) grade-*n* theories and (ii) generalized micromorphic theories. Grade-*n* theories incorporate higher-order derivatives of the usual displacement field; representative examples include the full second-gradient theory of Smyshlyaev and Fleck [26] and the couple-stress theory of Kim and Oh [28]. On the other hand, generalized micromorphic theories introduce degrees-of-freedom that are independent of the displacement field. In general, these micro degrees-of-freedom can be of arbitrary tensorial rank but are typically taken to be either scalar or vectorial. Representative generalized micromorphic single crystal plasticity models with scalar micro degrees-of-freedom have been introduced by Gurtin [16, 17] and Gurtin and co-workers [18, 109] and a number of other authors [77, 81, 110, 111], whereas theories including additional vectorial degrees-of-freedom have been introduced by Le and Stumpf [31], Clayton et al. [36], Naghdi and Srinivasa [29, 112], Shizawa and Zbib [80], and Forest [34, 35]. It is beyond the scope of this thesis to elaborate in detail the particulars of each formulation; however, due to the popularity of the Gurtin-type framework it is instructive to introduce and discuss this particular type of model in more detail which is pursued in subsequent sections. Discussion of micropolar single crystal plasticity, the focus of this research and a type of work-conjugate higher-order theory, is postponed until the more detailed treatment given in Chapter 3.

The previous discussion of low-order and non-work-conjugate higher-order theories of generalized single crystal plasticity has been undertaken from the perspective that they can be incorporated/coupled to

the solution of the standard mechanical initial-boundary value problem for the classical continuum without altering its structure. Since the mechanical initial-boundary value problem is altered for higher-order work-conjugate theories, the Gurtin-type theory is presented here with more completeness.

Kinematics

The Gurtin-type model to generalized single crystal plasticity is based on treating the set of slip system shears, $\{\gamma^\alpha\} = \{\gamma^1 \quad \gamma^2 \quad ... \quad \gamma^N\}$, as the additional scalar micro degrees-of-freedom. Here, "micro" is used to denote the higher-order degrees-of-freedom associated with fine scale kinematics that are not controllable in the classical theory. The main kinematical relations of the classical theory for infinitesimal strain presented in Section 2.3.1 are assumed to hold and are summarized as

$$\begin{aligned} \mathbf{H} &= \mathbf{H}^{\mathrm{e}} + \mathbf{H}^{\mathrm{p}} \\ \boldsymbol{\varepsilon} &= \mathrm{sym}(\mathbf{H}) = \boldsymbol{\varepsilon}^{\mathrm{e}} + \boldsymbol{\varepsilon}^{\mathrm{p}} \\ \mathbf{H}^{\mathrm{p}} &= \sum_\alpha \gamma^\alpha \mathbf{s}^\alpha \otimes \mathbf{n}^\alpha \\ \boldsymbol{\alpha} &= \mathbf{H}^{\mathrm{p}} \times \tilde{\nabla} \end{aligned} \tag{2.118}$$

Here, it is noted that the GND density tensor has been listed as a fundamental kinematic relation. As in the classical theory, the elastic material deformation is assumed to correspond to the lattice deformation, i.e., Eq. (2.21) holds. The key kinematic distinction between the present theory and those that have been previously discussed is that the slip system shears are taken to be *power-conjugate* degrees-of-freedom.

Balance Laws and Thermodynamics

Due to the non-standard nature of the force system introduced by Gurtin [17], the principle of virtual power [113] is employed to derive the mechanical balance laws. It is assumed that internal power is expended independently on the elastic distortion rate tensor as well as slip rate and its gradient such that the internal power density is given as

$$\mathfrak{p}_I = \boldsymbol{\sigma} : \dot{\mathbf{H}}^{\mathrm{e}} + \sum_{\alpha} (q^{\alpha}\dot{\gamma}^{\alpha} + \boldsymbol{\varsigma}^{\alpha} \cdot \vec{\nabla}\dot{\gamma}^{\alpha}) \tag{2.119}$$

where q^{α} and $\boldsymbol{\varsigma}^{\alpha}$ are scalar and vectorial microstresses, respectively. The scalar microstress is a force stress with units of force/length^2, whereas the vectorial microstress is a couple stress with units of force/length. Making use of Eqs. $(2.118)_{2,3}$ and (2.31), Eq. (2.119) may also be expressed in terms of the total distortion rate tensor as

$$\mathfrak{p}_I = \boldsymbol{\sigma} : \dot{\mathbf{H}} + \sum_{\alpha} [(q^{\alpha} - \tau^{\alpha})\dot{\gamma}^{\alpha} + \boldsymbol{\varsigma}^{\alpha} \cdot \vec{\nabla}\dot{\gamma}^{\alpha}] \tag{2.120}$$

When expressed in this form, it is clear that if the Cauchy stress is to be interpreted as power-conjugate to the total distortion rate tensor then a resolved effective stress, $p^{\alpha} \equiv q^{\alpha} - \tau^{\alpha}$, is power-conjugate to the slip rates. Since the displacements and slip rates are the fundamental continuum degrees-of-freedom, the external power density (neglecting body forces) is assumed to be of the form

$$\mathfrak{p}_E = \mathbf{T} \cdot \dot{\mathbf{u}} + \sum_{\alpha} \Xi^{\alpha}\dot{\gamma}^{\alpha} \tag{2.121}$$

where $\mathbf{T}$ and Ξ^{α} are the macro- and microtraction vectors, respectively. Given the assumed functional forms for the internal and external power densities, the principle of virtual power can be utilized to obtain the mechanical balance laws. The principle of virtual power consists of two requirements:

i) Power Balance: Given any subbody, P, of a continuum, R, the corresponding internal and external powers are balanced for all generalized virtual velocities

$$\int_P \mathfrak{p}_I(P,\mathcal{V})dV = \int_{\partial P} \mathfrak{p}_E(P,\mathcal{V})dA \qquad \forall\, \mathcal{V} \tag{2.122}$$

where the generalized virtual velocity is defined as $\mathcal{V} = \left\{ \delta\dot{\mathbf{u}}, \{\delta\dot{\gamma}^{\alpha}\} \right\}$.

ii) Frame indifference: Given any subbody, P, the internal power expenditure is null when the motion is rigid

$$\int_{p} \mathfrak{p}_I(P, \mathcal{V}) dV = 0 \quad \forall\, \mathcal{V} \in \mathcal{V}^R \tag{2.123}$$

where $\mathcal{V}^R$ is the set of rigid generalized velocities. A generalized virtual velocity is said to be rigid if [17]

$$\delta\dot{\mathbf{u}}(\mathbf{x}) = \mathbf{a} + \mathbf{c} \times \mathbf{x}, \quad \delta\dot{\mathbf{H}}^{\mathrm{e}} = -\boldsymbol{\epsilon} \cdot \mathbf{c}, \quad \{\delta\dot{\gamma}^{\alpha}\} = 0 \tag{2.124}$$

where $\mathbf{a}$ and $\mathbf{c}$ are constant vectors.

Applying the principle to determine the mechanical balance laws, a generalized virtual velocity without slip is first considered, $\{\delta\dot{\gamma}^{\alpha}\} = 0$. The virtual power balance is then given as

$$\int_{P} \boldsymbol{\sigma} : \delta\dot{\mathbf{H}} dV = \int_{\partial P} \mathbf{T} \cdot \delta\dot{\mathbf{u}} dA \tag{2.125}$$

Integrating by parts and applying the divergence theorem then leads to the following,

$$\int_{P} (\boldsymbol{\sigma} \cdot \bar{\nabla}) \cdot \delta\dot{\mathbf{u}} dV + \int_{\partial P} (\mathbf{T} - \boldsymbol{\sigma} \cdot \hat{\mathbf{n}}) \cdot \delta\dot{\mathbf{u}} dA = 0 \tag{2.126}$$

This relation must hold for all P and $\delta\dot{\mathbf{u}}$ and, therefore, one obtains the balance of linear momentum as

$$\boldsymbol{\sigma} \cdot \bar{\nabla} = \mathbf{0} \quad \forall \mathbf{x} \in R \tag{2.127}$$

and the macroscopic traction condition as

$$\mathbf{T} = \boldsymbol{\sigma} \cdot \hat{\mathbf{n}} \quad \forall \mathbf{x} \in \partial R \tag{2.128}$$

Next a rigid rotation velocity field is considered such that the distortion rate is a constant skew-symmetric tensor, i.e., $\delta\dot{\mathbf{H}} = -\boldsymbol{\epsilon} \cdot \mathbf{c}$. Appealing to the frame indifference requirement the following must hold,

$$\int_P \boldsymbol{\sigma} : \delta\dot{\mathbf{H}} dV = 0 \tag{2.129}$$

Since $\dot{\mathbf{H}} = -\dot{\mathbf{H}}^T$, Eq. (2.129) is satisfied only if

$$\boldsymbol{\sigma} = \boldsymbol{\sigma}^T \quad \forall \mathbf{x} \in R \tag{2.130}$$

which is nothing more than the classical angular momentum balance. To determine the microscopic force balance, a generalized virtual velocity is considered such that $\delta\dot{\mathbf{u}} = \mathbf{0}$ and the power balance is given by

$$\sum_\alpha \int_P [(q^\alpha - \tau^\alpha)\delta\dot{\gamma}^\alpha + \boldsymbol{\varsigma}^\alpha \cdot \vec{\nabla}\delta\dot{\gamma}^\alpha] dV = \sum_\alpha \int_{\partial P} \Xi^\alpha \delta\dot{\gamma}^\alpha dA \tag{2.131}$$

Integrating by parts and applying the divergence theorem leads to the following expression,

$$\sum_\alpha \int_P (q^\alpha - \tau^\alpha - \vec{\nabla} \cdot \boldsymbol{\varsigma}^\alpha)\delta\dot{\gamma}^\alpha dV + \sum_\alpha \int_{\partial P} (\boldsymbol{\varsigma}^\alpha \cdot \hat{\mathbf{n}} - \Xi^\alpha)\delta\dot{\gamma}^\alpha dA = 0 \tag{2.132}$$

Since this must hold for all P and $\{\delta\dot{\gamma}^\alpha\}$, the microscopic force balance is given as

$$\tau^\alpha + \vec{\nabla} \cdot \boldsymbol{\varsigma}^\alpha - q^\alpha = 0 \quad \forall \mathbf{x} \in R \tag{2.133}$$

with the corresponding microtraction condition given by

$$\Xi^\alpha = \boldsymbol{\varsigma}^\alpha \cdot \hat{\mathbf{n}} \quad \forall \mathbf{x} \in \partial R \tag{2.134}$$

The principle of virtual power applied to a continuum with displacements and slip system shears taken as basic degrees-of-freedom has lead to two distinct sets of mechanical balance laws: the usual "standard" macroscopic balances of linear and angular momentum given in Eqs. (2.127) and (2.130), respectively, and a non-standard microscopic force balance given in Eq. (2.133). The macroscopic and microscopic deformation processes are coupled by the presence of the resolved shear stress in the microscopic force balance. The microforce balance can be interpreted as a nonlocal yield condition where the second and third terms in Eq. (2.133), represent kinematic and isotropic components to slip resistance, respectively.

The weak form of the microforce balance given in Eq. (2.131) reveals that the microhard and microfree boundary conditions appropriate for the Gurtin-type model are given, respectively, as

$$\gamma^{\alpha} = 0 \quad \forall \mathbf{x} \in \partial R_{\gamma} \tag{2.135}$$

$$\boldsymbol{\varsigma}^{\alpha} \cdot \hat{\mathbf{n}} = 0 \quad \forall \mathbf{x} \in \partial R_{\varsigma} \tag{2.136}$$

The microhard and microfree conditions given above have similar physical implications as in the non-work-conjugate theory, namely, that a microhard condition describes a surface that would be impenetrable to dislocations and the microfree condition describes a surface that is a perfect dislocation sink. It is noted, however, that the microhard and microfree conditions in the Gurtin-type theory are essential and natural boundary conditions, respectively, whereas in the dislocation density flux-based theories they are natural and essential boundary conditions, respectively.

In prelude to deriving the state laws and dissipation inequality, it is noted that Gurtin [17, 18, 109, 114] does not use ISVs or pose constitutive equations in the same manner as has been done in the previous developments (cf. Eqs. (2.44), (2.45), and (2.86)-(2.95)). The only arguments admitted to the free energy are the elastic strains and the slip gradients (or some function of slip gradients), i.e., $\psi = \hat{\psi}(\boldsymbol{\varepsilon}^{\mathrm{e}}, \{\vec{\nabla}\gamma^{\alpha}\})$, both of which appear in the internal power density (see Eq. (2.120)). Additionally, Gurtin [18] proposes a decomposition of the vectorial microstress into *energetic* and *dissipative* parts, i.e.,

$$\begin{aligned} \boldsymbol{\varsigma}^{\alpha} &= \boldsymbol{\varsigma}^{\alpha}_{en} + \boldsymbol{\varsigma}^{\alpha}_{dis} \\ \boldsymbol{\varsigma}^{\alpha}_{en} &\equiv \rho \frac{\partial \psi}{\partial \vec{\nabla}\gamma^{\alpha}} \end{aligned} \tag{2.137}$$

Given that the vectorial microstress is a function of the slip gradients, it is seen with the aid of the microforce balance that the kinematic hardening term in Eq. (2.133) is related to second gradients of slip which is in agreement with the physically-based back stress derivations covered in Section 2.4.3. The energetic/dissipative decomposition of the thermodynamic stress, $\boldsymbol{\varsigma}^{\alpha}$, instead of the thermodynamic strain, $\vec{\nabla}\gamma^{\alpha}$, is commonly done in higher-order work-conjugate theories which treat the plastic slip rates or the plastic strain rate tensor as generalized velocities. It is interesting to note that on the one hand an

energetic/dissipative decomposition is introduced for the total macroscopic strain, $\boldsymbol{\varepsilon} = \boldsymbol{\varepsilon}^{\mathrm{e}} + \boldsymbol{\varepsilon}^{\mathrm{p}}$, yet it is the microscopic stress to which the energetic/dissipative decomposition is applied. Similar energetic/dissipative decompositions of the scalar microstress, q^{α}, have been proposed in some related works, but this is not a typical feature of Gurtin's crystal plasticity theories [17, 18, 109]. For isothermal deformation processes, the dissipation inequality of Eq. (2.26) holds, and the power density of internal forces is given by Eq. (2.119). Following the Coleman-Gurtin [61] thermodynamic procedure, the state laws are

$$\boldsymbol{\sigma} = \rho \frac{\partial \psi}{\partial \boldsymbol{\varepsilon}^{\mathrm{e}}} \quad , \quad \boldsymbol{\varsigma}_{en}^{\alpha} = \rho \frac{\partial \psi}{\partial \vec{\nabla} \gamma^{\alpha}} \tag{2.138}$$

and the reduced dissipation inequality is

$$\mathfrak{d} = \sum_{\alpha} (q^{\alpha} \dot{\gamma}^{\alpha} + \boldsymbol{\varsigma}_{dis}^{\alpha} \cdot \vec{\nabla} \dot{\gamma}^{\alpha}) \geq 0 \quad \forall \mathbf{x} \in R \tag{2.139}$$

which may also be expressed with the aid of the microforce balance as

$$\mathfrak{d} = \sum_{\alpha} [(\tau^{\alpha} + \vec{\nabla} \cdot \boldsymbol{\varsigma}^{\alpha}) \dot{\gamma}^{\alpha} + \boldsymbol{\varsigma}_{dis}^{\alpha} \cdot \vec{\nabla} \dot{\gamma}^{\alpha}] \geq 0 \quad \forall \mathbf{x} \in R \tag{2.140}$$

Interestingly, if the total mechanical dissipation rate, $\mathcal{D}$, is considered the following expression is obtained

$$\begin{aligned} \mathcal{D} &= \int_{R} \mathfrak{d} \, dV = \sum_{\alpha} \int_{R} [(\tau^{\alpha} + \vec{\nabla} \cdot \boldsymbol{\varsigma}^{\alpha}) \dot{\gamma}^{\alpha} + \boldsymbol{\varsigma}_{dis}^{\alpha} \cdot \vec{\nabla} \dot{\gamma}^{\alpha}] \\ &= \sum_{\alpha} \int_{R} (\tau^{\alpha} \dot{\gamma}^{\alpha} - \boldsymbol{\varsigma}_{en}^{\alpha} \cdot \vec{\nabla} \dot{\gamma}^{\alpha}) dV + \sum_{\alpha} \int_{\partial R} (\Xi^{\alpha} \dot{\gamma}^{\alpha}) dA \end{aligned} \tag{2.141}$$

where the term containing the divergence of the vectorial microstress in the first line of Eq. (2.141) has been integrated by parts and the divergence theorem has been applied. This expression reveals that the energetic portion of the vectorial microstress actually serves to decrease the mechanical dissipation rate and presumably reflects a stored energy due microstructural rearrangement due to higher-order gradient effects as discussed in dislocation-based model in Section 2.4.3. Equation (2.141) also shows that in addition to

the usual volumetric contribution to the mechanical dissipation rate due to the resolved shear stress acting on the slip system shearing rates there is a surface contribution due to the vectorial microtractions.

Constitutive Equations

Constitutive equations are required for the free energy function, the scalar, q^{α}, and vectorial, $\boldsymbol{\varsigma}^{\alpha}$, microstresses, and the evolution of the slip resistance. The methodology and terminology used to define the constitutive functions adheres to the ideology of Gurtin et al. [18]. The free energy is assumed to have the functional form

$$\psi_v = \tfrac{1}{2}\boldsymbol{\varepsilon}^{\mathrm{e}} : \mathbb{C} : \boldsymbol{\varepsilon}^{\mathrm{e}} + \tfrac{1}{2}\ell^2\mu\sum_{\alpha}\left\|\vec{\nabla}\gamma^{\alpha}\right\|^2 \tag{2.142}$$

where ℓ is a so-called "energetic" length scale. Inserting Eq. (2.142) into Eq. (2.138) leads to the following explicit state laws for the Cauchy stress and the energetic portion of the vectorial microstress, i.e.,

$$\boldsymbol{\sigma} = \mathbb{C} : \boldsymbol{\varepsilon}^{\mathrm{e}} \quad , \quad \boldsymbol{\varsigma}^{\alpha}_{en} = \mu\ell^2\vec{\nabla}\gamma^{\alpha} \tag{2.143}$$

The dissipative constitutive equations are introduced with the aid of an equivalent slip system deformation rate, $\dot{d}^{\alpha}$, which is defined to be

$$\dot{d}^{\alpha} = \sqrt{\left|\dot{\gamma}^{\alpha}\right|^2 + L^2\left\|\vec{\nabla}\dot{\gamma}^{\alpha}\right\|^2} \tag{2.144}$$

where L is a so-called "dissipative" length scale. The scalar dissipative microstress is posited to have the functional form

$$q^{\alpha} = g^{\alpha}\left(\frac{\dot{d}^{\alpha}}{\dot{d}_0}\right)^{1/m}\frac{\dot{\gamma}^{\alpha}}{\dot{d}^{\alpha}} \quad , \quad g^{\alpha} > 0 \tag{2.145}$$

where g^{α} is a drag stress-like parameter that is required to be strictly positive, d_0 is the reference equivalent deformation rate, and m is the inverse rate-sensitivity exponent. The drag stress effectively represents the slip resistance and is assumed to evolve according to the following general functional form

$$\dot{g}^{\alpha} = \sum_{\beta} h^{\alpha\beta}\left(\{\gamma^{\chi}\},\{\vec{\nabla}\gamma^{\chi}\}\right)d^{\beta} \tag{2.146}$$

where $h^{\alpha\beta}$ is a hardening matrix and as indicated in Eq. (2.146) the matrix components evolve as functions of both slip rates and their gradients. Gurtin [18, 115] does not frame slip system strength evolution equations in terms of dislocation densities as discussed in Sections 2.3.3 and 2.4.3 or give a specific evolution equation for the drag stress. Rather than invoking assumptions on their behalf, the discussion is continued without specifying the exact functional form of Eq. (2.146). Analogous to the scalar dissipative microstress, the dissipative portion of the vectorial microstress is assumed to be given as

$$\boldsymbol{\varsigma}^{\alpha}_{dis} = g^{\alpha}L^{2}\left(\frac{\dot{d}^{\alpha}}{\dot{d}_0}\right)^{1/m}\frac{\vec{\nabla}\dot{\gamma}^{\alpha}}{\dot{d}^{\alpha}} \tag{2.147}$$

Inserting Eqs. (2.145) and (2.147) into the dissipation rate density given in Eq. (2.139) yields the expression

$$\mathfrak{d} = \sum_{\alpha} g^{\alpha}\left(\frac{\dot{d}^{\alpha}}{\dot{d}_0}\right)^{1/m}\left[\frac{\left|\dot{\gamma}^{\alpha}\right|^{2} + L^{2}\left\|\vec{\nabla}\dot{\gamma}^{\alpha}\right\|^{2}}{\dot{d}^{\alpha}}\right] = \sum_{\alpha} g^{\alpha}\left(\frac{\dot{d}^{\alpha}}{\dot{d}_0}\right)^{1/m}\dot{d}^{\alpha} \tag{2.148}$$

In an effort to connect the theoretical developments of Gurtin et al. [18] to the models introduced in Sections 2.3, 2.4.3, and 2.4.4, a version of their theory without slip gradients is considered. The following conditions hold in the absence of slip gradients: $\{\boldsymbol{\varsigma}^{\alpha}\} = \{0\}$, $\dot{d}^{\alpha} = \mid \dot{\gamma}^{\alpha} \mid$, and $q^{\alpha} = \tau^{\alpha}$, and the mechanical dissipation rate density then simplifies to

$$\mathfrak{d} = \sum_{\alpha} g^{\alpha}\left(\frac{\mid \dot{\gamma}^{\alpha} \mid}{\dot{d}_0}\right)^{1/m} \mid \dot{\gamma}^{\alpha} \mid \tag{2.149}$$

Now consider the classical theory of single crystal plasticity with only isotropic hardening and a creep-type viscoplastic kinetic equation for the slip system shearing rate, i.e.,

$$\dot{\gamma}^{\alpha} = \dot{\gamma}_0 \left(\frac{\mid \tau^{\alpha} \mid}{g^{\alpha}} \right)^{m} \operatorname{sgn}(\tau^{\alpha}) \tag{2.150}$$

Here, the drag stress serves as the isotropic hardening variable in the absence of a threshold stress and there is no explicit yield surface in stress or strain space. The mechanical dissipation rate in the classical theory according to Gurtin's point of view (no back stress and no ISVs) [17, 18] is given as

$$\mathfrak{d} = \sum_{\alpha} \tau^{\alpha} \dot{\gamma}^{\alpha} \tag{2.151}$$

Solving Eq. (2.150) for the resolved shear stress and then substituting the result into Eq. (2.151) yields

$$\mathfrak{d} = \sum_{\alpha} g^{\alpha} \left(\frac{\mid \dot{\gamma}^{\alpha} \mid}{\dot{\gamma}_0} \right)^{1/m} \mid \dot{\gamma}^{\alpha} \mid \tag{2.152}$$

A comparison of Eqs (2.149) and (2.152) shows that the mechanical dissipation rate density in Gurtin's theory in the absence of slip gradients is identical to that of the classical theory if there is no back stress or traditional ISVs and provided that $\dot{\gamma}_0 = \dot{d}_0$. It is this particular interpretation of the classical theory that motivates Gurtin's choice of constitutive equations for the dissipative microstresses so that when there are no slip gradients, the classical theory is retrieved. Further comparison of the Gurtin-type model to that of the dislocation-based ISV frameworks introduced in the earlier sections is somewhat difficult due to the different philosophical perspectives from which the models are developed. On the one hand, the dislocation-based models embrace the ideology of introducing physically-based ISVs to capture both the increased slip resistance and the energy stored due to microstructural evolution, whereas Gurtin et al. [18] describe the increased flow resistance through similar isotropic hardening descriptions yet do not account for the additional energy stored during such processes. Another subtle difference is that constitutive equations in the dislocation-based models are introduced for the inelastic kinematic variables (plastic strain and ISV strains or dislocation densities) and the ISV stresses and strains are related through appropriate

constitutive moduli. Alternatively, the Gurtin [17] ideology is based on specifying constitutive equations for the thermodynamic stresses without clearly defining the corresponding work-conjugate thermodynamic strains. The two methodologies could be brought into closer alignment through a reinterpretation and reformulation of the ideas presented with this section, but would require invoking certain assumptions that the original authors might not agree with. Some of these aspects are further addressed in Chapter 3 following the introduction of the theory of micropolar single crystal plasticity, but for now the Gurtin model is presented in a manner analogous with original authors' intentions.

2.4.6 Discussion

The generalized single crystal plasticity theories elaborated upon in this section will be referred to as slip gradient-based models. These formulations all require the explicit calculation of slip gradients as part of the constitutive update, the global solution of equilibrium equations, or both. Therefore, the numerical implementation of such models requires modified finite element schemes [21, 22] or the use of higher-order interpolation functions as compared to the standard C^0-continuous methods to ensure consistency between the interpolated fields [18, 116]. Additionally, if the slip system shears or GND densities are taken as nodal DOF as in the higher-order theories, the finite element matrix bandwidth is significantly larder. For example, an fcc crystal with twelve slip systems would require twelve additional degrees-of-freedom per node in a full 3-D implementation of the Gurtin-type [18] theory and eighteen are required for the Evers-Bayley [14, 72] non-work-conjugate theory. A consequence of these modifications is an increased computational cost associated with the solution of initial-boundary value problems as compared to traditional C^0-continuous displacement-based finite element methods. While such theories offer an enhanced description of material behavior during heterogeneous deformation, the extent of the increased computational cost associated with the numerical implementation of these models provides some practical limitations on the size of the boundary value problems that can be solved. It is in part due to these limitations that this research focuses on the development of a micropolar theory of single crystal plasticity. The micropolar theory, in contrast to the slip gradient-base ones, introduces only three additional degrees-of-freedom per node in the 3-D case and may be implemented with C^0-continuous shape functions. These

issues are further addressed in the development of the micropolar theory in Chapter 3 and its numerical implementation, which is covered in Chapter 4.

2.5 Summary

This chapter has provided an overview of topics relevant to the formulation of theories of generalized single crystal plasticity. The classical theory of crystal plasticity is introduced within a dislocation-based constitutive framework, and nonlocal extensions representative of three classes of generalized continua have been discussed. Both the low-order and non-work-conjugate higher-order theories have been introduced conceptually as relatively straight-forward extensions of the classical theory, whereas the Gurtin-type work-conjugate higher-order theory promotes a different philosophical perspective regarding certain fundamental aspects such as the nature of energetic/dissipative decompositions of thermodynamic quantities and the use of traditional ISVs. The relative merits and weaknesses of each type of nonlocal theory have been discussed from both physical and practical perspectives. This study has been limited to infinitesimal deformations and plastic deformation due solely to dislocation glide while neglecting cross-slip and climb.

CHAPTER 3

MICROPOLAR SINGLE CRYSTAL PLASTICITY

3.1 Introduction

This chapter develops theories of micropolar single crystal plasticity which are presented as an alternative to the more common slip gradient-based approaches to generalized crystal plasticity. A micropolar [42] or Cosserat [43] continuum is a special case of the micromorphic continuum where each material point possesses microrotational degrees-of-freedom in addition to the displacements. Early works in phenomenological micropolar elastoplasticity are due to Besdo [44], Lippmann [45], and Sawczuk [46], while more recent contributions in this vein are due to Deborst [117, 118], Steinmann [48, 119-121], Grammenoudis and Tsakmakis [49, 122-124], Neff [50, 125] and Neff and Chelminski [126, 127]. Most relevant to the current research are the models of micropolar single crystal plasticity put forth by Forest and collaborators [34, 35, 37-40, 128].

The motivations for pursuing a micropolar theory of single crystal plasticity are several-fold and are based upon both practical and philosophical considerations. First, as discussed in Chapter 2, explicit slip gradient-based approaches require modified and/or higher-order FE methods which leads to a significantly higher computational cost associated with the solution of similar boundary value problems with equivalent discretization sizes as compared to a standard theory. In contrast, the micropolar continuum has only three additional DOF per node for the fully 3-D case and, since the microrotations are independent of displacements, standard C^0-continuous interpolation functions can be used in the numerical implementation. From a philosophical perspective, the adherence to the more "traditional" physical interpretation of elastic-plastic thermodynamics is appealing. Here, "traditional" is defined in the sense that the total deformation measures are separated into energetically recoverable (elastic) and energetically dissipative (plastic) parts, where the total deformation rates appear in the definition of the internal power density and only the elastic components (in addition to ISVs) explicitly appear in the free energy function. As such, the introduction of non-standard force systems that are work-conjugate to plastic strains and their

gradients and the associated microforce balances is avoided. The construction of yield criteria or flow rules for work-conjugate higher-order continuum theories can be done in one of two ways [129]: (i) a single criterion can be introduced in terms of a combined equivalent stress and inelastic rate or (ii) individual criteria can be specified for each conjugate stress/inelastic kinematic rate pair, a so-called multicriterion theory.

Building upon the previous works of Forest et al. [34, 35] within the framework of multicriterion micropolar single crystal plasticity, their phenomenological strength model is extended to a dislocation-based model. This is an important contribution as it enables one to establish the connections between micropolar single crystal plasticity and various aspects of slip gradient-based generalized crystal plasticity models, and in addition provides a more physically-based description of scale-dependent strengthening behavior than the former. Additionally, a new single criterion formulation is presented with an analogous but simplified strength model. The development of the single criterion model is motivated by related earlier works in phenomenological macroscopic micropolar elastoplasticity, and is the first such model of micropolar single crystal plasticity. The models are developed within the context of geometrically linear kinematics. This avoids certain issues associated with multiplicatively decomposed micropolar elastoplasticity at finite strains that are still open to debate, such as the appropriate elastic-plastic decompositions of deformation maps [35, 48, 120] and the specification of appropriate deformation measures [130, 131]. An infinitesimal deformation framework is sufficient for examining the scale-dependence of initial yield and the early strain-hardening regime, and attention is confined to these conditions in this research.

3.2 Kinematics

The motion of the classical continuum is completely determined by the displacement, $\mathbf{u}$, and the deformed state of the body is characterized by the deformation gradient, $\mathbf{F}$. In contrast, the motion of a micropolar continuum is defined by two independent motions which are determined by; the displacements,

$\mathbf{u}$, and the microrotation vector, $\bar{\phi}$. The two deformation maps associated with these DOF are the deformation gradient, $\mathbf{F}$, and the microrotation tensor, $\bar{\mathbf{R}}$, which is related to the microrotation vector as

$$\bar{\mathbf{R}} = \exp\left(-\boldsymbol{\epsilon} \cdot \bar{\phi}\right) = \exp\left(\bar{\boldsymbol{\Phi}}\right) \tag{3.1}$$

where , $\boldsymbol{\epsilon}$ is the alternating tensor and $\bar{\boldsymbol{\Phi}} = -\boldsymbol{\epsilon} \cdot \bar{\phi}$ is the skew-symmetric linear microrotation tensor. The two-point tensor $\bar{\mathbf{R}}$ can be thought of as a microdeformation map completely analogous to the deformation gradient, with the distinction that the deformation gradient describes the transformation of *material* vectors attached to continuum point while the microrotation tensor describes the transformation of *microstructural* vectors attached to the same point. Considering small deformations and rotations, material vectors deform according to Eq. $(2.20)_{1,2}$, i.e.,

$$d\mathbf{x} = \mathbf{F} \cdot d\mathbf{X} = d\mathbf{X} + (\boldsymbol{\varepsilon} + \boldsymbol{\omega}) \cdot d\mathbf{X} \tag{3.2}$$

while microstructural director vectors, $\mathbf{D}$, deform according to

$$\mathbf{d} = \bar{\mathbf{R}} \cdot \mathbf{D} = \mathbf{D} + \bar{\boldsymbol{\Phi}} \cdot \mathbf{D}, \tag{3.3}$$

where $\mathbf{d}$ is the deformed microstructural vector and the small deformation assumption has been used in the approximation $\bar{\mathbf{R}} = \exp\left(\bar{\boldsymbol{\Phi}}\right) \approx \mathbf{I} + \bar{\boldsymbol{\Phi}}$. A suitable set of linearized invariant deformation measures are the micropolar strain, $\bar{\boldsymbol{\varepsilon}}$, and torsion-curvature, $\bar{\boldsymbol{\kappa}}$, tensors defined as

$$\bar{\boldsymbol{\varepsilon}} = \mathbf{H} - \bar{\boldsymbol{\Phi}} = \mathbf{u}\overleftarrow{\nabla} + \boldsymbol{\epsilon} \cdot \bar{\phi} \tag{3.4}$$

$$\bar{\boldsymbol{\kappa}} = \bar{\phi}\overleftarrow{\nabla} \tag{3.5}$$

The overbar on the microrotation vector, linear microrotation tensor, strain, and torsion-curvature tensors is used to distinguish kinematic quantities used in the micropolar theory from those introduced in Chapter 2, and $\mathbf{H} = \mathbf{u}\overleftarrow{\nabla}$ is the distortion tensor. The micropolar strain tensor is generally non-symmetric, and is sometimes referred to as the relative deformation tensor. The symmetric part is just the classical small strain tensor since the microdeformation is purely rotational, i.e.,

$$\mathrm{sym}\left(\overline{\varepsilon}\right) = \tfrac{1}{2}\left(\mathbf{u}\overleftarrow{\nabla} + \vec{\nabla}\mathbf{u}\right) = \varepsilon \tag{3.6}$$

whereas the skew-symmetric part gives the difference between the material rotation and microrotation, i.e.,

$$\mathrm{skw}\left(\overline{\varepsilon}\right) = \tfrac{1}{2}\left(\mathbf{u}\overleftarrow{\nabla} - \vec{\nabla}\mathbf{u}\right) + \boldsymbol{\epsilon}\cdot\overline{\phi} = \boldsymbol{\omega} - \overline{\boldsymbol{\Phi}} \tag{3.7}$$

If the microrotation and material rotations coincide, the kinematic description reduces to that of the so-called constrained micropolar continuum (also referred to in the literature as indeterminate couple stress theory [132]) in which the couple stress is work conjugate to the gradient of *material* rotation.

The 2-D interpretation of these deformation measures is illustrated in Figure 3.1 for a material element under simple shear. The deformed state at a material point is characterized by considering the motion of two independent sets of initially orthogonal vectors, $d\mathbf{X}^1, d\mathbf{X}^2$ and $\mathbf{D}^1, \mathbf{D}^2$, the former being material vectors and the latter denoting the microstructural vectors (shown in red). During deformation the material and microstructural vectors are transformed into their respective counterparts, $d\mathbf{x}^1, d\mathbf{x}^2$ and $\mathbf{d}^1, \mathbf{d}^2$. The material vectors stretch and rotate, whereas the microstructural director vectors only rotate. The relevant micropolar tensorial shear strain components $\overline{\varepsilon}_{12}$ and $\overline{\varepsilon}_{21}$ are given as, $\overline{\varepsilon}_{12} = \overline{\phi}_3$ and, $\overline{\varepsilon}_{21} = u_{2,1} - \overline{\phi}_3$, where it is again emphasized that $\overline{\varepsilon}_{(12)}$ and $\overline{\varepsilon}_{(21)}$ are the usual tensorial shear strains from the standard theory, and $\overline{\varepsilon}_{[12]}$ and $\overline{\varepsilon}_{[21]}$ give the difference between the material and microrotations, i.e., the *relative* rotation of the microstructure with respect to the material.

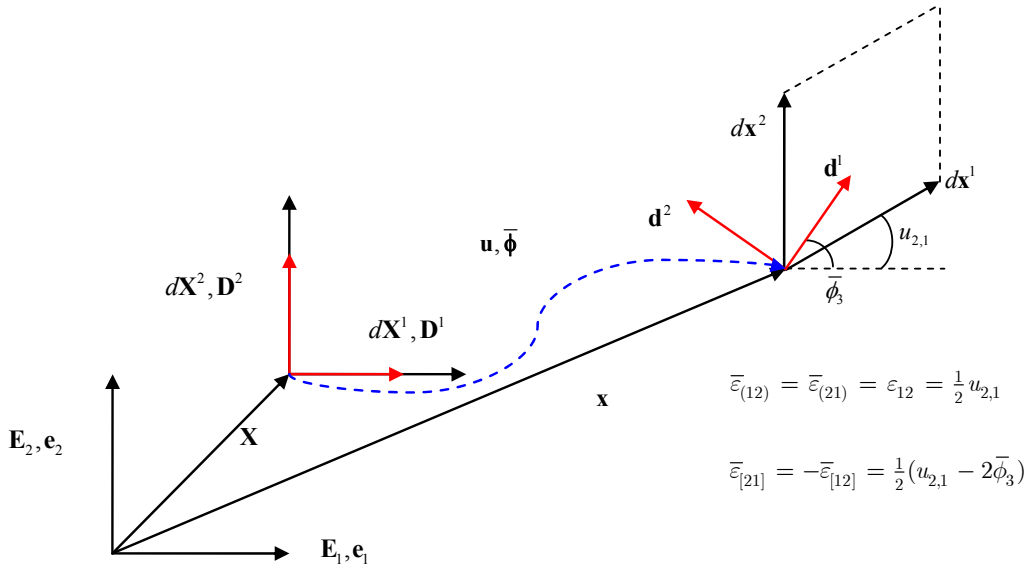

Figure 3.1: Geometric interpretation of the micropolar shear strains.

3.3 Balance Laws and Thermodynamics

In the absence of body forces and couples, the strong form of the linear and angular momentum balances for a micropolar continuum in static equilibrium are given as

$$\left.\begin{aligned} \boldsymbol{\sigma} \cdot \overleftarrow{\nabla} &= \mathbf{0} \\ \mathbf{m} \cdot \overleftarrow{\nabla} - \boldsymbol{\epsilon} : \boldsymbol{\sigma} &= \mathbf{0} \end{aligned}\right\} \quad \forall \mathbf{x} \in R \tag{3.8}$$

where $\boldsymbol{\sigma}$ is the Cauchy stress tensor work-conjugate to the micropolar strains and $\mathbf{m}$ is the couple stress tensor work-conjugate to the torsion-curvature. The micropolar continuum admits the prescription of the standard natural and essential boundary conditions given in Eqs. (2.24)-(2.25), and additional micro boundary conditions of the type

$$\mathbf{M} = \mathbf{m} \cdot \hat{\mathbf{n}} = \mathbf{M}^* \quad \forall \mathbf{x} \in \partial R_m \tag{3.9}$$

$$\bar{\Phi} = \bar{\Phi}^* \quad \forall \mathbf{x} \in \partial R_{\bar{\phi}} \tag{3.10}$$

where $\mathbf{M}^*$ and $\overline{\phi}^*$ are the prescribed couple stress tractions and microrotations, respectively. Here, ∂R_m and $\partial R_{\overline{\phi}}$ are the portions of the external boundary where couple tractions and microrotations are specified, respectively and $\partial R = \partial R_m \cup \partial R_{\overline{\phi}}$.

The free energy inequality introduced in Chapter 2 remains valid, i.e., $\mathfrak{p}_I \geq \rho\dot{\psi}$, but the expression for the power density of internal forces appropriate for the micropolar continuum must be used and is given as

$$\mathfrak{p}_I = \boldsymbol{\sigma} : \dot{\overline{\varepsilon}} + \mathbf{m} : \dot{\overline{\boldsymbol{\kappa}}} \tag{3.11}$$

The deformation power may be split into local, $\mathfrak{p}_{I-L}$, and nonlocal, $\mathfrak{p}_{I-NL}$, contributions as

$$\mathfrak{p}_{I-L} = \boldsymbol{\sigma} : \mathrm{sym}\left(\dot{\overline{\varepsilon}}\right) = \boldsymbol{\sigma} : \dot{\varepsilon} \tag{3.12}$$

$$\mathfrak{p}_{I-NL} = \boldsymbol{\sigma} : \mathrm{skw}\left(\dot{\overline{\varepsilon}}\right) + \mathbf{m} : \dot{\overline{\boldsymbol{\kappa}}} \tag{3.13}$$

It is clear from Eq. (3.13) that the nonlocal contribution vanishes when (i) material and microrotation rates coincide *and* (ii) the torsion-curvature rate is zero. For micropolar elastoplasticity within a geometrically linear framework, additive decompositions of strain and torsion-curvature are assumed to hold, i.e.,

$$\overline{\varepsilon} = \overline{\varepsilon}^{\mathrm{e}} + \overline{\varepsilon}^{\mathrm{p}} \tag{3.14}$$

$$\overline{\boldsymbol{\kappa}} = \overline{\boldsymbol{\kappa}}^{\mathrm{e}} + \overline{\boldsymbol{\kappa}}^{\mathrm{p}} \tag{3.15}$$

The free energy is assumed to be a function of the elastic strain, elastic torsion-curvature and a set (one for each slip system) of elastic strain-like scalar ISVs, $\{\zeta^\alpha\}$, i.e.,

$$\psi = \hat{\psi}\left(\overline{\varepsilon}^{\mathrm{e}}, \overline{\boldsymbol{\kappa}}^{\mathrm{e}}, \{\zeta^\alpha\}\right) \tag{3.16}$$

Following standard arguments the state laws and reduced dissipation inequality are obtained as

$$\boldsymbol{\sigma} = \rho \frac{\partial \psi}{\partial \overline{\boldsymbol{\varepsilon}}^{\mathrm{e}}} \quad , \quad \mathbf{m} = \rho \frac{\partial \psi}{\partial \overline{\boldsymbol{\kappa}}^{\mathrm{e}}} \quad , \quad \chi^{\alpha} = \rho \frac{\partial \psi}{\partial \zeta^{\alpha}} \tag{3.17}$$

$$\mathfrak{d} = \boldsymbol{\sigma} : \dot{\overline{\boldsymbol{\varepsilon}}}^{\mathrm{p}} + \mathbf{m} : \dot{\overline{\boldsymbol{\kappa}}}^{\mathrm{p}} - \sum_{\alpha} \chi^{\alpha} \dot{\zeta}^{\alpha} \geq 0 \tag{3.18}$$

where ρ is the mass density and χ^{α} is the thermodynamic force work conjugate to the thermodynamic displacement, ζ^{α}. Introducing a free energy function with quadratic dependence on its arguments, i.e.,

$$\psi_{v} = \tfrac{1}{2} \overline{\boldsymbol{\varepsilon}}^{\mathrm{e}} : \mathbb{C} : \overline{\boldsymbol{\varepsilon}}^{\mathrm{e}} + \tfrac{1}{2} \overline{\boldsymbol{\kappa}}^{\mathrm{e}} : \mathbb{D} : \overline{\boldsymbol{\kappa}}^{\mathrm{e}} + \tfrac{1}{2} \sum_{\alpha} \sum_{\beta} \zeta^{\alpha} E^{\alpha\beta} \zeta^{\beta} \tag{3.19}$$

where $\mathbb{C}$ and $\mathbb{D}$ are 4th rank elasticity tensors, $E^{\alpha\beta}$ is a symmetric positive-definite material modulus matrix, and the elasticity cross-term of the form $\overline{\boldsymbol{\kappa}}^{\mathrm{e}} : \mathbb{G} : \overline{\boldsymbol{\varepsilon}}^{\mathrm{e}}$ has been neglected since there can be no coupling between the force and couple stress elastic responses if the material possesses at least point symmetry [133]. Given Eq. (3.17), the state laws take the explicit forms

$$\boldsymbol{\sigma} = \mathbb{C} : \overline{\boldsymbol{\varepsilon}}^{\mathrm{e}} \quad , \quad \mathbf{m} = \mathbb{D} : \overline{\boldsymbol{\kappa}}^{\mathrm{e}} \quad , \quad \chi^{\alpha} = \sum_{\delta} E^{\alpha\delta} \zeta^{\delta} \tag{3.20}$$

3.4 Constitutive Equations

In the process of defining the material modulus tensors, $\mathbb{C}$, $\mathbb{D}$, and $E^{\alpha\beta}$, the evolution equations for $\dot{\overline{\boldsymbol{\varepsilon}}}^{\mathrm{p}}$, $\dot{\overline{\kappa}}^{\mathrm{p}}$, and $\dot{\zeta}^{\alpha}$, and the material strength model appropriate for a micropolar single crystal, the classical theory and its slip gradient-based extensions are used as a guide. With this in mind, the following assumptions are made:

A1. As in the classical linearized theory, the total distortion is decomposed into elastic and plastic parts, $\mathbf{u} \overleftarrow{\nabla} = \mathbf{H}^{\mathrm{e}} + \mathbf{H}^{\mathrm{p}}$.

A2. The micropolar plastic strain rate is equal to the plastic distortion rate, $\dot{\overline{\boldsymbol{\varepsilon}}}^{\mathrm{p}} \equiv \dot{\mathbf{H}}^{\mathrm{p}}$.

A3. Micropolar effects should be negligible during purely elastic deformations.

A4. Microrotations are identified as lattice rotations.

A5. Elastic material rotations, embodied by $\boldsymbol{\omega}^{e}$, should coincide with the lattice rotations, i.e., the skew symmetric force stresses should be small compared to the symmetric force stresses.

A6. The evolution of plastic torsion-curvature is due to the generation and accumulation of geometrically necessary dislocations (GNDs).

These assumptions provide the basis from which the remainder of the theory is derived, and it is noted here that a similar approach has been advanced in Forest et al. [34]. The first two assumptions are relatively straight forward, whereas the last three require further elaboration.

3.4.1 Micropolar Crystal Elasticity

The linear elastic state laws for a micropolar material are given in Eqs. (3.20), where the elasticity tensors obey the major symmetry relations $\mathbb{C}_{ijkl} = \mathbb{C}_{klij}, \mathbb{D}_{ijkl} = \mathbb{D}_{klij}$ which follows directly from the free energy definition given in Eq. (3.19). Additional material symmetries lead to further reductions in the number of independent elastic constants, and for crystalline materials the three most common symmetry classes considered are: isotropic (idealized), cubic (fcc/bcc), and hexagonal (hcp). An isotropic micropolar material requires the specification of six elastic constants, whereas crystals with cubic and hexagonal structure require eight and sixteen constants, respectively. In the classical theory of linear elasticity, isotropic, cubic, and hexagonal materials have two, three, and five independent elastic constants, respectively, meaning that an additional four, five, and eleven constants (considering these three symmetries), respectively, are needed to describe the elastic response of a micropolar solid. The complete list of symmetry groups and the associated number of independent elastic constants are given in Eringen [134]. For an elastically isotropic material the stress-strain relations are expressed as

$$\boldsymbol{\sigma} = \lambda\,\mathrm{tr}(\overline{\boldsymbol{\varepsilon}}^{\mathrm{e}})\mathbf{1} + 2\mu\,\mathrm{sym}(\overline{\boldsymbol{\varepsilon}}^{\mathrm{e}}) + 2\mu_{c}\,\mathrm{skw}(\overline{\boldsymbol{\varepsilon}}^{\mathrm{e}}) \tag{3.21}$$

$$\mathbf{m} = \alpha\,\mathrm{tr}(\overline{\boldsymbol{\kappa}}^{\mathrm{e}})\mathbf{1} + 2\beta\,\mathrm{sym}(\overline{\boldsymbol{\kappa}}^{\mathrm{e}}) + 2\gamma\,\mathrm{skw}(\overline{\boldsymbol{\kappa}}^{\mathrm{e}}) \tag{3.22}$$

where λ and μ are the usual Lamé's constants from the classical theory and μ_{c}, α, β, and γ are the additional micropolar constants. The elastic constitutive equations for cubic and hexagonal crystal symmetries are expressed most conveniently in a modified Voigt notation with the nine-dimensional stress and strain (resp. couple stress and torsion-curvature) vectors defined as

$$\{\sigma\} = \{\,\sigma_{11} \quad \sigma_{22} \quad \sigma_{33} \quad \sigma_{(23)} \quad \sigma_{(31)} \quad \sigma_{(12)} \quad \sigma_{[23]} \quad \sigma_{[31]} \quad \sigma_{[12]}\}^{T} \tag{3.23}$$

$$\{\overline{\varepsilon}^{\mathrm{e}}\} = \{\,\overline{\varepsilon}^{\mathrm{e}}_{11} \quad \overline{\varepsilon}^{\mathrm{e}}_{22} \quad \overline{\varepsilon}^{\mathrm{e}}_{33} \quad 2\overline{\varepsilon}^{\mathrm{e}}_{(23)} \quad 2\overline{\varepsilon}^{\mathrm{e}}_{(31)} \quad 2\overline{\varepsilon}^{\mathrm{e}}_{(12)} \quad 2\overline{\varepsilon}^{\mathrm{e}}_{[23]} \quad 2\overline{\varepsilon}^{\mathrm{e}}_{[31]} \quad 2\overline{\varepsilon}^{\mathrm{e}}_{[12]}\}^{T} \tag{3.24}$$

where the non-dilatational components of the vectors are defined with respect to the symmetric and skew-symmetric tensor components. The elasticity equations may then be expressed in matrix notation as

$$\{\sigma\} = [\mathbb{C}]\{\overline{\varepsilon}^{\mathrm{e}}\} \quad , \quad \{\mathrm{m}\} = [\mathbb{D}]\{\overline{\kappa}^{\mathrm{e}}\} \tag{3.25}$$

Denoting the 4th rank tensor $\mathbb{G}$ which symbolically represents either of the tensors $\mathbb{C}$ or $\mathbb{D}$, the symmetry of the constitutive tensors for cubic and hexagonal crystals are given, respectively, as

Cubic:

$$[\mathbb{G}] = \begin{bmatrix} G_{11} & G_{12} & G_{12} & 0 & 0 & 0 & 0 & 0 & 0 \\ G_{12} & G_{11} & G_{12} & 0 & 0 & 0 & 0 & 0 & 0 \\ G_{12} & G_{12} & G_{11} & 0 & 0 & 0 & 0 & 0 & 0 \\ 0 & 0 & 0 & G_{44} & 0 & 0 & 0 & 0 & 0 \\ 0 & 0 & 0 & 0 & G_{44} & 0 & 0 & 0 & 0 \\ 0 & 0 & 0 & 0 & 0 & G_{44} & 0 & 0 & 0 \\ 0 & 0 & 0 & 0 & 0 & 0 & G_{77} & 0 & 0 \\ 0 & 0 & 0 & 0 & 0 & 0 & 0 & G_{77} & 0 \\ 0 & 0 & 0 & 0 & 0 & 0 & 0 & 0 & G_{77} \end{bmatrix} \tag{3.26}$$

Hexagonal:

$$[\mathbb{G}] = \begin{bmatrix} G_{11} & G_{12} & G_{13} & 0 & 0 & 0 & 0 & 0 & 0 \\ G_{12} & G_{11} & G_{13} & 0 & 0 & 0 & 0 & 0 & 0 \\ G_{13} & G_{13} & G_{33} & 0 & 0 & 0 & 0 & 0 & 0 \\ 0 & 0 & 0 & G_{44} & 0 & 0 & G_{47} & 0 & 0 \\ 0 & 0 & 0 & 0 & G_{44} & 0 & 0 & G_{47} & 0 \\ 0 & 0 & 0 & 0 & 0 & G_{66} & 0 & 0 & 0 \\ 0 & 0 & 0 & G_{47} & 0 & 0 & G_{77} & 0 & 0 \\ 0 & 0 & 0 & 0 & G_{47} & 0 & 0 & G_{77} & 0 \\ 0 & 0 & 0 & 0 & 0 & 0 & 0 & 0 & G_{99} \end{bmatrix} \tag{3.27}$$

where $G_{66} = (G_{11} - G_{12}) / 2$ for the crystal with hexagonal symmetry.

3.4.2 Flow Criteria and ISV Kinetics

There are two ways in which to construct the flow criteria for generalized continua with higher-order stresses; the so-called single and multicriterion methodologies [129]. In a single criterion model with associative plastic flow a single relationship is employed between a combined equivalent stress and equivalent inelastic rate measure to define the onset and direction of plasticity. A general set of functional relationships for the flow potential of micropolar material within this context are given as

$$F\left(\boldsymbol{\sigma}, \mathbf{m}, L_p, r\right) = f\left(\boldsymbol{\sigma}, \mathbf{m}, L_p\right) - r \tag{3.28}$$

$$\dot{\bar{\varepsilon}}^{\mathrm{p}} = \dot{\lambda} \frac{\partial F}{\partial \boldsymbol{\sigma}} \quad , \quad \dot{\bar{\boldsymbol{\kappa}}}^{\mathrm{p}} = \dot{\lambda} \frac{\partial F}{\partial \mathbf{m}} \tag{3.29}$$

where F is the yield function, f is a scalar invariant function of the force stress, couple stress, and a characteristic plastic length scale, L_p, required for dimensional consistency, r is the yield stress, and $\dot{\lambda}$ is the plastic mutliplier. On the other hand, multicriterion models employ independent flow criteria for the plastic strain rate and plastic torsion-curvature rate. This is expressed by an analogous set of relations, i.e.,

$$F_\sigma\left(\boldsymbol{\sigma}, r_\sigma\right) = f_\sigma\left(\boldsymbol{\sigma}\right) - r_\sigma \quad , \quad F_m\left(\mathbf{m}, L_p, r_m\right) = f_m\left(\mathbf{m}, L_p\right) - r_m \tag{3.30}$$

$$\dot{\bar{\boldsymbol{\varepsilon}}}^{\mathrm{p}} = \dot{\lambda}_{\sigma} \frac{\partial F_{\sigma}}{\partial \boldsymbol{\sigma}} \quad , \quad \dot{\bar{\boldsymbol{\kappa}}}^{\mathrm{p}} = \dot{\lambda}_{m} \frac{\partial F_{m}}{\partial \mathbf{m}} \tag{3.31}$$

where all of the terms have the same interpretation as in the single criterion theory, but have been introduced independently with subscripts "σ" and "m" indicating the terms related to the plastic strain and torsion-curvature evolution, respectively. In this type of model, coupled strengthening/softening effects (plastic torsion-curvature induced strain hardening, for example) are accounted for through the prescription of evolution equations for r_{σ} and r_{m} which may, in general, be functions of both plastic parameters. This contrasts with the single criterion models where cross-coupling effects enter the formulation naturally as a result of employing a unified yield function.

MultiCriterion Flow Theory

Based on assumptions A2 and A6, the plastic strain and torsion-curvature rates may be generalized from Eq. (3.31) and written in terms of individual slip system contributions as

$$\dot{\bar{\boldsymbol{\varepsilon}}}^{\mathrm{p}} = \sum_{\alpha} \dot{\lambda}^{\alpha} \frac{\partial F^{\alpha}}{\partial \boldsymbol{\sigma}} = \sum_{\alpha} \dot{\lambda}^{\alpha} \mathbf{N}^{\alpha} \tag{3.32}$$

$$\dot{\bar{\boldsymbol{\kappa}}}^{\mathrm{p}} = \sum_{\alpha} \dot{\lambda}_{\perp}^{\alpha} \frac{\partial F_{\perp}^{\alpha}}{\partial \mathbf{m}} + \dot{\lambda}_{\odot}^{\alpha} \frac{\partial F_{\odot}^{\alpha}}{\partial \mathbf{m}} = \sum_{\alpha} \dot{\lambda}_{\perp}^{\alpha} \mathbf{N}_{\perp}^{\alpha} + \dot{\lambda}_{\odot}^{\alpha} \mathbf{N}_{\odot}^{\alpha} \tag{3.33}$$

In Eq.(3.33), separate terms have been introduced to account for excess edge ($\perp$) and screw ($\odot$) GND densities as suggested by Eqs. (2.68)-(2.70). The transition from Eq. (3.32) to a specific form and set of relations analogous to Eqs. (2.30)-(2.33) from the classical theory then follows directly given assumption A2, i.e.,

$$\dot{\bar{\boldsymbol{\varepsilon}}}^{\mathrm{p}} = \sum_{\alpha} \dot{\gamma}^{\alpha} \mathbf{Z}^{\alpha} \quad , \quad \mathbf{Z}^{\alpha} = \mathbf{s}^{\alpha} \otimes \mathbf{n}^{\alpha} \tag{3.34}$$

$$F^{\alpha} = \left| \tau_{eff}^{\alpha} \right| - r^{\alpha} \tag{3.35}$$

$$\tau_{eff}^{\alpha} = \boldsymbol{\sigma} : \mathbf{Z}^{\alpha} \tag{3.36}$$

$$\mathbf{N}^{\alpha} = \mathbf{Z}^{\alpha}\,\mathrm{sgn}(\tau^{\alpha}_{\mathit{eff}}) \tag{3.37}$$

$$\dot{\gamma}^{\alpha} = \dot{\lambda}^{\alpha}\,\mathrm{sgn}(\tau^{\alpha}_{\mathit{eff}}) \tag{3.38}$$

$$\dot{\lambda}^{\alpha} = \dot{\gamma}_0 \left(\left\langle F^{\alpha} \right\rangle \Big/ g^{\alpha} \right)^{m} \tag{3.39}$$

where we have used the notation, $\tau^{\alpha}_{\mathit{eff}}$, for the resolved shear stress to make the distinction that the driving force for slip in the micropolar theory contains a contribution from the skew-symmetric part of the stress tensor which is not present in the classical theory such that

$$\tau^{\alpha}_{\mathit{eff}} = \tau^{\alpha} - \tau^{\alpha}_{b} \tag{3.40}$$

$$\tau^{\alpha}_{\mathit{eff}} = \mathbf{s}^{\alpha} \cdot \boldsymbol{\sigma} \cdot \mathbf{n}^{\alpha} = \mathbf{s}^{\alpha} \cdot \big[\mathrm{sym}(\boldsymbol{\sigma}) + \mathrm{skw}(\boldsymbol{\sigma}) \big] \cdot \mathbf{n}^{\alpha} \tag{3.41}$$

$$\tau^{\alpha} = \mathbf{s}^{\alpha} \cdot \mathrm{sym}(\boldsymbol{\sigma}) \cdot \mathbf{n}^{\alpha} \tag{3.42}$$

$$\tau^{\alpha}_{b} = -\mathbf{s}^{\alpha} \cdot \mathrm{skw}(\boldsymbol{\sigma}) \cdot \mathbf{n}^{\alpha} \tag{3.43}$$

Here, τ^{α} is the classical resolved shear stress and τ^{α}_{b} is the component due the non-symmetric stresses which acts as a slip system level back stress. Furthermore, using the balance of angular momentum, Eq. $(3.8)_2$, an expression can be obtained for the skew symmetric part of the force stress tensor in terms of the couple stress tensor, i.e.,

$$\mathrm{skw}(\boldsymbol{\sigma}) = \tfrac{1}{2}\boldsymbol{\epsilon} \cdot (\mathbf{m} \cdot \overleftarrow{\nabla}) \tag{3.44}$$

Substitution of this expression into Eq. (3.43) and making use of the fact that $\mathbf{t}^{\alpha} = \mathbf{s}^{\alpha} \times \mathbf{n}^{\alpha}$ allows the back stress contribution to be written as

$$\tau^{\alpha}_{b} = -\tfrac{1}{2}\mathbf{t}^{\alpha} \cdot (\mathbf{m} \cdot \overleftarrow{\nabla}) \tag{3.45}$$

This shows that the back stress arises due to gradients in lattice torsion-curvature projected onto the slip plane. This is analogous to slip gradient-based frameworks which introduce back stresses as functions of

gradients in GNDs, i.e., gradients of lattice torsion-curvature. However, in the micropolar theory back stresses emerge as a consequence of the balance of angular momentum (see Eq. (3.43)) and not as a result of additional constitutive assumptions. This back stress contribution and its relation to other models of strain gradient crystal plasticity and the statistical theory of dislocations has been originally pointed out by Forest [38] for the case of single slip, where the result in Eq. (3.45) is given in a slightly different form. It is also worth noting that, as seen in Eq. (3.34), in contrast to the classical theory, the micropolar plastic strain tensor contains the plastic spin, i.e., $\dot{\boldsymbol{\omega}}^{\mathrm{p}} = skw(\mathbf{s}^{\alpha} \otimes \mathbf{n}^{\alpha})$.

Appealing to A6 and Eq. (2.68), a set of relations for the plastic torsion-curvature evolution due to changes in GND densities is proposed, i.e.,

$$\dot{\tilde{\boldsymbol{\kappa}}}^{\mathrm{p}} = \sum_{\alpha} \frac{\dot{\varphi}_{\perp}^{\alpha}}{L_{\perp}^{\alpha}} \mathbf{Y}_{\perp}^{\alpha} + \frac{\dot{\varphi}_{\odot}^{\alpha}}{L_{\odot}^{\alpha}} \mathbf{Y}_{\odot}^{\alpha} \tag{3.46}$$

$$\mathbf{Y}_{\perp}^{\alpha} = \mathbf{t}^{\alpha} \otimes \mathbf{s}^{\alpha} \quad , \quad \mathbf{Y}_{\odot}^{\alpha} = \mathbf{s}^{\alpha} \otimes \mathbf{s}^{\alpha} \tag{3.47}$$

$$F_{\perp}^{\alpha} = \left| \pi_{\perp}^{\alpha} \right| \Big/ L_{\perp}^{\alpha} - r_{\perp}^{\alpha} \quad , \quad F_{\odot}^{\alpha} = \left| \pi_{\odot}^{\alpha} \right| \Big/ L_{\odot}^{\alpha} - r_{\odot}^{\alpha} \tag{3.48}$$

$$\pi_{\perp}^{\alpha} = \mathbf{m} : \mathbf{Y}_{\perp}^{\alpha} \quad , \quad \pi_{\odot}^{\alpha} = \mathbf{m} : \mathbf{Y}_{\odot}^{\alpha} \tag{3.49}$$

$$\mathbf{N}_{\perp}^{\alpha} = \frac{1}{L_{\perp}^{\alpha}} \mathbf{Y}_{\perp}^{\alpha} \operatorname{sgn}\left(\pi_{\perp}^{\alpha} \right) \quad , \quad \mathbf{N}_{\odot}^{\alpha} = \frac{1}{L_{\odot}^{\alpha}} \mathbf{Y}_{\odot}^{\alpha} \operatorname{sgn}\left(\pi_{\odot}^{\alpha} \right) \tag{3.50}$$

$$\dot{\varphi}_{\perp}^{\alpha} = \dot{\lambda}_{\perp}^{\alpha} \operatorname{sgn}\left(\pi_{\perp}^{\alpha} \right) \quad , \quad \dot{\varphi}_{\odot}^{\alpha} = \dot{\lambda}_{\odot}^{\alpha} \operatorname{sgn}\left(\pi_{\odot}^{\alpha} \right) \tag{3.51}$$

$$\dot{\lambda}_{\perp}^{\alpha} = \dot{\varphi}_{\perp 0} \left(\left\langle F_{\perp}^{\alpha} \right\rangle \Big/ g_{\perp}^{\alpha} \right)^{n_{\perp}} \quad , \quad \dot{\lambda}_{\odot}^{\alpha} = \dot{\varphi}_{\odot 0} \left(\left\langle F_{\odot}^{\alpha} \right\rangle \Big/ g_{\odot}^{\alpha} \right)^{n_{\odot}} \tag{3.52}$$

where the dislocation dyad tensors $\mathbf{Y}_{\perp}^{\alpha}, \mathbf{Y}_{\odot}^{\alpha}$; characteristic plastic (dissipative) length scales $L_{\perp}^{\alpha}, L_{\odot}^{\alpha}$; resolved couple stresses $\pi_{\perp}^{\alpha}, \pi_{\odot}^{\alpha}$; and torsion-curvature threshold stresses $r_{\perp}^{\alpha}, r_{\odot}^{\alpha}$ have been introduced for edge ($\perp$) and screw ($\odot$) GND densities, respectively. It is noted that the screw dislocation dyad tensor used in this work differs from that employed in Forest et al. [34], where the expression $\mathbf{Y}_{\odot}^{\alpha} = \frac{1}{2}\mathbf{1} - \mathbf{s}^{\alpha} \otimes \mathbf{s}^{\alpha}$ is used in place of Eq. $(3.47)_2$. The interpretation of Eqs (3.46)-(3.52) in terms of yield functions, resolved driving forces, flow directions, etc. parallels the treatment of plastic slip

deformation modes in the classical theory. The threshold stresses $r_{\perp}^{\alpha}$ and $r_{\odot}^{\alpha}$ are expressed in units of force/length^2 in the yield functions of Eq. (3.48), but the products $r_{\perp}^{\alpha}L_{\perp}^{\alpha}$ and $r_{\odot}^{\alpha}L_{\odot}^{\alpha}$ represent the local threshold couple stresses (force/length) which, when exceeded, require the generation of GNDs to accommodate the local curvature. These plastic length scale parameters, $L_{\perp}^{\alpha}$ and $L_{\odot}^{\alpha}$, are not directly identifiable with any particular material microstructural feature (grain size, inclusion spacing, etc.) per se; however, we assume that they are related to the GND densities via the expressions

$$\dot{\varrho}_{G,\perp}^{\alpha} = -\frac{\dot{\varphi}_{\perp}^{\alpha}}{bL_{\perp}^{\alpha}} \quad , \quad \dot{\varrho}_{G,\odot}^{\alpha} = -\frac{\dot{\varphi}_{\odot}^{\alpha}}{bL_{\odot}^{\alpha}} \tag{3.53}$$

where we have been guided by a comparison of Eqs. (2.68), (2.70), and (3.46). Voyiadjis et al. [135] have shown that the "plastic" length scales entering their micropolar model for granular materials may vary depending on the loading conditions, microstructure, and deformation history. A comparison of the rate form of Eq. (2.71) with Eq. (3.53) shows that the role played by gradients of slip projected in the glide direction in the slip gradient-based extensions of crystal plasticity is subsumed into the plastic multipliers in the micropolar theory, i.e., $\dot{\varphi}_{\perp}^{\alpha} \Leftrightarrow L_{\perp}^{\alpha}\vec{\nabla}\dot{\gamma}^{\alpha} \cdot \mathbf{s}^{\alpha}$ and $\dot{\varphi}_{\odot}^{\alpha} \Leftrightarrow -L_{\odot}^{\alpha}\vec{\nabla}\dot{\gamma}^{\alpha} \cdot \mathbf{t}^{\alpha}$.

The model is completed by defining the slip system level ISV, ζ^{α}, the threshold stresses for slip and plastic torsion-curvature, and their respective evolution equations. The ISV is defined as a measure of the short-range internal elastic strain field caused by dislocations and taken to have the functional form

$$\zeta^{\alpha} = c_1 b\sqrt{\sum\nolimits_{\beta} h^{\alpha\beta}(\varrho_S^{\beta} + \varrho_G^{\beta})} \tag{3.54}$$

where c_1 is dislocation configuration-dependent material constant, b is the magnitude of the Burgers vector, $h^{\alpha\beta}$ is a slip system interaction matrix defining the relative contribution of dislocations lying in slip system β to the strain field on the α^{th} slip system, and ϱ_S^{β} and ϱ_G^{β} are the SSD and GND densities, respectively. Defining the ISV constitutive matrix $E^{\alpha\beta} = \mu\delta^{\alpha\beta}$ (see Eq. (3.19)), the state law between the ISV generalized stress and strain is then given as

$$\chi^{\alpha} = \mu\zeta^{\alpha} \tag{3.55}$$

The total slip system GND density is defined as in Eq. (2.75) and, with the aid of Eq. (3.53), the GND density evolution equation is given by

$$\dot{\varrho}_G^{\alpha} = -\frac{1}{\varrho_G^{\alpha}}\left(\varrho_{G,\perp}^{\alpha}\frac{\dot{\varphi}_{\perp}^{\alpha}}{bL_{\perp}^{\alpha}} + \varrho_{G,\odot}^{\alpha}\frac{\dot{\varphi}_{\odot}^{\alpha}}{bL_{\odot}^{\alpha}}\right) \tag{3.56}$$

The SSD density evolution equation is defined as [62]

$$\dot{\varrho}_S^{\alpha} = \frac{1}{b}\left(\frac{1}{l^{\alpha}} - 2y_c\varrho_S^{\alpha}\right)\mid\dot{\gamma}^{\alpha}\mid, \tag{3.57}$$

and the total dislocation density evolution equation is then given as

$$\dot{\varrho}^{\alpha} = \frac{1}{b}\left(\frac{1}{l^{\alpha}} - 2y_c\varrho_S^{\alpha}\right)\left|\dot{\gamma}^{\alpha}\right| - \frac{1}{\varrho_G^{\alpha}}\left(\varrho_{G,\perp}^{\alpha}\frac{\dot{\varphi}_{\perp}^{\alpha}}{bL_{\perp}^{\alpha}} + \varrho_{G,\odot}^{\alpha}\frac{\dot{\varphi}_{\odot}^{\alpha}}{bL_{\odot}^{\alpha}}\right) \tag{3.58}$$

It is noted here that l^{α}, as discussed in Chapter 2, could be defined in terms of the SSD or total density as shown in Eq. (2.78). Equations (3.54)-(3.58) define the evolution of the dislocation substructure and it is left to define the strength models for plastic shearing and torsion-curvature rates. Three different strength models are proposed. In the first version, it is assumed that the slip threshold is given by an enhanced Taylor relation, the plastic torsion-curvature thresholds are constant, and the mean free path is defined as function of both SSD and GND densities, as outlined next.

Strength Model Version 1

$$r^{\alpha} = r_0^{\alpha} + \mu c_1 b \sqrt{\sum\nolimits_{\beta} h^{\alpha\beta} (\varrho_S^{\beta} + \varrho_G^{\beta})} \tag{3.59}$$

$$l^{\alpha} = \frac{K}{\sqrt{\sum\nolimits_{\beta} a^{\alpha\beta} (\varrho_S^{\beta} + \varrho_G^{\beta})}} \tag{3.60}$$

$$r_{\perp}^{\alpha} = r_{\perp 0}^{\alpha} \quad , \quad r_{\odot}^{\alpha} = r_{\odot 0}^{\alpha} \tag{3.61}$$

where the newly introduced terms are the intrinsic (constant) flow resistances, $r_{\perp 0}^{\alpha}$ and $r_{\odot 0}^{\alpha}$, for plastic torsion-curvature due to edge and screw GNDs, respectively. The terms in Eqs. (3.59) and (3.60) have previously been given in Chapter 2 (see Eqs. (2.35) and (2.37)). The reduced dissipation inequality for this model is then given as

$$\begin{aligned} \mathfrak{d} = \sum_{\alpha} \Bigg(& \mid \tau_{eff}^{\alpha} \mid\mid \dot{\gamma}^{\alpha} \mid + \left| \pi_{\perp}^{\alpha} \right| \frac{\left| \dot{\varphi}_{\perp}^{\alpha} \right|}{L_{\perp}^{\alpha}} + \left| \pi_{\odot}^{\alpha} \right| \frac{\left| \dot{\varphi}_{\odot}^{\alpha} \right|}{L_{\odot}^{\alpha}} \Bigg) \cdots \\ & - \sum_{\alpha} \sum_{\beta} r^{\alpha} \left(H_1^{\alpha\beta} \mid \dot{\gamma}^{\beta} \mid - H_2^{\alpha\beta} \frac{\dot{\varphi}_{\perp}^{\beta}}{L_{\perp}^{\beta}} - H_3^{\alpha\beta} \frac{\dot{\varphi}_{\odot}^{\beta}}{L_{\odot}^{\beta}} \right) \geq 0 \end{aligned} \tag{3.62}$$

where τ_{eff}^{α} is the resolved shear stress (see Eq. (3.41)) and the matrices $H_1^{\alpha\beta}$, $H_2^{\alpha\beta}$, and $H_3^{\alpha\beta}$ are defined according to

$$H_1^{\alpha\beta} = \frac{c_1}{2} \frac{h^{\alpha\beta}}{\sqrt{\sum\nolimits_{\delta} h^{\alpha\delta} (\varrho_S^{\delta} + \varrho_G^{\delta})}} \left(\frac{1}{K} \sqrt{\sum\nolimits_{\chi} a^{\beta\chi} (\varrho_S^{\chi} + \varrho_G^{\chi})} - 2 y_c \varrho_S^{\beta} \right) \tag{3.63}$$

$$H_2^{\alpha\beta} = \frac{c_1}{2} \frac{h^{\alpha\beta}}{\sqrt{\sum\nolimits_{\delta} h^{\alpha\delta} (\varrho_S^{\delta} + \varrho_G^{\delta})}} \frac{\varrho_{G,\perp}^{\beta}}{\varrho_G^{\beta}} \tag{3.64}$$

$$H_3^{\alpha\beta} = \frac{c_1}{2} \frac{h^{\alpha\beta}}{\sqrt{\sum\nolimits_{\delta} h^{\alpha\delta} (\varrho_S^{\delta} + \varrho_G^{\delta})}} \frac{\varrho_{G,\odot}^{\beta}}{\varrho_G^{\beta}} \tag{3.65}$$

The second version assumes that the slip threshold is defined by a generalized Taylor relation, the plastic torsion-curvature thresholds are defined by Taylor-like relations in terms of the edge and screw GND

densities, respectively, and the mean free path is defined as a function of both SSD and GND densities. It is listed as follows.

Strength Model Version 2:

$$r^{\alpha} = r_0^{\alpha} + \mu c_1 b\sqrt{\sum\nolimits_{\beta} h^{\alpha\beta}(\varrho_S^{\beta} + \varrho_G^{\beta})} \tag{3.66}$$

$$l^{\alpha} = \frac{K}{\sqrt{\sum\nolimits_{\beta} a^{\alpha\beta}(\varrho_S^{\beta} + \varrho_G^{\beta})}} \tag{3.67}$$

$$r_{\perp}^{\alpha} = r_{\perp 0}^{\alpha} + \mu c_7 b\sqrt{\sum\nolimits_{\beta} h_{\perp}^{\alpha\beta} \mid \varrho_{G,\perp}^{\beta} \mid} \quad , \quad r_{\odot}^{\alpha} = r_{\odot 0}^{\alpha} + \mu c_8 b\sqrt{\sum\nolimits_{\beta} h_{\odot}^{\alpha\beta} \mid \varrho_{G,\odot}^{\beta} \mid} \tag{3.68}$$

The material constants c_7 and c_8 and interaction matrices $h_{\perp}^{\alpha\beta}$ and $h_{\odot}^{\alpha\beta}$ are analogous to c_1 and $h^{\alpha\beta}$ used in the slip threshold expression. The dissipation inequality for version 2 is also given by Eqs. (3.62)-(3.65). The third version does not employ the generalized Taylor relation to describe the slip threshold strength, which is defined as a function of the SSD density only. Similarly, the mean free path is also defined as a function of only the SSD density. The plastic torsion-curvature thresholds are taken to be defined as in Eq. (3.68). This version of the strength model completely decouples the strain and torsion-curvature hardening responses and the sole source of scale-dependent strengthening is that due to the gradient-dependent back stress. Decoupling the two material hardening descriptions is an attempt to reflect that, as discussed in Chapter 2, the SSD and GND densities are two independent moments of the total dislocation density which are allowed to evolve independently.

Strength Model Version 3:

$$r^{\alpha} = r_0^{\alpha} + \mu c_1 b\sqrt{\sum\nolimits_{\beta} h^{\alpha\beta}\varrho_S^{\beta}} \tag{3.69}$$

$$l^{\alpha} = \frac{K}{\sqrt{\sum\nolimits_{\beta} a^{\alpha\beta}\varrho_S^{\beta}}} \tag{3.70}$$

$$r_{\perp}^{\alpha} = r_{\perp 0}^{\alpha} + \mu c_7 b\sqrt{\sum\nolimits_{\beta} h_{\perp}^{\alpha\beta} \mid \varrho_{G,\perp}^{\beta} \mid} \quad , \quad r_{\odot}^{\alpha} = r_{\odot 0}^{\alpha} + \mu c_8 b\sqrt{\sum\nolimits_{\beta} h_{\odot}^{\alpha\beta} \mid \varrho_{G,\odot}^{\beta} \mid} \tag{3.71}$$

The reduced dissipation inequality for the third version of the strength model is given as

$$\begin{aligned}\mathfrak{d} = \sum_{\alpha}\Bigg(\mid \tau_{\mathit{eff}}^{\alpha} \mid\mid \dot{\gamma}^{\alpha} \mid + \Big|\pi_{\perp}^{\alpha}\Big| \frac{\Big|\dot{\varphi}_{\perp}^{\alpha}\Big|}{L_{\perp}^{\alpha}} + \Big|\pi_{\odot}^{\alpha}\Big| \frac{\Big|\dot{\varphi}_{\odot}^{\alpha}\Big|}{L_{\odot}^{\alpha}} \Bigg) \cdots \\ - \sum_{\alpha}\sum_{\beta} \chi^{\alpha} \left(H_{1}^{\alpha\beta} \mid \dot{\gamma}^{\beta} \mid - H_{2}^{\alpha\beta} \frac{\dot{\varphi}_{\perp}^{\beta}}{L_{\perp}^{\beta}} - H_{3}^{\alpha\beta} \frac{\dot{\varphi}_{\odot}^{\beta}}{L_{\odot}^{\beta}} \right) \geq 0\end{aligned} \tag{3.72}$$

where the matrices $H_{2}^{\alpha\beta}$ and $H_{3}^{\alpha\beta}$ are defined by Eqs. (3.64)-(3.65) and $H_{1}^{\alpha\beta}$ is defined as

$$H_{1}^{\alpha\beta} = \frac{c_{1}}{2} \frac{h^{\alpha\beta}}{\sqrt{\sum_{\delta} h^{\alpha\delta} (\varrho_{S}^{\delta} + \varrho_{G}^{\delta})}} \left(\frac{1}{K} \sqrt{\sum\nolimits_{\chi} a^{\beta\chi} \varrho_{S}^{\chi}} - 2 y_{c} \varrho_{S}^{\beta} \right) \tag{3.73}$$

Notice that since the slip threshold stress does not depend on the total dislocation density, r^{α} does not appear in the mechanical dissipation rate in Eq. (3.72).

Single Criterion Flow Theory

The single criterion theory possesses a few potentially advantageous features as compared to the multicriterion framework. Namely, it

i) Does not rely on the additive partition of the total dislocation density into SSD and GND contributions as a means to describe scale-dependent slip threshold hardening; a questionable proposition to some [78, 136, 137].

ii) Reduces the number of material parameters and evolution equations required to define the inelastic material response.

The appropriate generalization of Eq. (3.29) for the single criterion model is

$$\dot{\bar{\boldsymbol{\varepsilon}}}^{\mathrm{p}} = \sum_{\alpha} \dot{\lambda}^{\alpha} \frac{\partial F^{\alpha}}{\partial \boldsymbol{\sigma}} = \sum_{\alpha} \dot{\lambda}^{\alpha} \mathbf{N}^{\alpha} \tag{3.74}$$

$$\dot{\bar{\boldsymbol{\kappa}}}^{\mathrm{p}} = \sum_{\alpha} \dot{\lambda}^{\alpha} \frac{\partial F^{\alpha}}{\partial \mathbf{m}} = \sum_{\alpha} \dot{\lambda}^{\alpha} \left(\mathbf{N}_{\perp}^{\alpha} + \mathbf{N}_{\odot}^{\alpha} \right) \tag{3.75}$$

The yield function for the single criterion model is taken to have the form

$$F^{\alpha} = \hat{\tau}^{\alpha} - r^{\alpha} \quad , \quad \hat{\tau}^{\alpha} = \left(\left| \tau_{eff}^{\alpha} \right|^{p} + \left| \pi_{\perp}^{\alpha} / L_{\perp}^{\alpha} \right|^{p} + \left| \pi_{\odot}^{\alpha} / L_{\odot}^{\alpha} \right|^{p} \right)^{1/p} \tag{3.76}$$

where $\hat{\tau}^{\alpha}$ is an equivalent stress measure that is strictly analogous to that introduced in Shu and Fleck [27] for their second gradient crystal plasticity theory and p is an exponent that according to them "...in a loose sense it defines the interaction between statistically stored and geometrically necessary dislocations." In this research, we consider cases $p =$ 1,2 and the remaining relations for the model follow in a straight forward manner For $p = 1$,

$$\hat{\tau}^{\alpha} = \left| \tau_{eff}^{\alpha} \right| + \left| \pi_{\perp}^{\alpha} / L_{\perp}^{\alpha} \right| + \left| \pi_{\odot}^{\alpha} / L_{\odot}^{\alpha} \right| \tag{3.77}$$

$$\mathbf{N}^{\alpha} = \mathbf{Z}^{\alpha} \operatorname{sgn}(\tau_{eff}^{\alpha}) \tag{3.78}$$

$$\mathbf{N}_{\perp}^{\alpha} = \frac{1}{L_{\perp}^{\alpha}} \mathbf{Y}_{\perp}^{\alpha} \operatorname{sgn}(\pi_{\perp}^{\alpha}) \quad , \quad \mathbf{N}_{\odot}^{\alpha} = \frac{1}{L_{\odot}^{\alpha}} \mathbf{Y}_{\odot}^{\alpha} \operatorname{sgn}(\pi_{\odot}^{\alpha}) \tag{3.79}$$

$$\dot{\gamma}^{\alpha} = \dot{\lambda}^{\alpha} \operatorname{sgn}(\tau_{eff}^{\alpha}) \tag{3.80}$$

$$\dot{\varphi}_{\perp}^{\alpha} = \dot{\lambda}^{\alpha} \operatorname{sgn}(\pi_{\perp}^{\alpha}) \quad , \quad \dot{\varphi}_{\odot}^{\alpha} = \dot{\lambda}^{\alpha} \operatorname{sgn}(\pi_{\odot}^{\alpha}) \tag{3.81}$$

$$\dot{\lambda}^{\alpha} = \dot{\gamma}_{0} \left(\left\langle F^{\alpha} \right\rangle / g^{\alpha} \right)^{m} = \left| \dot{\gamma}^{\alpha} \right| = \left| \dot{\varphi}_{\perp}^{\alpha} \right| = \left| \dot{\varphi}_{\odot}^{\alpha} \right| \tag{3.82}$$

For $p = 2$,

$$\hat{\tau}^{\alpha} = \sqrt{\left| \tau_{eff}^{\alpha} \right|^{2} + \left| \pi_{\perp}^{\alpha} / L_{\perp}^{\alpha} \right|^{2} + \left| \pi_{\odot}^{\alpha} / L_{\odot}^{\alpha} \right|^{2}} \tag{3.83}$$

$$\mathbf{N}^{\alpha} = \mathbf{Z}^{\alpha} \frac{\tau_{eff}^{\alpha}}{\hat{\tau}^{\alpha}} \tag{3.84}$$

$$\mathbf{N}_{\perp}^{\alpha} = \frac{1}{(L_{\perp}^{\alpha})^{2}} \mathbf{Y}_{\perp}^{\alpha} \frac{\pi_{\perp}^{\alpha}}{\hat{\tau}^{\alpha}} \quad , \quad \mathbf{N}_{\odot}^{\alpha} = \frac{1}{(L_{\odot}^{\alpha})^{2}} \mathbf{Y}_{\odot}^{\alpha} \frac{\pi_{\odot}^{\alpha}}{\hat{\tau}^{\alpha}} \tag{3.85}$$

$$\dot{\gamma}^{\alpha} = \dot{\lambda}^{\alpha} \frac{\tau_{eff}^{\alpha}}{\hat{\tau}^{\alpha}} \tag{3.86}$$

$$\dot{\varphi}_{\perp}^{\alpha} = \dot{\lambda}^{\alpha} \frac{\pi_{\perp}^{\alpha}}{L_{\perp}^{\alpha} \hat{\tau}^{\alpha}} \quad , \quad \dot{\varphi}_{\odot}^{\alpha} = \dot{\lambda}^{\alpha} \frac{\pi_{\odot}^{\alpha}}{L_{\odot}^{\alpha} \hat{\tau}^{\alpha}} \tag{3.87}$$

$$\dot{\lambda}^{\alpha} = \dot{\gamma}_0 \left(\left\langle F^{\alpha} \right\rangle / g^{\alpha} \right)^m = \sqrt{\left| \dot{\gamma}^{\alpha} \right|^2 + \left| \dot{\varphi}_{\perp}^{\alpha} \right|^2 + \left| \dot{\varphi}_{\odot}^{\alpha} \right|^2} \tag{3.88}$$

Eqs. $(3.82)_{2\text{-}4}$ and Eq. $(3.88)_3$ can be proven in straight-forward fashion by insertion of Eqs. (3.80)-(3.81) into Eq. (3.82) and insertion of Eqs. (3.86)-(3.87) into Eq. (3.88), respectively. The plastic strain and torsion-curvature rates derived using these yield functions may be expressed as before as, i.e.,

$$\dot{\bar{\varepsilon}}^{\mathrm{p}} = \sum_{\alpha} \dot{\gamma}^{\alpha} \mathbf{Z}^{\alpha} \quad , \quad \dot{\bar{\boldsymbol{\kappa}}}^{\mathrm{p}} = \sum_{\alpha} \frac{\dot{\varphi}_{\perp}^{\alpha}}{L_{\perp}^{\alpha}} \mathbf{Y}_{\perp}^{\alpha} + \frac{\dot{\varphi}_{\odot}^{\alpha}}{L_{\odot}^{\alpha}} \mathbf{Y}_{\odot}^{\alpha} \tag{3.89}$$

where it is understood that the definitions given in Eqs. (3.77)-(3.88) are to be used in place of those introduced for the multicriterion model.

The slip system level ISVs are defined as in Eqs. (3.54)-(3.55) and the SSD density evolution equation for the single criterion model is defined as

$$\dot{\varrho}_S^{\alpha} = \frac{1}{b} \left(\frac{1}{K} \sqrt{\textstyle\sum_{\beta} a^{\alpha\beta} \varrho_S^{\beta}} - 2 y_c \varrho_S^{\alpha} \right) \dot{\lambda}^{\alpha} \tag{3.90}$$

where it is seen that the l^{α} is defined as a function of the SSD density only as in version 3 of the multicriterion strength model, and the GND density evolution equations for the single criterion model are obtained by substituting Eq. (3.81) (resp. (3.87)) in place of Eq. (3.51) in Eq. (3.53). The single criterion model requires only a single strength variable for each slip system and it is defined in terms of the SSD only, i.e.,

$$r^{\alpha} = r_0^{\alpha} + \mu c_1 b \sqrt{\textstyle\sum_{\beta} h^{\alpha\beta} \varrho_S^{\beta}} \tag{3.91}$$

Notice here, as in version 3 of the multicriterion theory, that $\chi^{\alpha} \neq r^{\alpha}$ since ζ^{α} is a function of the *total* dislocation density. It is also noted that the SSD density in Eq. (3.90) is different in character than that defined in Eq. (3.57) and in the first term of Eq. (3.58) for the slip gradient and multicriterion models, respectively. In those formulations the SSD density evolves according to the magnitude of the slip system

shearing rate, $|\,\dot{\gamma}^{\alpha}\,|$; however, since $\dot{\lambda}^{\alpha}$ in Eq. (3.90) is an equivalent inelastic rate as defined by either Eq. (3.82) or Eq. (3.88), it embodies effects due to both plastic slip and torsion-curvature evolution. This is a by-product of the natural coupling present within the single criterion framework, and in this way incorporates scale-dependent isotropic hardening in the absence of a Taylor relation based on the additive superposition of the SSD and GND densities. The reduced dissipation inequality for the above constitutive description is then given as

$$\mathfrak{d} = \sum_{\alpha} \hat{\tau}^{\alpha} \dot{\lambda}^{\alpha} - \sum_{\alpha} \sum_{\beta} \chi^{\alpha} H^{\alpha\beta} \dot{\lambda}^{\beta} \geq 0 \tag{3.92}$$

where the resolved shear stress has been replaced with the appropriate equivalent stress measure, $\hat{\tau}^{\alpha}$, and the matrix $H^{\alpha\beta}$ is defined for $p = 1$ as

$$\begin{aligned} H^{\alpha\beta} = \frac{c_1}{2} \frac{h^{\alpha\beta}}{\sqrt{\sum_{\delta} h^{\alpha\delta} (\varrho_S^{\delta} + \varrho_G^{\delta})}} \Bigg[\left(\frac{1}{K} \sqrt{\sum\nolimits_{\xi} a^{\beta\xi} \varrho_S^{\xi}} - 2 y_c \varrho_S^{\beta} \right) \cdots \\ + \frac{1}{\varrho_G^{\beta}} \left(\varrho_{G,\perp}^{\beta} \frac{\operatorname{sgn}(\pi_{\perp}^{\beta})}{L_{\perp}^{\beta}} + \varrho_{G,\odot}^{\beta} \frac{\operatorname{sgn}(\pi_{\odot}^{\beta})}{L_{\odot}^{\beta}} \right) \Bigg] \end{aligned} \tag{3.93}$$

and for $p = 2$ as

$$\begin{aligned} H^{\alpha\beta} = \frac{c_1}{2} \frac{h^{\alpha\beta}}{\sqrt{\sum_{\delta} h^{\alpha\delta} (\varrho_S^{\delta} + \varrho_G^{\delta})}} \Bigg[\left(\frac{1}{K} \sqrt{\sum\nolimits_{\xi} a^{\beta\xi} \varrho_S^{\xi}} - 2 y_c \varrho_S^{\beta} \right) \cdots \\ + \frac{1}{\varrho_G^{\beta}} \left(\varrho_{G,\perp}^{\beta} \frac{\pi_{\perp}^{\beta} \,/\, L_{\perp}^{\beta}}{L_{\perp}^{\beta} \hat{\tau}^{\beta}} + \varrho_{G,\odot}^{\beta} \frac{\pi_{\odot}^{\beta} \,/\, L_{\odot}^{\beta}}{L_{\odot}^{\beta} \hat{\tau}^{\beta}} \right) \Bigg] \end{aligned} \tag{3.94}$$

The simplified nature of the single criterion model with respect to the multicriterion model is advantageous only if the reduced nature of the constitutive description does not significantly limit the range and characteristics of the deformation behavior that can be captured. This is assessed in the benchmark numerical simulations performed in Chapter 5.

3.4.3 Material Parameter Selection

The various assumptions listed at the beginning at the beginning of Section 3.4 provide guidance in specifying and interpreting certain material parameters. Given A4 and Eq. (3.3), a slip system director vector, $\mathbf{D}^{\alpha}$, deforms according to

$$\mathbf{d}^{\alpha} = \mathbf{D}^{\alpha} + \bar{\mathbf{\Phi}} \cdot \mathbf{D}^{\alpha} \tag{3.95}$$

Assumptions A1 and A2 result in the micropolar elastic strain tensor being defined as

$$\bar{\varepsilon}^{\mathrm{e}} = \mathbf{H}^{\mathrm{e}} - \bar{\mathbf{\Phi}} \tag{3.96}$$

A5 asserts that the elastic material rotations should approximately coincide with the lattice rotations, a constraint that maintains a connection with the classical theory of crystal plasticity (see Eq. (2.21)). This constraint may be enforced by minimizing the skew-symmetric part of the elastic micropolar strain tensor, i.e.,

$$\mathrm{skw}(\bar{\varepsilon}^{\mathrm{e}}) = \boldsymbol{\omega}^{\mathrm{e}} - \bar{\mathbf{\Phi}} \tag{3.97}$$

Considering the isotropic constitutive relations given in Eq. (3.21), this can be achieved by prescribing large values for μ_c [34] such that the nonlocal strain energy contribution from this term (Eq. $(3.13)_1$) would become unbounded if $\mathrm{skw}(\bar{\varepsilon}^{\mathrm{e}})$ were non-negligible since $\boldsymbol{\sigma} : \mathrm{skw}(\bar{\varepsilon}^{\mathrm{e}}) = \mu_c \, || \, \mathrm{skw}(\bar{\varepsilon}^{\mathrm{e}}) \, ||^2$. Therefore, the μ_c parameter acts as an energetic penalty constraint forcing $\mathrm{skw}(\bar{\varepsilon}^{\mathrm{e}}) \approx 0 \Rightarrow \boldsymbol{\omega}^{\mathrm{e}} \approx \bar{\mathbf{\Phi}}$. The extension of this concept to other material symmetries should follow the same logic so as to minimize the development of skew-symmetric elastic strains. A consequence of this assumption is that prior to reaching the activation threshold for plastic torsion-curvature, the lattice rotation predicted by the micropolar theory is identical to that predicted by the classical theory. However, once activated, the plastic torsion-curvature will drive the lattice rotations which will necessarily differ from those obtained from the standard theory.

The remaining non-traditional material parameters are those related to the couple stress-curvature response. With regard to A3, we require that the micropolar effects should be negligible during purely

elastic deformations. Essentially, this is a requirement that the effective elastic stiffness of the micropolar crystal should not exceed that of its classical counterpart. Such behavior can result if large values of the couple stress elastic constants are used. From dimensional considerations, it is seen that the quotient of any given couple stress elastic constant to that of a force stress elastic constant has dimensions of length squared. These quotients represent "elastic" or "energetic" material length scales of the micropolar continuum. Referring to the constitutive relations given in Eqs. (3.21)-(3.22), a typical elastic length scale, ℓ_1, which commonly arises in the solution of 2-D initial-boundary value problems, is given as

$$\ell_1 = \sqrt{\frac{\beta + \gamma}{\mu}} \tag{3.98}$$

Additional elastic material length scales have been introduced by Cowin [138]. To satisfy assumption A3, these elastic length scales should be smaller than the characteristic dimensions of the material volume being modeled. These elastic length scales are to be distinguished from the plastic (dissipative) length scales ($L_{\perp}^{\alpha}$, $L_{\odot}^{\alpha}$) which are introduced in the plastic torsion-curvature evolution equations in Section 3.4.2. Since the intrinsic back stress arises due to gradients in lattice torsion-curvature, as demonstrated in Eq. (3.45), this allows for an interpretation of the couple stress and plastic torsion-curvature parameters as being related to the development of heterogeneous dislocation arrangements whose influence affects post-yield behavior. For example, consider the stress-strain response of a single crystal with no slip threshold evolution (no isotropic hardening). If there are no gradients in lattice torsion-curvature, the stress-strain response will be elastic-perfectly plastic as shown in Figure 3.2(a). Conversely, when there are appreciable gradients in lattice torsion-curvature there will be material strengthening due to the development of back stresses via Eq. (3.45). In the absence of plastic torsion-curvature, which can be accomplished in the multicriterion theory by specifying infinite plastic torsion-curvature thresholds and in the in the single criterion theory by specifying $L_{\perp}^{\alpha}, L_{\odot}^{\alpha} \gg \ell_1$, the kinematic hardening response is linear and the rate of hardening is proportional to the elastic length scale parameter, as shown in Figure 3.2(b). When plastic torsion-curvature is non-negligible, the initial kinematic hardening modulus is dictated by the elastic length scale parameter, whereas the deviation from the linear response is governed by the plastic torsion-curvature

threshold stresses and the magnitude of the plastic length scales, as shown in Figure 3.2(c). These deformation characteristics are further examined and demonstrated in the simulations performed in Chapter 5.

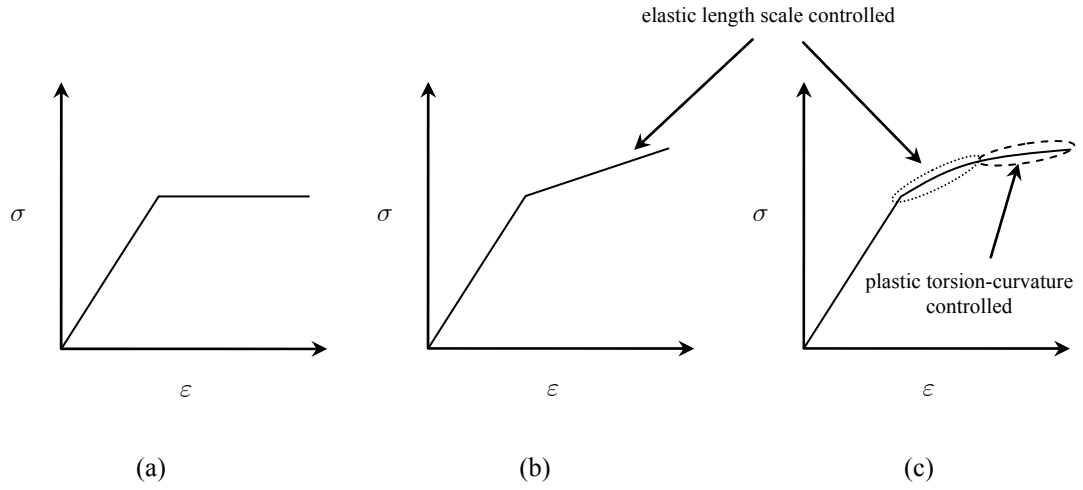

Figure 3.2: Qualitative 1-D stress-strain response for a micropolar single crystal with no slip threshold evolution (a) no gradient effects (b) gradient effects with energetic kinematic hardening only and (c) gradient effects with energetic-dissipative kinematic hardening.

3.5 Discussion

Analogue to an enhanced three-term decomposition of the material deformation

In a certain sense, the micropolar continuum may actually provide a more refined description of GND-related size effects than many of the slip gradient-based models. It has been argued by Hartley [139], Clayton and McDowell [36, 100], and more recently by Gerken and Dawson [73, 102] that the popular two-term decomposition of the strain (or deformation gradient for finite deformation) into elastic and plastic parts may be insufficient for describing the kinematics of non-homogeneously deforming crystalline materials within a classical continuum theory. These authors reason that the lattice deformation, $\mathbf{H}^{l}$, typically associated with the elastic material distortion, $\mathbf{H}^{e}$, should actually be decomposed into (at least)

two-terms: one associated with the removal of external tractions on the "released" (thought experiment) material volume element and another associated with the deformation heterogeneity that exists at finer length scales and/or between incompatibly deformed neighboring material elements. These approaches suggest a decomposition of the total distortion in the geometrically linear setting as

$$\mathbf{u}\overleftarrow{\nabla} = \mathbf{H}^{\mathrm{l}} + \mathbf{H}^{\mathrm{p}} = \mathbf{H}^{\mathrm{e}^*} + \mathbf{H}^{\mathrm{i}} + \mathbf{H}^{\mathrm{p}} \tag{3.99}$$

where $\mathbf{H}^{\mathrm{l}}$ is the total lattice distortion, $\mathbf{H}^{\mathrm{e}^*}$ is the lattice distortion associated with external (to the volume element) loading, and $\mathbf{H}^{\mathrm{i}}$ is the lattice distortion due to inhomogeneous (incompatible) deformation. One advantage of such models as compared to theories (classical or generalized) employing the two-term decomposition is that the accomodational elastic lattice strains that develop during heterogeneous plastic flow are distinguished from those resulting from external loading and directly enter the mechanical balance equations since, i.e.,

$$\boldsymbol{\sigma} = \mathbb{C} : \mathrm{sym}(\mathbf{H}^{\mathrm{e}^*} + \mathbf{H}^{\mathrm{i}}) \tag{3.100}$$

Therefore, the additional lattice kinematics due to deformation incompatibility are properly accounted for and the resulting back stresses enter the flow rule naturally, which is counter to approaches that insert the back stress due to GNDs directly into the yield function while retaining the two-term decomposition [14, 72, 140].

A challenge for this type of theory lies in the construction of the evolution equation for the incompatible lattice distortion. Gerken and Dawson [73] have cleverly addressed this issue by determining $\mathbf{H}^{\mathrm{i}}$ from the long-range strain fields produced by the GND distribution which is calculated in terms of the slip gradients according to Eq. (2.71). However, this approach, as handled in Gerken and Dawson [73], still involves the additional computational cost associated with the modified FE algorithms required to calculate slip gradients, the incompatible deformation tensor, and incorporating these features into the solution procedure. On the other hand, micropolar single crystal plasticity qualitatively embodies the advantageous features of the enhanced three-term decomposition while retaining the ability to use standard FE methods in the numerical implementation of the theory. Since the plastic torsion-curvature evolution in the micropolar theory is associated with the generation of GNDs, the associated elastic fields embodied by

$\bar{\boldsymbol{\kappa}}^{\mathrm{e}}$ would play a role analogous to the incompatible lattice distortions, $\mathbf{H}^{\mathrm{i}}$. This is further demonstrated by comparing the effective resolved shear stresses from the two theories, i.e,

$$\tau^{\alpha}_{\mathit{eff}} = \mathbf{s}^{\alpha} \cdot \boldsymbol{\sigma} \cdot \mathbf{n}^{\alpha} = \tau^{\alpha} - \tau^{\alpha}_{b} \tag{3.101}$$

$$\text{GD:}\ \ \tau^{\alpha} = \mathbb{C} : \mathrm{sym}(\mathbf{H}^{\mathrm{e}*}) : \mathbf{Z}^{\alpha} \quad , \quad \tau^{\alpha}_{b} = -\mathbb{C} : \mathrm{sym}(\mathbf{H}^{\mathrm{i}}) : \mathbf{Z}^{\alpha} \tag{3.102}$$

$$\text{MP:}\ \ \tau^{\alpha} = \mathbb{C} : \mathrm{sym}(\mathbf{H}^{\mathrm{e}}) : \mathbf{Z}^{\alpha} \quad , \quad \tau^{\alpha}_{b} = -\tfrac{1}{2}\mathbf{t}^{\alpha} \cdot ((\mathbb{D} : \bar{\boldsymbol{\kappa}}^{\mathrm{e}}) \cdot \tilde{\nabla}) \tag{3.103}$$

where the abbreviations GD (Gerken and Dawson) and MP (micropolar) have been used above. The key difference between the two approaches is that the additional contribution to the resolved shear stress in Eq. (3.102) results from the enhanced kinematic description of a continuum governed by the standard mechanical balance laws, whereas in Eq. (3.103) they emerge due to the presence of couple stresses and as a consequence of the balance of angular momentum. In fact, this may be a beneficial aspect of the model as the presence of GNDs has long been known as a potential source for couple stresses at coarse scales of observation due to the fluctuations of local stresses at finer scales [141]. It has been suggested that couple stresses may also develop in crystalline materials due to dislocation core distortions and multibody interatomic potentials [142], and Zhou and McDowell [143] have shown that couple stresses can arise from particle systems (e.g., nonlocal atomistic systems) *only* if non-central force interactions exist. The micropolar theory also contains an additional contribution to the mechanical dissipation embodied by the term, $\mathfrak{d}_{NL} = \boldsymbol{\sigma} : \mathrm{skw}(\dot{\bar{\boldsymbol{\varepsilon}}}^{\mathrm{p}}) + \mathbf{m} : \dot{\bar{\boldsymbol{\kappa}}}^{\mathrm{p}}$, that is not accounted for in the alternative GD approach.

Comparison to Gurtin-Type Single Crystal Plasticity

The Gurtin-type work-conjugate higher-order theory was introduced and discussed in Chapter 2, and the key feature of these types of models is that the slip system shears are taken as continuum degrees-of-freedom. Therefore, the slip system shearing rate is no longer a constitutively specified function and is instead a generalized displacement. As a result, the typical structure of the elastic-plastic constitutive formulation is altered. For example, instead of specifying a yield function (or flow rule) which defines a yield threshold and a flow direction, the Gurtin-type theory contains an additional microforce balance law that augments the usual balances of linear and angular momenta. Additionally, the Gurtin-type theory

introduces energetic-dissipative decompositions of thermodynamic stresses in addition to the elastic-plastic decomposition of the total strain tensor. Constitutive assumptions are made for the free energy and thermodynamic stresses such that in the absence of slip gradients, the classical theory is more or less retrieved. It is noted, that these models do not use ISVs in the traditional sense and they employ phenomenological descriptions of strain hardening. That being the case, to facilitate the comparison of the micropolar model to the Gurtin-type model the following discussion is presented from a point-of-view consistent with developments of Gurtin and co-workers [18, 109, 115]. The governing equations of Gurtin's theory are summarized below for ease of reference and Chapter 2 can be consulted for more in-depth explanation. The following discussion is more focused on the development of constitutive equations for the Gurtin-type framework that show the similarities between the micropolar theory and theirs.

Kinematic Relations

$$\begin{gathered}
\mathcal{U} = \{\mathbf{u}, \{\gamma^\alpha\}\} \\
\mathbf{H} = \mathbf{u}\vec{\nabla} = \mathbf{H}^{\mathrm{e}} + \mathbf{H}^{\mathrm{p}} \\
\varepsilon = \mathrm{sym}(\mathbf{H}) = \varepsilon^{\mathrm{e}} + \varepsilon^{\mathrm{p}} \\
\mathbf{H}^{\mathrm{p}} = \sum_\alpha \gamma^\alpha \mathbf{s}^\alpha \otimes \mathbf{n}^\alpha \\
\boldsymbol{\alpha} = \mathbf{H}^{\mathrm{p}} \times \vec{\nabla} = b \sum_\alpha \varrho^\alpha_{G,\perp} \mathbf{s}^\alpha \otimes \mathbf{t}^\alpha + \varrho^\alpha_{G,\odot} \mathbf{s}^\alpha \otimes \mathbf{s}^\alpha
\end{gathered} \tag{1.104}$$

Internal and External Power Densities

$$\begin{gathered}
\mathfrak{p}_I = \boldsymbol{\sigma} : \dot{\varepsilon}^{\mathrm{e}} + \sum_\alpha (q^\alpha \dot{\gamma}^\alpha + \boldsymbol{\varsigma}^\alpha \cdot \vec{\nabla} \dot{\gamma}^\alpha) \\
\mathfrak{p}_E = \mathbf{T} \cdot \dot{\mathbf{u}} + \sum_\alpha \Xi^\alpha \dot{\gamma}^\alpha
\end{gathered} \tag{3.105}$$

Mechanical Balance Laws

$$\begin{gathered}
\boldsymbol{\sigma} \cdot \vec{\nabla} = \mathbf{0} \\
\boldsymbol{\sigma} = \boldsymbol{\sigma}^T \\
\tau^\alpha + \vec{\nabla} \cdot \boldsymbol{\varsigma}^\alpha - q^\alpha = 0
\end{gathered} \tag{3.106}$$

Traction Definitions

$$\begin{gathered}
\mathbf{T} = \hat{\mathbf{n}} \cdot \boldsymbol{\sigma} \\
\Xi^\alpha = \boldsymbol{\varsigma}^\alpha \cdot \hat{\mathbf{n}}
\end{gathered} \tag{3.107}$$

Free Energy and State Laws

$$\psi_v = \hat{\psi}_v(\boldsymbol{\varepsilon}^{\mathrm{e}}, \{\nabla\gamma^{\alpha}\})$$

$$\boldsymbol{\sigma} = \frac{\partial \psi_v}{\partial \boldsymbol{\varepsilon}^{\mathrm{e}}} \tag{3.108}$$

$$\boldsymbol{\varsigma}_{en}^{\alpha} = \boldsymbol{\varsigma}^{\alpha} - \boldsymbol{\varsigma}_{dis}^{\alpha} = \frac{\partial \psi_v}{\partial \nabla\gamma^{\alpha}}$$

Mechanical Dissipation Rate

$$\mathfrak{d} = \sum_{\alpha} (q^{\alpha}\dot{\gamma}^{\alpha} + \boldsymbol{\varsigma}_{dis}^{\alpha} \cdot \vec{\nabla}\dot{\gamma}^{\alpha}) \geq 0 \tag{3.109}$$

Energetic Constitutive Equations

The constitutive equations presented in Chapter 2 for the Gurtin-type model included a rather simple functional relationship between the free energy density and the magnitude of slip gradient vector (see Eq. (2.142)). In recognition of the fact that gradients of slip normal to the slip plane do not lead to the generation of GNDs, Gurtin et al. [18] assert that the free energy should only depend on the in-plane slip gradients. Therefore, the microcouple stress lies in the slip plane and may be expressed in the following general form

$$\boldsymbol{\varsigma}^{\alpha} = \boldsymbol{\varsigma}_{\perp}^{\alpha} + \boldsymbol{\varsigma}_{\odot}^{\alpha}, \tag{3.110}$$

where $\boldsymbol{\varsigma}_{\perp}^{\alpha}$ is the edge component of the microcouple stress vector and is parallel to s^{α} and $\boldsymbol{\varsigma}_{\odot}^{\alpha}$ is the screw component and acts parallel to $\mathbf{t}^{\alpha}$. A free energy that is uncoupled and quadratic in the tangential gradients has been proposed by Gurtin et al. [18] as

$$\psi_v = \tfrac{1}{2}\boldsymbol{\varepsilon}^{\mathrm{e}} : \mathbb{C} : \boldsymbol{\varepsilon}^{\mathrm{e}} + \tfrac{1}{2} g_0 \ell^2 b^2 \sum_{\alpha} [(\varrho^{\alpha}_{G,\perp})^2 + (\varrho^{\alpha}_{G,\odot})^2] \tag{3.111}$$

where g_0 is a material parameter with units of stress and ℓ is an energetic length scale. The second term in Eq (3.111), which is associated with heterogeneous microstructural evolution, can be expressed in terms of the total slip system GND density with the aid of Eq. (2.75) as

$$\psi_v = \tfrac{1}{2}\boldsymbol{\varepsilon}^{\mathrm{e}} : \mathbb{C} : \boldsymbol{\varepsilon}^{\mathrm{e}} + \tfrac{1}{2} g_0 \ell^2 b^2 \sum_{\alpha} (\varrho^{\alpha}_{G})^2 \tag{3.112}$$

Notice that there is no contribution to the free energy due to the SSD density. Moreover, in contrast to earlier developments, the strain-like state variable is proportional to the GND density and not its square root. The energetic stresses are obtained from differentiation of Eq. (3.111) with respect to the elastic strain and slip gradients, i.e.,

$$\begin{aligned} \boldsymbol{\sigma} &= \mathbb{C} : \boldsymbol{\varepsilon}^{\mathrm{e}} \\ \boldsymbol{\varsigma}^{\alpha}_{en} &= \boldsymbol{\varsigma}^{\alpha}_{en,\perp} + \boldsymbol{\varsigma}^{\alpha}_{en,\odot} = g_0 \ell^2 b (\varrho^{\alpha}_{G,\perp} \mathbf{s}^{\alpha} + \varrho^{\alpha}_{G,\odot} \mathbf{t}^{\alpha}) \end{aligned} \tag{3.113}$$

Equation $(3.113)_1$ is the standard elasticity constitutive equation and Gurtin et al. [18] view the energetic microcouple stresses (second term) as "distributed Peach-Koehler forces" since they act perpendicular to the line directions of pure edge and screw dislocations; however, it is not implicit that this interpretation is accurate considering that the usual glide component of the Peach-Koehler force is defined in terms of the Cauchy stress, slip plane normal, and dislocation Burgers vectors, as given in Eq. (2.16), and there are contributions from the remote stress field and the stress fields due to all of the other dislocations.

Dissipative Constitutive Equations

The dissipative constitutive equations introduced in Chapter 2 were proposed within what effectively is a single criterion framework by making use of an effective inelastic rate as defined by Eq. (2.144). An alternative path is pursued here in terms of a multicriterion Gurtin-type formulation of the dissipative stresses as it enables a more straight-forward connection to the micropolar model. For example, the scalar dissipative microstress in the proposed multicriterion Gurtin model is expressed as

$$q^\alpha \;=\; g^\alpha \left(\frac{|\;\dot{\gamma}^\alpha\;|}{\dot{\gamma}_0} \right)^{1/m} \operatorname{sgn}\left(\dot{\gamma}^\alpha \right) \tag{3.114}$$

This equation is to be compared to the analogous expression given in Eq. (2.145) where the functional dependencies on the equivalent slip system deformation rate, $\dot{d}^\alpha$, have been replaced with a dependence only on the slip rates. The drag stress evolves according to an appropriately modified form of Eq. (2.146), i.e.,

$$\dot{g}^\alpha \;=\; \sum_\beta \Big(h_1^{\alpha\beta}(\{\gamma^\chi\},\{\vec{\nabla}\gamma^\chi\}) \;|\; \dot{\gamma}^\beta \;| + \mathbf{h}_2^{\alpha\beta}(\{\gamma^\chi\},\{\vec{\nabla}\gamma^\chi\}) \cdot \vec{\nabla}\dot{\gamma}^\beta \Big), \tag{3.115}$$

where the scalar, $h_1^{\alpha\beta}$, and vectorial, $\mathbf{h}_2^{\alpha\beta}$, slip system interaction matrix components may in general depend on the plastic slip and slip gradients on all slip systems. The general form of Eq. (3.115) has been motivated by assuming that the drag stress is defined by an enhanced Taylor relation, i.e.,

$$g^\alpha \;=\; g_0 \;+\; c_1 \mu b \sqrt{\textstyle\sum_\beta h^{\alpha\beta} (\varrho_S^\beta \;+\; \varrho_G^\beta)}\,, \tag{3.116}$$

where the evolution equations for the SSD and GND densities are defined as in Eqs. (2.77) and (2.76), respectively, and the mean free path is defined as in Eq. $(2.78)_2$. The dissipative component of the microcouple stress vector is introduced by again appealing to the edge-screw decomposition and also to Eq. (2.147), i.e.,

$$\boldsymbol{\varsigma}_{dis}^\alpha \;=\; \boldsymbol{\varsigma}_{dis,\perp}^\alpha \;+\; \boldsymbol{\varsigma}_{dis,\odot}^\alpha \;=\; -f_\perp^\alpha \mathbf{s}^\alpha \;+\; f_\odot^\alpha \mathbf{t}^\alpha\,, \tag{3.117}$$

where the signed scalar functions, $f_\perp^\alpha$ and $f_\odot^\alpha$, are defined analogously to Eq. (3.114), i.e.,

$$\begin{aligned} f_\perp^\alpha \;&=\; g_\perp^\alpha L_\perp^\alpha \left(\frac{|\;-\vec{\nabla}\dot{\gamma}^\alpha \cdot \mathbf{s}^\alpha\;|}{\dot{\gamma}_{\perp 0} \;/\; L_\perp^\alpha} \right)^{1/n_\perp} \operatorname{sgn}\left(-\vec{\nabla}\dot{\gamma}^\alpha \cdot \mathbf{s}^\alpha \right) \\ f_\odot^\alpha \;&=\; g_\odot^\alpha L_\odot^\alpha \left(\frac{|\;\vec{\nabla}\dot{\gamma}^\alpha \cdot \mathbf{t}^\alpha\;|}{\dot{\gamma}_{\odot 0} \;/\; L_\odot^\alpha} \right)^{1/n_\odot} \operatorname{sgn}\left(\vec{\nabla}\dot{\gamma}^\alpha \cdot \mathbf{t}^\alpha \right) \end{aligned} \tag{3.118}$$

where $g_{\perp}^{\alpha}$ and $g_{\odot}^{\alpha}$ are edge and screw drag stresses, $L_{\perp}^{\alpha}$ and $L_{\odot}^{\alpha}$ are edge and screw dissipative length scales, $\dot{\gamma}_{\perp 0}$ and $\dot{\gamma}_{\odot 0}$ are edge and screw reference deformation rates with units s^{-1}, and $n_{\perp}$ and $n_{\odot}$ are edge and screw inverse rate sensitivity exponents. These expressions can be interpreted as flow rules for the gradients of slip in the slip and transverse directions, respectively. The edge and screw drag stresses are assumed to have generalized evolution equations similar to that for slip given in Eq. (3.115), i.e.,

$$\begin{aligned} \dot{g}_{\perp}^{\alpha} &= \sum_{\beta} \Big(h_{\perp 1}^{\alpha\beta}(\{\gamma^{\chi}\},\{\vec{\nabla}\gamma^{\chi}\}) \mid \dot{\gamma}^{\beta} \mid + \mathbf{h}_{\perp 2}^{\alpha\beta}(\{\gamma^{\chi}\},\{\vec{\nabla}\gamma^{\chi}\}) \cdot \vec{\nabla}\dot{\gamma}^{\beta} \Big) \\ \dot{g}_{\odot}^{\alpha} &= \sum_{\beta} \Big(h_{\odot 1}^{\alpha\beta}(\{\gamma^{\chi}\},\{\vec{\nabla}\gamma^{\chi}\}) \mid \dot{\gamma}^{\beta} \mid + \mathbf{h}_{\odot 2}^{\alpha\beta}(\{\gamma^{\chi}\},\{\vec{\nabla}\gamma^{\chi}\}) \cdot \vec{\nabla}\dot{\gamma}^{\beta} \Big) \end{aligned} \tag{3.119}$$

Since the dissipative microstress and microcouple stress equations are independent of one another, Eqs. (3.114) and (3.117)-(3.118) can be inverted to obtain relations between the slip rates and slip rate gradients and their respective driving forces which are given by

$$\dot{\gamma}^{\alpha} = \dot{\gamma}_0 \left(\frac{\mid q^{\alpha} \mid}{g^{\alpha}} \right)^{m} \operatorname{sgn}\left(q^{\alpha} \right) \tag{3.120}$$

$$\begin{aligned} -\vec{\nabla}\dot{\gamma}^{\alpha} \cdot \mathbf{s}^{\alpha} &= \frac{\dot{\gamma}_{\perp 0}}{L_{\perp}^{\alpha}} \left(\frac{\mid \boldsymbol{\varsigma}_{\perp}^{\alpha} \cdot \mathbf{s}^{\alpha} \mid}{g_{\perp}^{\alpha} L_{\perp}^{\alpha}} \right)^{n_{\perp}} \operatorname{sgn}\left(\boldsymbol{\varsigma}_{\perp}^{\alpha} \cdot \mathbf{s}^{\alpha} \right) \\ \vec{\nabla}\dot{\gamma}^{\alpha} \cdot \mathbf{t}^{\alpha} &= \frac{\dot{\gamma}_{\odot 0}}{L_{\odot}^{\alpha}} \left(\frac{\mid \boldsymbol{\varsigma}_{\odot}^{\alpha} \cdot \mathbf{t}^{\alpha} \mid}{g_{\odot}^{\alpha} L_{\odot}^{\alpha}} \right)^{n_{\odot}} \operatorname{sgn}\left(\boldsymbol{\varsigma}_{\odot}^{\alpha} \cdot \mathbf{t}^{\alpha} \right) \end{aligned} \tag{3.121}$$

Here, coaxiality of the power-conjugate stresses and inelastic rates has been assumed, i.e., $\operatorname{sgn}(\dot{\gamma}^{\alpha}) = \operatorname{sgn}(q^{\alpha})$, $\operatorname{sgn}(-\vec{\nabla}\dot{\gamma}^{\alpha} \cdot \mathbf{s}^{\alpha}) = \operatorname{sgn}(\varsigma_{\perp}^{\alpha} \cdot \mathbf{s}^{\alpha})$, and $\operatorname{sgn}(\vec{\nabla}\dot{\gamma}^{\alpha} \cdot \mathbf{t}^{\alpha}) = \operatorname{sgn}(\varsigma_{\odot}^{\alpha} \cdot \mathbf{t}^{\alpha})$. With the aid of the microforce balance (see Eq. $(3.106)_3$) Eq. (3.120) may be expressed as

$$\dot{\gamma}^{\alpha} = \dot{\gamma}_0 \left(\frac{\mid \tau^{\alpha} + \vec{\nabla} \cdot \boldsymbol{\varsigma}^{\alpha} \mid}{g^{\alpha}} \right)^{m} \operatorname{sgn}(\tau^{\alpha} + \vec{\nabla} \cdot \boldsymbol{\varsigma}^{\alpha}) \tag{3.122}$$

This is a familiar expression for the slip rate evolution, in which the second term in the numerator inside the parenthesis acts as the kinematic hardening variable and the drag stress acts the isotropic hardening

variable. Similarly, the expressions given in Eqs. (3.118) and (3.121) may be written in terms of the edge and screw GND densities by using the rate form of Eq. (2.71). Considering only the edge GND density equations for the sake of brevity, Eqs. (3.118)1 and (3.121)1 are expressed as

$$f_{\perp}^{\alpha} = g_{\perp}^{\alpha} L_{\perp}^{\alpha} \left(\frac{| \dot{\varrho}_{G,\perp}^{\alpha} |}{\dot{\varrho}_{G,\perp 0}} \right)^{1/n_{\perp}} \operatorname{sgn}\left(\dot{\varrho}_{G,\perp}^{\alpha} \right) \tag{3.123}$$

$$\dot{\varrho}_{G,\perp}^{\alpha} = \dot{\varrho}_{G,\perp 0} \left(\frac{| \boldsymbol{\varsigma}_{\perp}^{\alpha} \cdot \mathbf{s}^{\alpha} |}{g_{\perp}^{\alpha} L_{\perp}^{\alpha}} \right)^{n_{\perp}} \operatorname{sgn}\left(\boldsymbol{\varsigma}_{\perp}^{\alpha} \cdot \mathbf{s}^{\alpha} \right) \tag{3.124}$$

where $\dot{\varrho}_{G,\perp}^{\alpha}$ is the edge GND density evolution equation and $\dot{\varrho}_{G,\perp 0}^{\alpha} = \dot{\gamma}_{\perp 0} \,/\, b L_{\perp}^{\alpha}$ is a reference rate of edge GND density. Finally, Eqs.(3.122) and (3.121) can be inserted into Eq. (3.109) and the mechanical dissipation rate is then expressed as

$$\begin{aligned} \mathfrak{d} = \sum_{\alpha} \Bigg(& \dot{\gamma}_0 \left(\frac{| \tau^{\alpha} + \vec{\nabla} \cdot \boldsymbol{\varsigma}^{\alpha} |}{g^{\alpha}} \right)^{m} | \tau^{\alpha} + \vec{\nabla} \cdot \boldsymbol{\varsigma}^{\alpha} | + \dot{\gamma}_{\perp 0} \left(\frac{| \boldsymbol{\varsigma}_{\perp}^{\alpha} \cdot \mathbf{s}^{\alpha} |}{g_{\perp}^{\alpha} L_{\perp}^{\alpha}} \right)^{n_{\perp}} \frac{| \boldsymbol{\varsigma}_{\perp}^{\alpha} \cdot \mathbf{s}^{\alpha} |}{L_{\perp}^{\alpha}} \cdots \\ & + \dot{\gamma}_{\odot 0} \left(\frac{| \boldsymbol{\varsigma}_{\odot}^{\alpha} \cdot \mathbf{t}^{\alpha} |}{g_{\odot}^{\alpha} L_{\odot}^{\alpha}} \right)^{n_{\odot}} \frac{| \boldsymbol{\varsigma}_{\odot}^{\alpha} \cdot \mathbf{t}^{\alpha} |}{L_{\odot}^{\alpha}} \Bigg) \geq 0 \end{aligned} \tag{3.125}$$

It is easy to see from Eq. (3.125) that the dissipation inequality is unconditionally satisfied for the Gurtin-type theory since each term is individually positive; this results from the omission of ISVs as arguments in the free energy which then do not appear in the internal power density.

Decomposition of the Inverted Flow Rule

The energetic-dissipative decomposition, $\boldsymbol{\varsigma}^{\alpha} = \boldsymbol{\varsigma}_{en}^{\alpha} + \boldsymbol{\varsigma}_{dis}^{\alpha}$, of the microcouple stress allows the microforce balance to be expressed as

$$\tau^{\alpha} + \underbrace{\vec{\nabla} \cdot \boldsymbol{\varsigma}_{en}^{\alpha}}_{\text{energetic hardening}} = \underbrace{q^{\alpha} - \vec{\nabla} \cdot \boldsymbol{\varsigma}_{dis}^{\alpha}}_{\text{dissipative hardening}} \tag{3.126}$$

where the energetic and dissipative contributions to hardening have been separated. Notice that there is both energetic and dissipative kinematic hardening and only dissipative isotropic hardening. Inserting the constitutive equations given in Eqs. $(3.113)_2$, (3.114), and (3.117)-(3.118) into Eq. (3.126) then yields

$$\begin{aligned}\tau^{\alpha} + \vec{\nabla}\cdot[g_0\ell^2 b(\varrho^{\alpha}_{G,\perp}\mathbf{s}^{\alpha} + \varrho^{\alpha}_{G,\odot}\mathbf{t}^{\alpha})] = g^{\alpha}\left(\frac{|\,\dot{\gamma}^{\alpha}\,|}{\dot{\gamma}_0}\right)^{1/m}\operatorname{sgn}\left(\dot{\gamma}^{\alpha}\right)\cdots \\ + \vec{\nabla}\cdot\left[g^{\alpha}_{\perp}L^{\alpha}_{\perp}\left(\frac{|\,\dot{\varrho}^{\alpha}_{G,\perp}\,|}{\dot{\varrho}_{G,\perp 0}}\right)^{1/n_{\perp}}\operatorname{sgn}\left(\dot{\varrho}^{\alpha}_{G,\perp}\right)\mathbf{s}^{\alpha} - g^{\alpha}_{\odot}L^{\alpha}_{\odot}\left(\frac{|\,\dot{\varrho}^{\alpha}_{G,\odot}\,|}{\dot{\varrho}_{G,\odot 0}}\right)^{1/n_{\perp}}\operatorname{sgn}\left(\dot{\varrho}^{\alpha}_{G,\odot}\right)\mathbf{t}^{\alpha}\right]\end{aligned} \tag{3.127}$$

This result will be compared to an analogous expression obtained from the multicriterion micropolar theory of single crystal plasticity in subsequent discussion.

Relationship to the Multicriterion Theory of Micropolar Single Crystal Plasticity

In an effort to make a more clear connection to the micropolar theory of single crystal plasticity, the multicriterion flow rule presented in Chapter 3 is reexamined from a perspective more closely aligned with that of Gurtin et al. [51] with regard to certain constitutive assumptions. Specifically, a simplified free energy function which only includes functional dependencies on the elastic strains and torsion-curvatures is considered. Additionally, flow rules without elastic thresholds are adopted. For the present analysis, Eqs. (3.39), (3.52), and (3.19) are replaced, respectively, with the following

$$\dot{\lambda}^{\alpha} = \dot{\gamma}_0\left(\frac{|\,\tau^{\alpha}_{eff}\,|}{g^{\alpha}}\right)^{m} \tag{3.128}$$

$$\dot{\lambda}^{\alpha}_{\perp} = \dot{\varphi}_{\perp 0}\left(\frac{|\,\pi^{\alpha}_{\perp}\,|}{g^{\alpha}_{\perp}L^{\alpha}_{\perp}}\right)^{n_{\perp}} \quad , \quad \dot{\lambda}^{\alpha}_{\odot} = \dot{\varphi}_{\odot 0}\left(\frac{|\,\pi^{\alpha}_{\odot}\,|}{g^{\alpha}_{\odot}L^{\alpha}_{\odot}}\right)^{n_{\odot}} \tag{3.129}$$

$$\psi_v = \tfrac{1}{2}\overline{\boldsymbol{\varepsilon}}^{\mathrm{e}} : \mathbb{C} : \overline{\boldsymbol{\varepsilon}}^{\mathrm{e}} + \tfrac{1}{2}g_0\ell^2\left\|\overline{\boldsymbol{\kappa}}^{\mathrm{e}}\right\|^2 \tag{3.130}$$

In Eq. (3.130) the free energy is assumed to depend on the magnitude of the elastic torsion-curvature tensor and as in Eq. (3.111) g_0 is a material parameter with units of stress and ℓ is an energetic length scale. The

isotropic hardening variables, g^{α} , $g_{\perp}^{\alpha}$, and $g_{\odot}^{\alpha}$, are assumed to have the following general forms analogous to Eqs. (3.115) and (3.119), i.e.,

$$\dot{g}^{\alpha} = \sum_{\beta} \Big(h^{\alpha\beta} \mid \dot{\gamma}^{\beta} \mid + h_{1\perp}^{\alpha\beta} \dot{\varphi}_{\perp}^{\beta} + h_{2\odot}^{\alpha\beta} \dot{\varphi}_{\odot}^{\beta} \Big) \tag{3.131}$$

$$\begin{aligned} \dot{g}_{\perp}^{\alpha} &= \sum_{\beta} \Big(h_{\perp}^{\alpha\beta} \mid \dot{\gamma}^{\beta} \mid + h_{\perp\perp}^{\alpha\beta} \dot{\varphi}_{\perp}^{\beta} + h_{\perp\odot}^{\alpha\beta} \dot{\varphi}_{\odot}^{\beta} \Big) \\ \dot{g}_{\odot}^{\alpha} &= \sum_{\beta} \Big(h_{\odot}^{\alpha\beta} \mid \dot{\gamma}^{\beta} \mid + h_{\odot\perp}^{\alpha\beta} \dot{\varphi}_{\perp}^{\beta} + h_{\odot\odot}^{\alpha\beta} \dot{\varphi}_{\odot}^{\beta} \Big) \end{aligned} \tag{3.132}$$

Here, it is to be understood that each of the interaction matrices given in Eqs. (3.131) and (3.132) may, in general, be a function of $\{\gamma^{\alpha}\}$, $\{\varphi_{\perp}^{\alpha}\}$, and $\{\varphi_{\odot}^{\alpha}\}$.

The explicit state laws for this version of the multicriterion theory are obtained from Eq. (3.130) as

$$\boldsymbol{\sigma} = \mathbb{C} : \overline{\boldsymbol{\varepsilon}}^{\mathrm{e}} \quad , \quad \mathbf{m} = g_0 \ell^2 \overline{\boldsymbol{\kappa}}^{\mathrm{e}} \tag{3.133}$$

which are to be compared to Eq. (3.113); the similarities between the energetic vectorial microcouple stress from the Gurtin-type theory to the tensorial couple stress of the micropolar theory are obvious. While there are certainly differences between the two higher-order stresses it is argued that they have similar impacts and physical implications with regard to material behavior. The most noteworthy difference between the two measures is their tensorial rank, which is due to the difference in torsion-curvature measures employed by the two theories. The Gurtin-type theory with an uncoupled energy as in Eq. (3.112) can be thought of as employing a planar torsion-curvature measure, $\boldsymbol{\kappa}_{\mathrm{G}}^{\alpha}$, defined as

$$\boldsymbol{\kappa}_{\mathrm{G}}^{\alpha} = b(\varrho_{G,\perp}^{\alpha} \mathbf{s}^{\alpha} + \varrho_{G,\odot}^{\alpha} \mathbf{t}^{\alpha}) \tag{3.134}$$

In some regards, a more rigorous comparison is difficult due to the different philosophical perspectives of the two theories. For example, as previously discussed, the Gurtin-type theories employ an energetic-dissipative decomposition of the microcouple stress, whereas the micropolar model achieves a similar effect through the elastic-plastic (energetic-dissipative) decomposition of the torsion-curvature. A key difference between these two ideologies as it relates to material response is that of nonlocal effects; in

general such effects, are present during elastic deformations for the micropolar continuum, but are restricted to the inelastic regime for the Gurtin-type theory. However, the separation of the microcouple stress in the Gurtin-type theory into energetic and dissipative parts is essentially amounts to an implicit additive decomposition of the slip gradient into elastic and plastic parts, i.e., $\vec{\nabla}\gamma^{\alpha} = \vec{\nabla}\gamma_{\mathrm{e}}^{\alpha} + \vec{\nabla}\gamma_{\mathrm{p}}^{\alpha}$, where the subscripts denote the elastic and plastic parts of the slip gradient, respectively. Since the slip system shears are treated as generalized displacements within the Gurtin-type framework, it is natural to think of the slip gradients as being the corresponding generalized (micro)strain measure which could be decomposed into elastic and plastic parts. Although, this is not the approach as set forth by Gurtin et al. [18], the physical implication is that energy is both stored and dissipated due to gradients of slip.

To further compare the two models, the mechanical dissipation rate for the new version of the multicriterion theory is expressed with the aid of Eqs. (3.128) and (3.129) as

$$\begin{aligned}\mathfrak{d} = \sum_{\alpha}\Bigg(& \dot{\gamma}_0 \left(\frac{|\, \tau^{\alpha} + \tfrac{1}{2}\mathbf{t}^{\alpha}\cdot(\mathbf{m}\cdot\vec{\nabla})\,|}{g^{\alpha}} \right)^{m} |\, \tau^{\alpha} + \tfrac{1}{2}\mathbf{t}^{\alpha}\cdot(\mathbf{m}\cdot\vec{\nabla})\,| \cdots \\ & + \dot{\varphi}_{\perp 0}\left(\frac{|\, \pi_{\perp}^{\alpha}\,|}{g_{\perp}^{\alpha} L_{\perp}^{\alpha}} \right)^{n_{\perp}} \frac{\left|\pi_{\perp}^{\alpha}\right|}{L_{\perp}^{\alpha}} + \dot{\varphi}_{\odot 0}\left(\frac{|\, \pi_{\odot}^{\alpha}\,|}{g_{\odot}^{\alpha} L_{\odot}^{\alpha}} \right)^{n_{\odot}} \frac{\left|\pi_{\odot}^{\alpha}\right|}{L_{\odot}^{\alpha}} \Bigg) \geq 0\end{aligned} \tag{3.135}$$

where the effective resolved shear stress, τ_{eff}^{α}, has been expressed with the aid of Eqs. (3.40) and (3.45). Comparing Eq. (3.135) to Eq. (3.125) the similarity between the two expressions is obvious, with analogous roles being played by the following terms:

MP	Gurtin
$\tfrac{1}{2}\mathbf{t}^{\alpha}\cdot(\mathbf{m}\cdot\vec{\nabla})$	$\Leftrightarrow \vec{\nabla}\cdot\boldsymbol{\varsigma}^{\alpha}$
$\pi_{\perp}^{\alpha}$	$\Leftrightarrow \boldsymbol{\varsigma}_{\perp}^{\alpha}\cdot\mathbf{s}^{\alpha}$
$\pi_{\odot}^{\alpha}$	$\Leftrightarrow \boldsymbol{\varsigma}_{\odot}^{\alpha}\cdot\mathbf{t}^{\alpha}$

(3.136)

Clearly, the dissipation inequality is unconditionally satisfied for this version/interpretation of the multicriterion micropolar theory and is thermodynamically consistent in the sense implied by Gurtin et al.

[18]. Taking the comparison even further by examining the inverted flow rule for slip (Eq. (3.38)) and making use of the micropolar energetic-dissipative decomposition, $\overline{\boldsymbol{\kappa}} = \overline{\boldsymbol{\kappa}}^{\mathrm{e}} + \overline{\boldsymbol{\kappa}}^{\mathrm{p}}$, the following is obtained

$$\begin{aligned} \tau^{\alpha} + \frac{1}{2} g_0 \ell^2 \, \mathbf{t}^{\alpha} \cdot (\overline{\boldsymbol{\kappa}} \cdot \overset{\leftarrow}{\nabla}) = g^{\alpha} \left(\frac{| \, \dot{\gamma}^{\alpha} \, |}{\dot{\gamma}_0} \right)^{1/m} \operatorname{sgn}\left(\dot{\gamma}^{\alpha} \right) \cdots \\ + \frac{1}{2} g_0 \ell^2 b \, \mathbf{t}^{\alpha} \cdot \left[\left(\sum_{\beta} \varrho^{\beta}_{G,\perp} \mathbf{t}^{\beta} \otimes \mathbf{s}^{\beta} + \varrho^{\beta}_{G,\odot} \mathbf{s}^{\beta} \otimes \mathbf{s}^{\beta} \right) \cdot \overset{\leftarrow}{\nabla} \right] \end{aligned} \tag{3.137}$$

As in Eq. (3.127), the energetic hardening term has been left on the LHS of Eq. (3.137), while the dissipative terms have been moved to the RHS. This expression is similar to the equivalent expression resulting from the multicriterion Gurtin-type theory given in Eq. (3.127). Yet, as to be expected, there are a few subtle differences that are by and large restricted to the gradient-dissipative term. The gradient-dissipative term in the Gurtin-type theory depends on the gradients of the rate of the GND densities, whereas in the micropolar theory it depends on the gradients of the current value of the GND densities. Additionally, *both* energetic and dissipative length scales appear in the gradient dissipative term for the micropolar theory since $\varrho^{\alpha}_{G,\perp} = -\varphi^{\alpha}_{\perp} \, / \, b L^{\alpha}_{\perp}$ and $\varrho^{\alpha}_{G,\odot} = -\varphi^{\alpha}_{\odot} \, / \, b L^{\alpha}_{\odot}$. As a result, the ratio of the energetic-to-dissipative length scales is an important parameter that controls the kinematic hardening response in the micropolar models. In contrast, only the dissipative length scales are contained in the gradient-dissipative term in the Gurtin-type theory. The differences between the gradient-dissipative terms in the inverted flow rule, as previously discussed, are due to applying the energetic-dissipative decomposition to the microcouple stress instead of the microstrain (slip gradient). It is also worth noting that the inverted flow rule in the Gurtin-type theory contains terms only pertaining to the slip system under consideration, while the micropolar theory, due to its use of a non-planar tensorial torsion-curvature measure, incorporates the influence of all slip systems. However, this is not seen to be a limitation of the Gurtin-type theory as this can be remedied by choosing a free energy that has a coupled dependence on the GND densities, e.g.,

$$\psi_v = \tfrac{1}{2} \boldsymbol{\varepsilon}^{\mathrm{e}} : \mathbb{C} : \boldsymbol{\varepsilon}^{\mathrm{e}} + \tfrac{1}{2} \sum_{\alpha} \sum_{\beta} \varrho^{\alpha}_{G} C^{\alpha\beta} \varrho^{\beta}_{G} \tag{3.138}$$

where the material modulus matrix, $C^{\alpha\beta}$, has units of force $\times$ length^2. Equation (3.138) leads to a microcouple stress on slip system α that is a function of the GND densities on all other slip systems.

A comparison of the single criterion micropolar model and the model advanced by Gurtin et al. [18] could be carried out; however, the connections between the Gurtin-type and micropolar models are most easily seen in the multicriterion format. Obviously, there will be differences in the final expressions obtained in such a comparison with respect to what has just been presented, but these are due to the fundamental differences between the multi and single criterion methodologies and no additional insight is gained by carrying out the analysis. For this reason and for the sake of brevity, this analysis is omitted.

3.6 Summary

This chapter has been concerned with the development of dislocation-based strength models of micropolar single crystal plasticity where the classical and nonlocal slip gradient-based theories have been used as guides. General aspects of the micropolar continuum have been covered and models based on both single and multicriterion flow rules have been established. The multicriterion models have built on the prior work of Forest et al. [34, 35] by replacing their phenomenological strength model with dislocation-based models, and the single criterion model represents an original contribution of this research. It has been shown that, as a consequence of the angular momentum balance, the micropolar theory includes a natural kinematic hardening mechanism for slip which arises due to gradients in lattice torsion-curvature. This is in agreement with the well-accepted notion that the long-range back stresses arising due to polar dislocation densities are proportional to *gradients* in GND densities (second gradients of slip). Connections between the micropolar theory and theories featuring: (i) enhanced decompositions of the standard deformation and (ii) the slip system shears as treated as generalized displacements (Gurtin-type) have been established. It is proposed that the micropolar theory of single crystal plasticity is able to capture the all of the relevant physical aspects of the slip gradient-based models while offering a simpler and more efficient numerical implementation.

CHAPTER 4

NUMERICAL IMPLEMENTATION

4.1 Introduction

This chapter presents a two-dimensional finite element implementation appropriate for the micropolar continuum along with the constitutive update algorithms for the single crystal viscoplasticity models presented in Chapter 3. The user element (UEL) subroutine interface within Abaqus/Standard [51] has been employed to implement the element-level equations, which leaves the element assembly operations and the global equilibrium iterations to be performed by Abaqus. The UEL implementation is benchmarked and validated through a series of comparisons to solutions of mechanical initial-boundary value problems with known analytical solutions, and also by demonstrating convergent behavior in a problem exhibiting strain localization.

4.2 Finite Element Implementation

4.2.1 Principle of Virtual Work

The weak form of the mechanical balance laws required for the finite element implementation are derived in standard fashion (cf. [144]) from the local forms of the linear and angular momentum balances given in Eqs (3.8). The linear and angular momentum balance equations, neglecting body forces and inertial effects, are multiplied by arbitrary variations in the displacement, $\delta\mathbf{u}$, and microrotation, $\delta\bar{\phi}$, fields, respectively, and integrated over an arbitrary volume, i.e.,

$$\int_R \left(\boldsymbol{\sigma} \cdot \overset{\leftarrow}{\nabla} \right) \cdot \delta\mathbf{u} \, dV = 0 \tag{4.1}$$

$$\int_R \left(\mathbf{m} \cdot \overset{\leftarrow}{\nabla} - \boldsymbol{\epsilon} : \boldsymbol{\sigma} \right) \cdot \delta\bar{\phi} \, dV = 0 \tag{4.2}$$

Integrating by parts and applying the divergence theorem, one obtains

$$\int_{\partial R} \delta\mathbf{u} \cdot \boldsymbol{\sigma} \cdot \mathbf{n} dS = \int_R \boldsymbol{\sigma} : \delta\mathbf{u}\bar{\nabla} dV \tag{4.3}$$

$$\int_{\partial R} \delta\bar{\Phi} \cdot \mathbf{m} \cdot \mathbf{n} dA = \int_R \left[\mathbf{m} : \delta\bar{\Phi}\bar{\nabla} + \left(\boldsymbol{\epsilon} : \boldsymbol{\sigma} \right) \cdot \delta\bar{\Phi} \right] dV \tag{4.4}$$

Adding Eqs. (4.3) and (4.4) and making use of the deformation-displacement relations given in Eqs. (3.4)-(3.5) and the traction vector definitions given in Eqs. (2.24) and (3.9), the weak form of the mechanical equilibrium equations (principle of virtual work) suitable for the finite element implementation is obtained as

$$\int_{\partial R} \left(\mathbf{T} \cdot \delta\mathbf{u} + \mathbf{M} \cdot \delta\bar{\Phi} \right) dA = \int_R \left(\boldsymbol{\sigma} : \delta\bar{\varepsilon} + \mathbf{m} : \delta\bar{\boldsymbol{\kappa}} \right) dV \tag{4.5}$$

4.2.2 Finite Element Discretization

The development of isoparametric linear quadrilateral and triangle elements appropriate for two-dimensional plane problems is presented in this section. The relevant degrees-of-freedom are the displacements in the x_1 and x_2 directions, u_1 and u_2, and the microrotation about the x_3 axis, $\bar{\phi}_3$. Therefore, the non-trivial components of the micropolar strain and torsion-curvature tensors are $\bar{\varepsilon}_{11}$, $\bar{\varepsilon}_{22}$, $\bar{\varepsilon}_{12}$, $\bar{\varepsilon}_{21}$, $\bar{\kappa}_{31}$, and $\bar{\kappa}_{32}$. In an isoparametric formulation, the element spatial coordinates and kinematic degrees are freedom are interpolated from the nodal values using the same set of shape functions, i.e.,

$$x_i = \sum\nolimits_I N_I x_i^I \tag{4.6}$$

$$u_i = \sum\nolimits_I N_I u_i^I \quad , \quad \bar{\phi}_i = \sum\nolimits_I N_I \bar{\phi}_i^I \tag{4.7}$$

where x_i, u_i, and $\bar{\phi}_i$ are the continuum approximations within the element to the positional coordinate, displacement, and microrotation fields, respectively; x_i^I, u_i^I, and $\bar{\phi}_i^I$ are the corresponding nodal values of the same fields for the I^{th} node, and N_I are the shape functions for the I^{th} node.

Linear Quadrilateral Element

The parent element for the four-noded quadrilateral element (Q4) is shown in Figure 4.1, where the nodal coordinates are given with respect to the natural element basis. The shape functions for this element are given as

$$N_I = \tfrac{1}{4}\left(1 + r_1^I r_1\right)\left(1 + r_2^I r_2\right) \tag{4.8}$$

where $\left(r_1^I, r_2^I\right)$ are the natural coordinates of the I^{th} node. The derivatives of the shape functions with respect to the global coordinate system which are needed to calculate the element strains are obtained by making use of the chain rule, i.e.,

$$\partial_{x_i} N_I = \partial_{r_1} N_I \partial_{x_i} r_1 + \partial_{r_2} N_I \partial_{x_i} r_2 \tag{4.9}$$

where the notation $\partial_{(\cdot)}(*)$ indicates the partial derivative of $(*)$ with respect to $(\cdot)$. The derivatives of the shape functions with respect to the natural coordinates are easily calculated from Eq. (4.8) and are given as

$$\partial_{r_1} N_I = \tfrac{1}{4} r_1^I \left(1 + r_2^I r_2\right) \quad , \quad \partial_{r_2} N_I = \tfrac{1}{4} r_2^I \left(1 + r_1^I r_1\right) \tag{4.10}$$

The derivatives of the natural coordinates with respect to the global coordinates are not directly available; however, these expressions may be obtained by making use of the chain rule and Eq. (4.6) in the following manner. The derivative of a given quantity $(*)$ with respect to the natural element coordinates may be expressed as

$$\partial_{r_i}(*) = \partial_{r_i} x_1 \partial_{x_1}(*) + \partial_{r_i} x_2 \partial_{x_2}(*) \tag{4.11}$$

The derivative of the global coordinates with respect to the element natural coordinates is determined from Eq. (4.6) as

$$\partial_{r_j} x_i = \sum\nolimits_I \partial_{r_j} N_I x_i^I \tag{4.12}$$

Rewriting Eq. (4.11) in matrix form for convenience and inverting leads to an expression for the global coordinate derivatives in terms of readily computable quantities, i.e.,

$$\begin{Bmatrix} \partial_{r_1} \\ \partial_{r_2} \end{Bmatrix} = \begin{bmatrix} \partial_{r_1} x_1 & \partial_{r_1} x_2 \\ \partial_{r_2} x_1 & \partial_{r_2} x_2 \end{bmatrix} \begin{Bmatrix} \partial_{x_1} \\ \partial_{x_2} \end{Bmatrix} \Rightarrow \begin{Bmatrix} \partial_{x_1} \\ \partial_{x_2} \end{Bmatrix} = \begin{bmatrix} \partial_{r_1} x_1 & \partial_{r_1} x_2 \\ \partial_{r_2} x_1 & \partial_{r_2} x_2 \end{bmatrix}^{-1} \begin{Bmatrix} \partial_{r_1} \\ \partial_{r_2} \end{Bmatrix} \tag{4.13}$$

where $J_{ij} = \partial_{r_i} x_j$ is the Jacobian matrix relating the natural coordinate derivatives to the global coordinate derivatives. At this point, all of the necessary preliminaries are in order to derive the element matrices for the bilinear quadrilateral element.

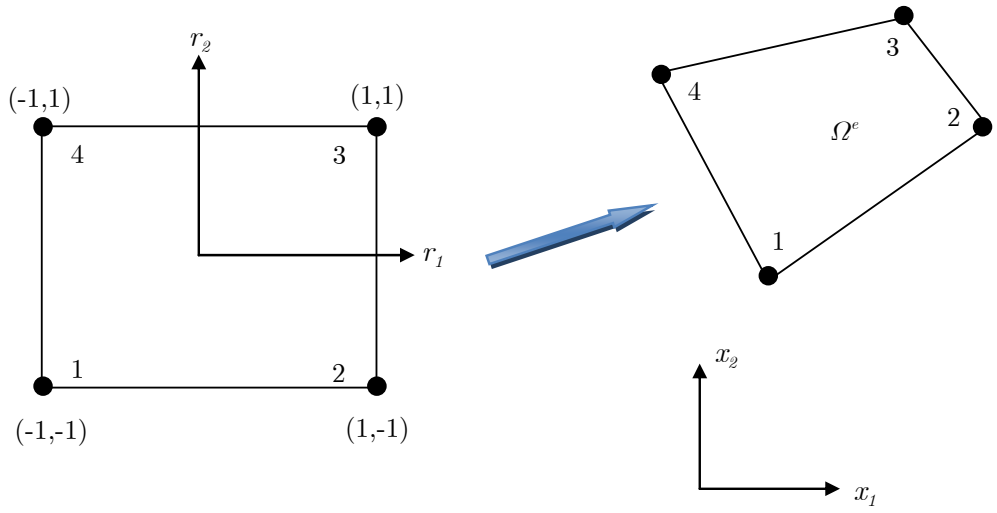

Figure 4.1: Parent isoparametric element for the bilinear quadrilateral (Q4) element.

The micropolar continuum displacement vector, $\{\mathrm{u}\}$, is expressed in terms of the shape functions and the nodal displacement vector by expressing Eqs. (4.6) and (4.7) in a compact matrix notation as

$$\{\mathrm{u}\} = \begin{Bmatrix} u_1 & u_2 & \bar{\phi}_3 \end{Bmatrix}^T = [\mathrm{N}]\{\mathrm{a}\} \tag{4.14}$$

where the shape function matrix, $\left[\mathrm{N}\right]$, and the nodal displacement vector, $\left\{\mathrm{a}\right\}$, are given as

$$\begin{aligned}\left[\mathrm{N}\right] &= \left[\left[\mathrm{N}_1\right] \;\; \left[\mathrm{N}_2\right] \;\; \left[\mathrm{N}_3\right] \;\; \left[\mathrm{N}_4\right]\right] \\ \left[\mathrm{N}_\mathrm{I}\right] &= \begin{bmatrix} N_I & 0 & 0 \\ 0 & N_I & 0 \\ 0 & 0 & N_I \end{bmatrix} \quad , \quad I = 1,2,3,4\end{aligned} \tag{4.15}$$

$$\begin{aligned}\left\{\mathrm{a}\right\} &= \left\{\left\{\mathrm{u}^1\right\}^T \;\; \left\{\mathrm{u}^2\right\}^T \;\; \left\{\mathrm{u}^3\right\}^T \;\; \left\{\mathrm{u}^4\right\}^T\right\}^T \\ \left\{\mathrm{u}^\mathrm{I}\right\} &= \left\{u_1^I \;\; u_2^I \;\; \bar{\phi}_3^I\right\}^T \quad , \quad I = 1,2,3,4\end{aligned} \tag{4.16}$$

where $\left[\mathrm{N}\right]$ is a 3 $\times$ 12 matrix and $\left\{\mathrm{a}\right\}$ is a 12 $\times$ 1 column vector and as before the superscript refers to the I^{th} node. Introducing the micropolar strain vector, $\left\{\bar{\mathrm{E}}\right\}$, as

$$\left\{\bar{\mathrm{E}}\right\} = \left\{\bar{\varepsilon}_{11} \;\; \bar{\varepsilon}_{22} \;\; \bar{\varepsilon}_{12} \;\; \bar{\varepsilon}_{21} \;\; \bar{\kappa}_{31} \;\; \bar{\kappa}_{32}\right\}^T \tag{4.17}$$

the relationship between $\left\{\bar{\mathrm{E}}\right\}$ and the nodal displacement vector is symbolically expressed in terms of the strain-displacement matrix, $\left[\mathrm{B}\right]$, i.e.,

$$\left\{\bar{\mathrm{E}}\right\} = \left[\mathrm{B}\right]\left\{\mathrm{a}\right\} \tag{4.18}$$

where the strain-displacement matrix is populated with the appropriate components of the shape functions and their derivatives. For a fully integrated Q4 element, the strain-displacement matrix has the form

$$\begin{aligned}\left[\mathrm{B}\right] &= \left[\left[\mathrm{B}_1\right] \;\; \left[\mathrm{B}_2\right] \;\; \left[\mathrm{B}_3\right] \;\; \left[\mathrm{B}_4\right]\right] \\ \left[\mathrm{B}_\mathrm{I}\right] &= \begin{bmatrix} \partial_{x_1} N_I & 0 & 0 \\ 0 & \partial_{x_2} N_I & 0 \\ \partial_{x_2} N_I & 0 & N_I \\ 0 & \partial_{x_1} N_I & -N_I \\ 0 & 0 & \partial_{x_1} N_I \\ 0 & 0 & \partial_{x_2} N_I \end{bmatrix} \quad , \quad I = 1,2,3,4\end{aligned} \tag{4.19}$$

It is well-established that linear quadrilateral elements are prone to volumetric locking under plane strain conditions for incompressible or nearly incompressible material behavior when the element is fully integrated [144]. Several different techniques have been proposed to eliminate this limitation of the Q4 element; the $\overline{B}$ (read B-bar) method, which is a form of reduced integration developed by Hughes [145], is employed in this research. The $\overline{B}$ method is based on integrating the dilatational and deviatoric parts of the strain tensor independently, such that full integration is performed for the deviatoric components whereas the averaged (over the element) dilatational strain components are used in the formation of the element matrices. The total strain tensor admits the aforementioned decomposition, i.e.,

$$\overline{\boldsymbol{\varepsilon}} = \overline{\boldsymbol{\varepsilon}}^{d} + \tilde{\overline{\boldsymbol{\varepsilon}}}^{h} \tag{4.20}$$

where $\overline{\boldsymbol{\varepsilon}}^{d}$ and $\tilde{\overline{\boldsymbol{\varepsilon}}}^{h}$ are the deviatoric and average dilatational (or hydrostatic) strains, respectively, and are given as

$$\overline{\boldsymbol{\varepsilon}}^{d} = \overline{\boldsymbol{\varepsilon}} - \tfrac{1}{3}\mathrm{tr}\left(\overline{\boldsymbol{\varepsilon}}\right)\mathbf{I} \tag{4.21}$$

$$\tilde{\overline{\boldsymbol{\varepsilon}}}^{h} = \tfrac{1}{V^{e}}\int_{\Omega^{e}} \overline{\boldsymbol{\varepsilon}}^{h} dV \quad , \quad \overline{\boldsymbol{\varepsilon}}^{h} = \tfrac{1}{3}\mathrm{tr}\left(\overline{\boldsymbol{\varepsilon}}\right)\mathbf{I} \tag{4.22}$$

To demonstrate how this assumption modifies the strain-displacement matrix, consider the $\overline{\varepsilon}_{11}$ component of the strain tensor such that the deviatoric and average hydrostatic contributions for a state of plane strain are given as

$$\overline{\varepsilon}_{11}^{d} = \sum\nolimits_{I} \partial_{x_1} N_I u_1^I - \tfrac{1}{3}\sum\nolimits_{I}\left(\partial_{x_1} N_I u_1^I + \partial_{x_2} N_I u_2^I\right) \tag{4.23}$$

$$\tilde{\overline{\varepsilon}}_{11}^{h} = \tfrac{1}{3}\sum\nolimits_{I}\left(\partial_{x_1} \tilde{N}_I u_1^I + \partial_{x_2} \tilde{N}_I u_2^I\right) \tag{4.24}$$

where $\partial_{x_i}\tilde{N}_I$ are the volume averaged derivatives of the shape functions, i.e.,

$$\partial_{x_i}\tilde{N}_I = \tfrac{1}{V^{e}}\int_{\Omega^{e}} \partial_{x_i} N_I dV \tag{4.25}$$

Adding Eqs. (4.23) and (4.24), performing the analogous procedure for the $\overline{\varepsilon}_{22}$ component of strain and appropriately regrouping the terms, allows one to write the strain-displacement matrix for the $\overline{B}$ method as

$$\left[\overline{\mathrm{B}}\right] = \left[\left[\overline{\mathrm{B}}_1\right] \;\; \left[\overline{\mathrm{B}}_2\right] \;\; \left[\overline{\mathrm{B}}_3\right] \;\; \left[\overline{\mathrm{B}}_4\right]\right] \tag{4.26}$$

$$\left[\overline{\mathrm{B}}_\mathrm{I}\right] = \begin{bmatrix} \partial_{x_1} N_I + \frac{1}{3}\left(\partial_{x_1}\tilde{N}_I - \partial_{x_1} N_I\right) & \frac{1}{3}\left(\partial_{x_2}\tilde{N}_I - \partial_{x_2} N_I\right) & 0 \\ \frac{1}{3}\left(\partial_{x_1}\tilde{N}_I - \partial_{x_1} N_I\right) & \partial_{x_2} N_I + \frac{1}{3}\left(\partial_{x_2}\tilde{N}_I - \partial_{x_2} N_I\right) & 0 \\ \partial_{x_2} N_I & 0 & N_I \\ 0 & \partial_{x_1} N_I & -N_I \\ 0 & 0 & \partial_{x_1} N_I \\ 0 & 0 & \partial_{x_2} N_I \end{bmatrix} \quad , \quad I = 1,2,3,4$$

where the strain vector is now given as $\left\{\overline{\mathrm{E}}\right\} = \left[\overline{\mathrm{B}}\right]\left\{\mathrm{a}\right\}$. Comparing Eq. (4.26) to Eq. (4.19) it is clear that the differences between the two strain-displacement matrices are contained within the first two rows, i.e., those associated with the dilatational components of strain.

Introducing the stress, $\left\{\Sigma\right\}$, and traction vectors, $\left\{\mathrm{T}\right\}$, the principle of virtual work given in Eq. (4.5) may be expressed in matrix notation as

$$\int_{\partial\Omega^e} \left\{\delta\mathrm{u}\right\}^T \left\{\mathrm{T}\right\} dA = \int_{\Omega^e} \left\{\delta\overline{\mathrm{E}}\right\}^T \left\{\Sigma\right\} dV \tag{4.27}$$

where the stress and traction vectors are defined as

$$\left\{\Sigma\right\} = \left\{\sigma_{11} \quad \sigma_{22} \quad \sigma_{12} \quad \sigma_{21} \quad m_{31} \quad m_{32}\right\}^T \tag{4.28}$$

$$\left\{\mathrm{T}\right\} = \left\{T_1 \quad T_2 \quad M_3\right\}^T \tag{4.29}$$

Expressing the virtual continuum displacements and strains in terms of the nodal displacement vector, i.e.,

$$\left\{\delta\mathrm{u}\right\} = \left[\mathrm{N}\right]\left\{\delta\mathrm{a}\right\} \quad , \quad \left\{\delta\overline{\mathrm{E}}\right\} = \left[\overline{\mathrm{B}}\right]\left\{\delta\mathrm{a}\right\} \tag{4.30}$$

and substituting back into Eq. (4.27), gives

$$\left\{\delta\mathrm{a}\right\}^T \int_{\partial\Omega^e} \left[\mathrm{N}\right]^T \left\{\mathrm{T}\right\} dA = \left\{\delta\mathrm{a}\right\}^T \int_{\Omega^e} \left[\overline{\mathrm{B}}\right]^T \left\{\Sigma\right\} dV \tag{4.31}$$

where the virtual nodal displacement vector has been pulled outside of the volume integral. Since the virtual nodal displacements are arbitrary, they may be dropped from the previous equation, which leads to the final form of the discretized finite element equations for the 2-D micropolar continuum with linear kinematics, i.e.,

$$\int_{\partial\Omega^e} \left[\mathrm{N}\right]^T \left\{\mathrm{T}\right\} dA = \int_{\Omega^e} \left[\bar{\mathrm{B}}\right]^T \left\{\Sigma\right\} dV \tag{4.32}$$

where the LHS and RHS of Eq. (4.32) are the forces to due external and internal working, respectively. As previously mentioned, the global element assembly operations and general solution procedures are performed by Abaqus [146]. Within the UEL subroutine call, the out-of-balance nodal load vector (the residual), $\{\mathcal{R}\}$, and the tangent stiffness matrix, $[\mathcal{K}]$, and the updated material state must be returned as arguments to the main program. The residual vector and tangent stiffness matrix are defined, respectively, as

$$\left\{\mathcal{R}\right\} = \int_{\partial\Omega^e} \left[\mathrm{N}\right]^T \left\{\mathrm{T}\right\} dA - \int_{\Omega^e} \left[\bar{\mathrm{B}}\right]^T \left\{\Sigma\right\} dV \tag{4.33}$$

$$\left[\mathcal{K}\right] = \frac{\partial\left\{\Delta \mathrm{f}^{\mathrm{int}}\right\}}{\partial\left\{\Delta \mathrm{a}\right\}} = \int_{\Omega^e} \left[\bar{\mathrm{B}}\right]^T \left[\mathbb{C}^{alg}\right] \left[\bar{\mathrm{B}}\right] dV \tag{4.34}$$

where $\left[\mathbb{C}^{alg}\right]$ is the constitutive tangent matrix and is obtained via consistent linearization of the constitutive update algorithm, which is subsequently discussed in Section 4.2.3. The integration of the element matrices is performed numerically in standard fashion using 2×2 Gaussian quadrature over the natural element coordinates such that a volume integral in the ambient space is calculated as

$$\int_{\Omega^e} f\left(x_i\right) dV = \int_{\Omega^\square} f\left(r_i\right) \left|J\right| dV = \sum\nolimits_Q f\left(r_i^Q\right) \left|J\left(r_i^Q\right)\right| \overline{w}\left(r_i^Q\right) \tag{4.35}$$

where $f\left(x_i\right)$ is any arbitrary function, Ω^e is the element domain in the global coordinate system, $\Omega^\square$ is the element domain in the natural coordinate system, $\left|J\right|$ is the determinant of the Jacobian matrix in Eq. (4.13), r_i^Q are the natural coordinates of the Q^{th} integration point, and $\overline{w}$ is the combined weighting factor.

Linear Triangular Element

The implementation of a linear triangular element is briefly covered in this section taking advantage of the concepts introduced in the previous section. The triangular elements are employed sparingly in this research as they will be used only in situations where regular mapped meshes of quadrilateral elements cannot be efficiently created. The local and global representation of the of the LT element are shown in Figure 4.2.

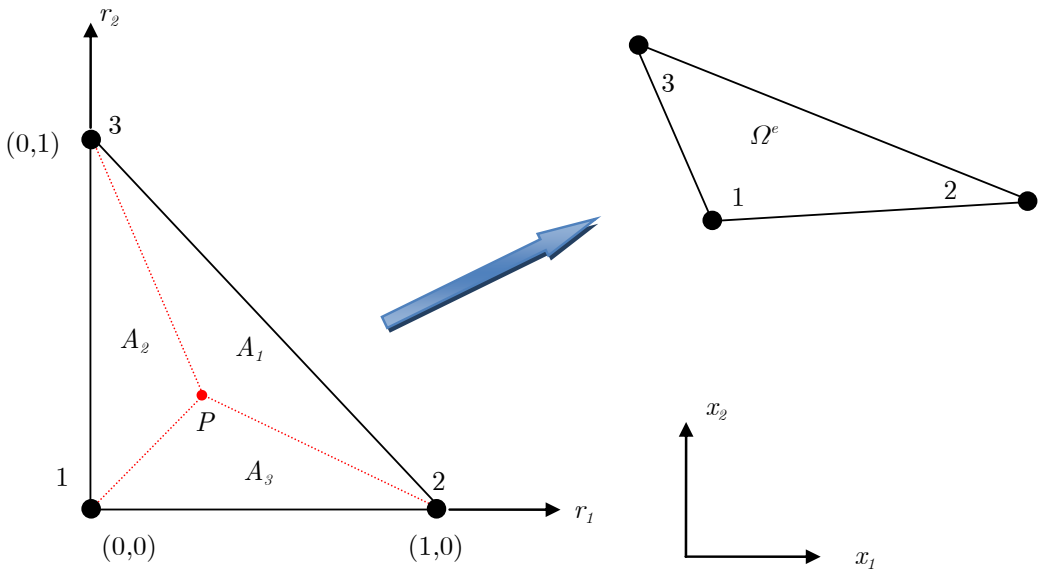

Figure 4.2: Parent isoparametric element for the linear triangular (LT) element.

The isoparametric shape functions for the LT element are given as

$$N_1 = 1 - r_1 - r_2, \quad N_2 = r_1, \quad N_3 = r_2 \tag{4.36}$$

where the shape functions are the area coordinates [147] of a general point within the interior of the triangle, i.e.,

$$N_I = \frac{A_I}{A} \quad I = 1,2,3 \tag{4.37}$$

The definition of the areas in Eq. (4.37) is given with respect to the interior point P in Figure 4.2. The shape function derivatives with respect to the natural coordinates are calculated from Eq. (4.36) as

$$\begin{aligned} \partial_{r_1} N_1 &= -1, \quad \partial_{r_1} N_2 = 1, \quad \partial_{r_1} N_3 = 0 \\ \partial_{r_2} N_1 &= -1, \quad \partial_{r_2} N_2 = 0, \quad \partial_{r_2} N_3 = 1 \end{aligned} \tag{4.38}$$

The derivatives of the shape functions with respect to global coordinates are determined as before by using Eqs. (4.13) and (4.6). The shape function matrix and the strain-displacement matrix appropriate for the LT element are given by the expressions

$$\left[\mathrm{N}\right] = \left[\left[\mathrm{N}_1\right] \;\; \left[\mathrm{N}_2\right] \;\; \left[\mathrm{N}_3\right]\right] \tag{4.39}$$

$$\left[\mathrm{B}\right] = \left[\left[\mathrm{B}_1\right] \;\; \left[\mathrm{B}_2\right] \;\; \left[\mathrm{B}_3\right]\right] \tag{4.40}$$

where $\left[\mathrm{N}_\mathrm{I}\right]$ and $\left[\mathrm{B}_\mathrm{I}\right]$ are defined by Eqs. (4.15) and (4.19), respectively. With the substitution of Eqs. (4.36), (4.39), and (4.40) in for Eqs. (4.8), (4.15), and (4.19), respectively, the FE discretization and $\bar{B}$ method developed in the previous section applies to the LT element. Unlike the classical theory, the strain for a micropolar continuum is not constant throughout the LT element due to the presence of the microrotations in the shear strain definition, e.g., the $\bar{\varepsilon}_{33}$ component of $\left[\mathrm{B}_\mathrm{I}\right]$ in Eq. (4.19). Therefore, the element matrices are integrated with a 3-point Gaussian quadrature formula appropriate for triangular domains [147].

4.2.3 Constitutive Update

This section covers the algorithmic treatment for integrating the constitutive equations presented in Chapter 3 for both the single and multicriterion theories. Within the context of the displacement-based implicit FE method, the integration procedure is strain/deformation driven. That is to say the role of the constitutive update is to determine the stress and updated material state at the end of the time step based on the known equilibrium solution from the previous time step and the current approximation to the displacement field, i.e., given the strain increment, $\Delta\mathbf{E}$, and the previous equilibrium state defined by the

set, ${}^{t}\left\{\boldsymbol{\Sigma}, \mathbf{E}^{\mathrm{p}}, \boldsymbol{\zeta}\right\}$, determine the updated state expressed by ${}^{\tau}\left\{\boldsymbol{\Sigma}, \mathbf{E}^{\mathrm{p}}, \boldsymbol{\zeta}\right\}$ where the left superscripts denote the total time at the end of the previous equilibrium solution, t, and current step, τ, respectively. The generic elements in the previously introduced sets are meant to represent all relevant stress, $\boldsymbol{\Sigma}$, plastic strain, $\mathbf{E}^{\mathrm{p}}$, and internal state variable, $\boldsymbol{\zeta}$, measures for the continuum and constitutive model under consideration. The constitutive integration algorithm presented is a rate-tangent modulus scheme which is an explicit method. The rate-tangent method has been implemented in all versions of the UEL used in this research; however, it will be advantageous to move to a return-mapping algorithm for increased stability and computational efficiency when solving large scale problems.

Rate-Tangent Integration Scheme

In the rate-tangent method, all variables except for the plastic increments are integrated via the forward Euler method, and the plastic increments are determined by solving a set of algebraic equations derived from forward-gradient expansions of the flow rules. The rate-tangent theory applied to the classical theory of crystal plasticity is given by Peirce et al. [148], and it has also been adapted to the second gradient theory of Shu and Fleck [27]. Subsequent extensions to handle the micropolar constitutive models are covered in the following subsections. The symbol "Δ" is used to denote an increment of a given variable, x, such that $\Delta x = {}^{\tau}x - {}^{t}x$ where ${}^{\tau}x$ and ${}^{t}x$ are the values of the variable at the end and the beginning of a time increment, respectively. Although several variations of the constitutive models have been proposed in Chapter 3, the update procedure is only developed for one version of the multi- and single criterion models. The relevant relations for any given strength model can be derived in procedurally similar fashion.

Multicriterion Flow Rule

The rate-tangent method is developed for the constitutive model referred to as "*Strength Model Version 2*" (see Section 3.4.2) in this section. This particular strength model features a threshold stress for slip that depends on both SSD and GND densities and a curvature threshold stress that depends on the GND density. The incremental constitutive relations for this model are given as

$$^{\tau}\overline{\boldsymbol{\varepsilon}} = {}^{t}\overline{\boldsymbol{\varepsilon}} + \Delta\overline{\boldsymbol{\varepsilon}} \tag{4.41}$$

$$^{\tau}\overline{\boldsymbol{\kappa}} = {}^{t}\overline{\boldsymbol{\kappa}} + \Delta\overline{\boldsymbol{\kappa}} \tag{4.42}$$

$$^{\tau}\overline{\boldsymbol{\varepsilon}}^{\mathrm{p}} = {}^{t}\overline{\boldsymbol{\varepsilon}}^{\mathrm{p}} + \sum\nolimits_{\alpha} {}^{t}\mathbf{N}^{\alpha}\Delta\lambda^{\alpha} \tag{4.43}$$

$$^{\tau}\overline{\boldsymbol{\kappa}}^{\mathrm{p}} = {}^{t}\overline{\boldsymbol{\kappa}}^{\mathrm{p}} + \sum\nolimits_{\alpha} {}^{t}\mathbf{N}_{\perp}^{\alpha}\Delta\lambda_{\perp}^{\alpha} \tag{4.44}$$

$$^{\tau}\varrho_{S}^{\alpha} = {}^{t}\varrho_{S}^{\alpha} + \frac{1}{b}\left(\frac{1}{K}\sqrt{\sum\nolimits_{\beta} a^{\alpha\beta}\,{}^{t}\varrho^{\beta}} - 2y_{c}\,{}^{t}\varrho_{S}^{\alpha}\right)\Delta\lambda^{\alpha} \tag{4.45}$$

$$^{\tau}\varrho_{G}^{\alpha} = {}^{t}\varrho_{G}^{\alpha} - \frac{\Delta\lambda_{\perp}^{\alpha}}{bL_{\perp}^{\alpha}}\operatorname{sgn}\left({}^{t}\pi_{\perp}^{\alpha}\right)\operatorname{sgn}\left({}^{t}\varrho_{G,\perp}^{\alpha}\right) \tag{4.46}$$

$$\begin{aligned} ^{\tau}r^{\alpha} = {}^{t}r^{\alpha} + \frac{c_{1}\mu}{2}\sum\nolimits_{\beta}\Bigg\{\frac{h^{\alpha\beta}}{\sqrt{\sum_{\delta} h^{\alpha\delta}\,{}^{t}\varrho^{\delta}}}\Bigg[\left(\frac{1}{K}\sqrt{\sum\nolimits_{\chi} a^{\beta\chi}\,{}^{t}\varrho^{\chi}} - 2y_{c}\,{}^{t}\varrho_{S}^{\beta}\right)\Delta\lambda^{\beta} \cdots \\ - \frac{\Delta\lambda_{\perp}^{\beta}}{L_{\perp}^{\beta}}\operatorname{sgn}\left({}^{t}\pi_{\perp}^{\beta}\right)\operatorname{sgn}\left({}^{t}\varrho_{G,\perp}^{\beta}\right)\Bigg]\Bigg\} \end{aligned} \tag{4.47}$$

$$^{\tau}r_{\perp}^{\alpha} = {}^{t}r_{\perp}^{\alpha} - \frac{c_{7}\mu}{2}\sum\nolimits_{\beta}\frac{h_{\perp}^{\alpha\beta}}{\sqrt{\sum_{\delta} h_{\perp}^{\alpha\delta}\left|{}^{t}\varrho_{G,\perp}^{\delta}\right|}}\frac{\Delta\lambda_{\perp}^{\beta}}{L_{\perp}^{\beta}}\operatorname{sgn}\left({}^{t}\pi_{\perp}^{\beta}\right)\operatorname{sgn}\left({}^{t}\varrho_{G,\perp}^{\beta}\right) \tag{4.48}$$

$$^{\tau}\boldsymbol{\sigma} = \mathbb{C} : \left({}^{\tau}\overline{\boldsymbol{\varepsilon}} - {}^{\tau}\overline{\boldsymbol{\varepsilon}}^{\mathrm{p}}\right) \tag{4.49}$$

$$^{\tau}\mathbf{m} = \mathbb{D} : \left({}^{\tau}\overline{\boldsymbol{\kappa}} - {}^{\tau}\overline{\boldsymbol{\kappa}}^{\mathrm{p}}\right) \tag{4.50}$$

The plastic increments are determined from the generalized trapezoid rule as

$$\Delta\lambda^{\alpha} = \Delta t\left[\left(1-\theta\right){}^{t}\dot{\lambda}^{\alpha} + \theta\,{}^{\tau}\dot{\lambda}^{\alpha}\right] \tag{4.51}$$

$$\Delta\lambda_{\perp}^{\alpha} = \Delta t\left[\left(1-\theta\right){}^{t}\dot{\lambda}_{\perp}^{\alpha} + \theta\,{}^{\tau}\dot{\lambda}_{\perp}^{\alpha}\right] \tag{4.52}$$

where θ is an integration parameter that is equal to one for fully implicit backward Euler integration and equal to zero for forward Euler explicit integration. The plastic parameters at the end of the time increment are approximated by forward-gradient expansions about the state at time t as

$$ {}^{\tau}\dot{\lambda}^{\alpha} = {}^{t}\dot{\lambda}^{\alpha} + \frac{\partial {}^{t}\dot{\lambda}^{\alpha}}{\partial {}^{t}\tau^{\alpha}_{eff}}\Delta\tau^{\alpha}_{eff} + \frac{\partial {}^{t}\dot{\lambda}^{\alpha}}{\partial {}^{t}r^{\alpha}}\Delta r^{\alpha} \tag{4.53} $$

$$ {}^{\tau}\dot{\lambda}^{\alpha}_{\perp} = {}^{t}\dot{\lambda}^{\alpha}_{\perp} + \frac{\partial {}^{t}\dot{\lambda}^{\alpha}_{\perp}}{\partial {}^{t}\pi^{\alpha}_{\perp}}\Delta\pi^{\alpha}_{\perp} + \frac{\partial {}^{t}\dot{\lambda}^{\alpha}_{\perp}}{\partial {}^{t}r^{\alpha}_{\perp}}\Delta r^{\alpha}_{\perp} \tag{4.54} $$

where τ^{α}_{eff} is the resolved shear stress, $\pi^{\alpha}_{\perp}$ is the resolved couple stress projected on the edge GND dyad, and the derivative terms in Eqs. (4.53)-(4.54) are equal to

$$ \frac{\partial {}^{t}\dot{\lambda}^{\alpha}}{\partial {}^{t}\tau^{\alpha}_{eff}} = \frac{m\,{}^{t}\dot{\gamma}^{\alpha}}{\left\langle \left| {}^{t}\tau^{\alpha}_{eff} \right| - {}^{t}r^{\alpha} \right\rangle} \quad , \quad \frac{\partial {}^{t}\dot{\lambda}^{\alpha}}{\partial {}^{t}r^{\alpha}} = -\frac{m\,{}^{t}\dot{\lambda}^{\alpha}}{\left\langle \left| {}^{t}\tau^{\alpha}_{eff} \right| - {}^{t}r^{\alpha} \right\rangle} \tag{4.55} $$

$$ \frac{\partial {}^{t}\dot{\lambda}^{\alpha}_{\perp}}{\partial {}^{t}\pi^{\alpha}_{\perp}} = \frac{n_{\perp}\,{}^{t}\dot{\varphi}^{\alpha}_{\perp}}{L^{\alpha}_{\perp}\left\langle \left| {}^{t}\pi^{\alpha}_{\perp}/L^{\alpha}_{\perp} \right| - {}^{t}r^{\alpha}_{\perp} \right\rangle} \quad , \quad \frac{\partial {}^{t}\dot{\lambda}^{\alpha}_{\perp}}{\partial {}^{t}r^{\alpha}_{\perp}} = -\frac{n_{\perp}\,{}^{t}\dot{\lambda}^{\alpha}_{\perp}}{L^{\alpha}_{\perp}\left\langle \left| {}^{t}\pi^{\alpha}_{\perp}/L^{\alpha}_{\perp} \right| - {}^{t}r^{\alpha}_{\perp} \right\rangle} \tag{4.56} $$

The resolved force and couple stress increments are expressed as

$$ \Delta\tau^{\alpha}_{eff} = {}^{t}\mathbf{Z}^{\alpha} : \Delta\boldsymbol{\sigma} = {}^{t}\mathbf{Z}^{\alpha} : \mathbb{C} : \left(\Delta\overline{\boldsymbol{\varepsilon}} - \sum\nolimits_{\beta} {}^{t}\mathbf{N}^{\beta}\Delta\lambda^{\beta} \right) \tag{4.57} $$

$$ \Delta\pi^{\alpha}_{\perp} = {}^{t}\mathbf{Y}^{\alpha}_{\perp} : \Delta\mathbf{m} = {}^{t}\mathbf{Y}^{\alpha}_{\perp} : \mathbb{D} : \left(\Delta\overline{\boldsymbol{\kappa}} - \sum\nolimits_{\beta} {}^{t}\mathbf{N}^{\beta}_{\perp}\Delta\lambda^{\beta}_{\perp} \right) \tag{4.58} $$

and the increments in the slip and curvature thresholds are given in Eqs. (4.47) and (4.48) as

$$ \Delta r^{\alpha} = \frac{c_1\mu}{2}\sum\nolimits_{\beta}\left\{ \frac{h^{\alpha\beta}}{\sqrt{\sum_{\delta} h^{\alpha\delta}\,{}^{t}\varrho^{\delta}}}\left[\left(\frac{1}{K}\sqrt{\sum\nolimits_{\chi} a^{\beta\chi}\,{}^{t}\varrho^{\chi}} - 2y_c\,{}^{t}\varrho^{\beta}_{S} \right)\Delta\lambda^{\beta} \cdots \right.\right. $$
$$ \left.\left. - \frac{\Delta\lambda^{\beta}_{\perp}}{L^{\beta}_{\perp}}\operatorname{sgn}\left({}^{t}\pi^{\beta}_{\perp} \right)\operatorname{sgn}\left({}^{t}\varrho^{\beta}_{G,\perp} \right) \right] \right\} \tag{4.59} $$

$$ \Delta r^{\alpha}_{\perp} = -\frac{c_7\mu}{2}\sum\nolimits_{\beta}\frac{h^{\alpha\beta}_{\perp}}{\sqrt{\sum_{\delta} h^{\alpha\delta}_{\perp}\left| {}^{t}\varrho^{\delta}_{G,\perp} \right|}}\frac{\Delta\lambda^{\beta}_{\perp}}{L^{\beta}_{\perp}}\operatorname{sgn}\left({}^{t}\pi^{\beta}_{\perp} \right)\operatorname{sgn}\left({}^{t}\varrho^{\beta}_{G,\perp} \right) \tag{4.60} $$

Insertion of Eqs. (4.53)-(4.60) into the generalized trapezoid rules given in Eqs. (4.51)-(4.52) leads to a coupled set of algebraic equations for the plastic increments, i.e.,

$$\Delta\lambda^{\alpha} = \Delta t\, {}^{t}\dot{\lambda}^{\alpha} + \theta\Delta t\Big\{ {}^{t}\mathbf{Z}'^{\alpha} : \mathbb{C} : \Delta\overline{\boldsymbol{\varepsilon}} \cdots - \sum\nolimits_{\beta}\Big[\Big({}^{t}\mathbf{Z}'^{\alpha} : \mathbb{C} : {}^{t}\mathbf{N}^{\beta} - {}^{t}H_{1}'^{\alpha\beta}\Big)\Delta\lambda^{\beta} - {}^{t}H_{2}'^{\alpha\beta}\Delta\lambda_{\perp}^{\beta}\Big]\Big\} \tag{4.61}$$

$$\Delta\lambda_{\perp}^{\alpha} = \Delta t\, {}^{t}\dot{\lambda}_{\perp}^{\alpha} + \theta\Delta t\Big\{ {}^{t}\mathbf{Y}_{\perp}'^{\alpha} : \mathbb{D} : \Delta\overline{\boldsymbol{\kappa}} \cdots - \sum\nolimits_{\beta}\Big({}^{t}\mathbf{Y}_{\perp}'^{\alpha} : \mathbb{D} : {}^{t}\mathbf{N}_{\perp}^{\beta} - {}^{t}H_{3}'^{\alpha\beta}\Big)\Delta\lambda_{\perp}^{\beta}\Big\} \tag{4.62}$$

The tensors and matrices ${}^{t}\mathbf{Z}'^{\alpha}$, ${}^{t}H_{1}'^{\alpha\beta}$, ${}^{t}H_{2}'^{\alpha\beta}$, ${}^{t}\mathbf{Y}_{\perp}'^{\alpha}$, and ${}^{t}H_{3}'^{\alpha\beta}$ are defined as

$${}^{t}\mathbf{Z}'^{\alpha} = \frac{\partial\, {}^{t}\dot{\lambda}^{\alpha}}{\partial\, {}^{t}\tau_{\mathit{eff}}^{\alpha}}\, {}^{t}\mathbf{Z}^{\alpha} \tag{4.63}$$

$${}^{t}H_{1}'^{\alpha\beta} = \frac{\partial\, {}^{t}\dot{\lambda}^{\alpha}}{\partial\, {}^{t}r^{\alpha}}\frac{c_{1}\mu}{2}\frac{h^{\alpha\beta}}{\sqrt{\sum_{\delta} h^{\alpha\delta}\, {}^{t}\varrho^{\delta}}}\left(\frac{1}{K}\sqrt{\sum\nolimits_{\chi} a^{\beta\chi}\, {}^{t}\varrho^{\chi}} - 2y_{c}\, {}^{t}\varrho_{S}^{\beta}\right) \tag{4.64}$$

$${}^{t}H_{2}'^{\alpha\beta} = -\frac{\partial\, {}^{t}\dot{\lambda}^{\alpha}}{\partial\, {}^{t}r^{\alpha}}\frac{c_{1}\mu}{2}\frac{h^{\alpha\beta}}{\sqrt{\sum_{\delta} h^{\alpha\delta}\, {}^{t}\varrho^{\delta}}}\frac{1}{L_{\perp}^{\beta}}\operatorname{sgn}\Big({}^{t}\pi_{\perp}^{\beta}\Big)\operatorname{sgn}\Big({}^{t}\varrho_{G,\perp}^{\beta}\Big) \tag{4.65}$$

$${}^{t}\mathbf{Y}_{\perp}'^{\alpha} = \frac{\partial\, {}^{t}\dot{\lambda}_{\perp}^{\alpha}}{\partial\, {}^{t}\pi_{\perp}^{\alpha}}\, {}^{t}\mathbf{Y}_{\perp}^{\alpha} \tag{4.66}$$

$${}^{t}H_{3}'^{\alpha\beta} = -\frac{\partial\, {}^{t}\dot{\lambda}_{\perp}^{\alpha}}{\partial\, {}^{t}r_{\perp}^{\alpha}}\frac{c_{7}\mu}{2}\frac{h_{\perp}^{\alpha\beta}}{\sqrt{h_{\perp}^{\alpha\delta}\left|\, {}^{t}\varrho_{G,\perp}^{\delta}\right|}}\frac{1}{L_{\perp}^{\beta}}\operatorname{sgn}\Big({}^{t}\pi_{\perp}^{\beta}\Big)\operatorname{sgn}\Big({}^{t}\varrho_{G,\perp}^{\beta}\Big) \tag{4.67}$$

The terms containing the plastic increments in Eqs. (4.61) and (4.62) are gathered on the left hand side enabling them to be expressed in a more convenient matrix notation as

$$\sum\nolimits_{\beta} M_{1}^{\alpha\beta}\Delta\lambda^{\beta} + \sum\nolimits_{\beta} M_{2}^{\alpha\beta}\Delta\lambda_{\perp}^{\beta} = R_{1}^{\alpha} \tag{4.68}$$

$$\sum\nolimits_{\beta} M_{3}^{\alpha\beta}\Delta\lambda_{\perp}^{\beta} = R_{2}^{\alpha} \tag{4.69}$$

where the matrices, $M_{1}^{\alpha\beta}$, $M_{2}^{\alpha\beta}$, and $M_{3}^{\alpha\beta}$, and vectors, R_{1}^{α} and R_{2}^{α}, are given by the expressions

$$M_{1}^{\alpha\beta} = \delta^{\alpha\beta} + \theta\Delta t\Big({}^{t}\mathbf{Z}'^{\alpha} : \mathbb{C} : {}^{t}\mathbf{N}^{\beta} - {}^{t}H_{1}'^{\alpha\beta}\Big) \tag{4.70}$$

$$M_2^{\alpha\beta} = -\theta\Delta t\, {}^t H_2'^{\alpha\beta} \tag{4.71}$$

$$M_3^{\alpha\beta} = \delta^{\alpha\beta} + \theta\Delta t\Big({}^t\mathbf{Y}_\perp'^{\alpha} : \mathbb{D} : {}^t\mathbf{N}_\perp^{\beta} - {}^t H_3'^{\alpha\beta} \Big) \tag{4.72}$$

$$R_1^{\alpha} = \Delta t\, {}^t\dot{\lambda}^{\alpha} + \theta\Delta t\, {}^t\mathbf{Z}'^{\alpha} : \mathbb{C} : \Delta\overline{\boldsymbol{\varepsilon}} \tag{4.73}$$

$$R_2^{\alpha} = \Delta t\, {}^t\dot{\lambda}_\perp^{\alpha} + \theta\Delta t\, {}^t\mathbf{Y}_\perp'^{\alpha} : \mathbb{D} : \Delta\overline{\boldsymbol{\kappa}} \tag{4.74}$$

Inspection of Eq. (4.69) reveals that the plastic rotation increments do not depend on the plastic slip increments; therefore, the plastic rotation increments may be determined first and can then be inserted into Eq. (4.68) to solve for the plastic slip increments.

In the most general case, an elastoplastic micropolar constitutive model has four sets of tangent moduli that need to be determined. However, this is not the case for the multicriterion constitutive model presently being considered as the plastic rotational increments do not depend on the plastic slip increments, and is the reason that Eq. (4.69) could be solved directly. The four sets of tangent moduli are defined as

$$\mathbb{C} = \frac{\partial\Delta\boldsymbol{\sigma}}{\partial\Delta\overline{\boldsymbol{\varepsilon}}} \quad , \quad \mathbb{B} = \frac{\partial\Delta\boldsymbol{\sigma}}{\partial\Delta\overline{\boldsymbol{\kappa}}} \tag{4.75}$$

$$\mathbb{D} = \frac{\partial\Delta\mathbf{m}}{\partial\Delta\overline{\boldsymbol{\kappa}}} \quad , \quad \mathbb{A} = \frac{\partial\Delta\mathbf{m}}{\partial\Delta\overline{\boldsymbol{\varepsilon}}} \tag{4.76}$$

For the current model, $\mathbb{A} = \mathbf{0}$. The algorithmic moduli appropriate for the current constitutive model are determined by solving for the plastic increments using Eqs. (4.68) and (4.69), i.e.,

$$\Delta\lambda_\perp^{\alpha} = \sum\nolimits_\beta M_3^{\alpha\beta-1} R_2^{\beta} \tag{4.77}$$

$$\Delta\lambda^{\alpha} = \sum\nolimits_\beta M_1^{\alpha\beta-1}\Big(R_1^{\beta} - \sum\nolimits_\chi \sum\nolimits_\delta M_2^{\beta\chi} M_3^{\chi\delta-1} R_2^{\delta} \Big) \tag{4.78}$$

These expressions are substituted into the incremental stress-strain relations, i.e.,

$$\Delta\boldsymbol{\sigma} = \mathbb{C} : \Big(\Delta\overline{\boldsymbol{\varepsilon}} - \sum\nolimits_\alpha {}^t\mathbf{N}^{\alpha}\Delta\lambda^{\alpha} \Big) \tag{4.79}$$

$$\Delta\mathbf{m} = \mathbb{D} : \Big(\Delta\overline{\boldsymbol{\kappa}} - \sum\nolimits_\alpha {}^t\mathbf{N}_\perp^{\alpha}\Delta\lambda_\perp^{\alpha} \Big) \tag{4.80}$$

which after differentiation yield the following

$$\mathbb{C}^{alg} = \mathbb{C} - \theta\Delta t \sum\nolimits_{\alpha}\sum\nolimits_{\beta} \mathbb{C} : {}^{t}\mathbf{N}^{\alpha} M_1^{\alpha\beta-1}\, {}^{t}\mathbf{Z}'^{\beta} : \mathbb{C} \tag{4.81}$$

$$\mathbb{B}^{alg} = \theta\Delta t \sum\nolimits_{\alpha}\sum\nolimits_{\beta}\sum\nolimits_{\chi}\sum\nolimits_{\delta} \mathbb{C} : {}^{t}\mathbf{N}^{\alpha} M_1^{\alpha\beta-1} M_2^{\beta\chi} M_3^{\chi\delta-1}\, {}^{t}\mathbf{Y}'^{\delta}_{\perp} : \mathbb{D} \tag{4.82}$$

$$\mathbb{D}^{alg} = \mathbb{D} - \sum\nolimits_{\alpha}\sum\nolimits_{\beta} \mathbb{D} : {}^{t}\mathbf{N}^{\alpha}_{\perp} M_3^{\alpha\beta-1}\, {}^{t}\mathbf{Y}'^{\beta}_{\perp} : \mathbb{D} \tag{4.83}$$

Single Criterion Flow Rule

The rate-tangent integration method is developed for the single criterion model with an effective stress exponent of $p = 2$. The incremental relations for the single criterion model are Eqs. (4.41)-(4.44) and (4.49)-(4.50), which are supplemented with the ISV incremental equations appropriate for this model, i.e.,

$${}^{\tau}\varrho_S^{\alpha} = {}^{t}\varrho_S^{\alpha} + \frac{1}{b}\left(\frac{1}{K}\sqrt{\sum\nolimits_{\beta} a^{\alpha\beta}\, {}^{t}\varrho_S^{\beta}} - 2y_c\, {}^{t}\varrho_S^{\alpha}\right)\Delta\lambda^{\alpha} \tag{4.84}$$

$${}^{\tau}\varrho_G^{\alpha} = {}^{t}\varrho_G^{\alpha} - \frac{\Delta\lambda_{\perp}^{\alpha}}{bL_{\perp}^{\alpha}} \frac{{}^{t}\pi_{\perp}^{\alpha}}{L_{\perp}^{\alpha}\, {}^{t}\hat{\tau}^{\alpha}} \operatorname{sgn}\left({}^{t}\varrho_{G,\perp}^{\alpha}\right) \tag{4.85}$$

$${}^{\tau}r^{\alpha} = {}^{t}r^{\alpha} + \frac{c_1\mu}{2}\sum\nolimits_{\beta} \frac{h^{\alpha\beta}}{\sqrt{\sum_{\delta} h^{\alpha\delta}\, {}^{t}\varrho_S^{\delta}}}\left[\left(\frac{1}{K}\sqrt{\sum\nolimits_{\chi} a^{\beta\chi}\, {}^{t}\varrho_S^{\chi}} - 2y_c\, {}^{t}\varrho_S^{\beta}\right)\Delta\lambda^{\beta}\right. \tag{4.86}$$

The plastic increment is determined by the generalized trapezoid rule and plastic parameter at the end of the time increment is given by the appropriate forward-gradient expansion, i.e.,

$$\Delta\lambda^{\alpha} = \Delta t\left[\left(1-\theta\right){}^{t}\dot{\lambda}^{\alpha} + \theta\, {}^{\tau}\dot{\lambda}^{\alpha}\right] \tag{4.87}$$

$${}^{\tau}\dot{\lambda}^{\alpha} = {}^{t}\dot{\lambda}^{\alpha} + \frac{\partial {}^{t}\dot{\lambda}^{\alpha}}{\partial {}^{t}\tau_{eff}^{\alpha}}\Delta\tau_{eff}^{\alpha} + \frac{\partial {}^{t}\dot{\lambda}^{\alpha}}{\partial {}^{t}\pi_{\perp}^{\alpha}}\Delta\pi_{\perp}^{\alpha} + \frac{\partial {}^{t}\dot{\lambda}^{\alpha}}{\partial {}^{t}r^{\alpha}}\Delta r^{\alpha} \tag{4.88}$$

For $p = 2$, the effective slip system flow stress has the following form for plane problems

$$\hat{\tau}^{\alpha} = \left(\left| \tau_{eff}^{\alpha} \right|^2 + \left| \pi_{\perp}^{\alpha} / L_{\perp}^{\alpha} \right|^2 \right)^{\frac{1}{2}} \tag{4.89}$$

Therefore, the derivatives of viscoplastic relation for the plastic parameter are given as

$$\frac{\partial\, {}^{t}\dot{\lambda}^{\alpha}}{\partial\, {}^{t}\tau_{eff}^{\alpha}} = \frac{m\, {}^{t}\dot{\lambda}^{\alpha}}{\left\langle\, {}^{t}\hat{\tau}^{\alpha} - {}^{t}r^{\alpha} \right\rangle} \frac{{}^{t}\tau_{eff}^{\alpha}}{{}^{t}\hat{\tau}^{\alpha}} \quad , \quad \frac{\partial\, {}^{t}\dot{\lambda}^{\alpha}}{\partial\, {}^{t}\pi_{\perp}^{\alpha}} = \frac{m\, {}^{t}\dot{\lambda}^{\alpha}}{\left\langle\, {}^{t}\hat{\tau}^{\alpha} - {}^{t}r^{\alpha} \right\rangle} \frac{{}^{t}\pi_{\perp}^{\alpha}}{L_{\perp}^{\alpha}\, {}^{t}\hat{\tau}^{\alpha}}$$
$$\frac{\partial\, {}^{t}\dot{\lambda}^{\alpha}}{\partial\, {}^{t}r^{\alpha}} = -\frac{m\, {}^{t}\dot{\lambda}^{\alpha}}{\left\langle\, {}^{t}\hat{\tau}^{\alpha} - {}^{t}r^{\alpha} \right\rangle} \tag{4.90}$$

The incremental force and couple stress relations are the same as in Eqs. (4.57) and (4.58) while the threshold stress increment is given in Eq. (4.86) as

$$\Delta r^{\alpha} = \frac{c_1 \mu}{2} \sum\nolimits_{\beta} \frac{h^{\alpha\beta}}{\sqrt{\sum_{\delta} h^{\alpha\delta}\, {}^{t}\varrho_S^{\delta}}} \left(\frac{1}{K} \sqrt{\sum\nolimits_{\chi} a^{\beta\chi}\, {}^{t}\varrho_S^{\chi}} - 2 y_c\, {}^{t}\varrho_S^{\beta} \right) \Delta\lambda^{\beta} \tag{4.91}$$

Combining Eqs. (4.87)-(4.91) leads to a single equation to be solved for the plastic increments, i.e.,

$$\Delta\lambda^{\alpha} = \Delta t\, {}^{t}\dot{\lambda}^{\alpha} + \theta \Delta t \Big[{}^{t}\mathbf{Z}'^{\alpha} : \mathbb{C} : \Delta\overline{\boldsymbol{\varepsilon}} + {}^{t}\mathbf{Y}_{\perp}'^{\alpha} : \mathbb{D} : \Delta\overline{\boldsymbol{\kappa}} \cdots$$
$$- \sum\nolimits_{\beta} \Big({}^{t}\mathbf{Z}'^{\alpha} : \mathbb{C} : {}^{t}\mathbf{N}^{\beta} + {}^{t}\mathbf{Y}_{\perp}'^{\alpha} : \mathbb{D} : {}^{t}\mathbf{N}_{\perp}^{\beta} - {}^{t}H_1'^{\alpha\beta} \Big) \Delta\lambda^{\beta} \Big] \tag{4.92}$$

$$\sum\nolimits_{\beta} M^{\alpha\beta} \Delta\lambda^{\beta} = R^{\alpha} \tag{4.93}$$

where ${}^{t}H_1'^{\alpha\beta}$, $M^{\alpha\beta}$ and R^{α} are defined for the single criterion model as

$${}^{t}H_1'^{\alpha\beta} = \frac{\partial\, {}^{t}\dot{\lambda}^{\alpha}}{\partial\, {}^{t}r^{\alpha}} \frac{c_1 \mu}{2} \frac{h^{\alpha\beta}}{\sqrt{\sum_{\delta} h^{\alpha\delta}\, {}^{t}\varrho_S^{\delta}}} \left(\frac{1}{K} \sqrt{\sum\nolimits_{\chi} a^{\beta\chi}\, {}^{t}\varrho_S^{\chi}} - 2 y_c\, {}^{t}\varrho_S^{\beta} \right) \tag{4.94}$$

$$M^{\alpha\beta} = \delta^{\alpha\beta} + \theta \Delta t \Big({}^{t}\mathbf{Z}'^{\alpha} : \mathbb{C} : {}^{t}\mathbf{N}^{\beta} + {}^{t}\mathbf{Y}_{\perp}'^{\alpha} : \mathbb{D} : {}^{t}\mathbf{N}_{\perp}^{\beta} - {}^{t}H_1'^{\alpha\beta} \Big) \tag{4.95}$$

$$R^{\alpha} = \Delta t\, {}^{t}\dot{\lambda}^{\alpha} + \theta \Delta t \Big({}^{t}\mathbf{Z}'^{\alpha} : \mathbb{C} : \Delta\overline{\boldsymbol{\varepsilon}} + {}^{t}\mathbf{Y}_{\perp}'^{\alpha} : \mathbb{D} : \Delta\overline{\boldsymbol{\kappa}} \Big) \tag{4.96}$$

The constitutive update is formally achieved as in the earlier developments by solving Eq. (4.93) for the plastic increments and then updating the incremental relations. The constitutive tangent moduli for the single criterion model are given as

$$\mathbb{C}^{alg} = \mathbb{C} - \theta\Delta t \sum_{\alpha}\sum_{\beta} \mathbb{C} : {}^{t}\mathbf{N}^{\alpha} M^{\alpha\beta-1} {}^{t}\mathbf{Z}'^{\beta} : \mathbb{C} \tag{4.97}$$

$$\mathbb{B}^{alg} = -\theta\Delta t \sum_{\alpha}\sum_{\beta} \mathbb{C} : {}^{t}\mathbf{N}^{\alpha} M^{\alpha\beta-1} {}^{t}\mathbf{Y}_{\perp}'^{\beta} : \mathbb{D} \tag{4.98}$$

$$\mathbb{D}^{alg} = \mathbb{D} - \theta\Delta t \sum_{\alpha}\sum_{\beta} \mathbb{D} : {}^{t}\mathbf{N}_{\perp}^{\alpha} M^{\alpha\beta-1} {}^{t}\mathbf{Y}_{\perp}'^{\beta} : \mathbb{D} \tag{4.99}$$

$$\mathbb{A}^{alg} = -\theta\Delta t \sum_{\alpha}\sum_{\beta} \mathbb{D} : {}^{t}\mathbf{N}_{\perp}^{a} M^{\alpha\beta-1} {}^{t}\mathbf{Z}'^{\beta} : \mathbb{C} \tag{4.100}$$

It is noted that the inherently coupled nature of plastic flow due to the use of a single yield criteria is reflected by the fact that all four sets of material tangent moduli are nonzero for the single criterion model. It is clear from the inspection of Eq. (4.95) that even in the absence of threshold stress evolution (i.e., ${}^{t}H_{1}'^{\alpha\beta} = 0$), the cross-term tangent moduli, $\mathbb{B}^{alg}$ and $\mathbb{A}^{alg}$, are nonzero; this is not the case for a general multicriterion model.

4.3 User Element Subroutine Benchmark and Validation

The finite element formulation and implementation are verified by considering three initial-boundary value problems: (i) simple shearing of a constrained semi-infinite layer, (ii) the stress concentration at a circular notch, and (iii) strain-localization in a strain-softening bar. The first two problems are examined for an isotropic linearly elastic micropolar continuum and have well-known analytical solutions, which are used to demonstrate the basic performance of the element and to establish convergence rates for the kinematic solution variables as a function of FE discretization size. The third problem does not have an analytical solution and is intended to demonstrate that the FE solutions for the regularized micropolar continuum display convergent behavior with mesh refinement, as distinct from pathological localization of solutions obtained using classical local continuum theory.

4.3.1 Simple Shear of a Constrained Semi-Infinite Layer

The initial-boundary value problem considered here is shown schematically in Figure 4.3. The layer of material is assumed to be infinite in the direction of the applied displacement (x_1 -direction), thereby rendering the problem spatially 1-D with all field variables depending only on the x_2 -coordinate. The relevant kinematic DOF are the displacement in the x_1 -direction, $u_1(x_2)$, and the microrotation about the x_3 -axis, $\overline{\phi}_3(x_2)$.

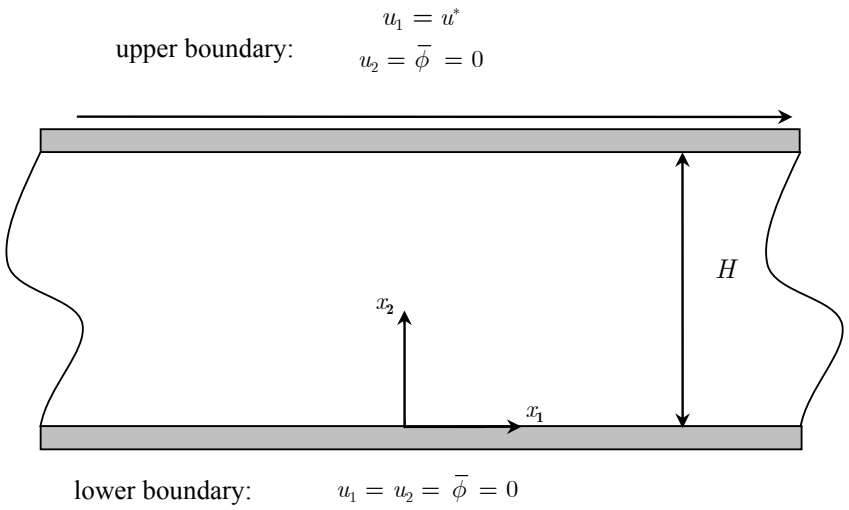

Figure 4.3: Geometry and boundary conditions for the constrained shear initial-boundary value problem.

Under these conditions, the nonzero generalized strain and stress components are given, respectively, as

$$\overline{\varepsilon}_{12} = u_{1,2} + \overline{\phi}_3 \quad , \quad \overline{\varepsilon}_{21} = -\overline{\phi}_3$$
$$\overline{\kappa}_{32} = \overline{\phi}_{3,2} \tag{4.101}$$

$$\sigma_{12} = \left(\mu + \mu_c\right)\overline{\varepsilon}_{12} + \left(\mu - \mu_c\right)\overline{\varepsilon}_{21} \quad , \quad \sigma_{21} = \left(\mu - \mu_c\right)\overline{\varepsilon}_{12} + \left(\mu + \mu_c\right)\overline{\varepsilon}_{21}$$
$$m_{23} = \left(\beta - \gamma\right)\overline{\kappa}_{32} \quad , \quad m_{32} = \left(\beta + \gamma\right)\overline{\kappa}_{32} \tag{4.102}$$

The non-trivially satisfied equilibrium equations are given as

$$\sigma_{12,2} = 0$$
$$m_{32,2} - \left(\sigma_{12} - \sigma_{21}\right) = 0 \tag{4.103}$$

Insertion of Eqs. (4.101) and (4.102) into (4.103) yields the following set of coupled partial differential equations for the for two variables, u_1 and $\overline{\phi}_3$, i.e.,

$$\left(\mu + \mu_c\right)u_{1,22} + 2\mu_c\overline{\phi}_{3,2} = 0$$
$$\left(\beta + \gamma\right)\overline{\phi}_{3,22} - 2\mu_c\left(u_{1,2} + 2\overline{\phi}_3\right) = 0 \tag{4.104}$$

Using the simplified notation $u_1 \equiv u$ and $\overline{\phi}_3 \equiv \overline{\phi}$ and using "prime" to designate differentiation with respect to the x_2-coordinate, Eq. (4.104) may be concisely expressed as

$$u'' + 2N_c^2\overline{\phi}' = 0$$
$$\overline{\phi}'' - \frac{2N_c^2}{\left(1 - N_c^2\right)\ell_1^2}\left(u' + 2\overline{\phi}\right) = 0 \tag{4.105}$$

where the following relationships between micropolar elastic material constants have been used

$$N_c^2 = \frac{\mu_c}{\mu + \mu_c} \quad , \quad \ell_1 = \sqrt{\frac{\beta + \gamma}{\mu}} \tag{4.106}$$

The Dirichlet boundary conditions are

$$u\left(0\right) = 0 \quad , \quad u\left(H\right) = \Gamma H = u^*$$
$$\overline{\phi}\left(0\right) = \overline{\phi}\left(H\right) = 0 \tag{4.107}$$

where $\Gamma^* = u^* / H$ is the average macroscopically applied shear strain and the solution is given as

$$\overline{\phi}\left(x_2\right) = -u^* \frac{\sinh\left(\frac{x_2}{\ell_2}\right) + \sinh\left(\frac{H - x_2}{\ell_2}\right) - \sinh\left(\frac{H}{\ell_2}\right)}{2\left[N_c \ell_1 \left(\cosh\left(\frac{H}{\ell_2}\right) - 1\right) - H \sinh\left(\frac{H}{\ell_2}\right)\right]} \tag{4.108}$$

$$u\left(x_2\right) = u^* \frac{\cosh\left(\frac{x_2}{\ell_2}\right) - \cosh\left(\frac{H - x_2}{\ell_2}\right) - \frac{2x_2}{N_c \ell_1} \sinh\left(\frac{H}{\ell_2}\right) + \cosh\left(\frac{H}{\ell_2}\right) - 1}{2\left[\cosh\left(\frac{H}{\ell_2}\right) - \frac{H}{N_c \ell_1} \sinh\left(\frac{H}{\ell_2}\right) - 1\right]} \tag{4.109}$$

where the additional material length scale, $\ell_2 = \ell_1 / 2N_c$, has been introduced. Therefore, in addition to layer thickness, H, the mechanical response depends on two material parameters, ℓ_1 and ℓ_2 (or alternatively N_c). Recall, that the parameter N_c is related to the relative rotational stiffness of the micropolar continuum, such that the solution to the constrained shear problem not only depends on the intrinsic material bending stiffness, as manifested by ℓ_1, but also on the difference between the material rotations and microrotations. Analytical solutions to this problem have been previously developed in the works of Diebels and Steeb [149] and Neff and Münch [150]. The solution to this initial-boundary value problem for a full second-gradient continuum (for the displacement field) has been derived by Luscher [151] and is given here for comparison as

$$\tilde{u}\left(x_2\right) = u^* \frac{\cosh\left(\frac{x_2}{\ell_*}\right) - \cosh\left(\frac{H - x_2}{\ell_*}\right) - \frac{x_2}{\ell_*} \sinh\left(\frac{H}{\ell_*}\right) + \cosh\left(\frac{H}{\ell_*}\right) - 1}{2\left[\cosh\left(\frac{H}{\ell_*}\right) - 1\right] - \frac{H}{\ell_*} \sinh\left(\frac{H}{\ell_*}\right)} \tag{4.110}$$

where the tilde has been added to Eq. (4.110) to distinguish it from the previously given micropolar displacement field. A comparison of the two solutions reveals that they are quite similar with the distinction being that the second-gradient response is dependent only on a single material length scale, i.e.,

$\ell_* = \sqrt{2(a_3 + a_4)/\mu}$ where a_3 and a_4 are higher-order material constants appropriate for the second-gradient theory with units of force. The analogy between the micropolar material length scale, ℓ_1, given in Eq. $(4.106)_2$ and the second-gradient length scale is obvious; however, the role played by each is different. The functional dependence of the second-gradient solution on ℓ_* is replaced by ℓ_2 (not by ℓ_1) in the micropolar solution. Only in the case where $N_c = 1$ *would* the two solutions coincide where $\ell_* = \ell_1 / 2$. However, if $N_c = 1$ the problem becomes ill-posed due to division by zero (see Eq. $(4.105)_2$), and the strongest statement that can be made is that the two solutions will approximately coincide when $N_c \approx 1$.

Prior to comparing the FE simulation results to those obtained from the analytical solution, it is useful to explore the range of predicted behaviors for different sets of material parameters. For brevity, only a few representative solutions are given here. The response of a 1μm thick layer is presented for two values of the micropolar coupling constant, $N_c \in \{0.25, 0.99\}$, and for each value of N_c four different effective layer thicknesses are considered, i.e., $H / \ell_1 \in \{2,10,50,1000\}$, leading to a total of 8 different simulation cases. This range of material parameters has been chosen to explore a wide range of material response. Films with smaller values of the coupling parameter will allow more deviation between the material rotations and microrotations, and films with smaller effective film thicknesses will have a higher bending stiffness. A shear modulus representative of aluminum is used, $\mu = 26.3$ GPa, and it assumed without loss of generality that $\alpha = \beta$ (see Eq. (4.105)) so that ℓ_1 is determined by a single constitutive parameter. For ease of reference throughout the remainder of this subsection the simulated cases, labeled 1-8, are listed with their corresponding material constants in Table 4.1.

Table 4.1: Test cases and the associated nonlocal material parameters for the constrained shear simulations for an elastic material.

Case	N_c	H / ℓ_1	β (MPa-nm^2)
1A	0.25	1000	1.315E+04
2A	0.25	50	5.260E+06
3A	0.25	10	1.315E+08
4A	0.25	2	3.288E+09
5A	0.99	1000	1.315E+04
6A	0.99	50	5.260E+06
7A	0.99	10	1.315E+08
8A	0.99	2	3.288E+09

The analytical solutions for each case are presented in Figure 4.4 in terms of the normalized response variables, $\bar{\phi} / \phi$ and $\Delta u / u^*$, where $\phi = -\Gamma / 2$ is the material rotation angle that would be predicted by the classical theory of elasticity and $\Delta u = u - \Gamma x_2$ is the shear difference [150]. The shear difference is chosen as the representative response variable instead of the displacement field to more clearly highlight how changes in material parameters influence the displacement field.

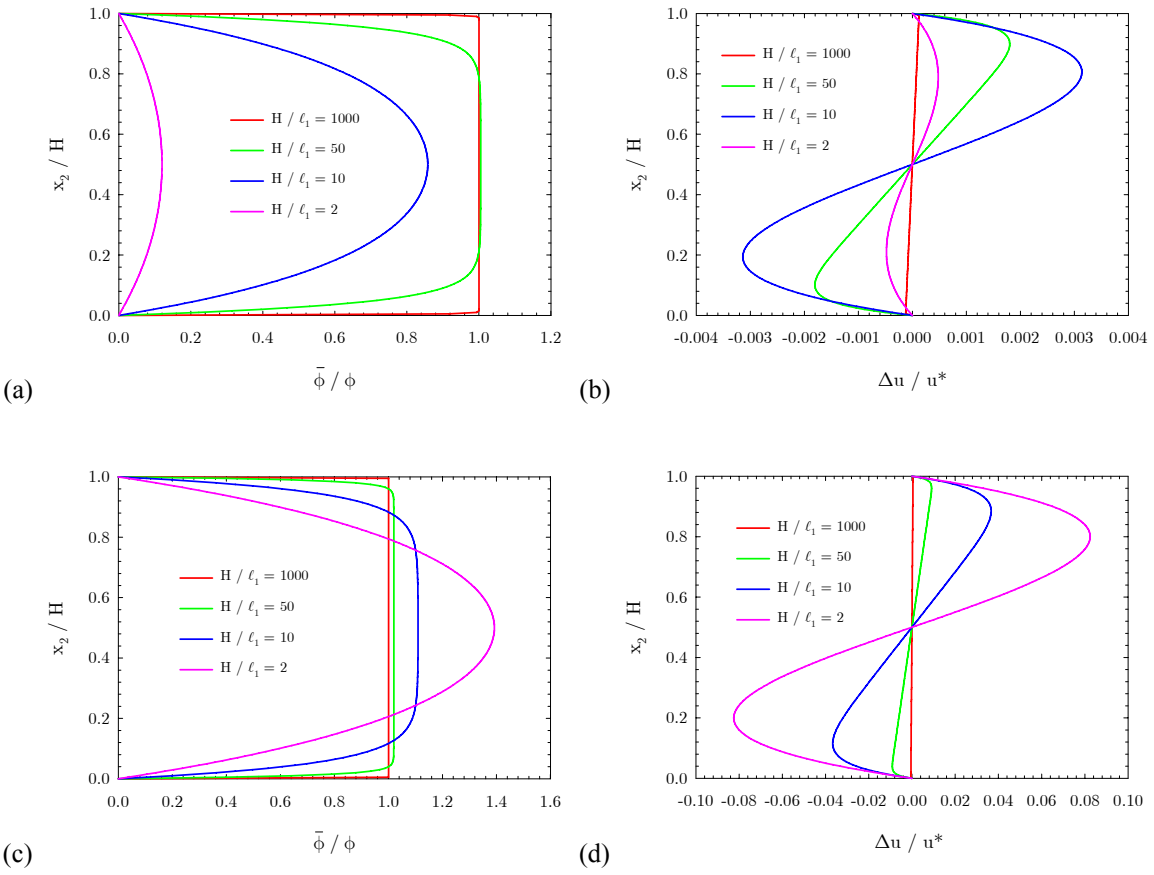

Figure 4.4: Analytical solutions for the normalized response variables for Cases 1-4A ($N_c = 0.25$) (a) and (b) and for Cases 5-8A ($N_c = 0.99$) (c) and (d).

An examination of the normalized microrotation profiles reveals that two different trends in behavior are exhibited for the different values of the coupling parameter as the length scale is varied. For both values of the coupling parameter considered, the microrotations for the largest effective film thicknesses have a negligible boundary layer and display essentially uniform microrotations throughout the film thickness with the magnitude of the microrotation corresponding to that which would be predicted by a classical continuum model. In other words, as the effective film thickness approaches infinity (negligible material length scales) the result approaches that of the classical continuum. As the material length scale is increased for $N_c = 0.25$, the boundary layer increases and the magnitude of the microrotation either

remains approximately the same (Case 2A) or decreases (Cases 3A and 4A) with respect to the baseline case. In contrast, for $N_c = 0.99$, an increase in the material length scale coincides with increases in the boundary layer width *and* the peak magnitude of the microrotation with respect to the baseline case. Turning attention to the shear difference plots ($\Delta u / u^*$), different trends are also observed with respect to changes in the material length parameter for the different values of the coupling parameter. It is noteworthy to point out that the shear difference is an order of magnitude lower for Cases 1-4A as compared to Cases 5-8A, and also that for $N_c = 0.25$ continued increases in the material length scale do not correspond with increases in the peak magnitude of Δu. In this case, the peak magnitude of the shear difference increases with decreases in the effective film thickness (Cases 2A and 3A) up to a certain critical length scale, which lies somewhere between $10 \geq H / \ell_1 \geq 2$. Case 4A, which considers the smallest effective film thickness, exhibits a marked decrease in the maximum shear difference as compared to Cases 2A and 3A. On the other hand, in Cases 5-8A ($N_c = 0.99$) this type of transitional behavior is not seen, at least not for the material length scales considered here, and a consistent increase in the shear difference is seen to coincide with increases in the material length scale parameter.

To evaluate the performance of the UEL subroutine, a select number of simulation cases are considered which represent a broad range of the qualitative response characteristics displayed in Figure 4.4. Simulation cases with large (Case 8A), moderate (Case 2A), and negligible (Case 5A) boundary layer widths are considered, where the boundary layer width is defined in terms of the uniformity of the microrotation field throughout the layer. For example, Case 5A has a nearly uniform microrotation field throughout the layer except for regions near the top and bottom surfaces (see Figure 4.7(a),(b)). This is representative of a very narrow boundary layer. On the other hand, the microrotation field for Case 8A is parabolic attaining a maximum value at the half-layer height as shown in Figure 4.6, and represents a large (over the entire thickness) boundary layer. A fourth case, denoted Case 9A, is considered where the non-traditional elastic constants are negligible, i.e., $N_c = 0.001$ and $H / \ell_1 = 1000$. Although plots of the normalized response variables are not shown for Case 9A, their qualitative features are similar to those of Case 8A.

The FE simulation results are given in Figure 4.5-Figure 4.7, where the normalized response variables are plotted versus the analytical solutions for various discretization sizes. The mesh densities are uniform in the x_2-direction and a single element is used in the x_1-direction with appropriate periodic boundary conditions applied on the displacements and microrotations on the left and right faces of the mesh. The mesh densities are indicated in the figure captions such that "Mesh 20" is indicative of a mesh that has 20 elements through the thickness of the layer. Visual inspection of the results shown in Figure 4.5 and Figure 4.6 indicate that mesh densities of 50 elements are sufficient for accurately capturing the kinematic response for Cases 2A and 8A; however, a significantly higher mesh density of 5000 elements, as shown in Figure 4.7(b), still does not quite match the analytical solution for Case 5A. A quantitative analysis of the convergence behavior and the observed rates of convergence for the different simulation cases are given in Figure 4.8 and Table 4.2, respectively, for both the microrotation and displacement fields. In determining the error between the FE and analytical solutions, an error ansatz must be adopted. A number of different error measures could be considered as discussed in Belytschko et al. [144], but in this work a measure employing the $\mathcal{L}_2$ norm for continuous functions is adopted. The $\mathcal{L}_2$ norm is defined as

$$\left\| f(x) \right\|_{\mathcal{L}_2} = \left\{ \int_{\Omega} \left[f(x) \right]^2 d\Omega \right\}^{1/2} \tag{4.111}$$

where $f(x)$ denotes an arbitrary continuous function and Ω is the domain of the function. A normalized error measure is then introduced as

$$\text{error} = \frac{\left\| \hat{a}(x) - a(x) \right\|_{\mathcal{L}_2}}{\left\| \hat{a}(x) \right\|_{\mathcal{L}_2}} \tag{4.112}$$

where $\hat{a}(x)$ is the solution field obtained from the FE analysis and $a(x)$ is the field obtained from the analytical solution. The error measure is assumed to behave asymptotically with respect to mesh refinement such that it can be described by the general power-law form, i.e.,

$$\text{error} = C\left(\frac{h}{H}\right)^{p} \tag{4.113}$$

where C is a constant, h is the element size, H is the layer thickness (see Figure 4.3), and p is the exponent indicating the order of convergence. Figure 4.8 shows the computed error in the FE solutions plotted against the relative element thickness, h / H. Except for the displacement field in simulation Case 9A, all of the simulation results display monotonic convergence behavior with the rate of convergence given in Table 4.2. Recall that for simulation Case 9A, the non-traditional elastic constants are negligible and it is not surprising that there is no improvement in the displacement field approximation with mesh refinement. It is noteworthy that the order of convergence for all cases, excluding Case 5A (and the previously mentioned displacement field for Case 9A), is approximately $p \approx 1.7\text{-}2.0$ even though the displacement and rotation fields are bilinearly interpolated throughout the element. As might be expected, the simulation case with the sharpest boundary layer transition, Case 5A, displays the worst convergence behavior with orders of convergence equal to 0.42 and 0.67 for the microrotation and displacement fields, respectively. The large gradients in the kinematic fields for this case are the cause of the slower rate of convergence. Despite the lower-order of convergence for this particular simulation case, the element performance is deemed to be acceptable and enables one to conclude that the basic element functions and algorithms are performing as intended since the analytical solution is being approached.

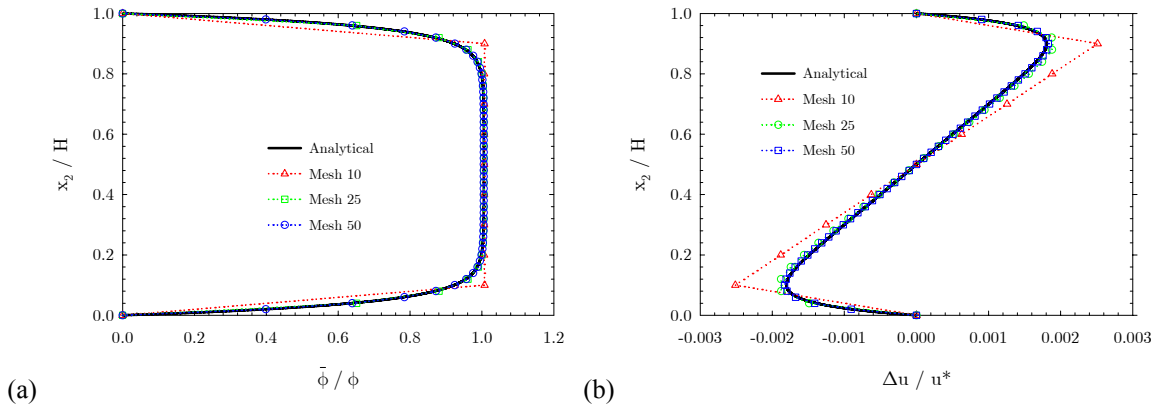

Figure 4.5: Comparison of the normalized response variables obtained from the analytical solution to FE results for different discretization sizes for Case 2A (a) normalized microrotation and (b) normalized shear difference.

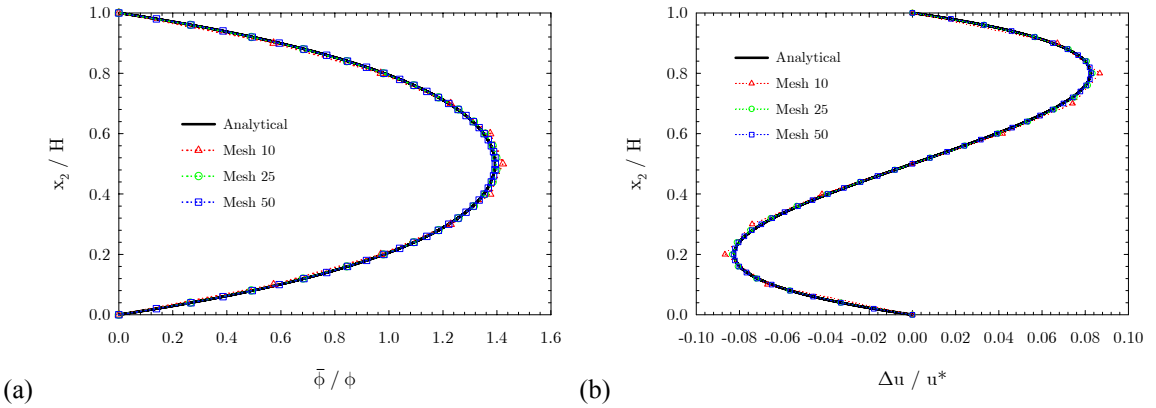

Figure 4.6: Comparison of the normalized response variables obtained from the analytical solution to FE results for different discretization sizes for Case 8A (a) normalized microrotation and (b) normalized shear difference.

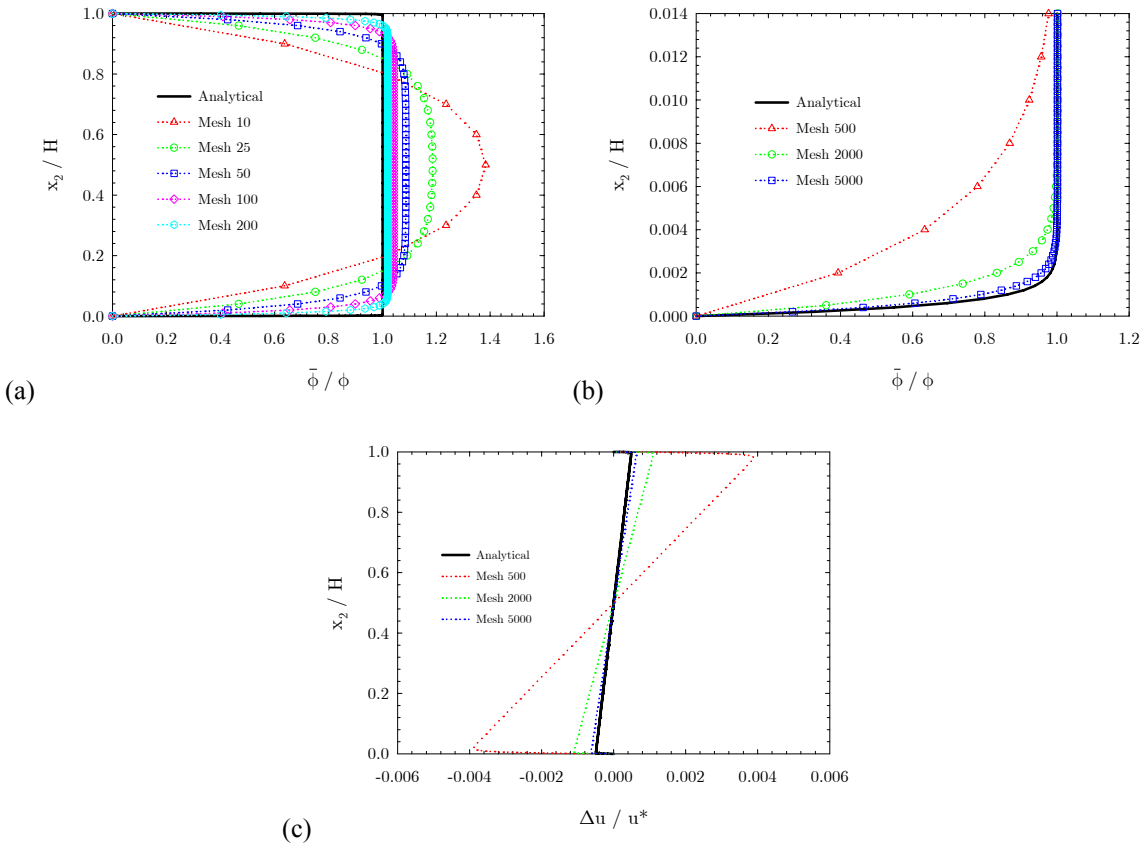

Figure 4.7: Comparison of the normalized response variables obtained from the analytical solution to FE results for different discretization sizes for Case 5A (a) normalized microrotation (b) exploded view of normalized microrotation and (c) normalized shear difference.

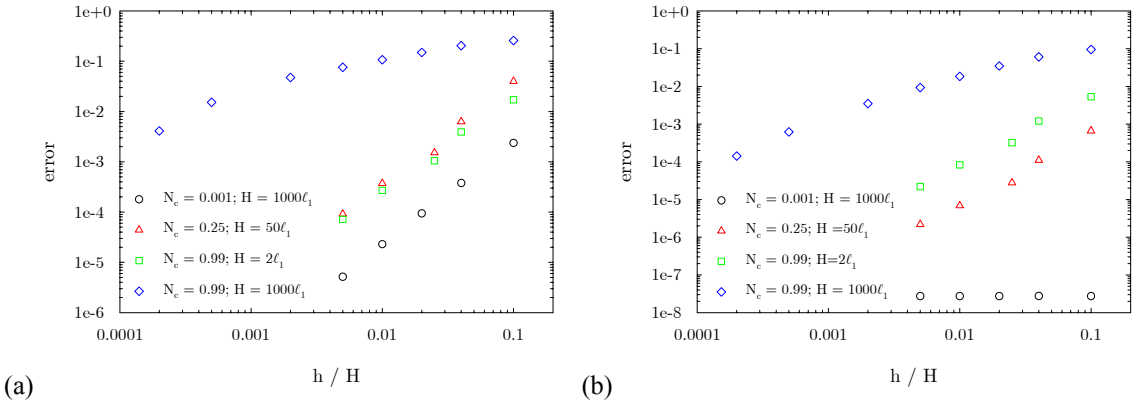

Figure 4.8: Normalized error plotted against the relative element thickness for different mesh sizes for the (a) microrotation and (b) displacement fields.

Table 4.2: Observed order of convergence, p, for the error based on the $\mathcal{L}_2$ norm for the microrotation and displacement fields for select simulation cases.

Case	N_c	$H \,/\, \ell_1$	β (MPa-nm^2)	exponent p	
				$\overline{\phi}$	u
2A	0.25	50	5.260E+06	2.08	2.02
5A	0.99	1000	1.315E+04	0.42	0.67
8A	0.99	2	3.288E+09	1.72	1.73
9A	0.001	1000	1.315E+04	2.00	0

4.3.2 Stress Concentration at a Circular Notch

Given that the implementation has been validated in the solution of the constrained shear problem with respect to accurately capturing the microrotation and displacement fields for a range of non-traditional elastic constants, a second initial-boundary value problem which features gradients in the stress fields is simulated to further test the UEL subroutine. The initial-boundary value problem considered is a plate with a circular notch subjected to remote uniaxial tension, and the analytical distribution of the principal stress component and the stress concentration factor are compared to FE simulation results for different mesh sizes. This is a fairly standard problem used to validate and benchmark the performance of various micropolar FE implementations [152-156]. The analytical solution to this problem can be found in Eringen [134] and was originally derived by Kaloni and Ariman [157]. Consider an infinite plate with circular notch of radius, R, subjected to a remote tension, P, at $x_1 = \infty$ as shown in Figure 4.9.

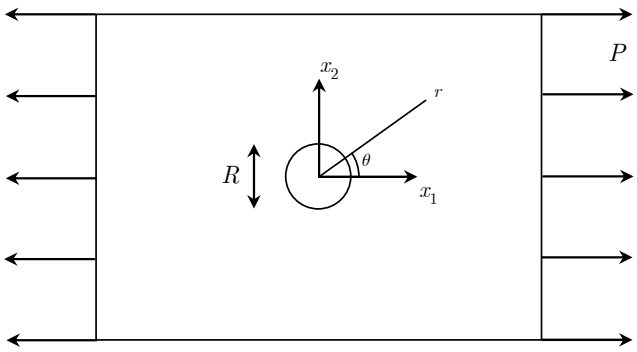

Figure 4.9: Geometry and boundary conditions for stress concentration initial-boundary value problem.

Considering a cylindrical coordinate system whose origin is located at the center of the notch, the analytical solution for the $\sigma_{\theta\theta}$ component of stress is given as

$$\begin{aligned}\sigma_{\theta\theta} &= \frac{P}{2}\left(1-\cos 2\theta\right) - \frac{A_1}{r^2} + \left(\frac{6A_2}{r^4} - \frac{6A_4}{r^4}\right)\cos 2\theta \cdots \\ &\quad -\frac{2A_5}{\ell_2 r}\left[\frac{3\ell_2}{r}K_0\left(\frac{r}{\ell_2}\right) + \left(1+\frac{6\ell_2^2}{r^2}\right)K_1\left(\frac{r}{\ell_2}\right)\right]\cos 2\theta\end{aligned} \tag{4.114}$$

where the constants A_i have the definitions

$$\begin{aligned}A_1 = -\frac{P}{2}R^2 \quad , \quad A_2 = -\frac{PR^4\left(1-F_1\right)}{4\left(1+F_1\right)} \quad , \quad A_4 = \frac{\left(1-\nu\right)R^2\ell_1^2 P}{1+F_1} \\ A_5 = -\frac{PR\ell_2 F_1}{\left(1+F_1\right)K_1\left(R\,/\,\ell_2\right)}\end{aligned} \tag{4.115}$$

Here, F_1 is defined as

$$F_1 \equiv 8\left(1-\nu\right)N_c^2\left[4+\frac{R^2}{\ell_2^2}+\frac{2R}{\ell_2}\frac{K_0\left(R\,/\,\ell_2\right)}{K_1\left(R\,/\,\ell_2\right)}\right]^{-1} \tag{4.116}$$

Both the stress concentration factor, $K_\sigma = \sigma_{\theta\theta}(r = 0, \theta = \pi / 2) / P$, and the $\sigma_{\theta\theta}$ stress component for $\theta = \pi / 2$ are compared to the results of the finite element simulations for the different combinations of non-traditional elastic constants listed in Table 4.3. The classical elastic constants are taken to be $\mu = 25$ GPa and $\nu = 0.3$.

Table 4.3: Test cases and the associated nonlocal material parameters for the stress concentration simulations for an elastic material.

Case	N_c	R / ℓ_1	β (MPa-mm^2)
1B	10^{-4}	10	1.25
2B	10^{-4}	1	12.5
3B	10^{-4}	0.1	12,500
4B	0.5	10	1.25
5B	0.5	1	12.5
6B	0.5	0.1	12,500
7B	0.99	10	1.25
8B	0.99	1	12.5
9B	0.99	0.1	12,500

The FE simulation is setup as a quarter symmetry model with symmetry boundary conditions applied along the bottom ($x_2 = 0$) and left ($x_1 = 0$) faces of the mesh, and the remote load has been applied in the x_2-direction. Since the analytical solution is derived for an infinite plate, the edge length of the quarter symmetry FE model is taken to be $H = 100R$ in order to minimize the influence of boundary effects on the stress fields in the near-notch region. It is noted that the analytical solution was derived for remote loading in the x_1 direction; accordingly, the stress distribution and stress concentration factor along the plane $x_2 = 0$ and at point $(R / 2, 0)$, respectively, from the FE simulations are compared with the analytical solution to account for the change in loading direction. Three different mesh densities are considered, as shown in Figure 4.10, with 8, 16, and 32 elements, respectively, along the perimeter of the notch. Figure 4.10(a) shows the typical mapped mesh pattern used in the far-field region. A uniform

displacement boundary condition is applied to the top surface of the plate such that a unit 1 MPa remote σ_{22} stress field is induced. The boundary conditions are stated as

$$\begin{aligned} u_2(x_1,0) &= \overline{\phi}_3(x_1,0) = 0 \\ u_2(0,x_2) &= \overline{\phi}_3(0,x_2) = 0 \\ u_2(x_1,H) &= 0.14\mu\text{m} \end{aligned} \tag{4.117}$$

where H is the edge length of the FE model.

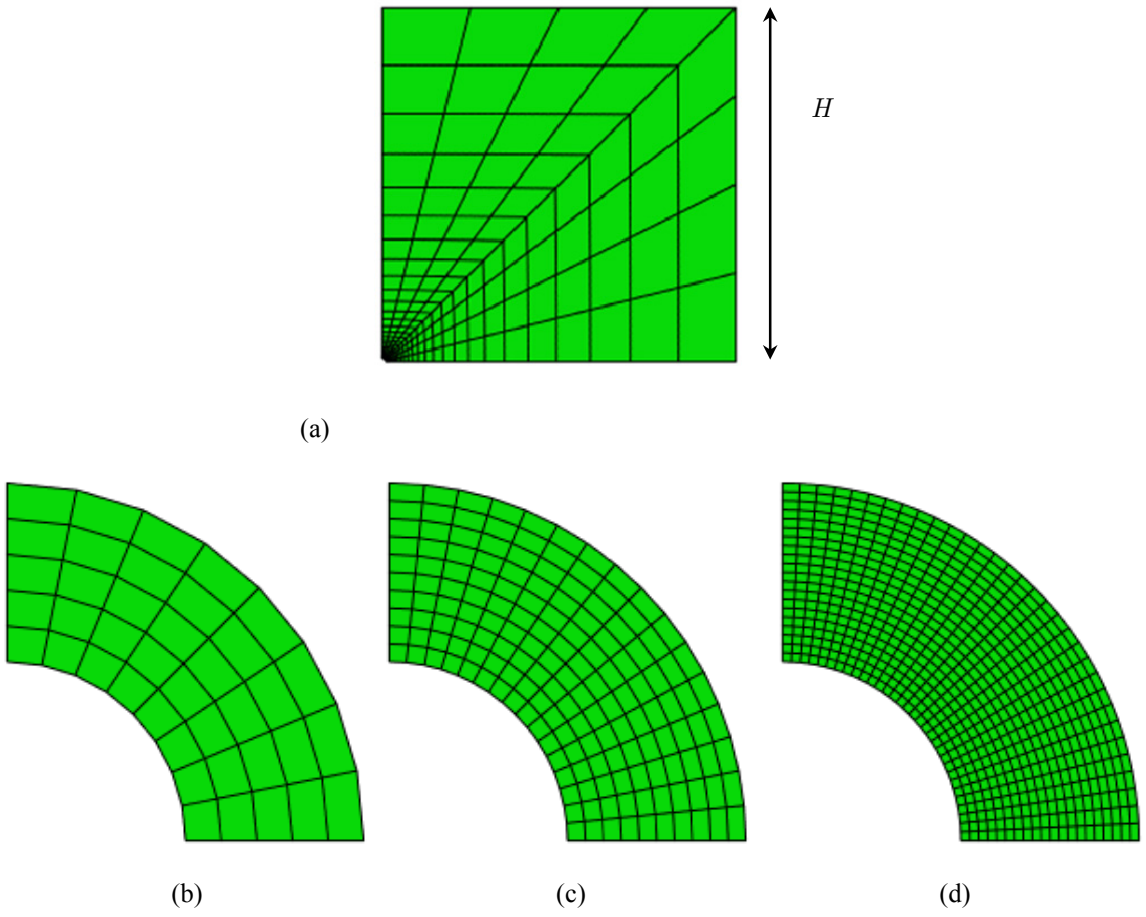

Figure 4.10: Finite element discretizations used in the mesh convergence study for the stress concentration at a circular notch (a) typical far-field mesh (b) Mesh 8 (c) Mesh 16 and (d) Mesh 32.

The stress concentration factors obtained from the FE simulations for all considered cases are given in Table 4.4 along with the corresponding values obtained from the analytical solution, the relative error, and the order of convergence. Unlike the previous error analysis for the constrained shear problem, a local error measure is employed here and is defined as

$$\text{error} = \frac{\left| \hat{K}_\sigma - K_\sigma \right|}{\hat{K}_\sigma} \tag{4.118}$$

where $\hat{K}_\sigma$ and K_σ are the FE and analytical stress concentration factors, respectively. Inspection of the results shows that all simulation test cases have an error of less than 5% for the finest discretization size, with all but Case 7B being characterized by an error of less than 2%. As compared to the constrained shear FE solution, the order of convergence for the stress concentration factor is generally lower and ranges from $p = 1.08\text{-}1.41$. Interestingly, slightly higher convergence rates are observed for Cases 7-9B which employ large values of the micropolar coupling parameter ($N_c = 0.99$) as compared to the other cases, and is counter to the trend observed in the constrained shear problem. It is also noted that, as in the constrained shear problem, the simulation cases associated with the largest values of the micropolar coupling parameter display larger errors with respect to the analytical solution regardless of the mesh density, and the largest error observed in the solution of both initial-boundary value problems corresponds to cases with large micropolar coupling constants and small elastic material length scales, i.e., Cases 5A and 7B. The connection between material descriptions using a large value of N_c and the associated increase in error can be rationalized in terms of the significant increase in the element stiffness that results from using very large values of the micropolar coupling parameter. To further demonstrate the element performance, the σ_{22} component of the stress tensor is plotted versus position from the notch for select simulation cases as shown in Figure 4.11. These plots reveal that for Case 7B (the simulation with the largest error in K_σ), that very good agreement between the FE and analytical solutions is obtained within a few element spacings from the notch root, even for the coarsest mesh. This implies that if a global error measure such as that introduced in Eq. (4.112) had been used to evaluate the element performance for this initial-boundary value problem that the measured discrepancy between the two solutions would be even less. To

further illustrate this point, the σ_{22} contours are shown in Figure 4.12 for Case 7B, where the legend has been cropped to have a maximum value equal to that predicted by the analytical solution. Figure 4.11 demonstrates, at least for the two finest meshes, that changes in the predicted stress field in the near-notch region are primarily restricted to the first few rows of elements in from the notch perimeter.

Table 4.4: A comparison of the analytical and FE stress concentration factors for three different mesh densities.

Case	Analytical	Mesh 8	error	Mesh 16	error	Mesh 32	error	p
1B	3.000	2.801	0.0710	2.904	0.0331	2.953	0.0159	1.08
2B	3.000	2.801	0.0710	2.904	0.0331	2.953	0.0159	1.08
3B	3.000	2.801	0.0710	2.904	0.0331	2.953	0.0159	1.08
4B	2.978	2.775	0.0732	2.881	0.0337	2.933	0.0153	1.13
5B	2.641	2.489	0.0611	2.566	0.0292	2.605	0.0138	1.07
6B	2.487	2.354	0.0565	2.421	0.0273	2.455	0.0130	1.06
7B	2.975	2.366	0.2574	2.679	0.1105	2.858	0.0409	1.33
8B	2.340	2.116	0.1059	2.239	0.0451	2.299	0.0178	1.28
9B	1.865	1.726	0.0806	1.811	0.0299	1.844	0.0114	1.41

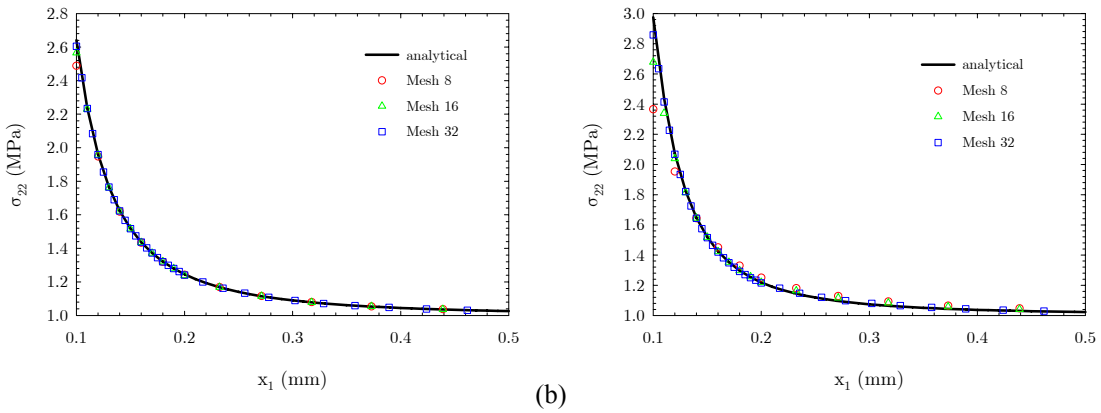

Figure 4.11: Representative plots of σ_{22} versus position along the line $x_2 = 0$ for the different mesh densities: (a) Case 5B and (b) Case 7B.

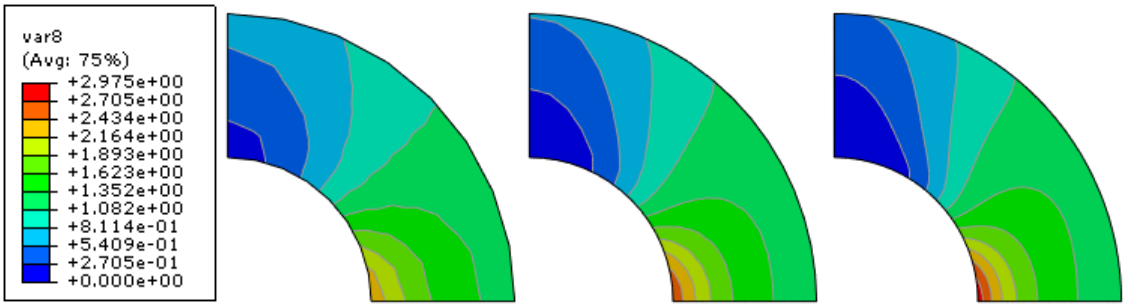

Figure 4.12: Contours of σ_{22} in the near-notch region for Case 7B (a) Mesh 8 (b) Mesh 16 and (c) Mesh 32.

4.3.3 Strain Localization in a Strain-Softening Bar

The previous two code validation problems have demonstrated that the element is performing as intended in the solution of elastic initial-boundary value problems. In an effort to establish that the constitutive update is performing adequately for the full range of capabilities, an initial-boundary value problem utilizing an elastic-plastic constitutive description is solved. The specific problem examined is that of strain-softening plate subjected to a uniform axial displacement, as shown in Figure 4.13. This sort of initial-boundary value problem is often used to demonstrate and establish the mesh regularization capabilities of nonlocal continuum theories, as compared to the classical local continuum theory which yields non-convergent solutions to such problems due to the lack of material length scale in the governing equations. Similar strain localization studies using micropolar continuum theories have been performed by de Borst [158], de Borst and Sluys [159], and Sharbati and Naghdabadi [155]. Convergence of both the global response given in terms of the force-displacement curve and the local response given in terms of the peak principal plastic strain component across the midsection of the plate are investigated and demonstrated.

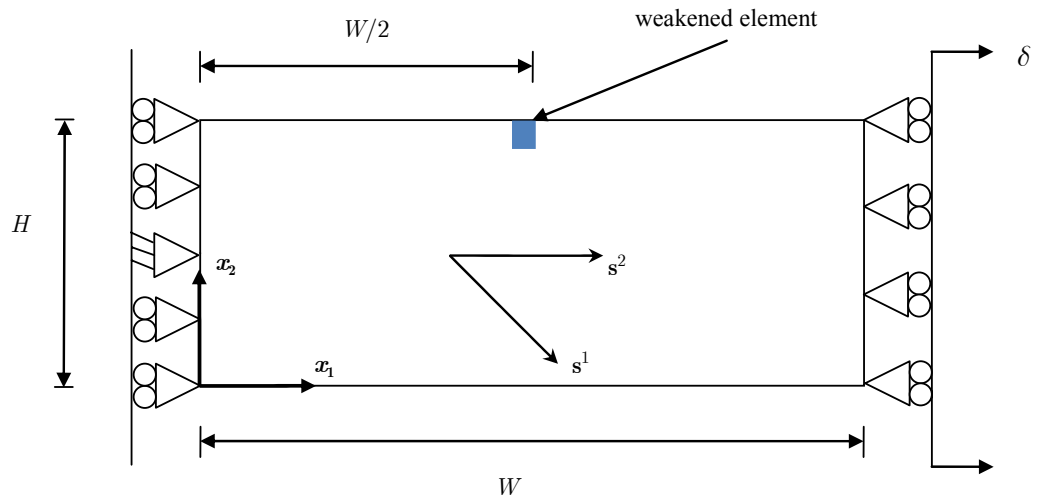

Figure 4.13: Geometry and boundary conditions for the strain-localization initial-boundary value problem.

The geometry and boundary conditions applied to the rectangular plate of dimensions 120 mm × 60 mm are given in Figure 4.13. The left edge of the plate is constrained against displacement in the x_1-direction and the midpoint along this edge also constrained from displacement in the x_2-direction to eliminate rigid body modes of deformation. The top and bottom surfaces are traction free and a uniform displacement, δ, is applied to the right edge of the plate. The formal statement of the boundary conditions is given as

$$u_1(0, x_2) = 0 \quad , \quad u_2(0, H \,/\, 2) = 0$$
$$u_1(W, x_2) = 4.2\,\mathrm{mm} \tag{4.119}$$

The single criterion constitutive model is used in this series of simulations with the slip systems oriented such that a single system ($\mathbf{s}^2$) is aligned along the x_1-axis (see Figure 4.13), and the material parameters are given in Table 4.5 and have been taken in accord with those used in Sharbati and Naghdabadi [155]. To this end, one should not pay too much attention to the actual values of the constants in relation to their physical meaning since the model advanced by them is phenomenological and the simulation is intended,

as in the present case, merely to serve as a computational exercise to demonstrate the numerical performance of the FE implementation. The strain-softening constitutive behavior is prescribed be setting the dislocation segment length constant, K, to zero while specifying the capture radius, y_c, to a positive value. This is equivalent to specifying a linear softening modulus. A weakened element with a lower initial slip threshold strength ($\varrho_{S0} = 2.85\times10^{10}$ mm^{-2}), as shown in Figure 4.13, is used to trigger the strain localization.

Table 4.5: Material parameters used in strain localization simulations for an elastic-viscopolastic material.

Parameter	Symbol	Magnitude	Unit
Young's modulus	E	4	GPa
Poisson's ratio	ν	0.49	-
Coupling parameter	N_c	0.75	-
Elastic length scale	ℓ_e	4	mm
Plastic length scale	$L_\perp$	4	mm
Reference threshold stress	r_0	0	MPa
Threshold stress strength coefficient	c_1	0.5	-
Burgers vector magnitude	b	0.3	nm
Dislocation interaction coefficients	$h^{\alpha\beta}$	$\delta^{\alpha\beta}$	-
Initial SSD density	ϱ_{S0}	3.02×10^{10}	mm^{-2}
Dislocation immobilization coefficients	$a^{\alpha\beta}$	$\delta^{\alpha\beta}$	-
Dislocation segment length constant	K	0	-
Dislocation capture radius	y_c	0.75	nm
Reference slip rate	$\dot{\gamma}_0$	10^{-3}	s^{-1}
Drag stress	g	8	MPa
Inverse rate sensitivity exponent	m	20	-

The FE simulations are performed for a number of mesh discretizations; the meshes are comprised of uniform distributions of the Q4 element, and the mesh density is indicated in the results by the number of elements in the x_1-direction. For example, "Mesh 400" indicates that 400 elements have been used along the width of the plate. Prior to delving into the results obtained using the micropolar model of crystal plasticity, simulation results acquired using a classical local crystal plasticity constitutive description are examined. Figure 4.14 shows the force-deflection response predicted by the classical theory for four different mesh densities. While the initial post-yield behavior is the same for each discretization, a mesh-dependent deviation in the simulated response curves is seen to occur around an applied displacement of approximately $\delta \approx$ 3.3 mm. The general trends observed in the force-deflection responses as a function mesh density are such that the coarser meshes begin deviate at lower applied displacements and display smaller load drops, whereas simulations with finer discretizations maintain the linear softening behavior for a longer duration and exhibit much larger load drops. For example, the force-displacement curve for Mesh 20 begins to depart from the linear behavior around $\delta \approx$ 3.3 mm and the load drop between this point and

the final applied displacement is approximately $\Delta f_{20} \approx 900$ N, whereas for Mesh 280 there is an abrupt load drop at $\delta \approx 4$ mm equal to $\Delta f_{280} \approx 3600$ N. Since there is no regularizing length scale in the local constitutive formulation, the element size dictates the localization behavior such that as the mesh is refined, the peak intensity of the plastic strains within the localization zone increases and the localization band decreases in thickness, as shown in Figure 4.15 and Figure 4.16, respectively. Figure 4.16 contains contour plots of $\varepsilon_{11}^{\mathrm{p}}$ for the four discretizations considered where the contour legend has been cropped in accordance with the micropolar results that are as of yet to be presented. The main points to take away from this Figure are the decreasing thickness in the localization band with continued mesh refinement, and also that for the two finest discretizations secondary and tertiary localization bands are seen to form, which further underscores that the simulations are not converging to a unique solution. This claim is also supported by the plots shown in Figure 4.15 where it is seen that the maximum value of $\varepsilon_{11}^{\mathrm{p}}$ along the midsection of the plate increases in divergent manner with decreases in element size. These are well-known limitations of classical continuum theories that arise in the numerical solution of initial-boundary value problems exhibiting localization behavior.

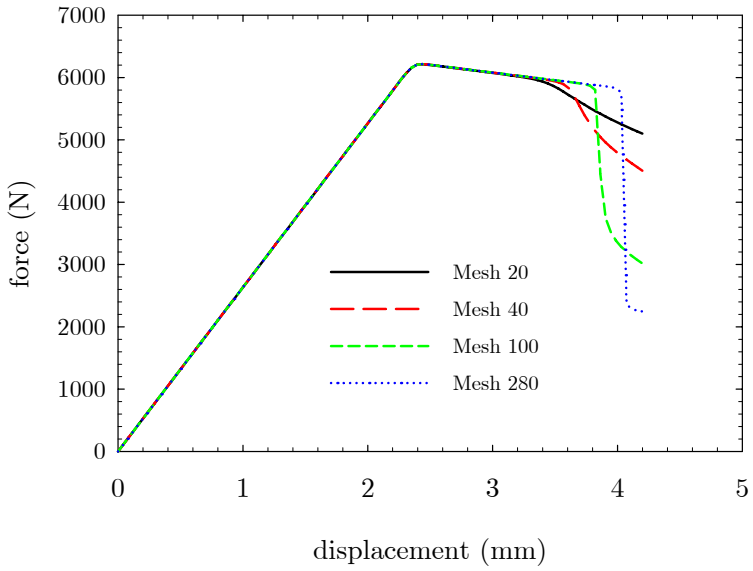

Figure 4.14: Force-displacement curves for the strain-softening plate obtained using the classical local crystal plasticity model for different FE discretizations.

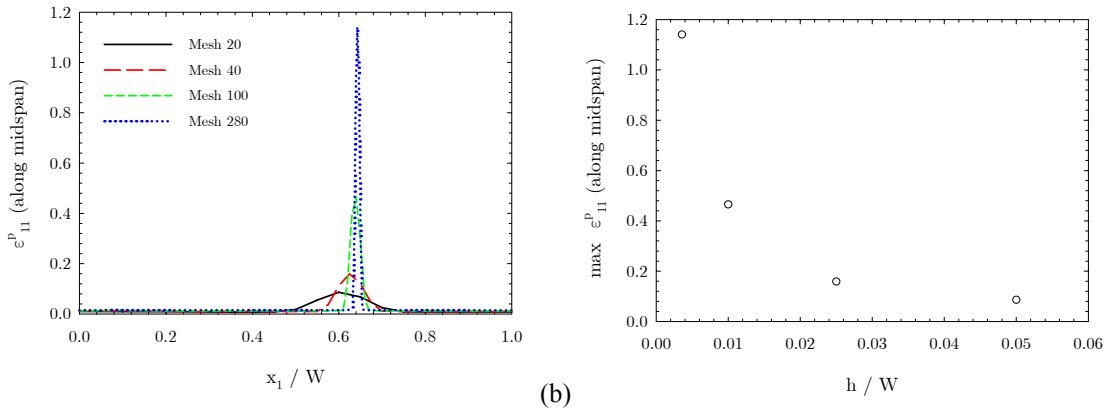

(a) (b)

Figure 4.15: (a) Plot of $\varepsilon_{11}^{\mathrm{p}}$ versus normalized position along the line $x_2 = H / 2$ for the strain-softening plate as predicted by classical crystal plasticity for various mesh densities and (b) the peak value of $\varepsilon_{11}^{\mathrm{p}}$ along this line plotted as a function of normalized element size.

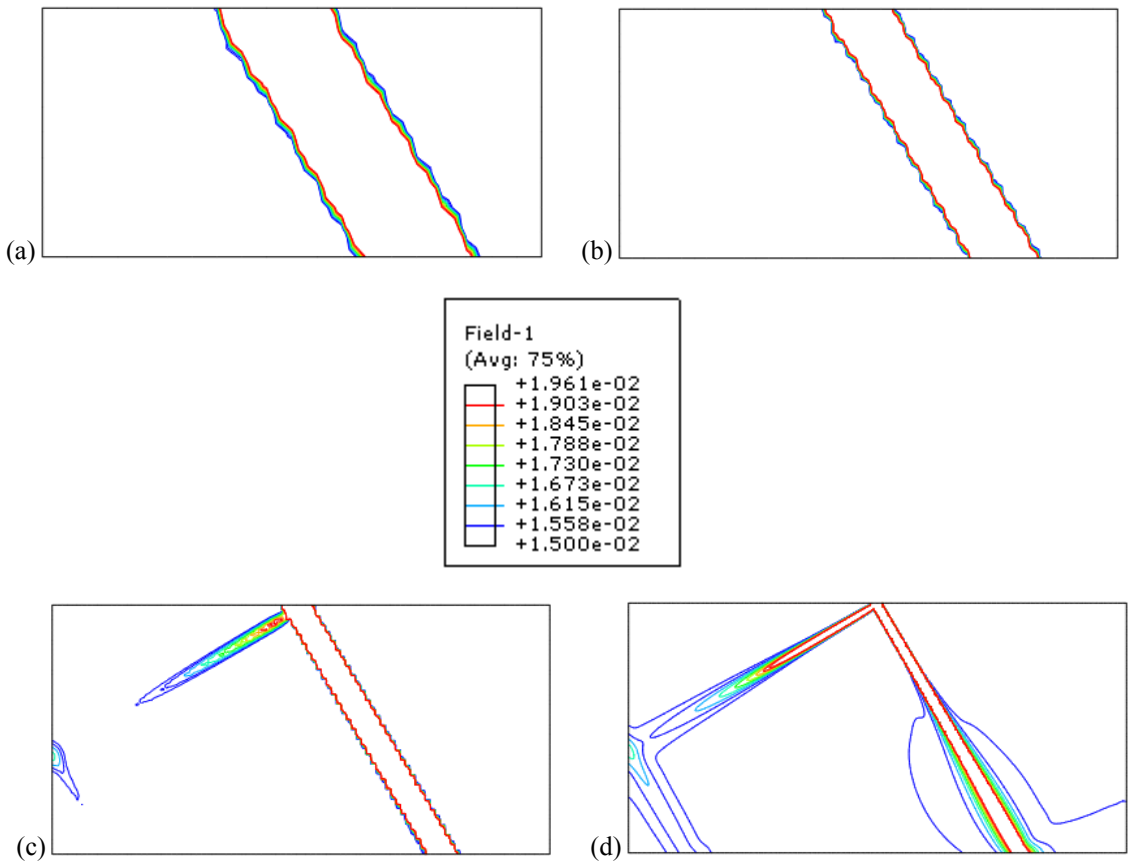

Figure 4.16: Contours of ε_{11}^{p} for the strain-softening plate obtained using the classical crystal plasticity model for different FE discretizations (a) Mesh 20 (b) Mesh 40 (c) Mesh 100 and (d) Mesh 280.

Turning attention to the results of the FE simulations employing the micropolar crystal plasticity constitutive model, it is seen in Figure 4.17 that the global response is stable and does in fact converge to a unique solution when the mesh density is increased. The exploded view of the force-deflection response given in Figure 4.17(b) reveals some slight deviations for the coarser meshes (Mesh 20 and Mesh 100), and identical results for the remaining discretizations indicating that the solution has converged with respect to this aspect of the deformation behavior. In Figure 4.18, the distributions of $\overline{\varepsilon}_{11}^{p}$ along the midspan of the plate are shown for various mesh densities, and it is in contrast to the results obtained from the classical theory that the micropolar model appears to be converging to a unique solution, albeit rather slowly.

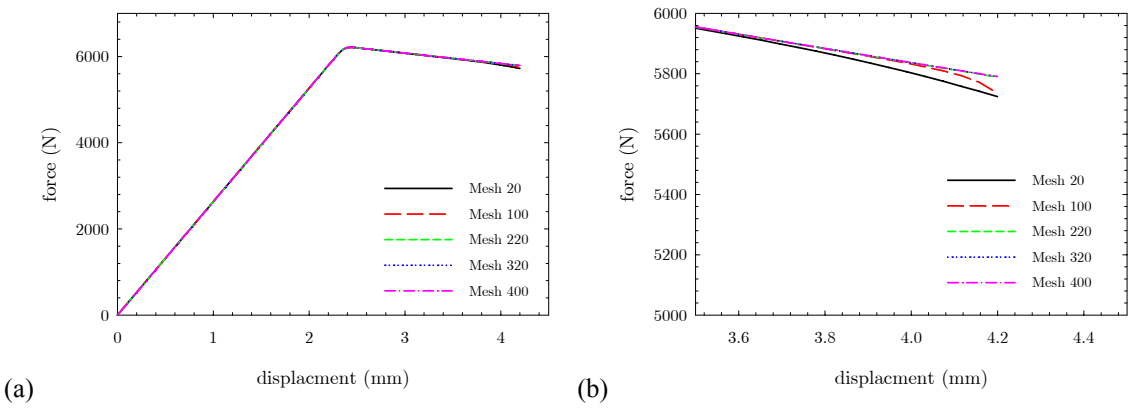

Figure 4.17: Force-displacement curves for the strain-softening plate obtained using the micropolar crystal plasticity model for different FE discretizations (a) normal view and (b) zoomed view.

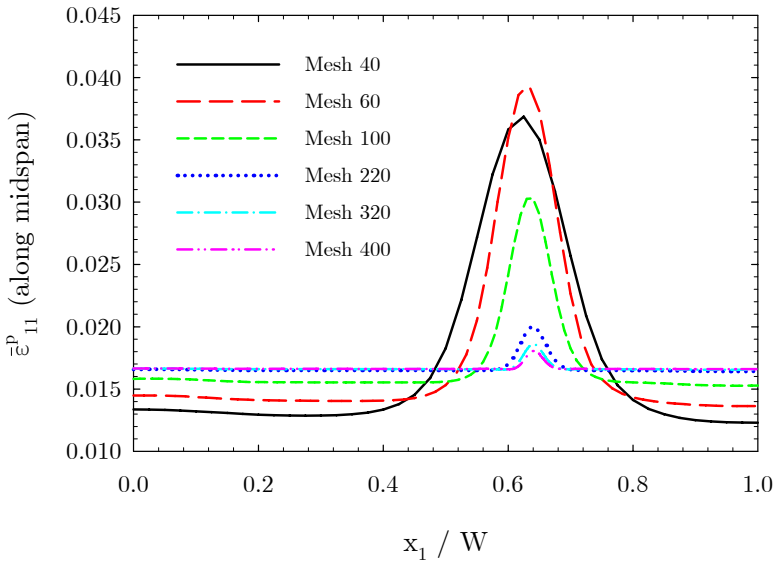

Figure 4.18: Distributions of $\bar{\varepsilon}^{p}_{11}$ versus normalized position along the midspan ($x_2 = H / 2$) of the strain-softening plate obtained using the micropolar crystal plasticity model for different FE discretizations.

To determine the rate of convergence for this local aspect of the deformation response, the peak value of $\overline{\varepsilon}_{11}^{\mathrm{p}}$ along the midplane of the plate for each mesh density is plotted as a function of normalized element size as shown in Figure 4.19(a). These results indicate that the convergence behavior is non-monotonic over the entire range of discretization sizes considered, and in fact the solution is seen to decrease in accuracy with mesh refinement when the normalized element size is in the range of $0.017 \leq h / W \leq 0.06$. However, below a certain critical size ($h / W = 0.012$) the solutions display the expected monotonic convergence behavior with further decreases in element size. Since an analytical solution is unavailable for this initial-boundary value problem, an estimated solution is obtained by extrapolating the converging series of results as shown in Figure 4.19(b). The extrapolated maximum value is calculated to be $\overline{\varepsilon}_{11}^{\mathrm{p}} = 0.017$, and the error in the FE simulations calculated based on this approximate solution are given in Figure 4.19(c) where a local error measure as introduced in Eq. (4.118) has been used. The order of convergence for the local response has been determined to be $p = 1.84$, and is in agreement with the convergence rates obtained for the previous validation problems given in Sections 4.3.1 and 4.3.2. Although, it is again pointed out that this convergence rate has been determined from a limited subset of the available FE simulation data. As a final demonstration of the convergent behavior of the FE solutions and also to contrast with the results from the classical theory given in Figure 4.16, contours of $\overline{\varepsilon}_{11}^{\mathrm{p}}$ for various FE discretizations obtained using the micropolar constitutive model are given in Figure 4.20. The contour plots reveal that as the mesh density is increased, unlike the FE results obtained using the classical theory, the width of the localization band stabilizes and no additional localization bands are formed.

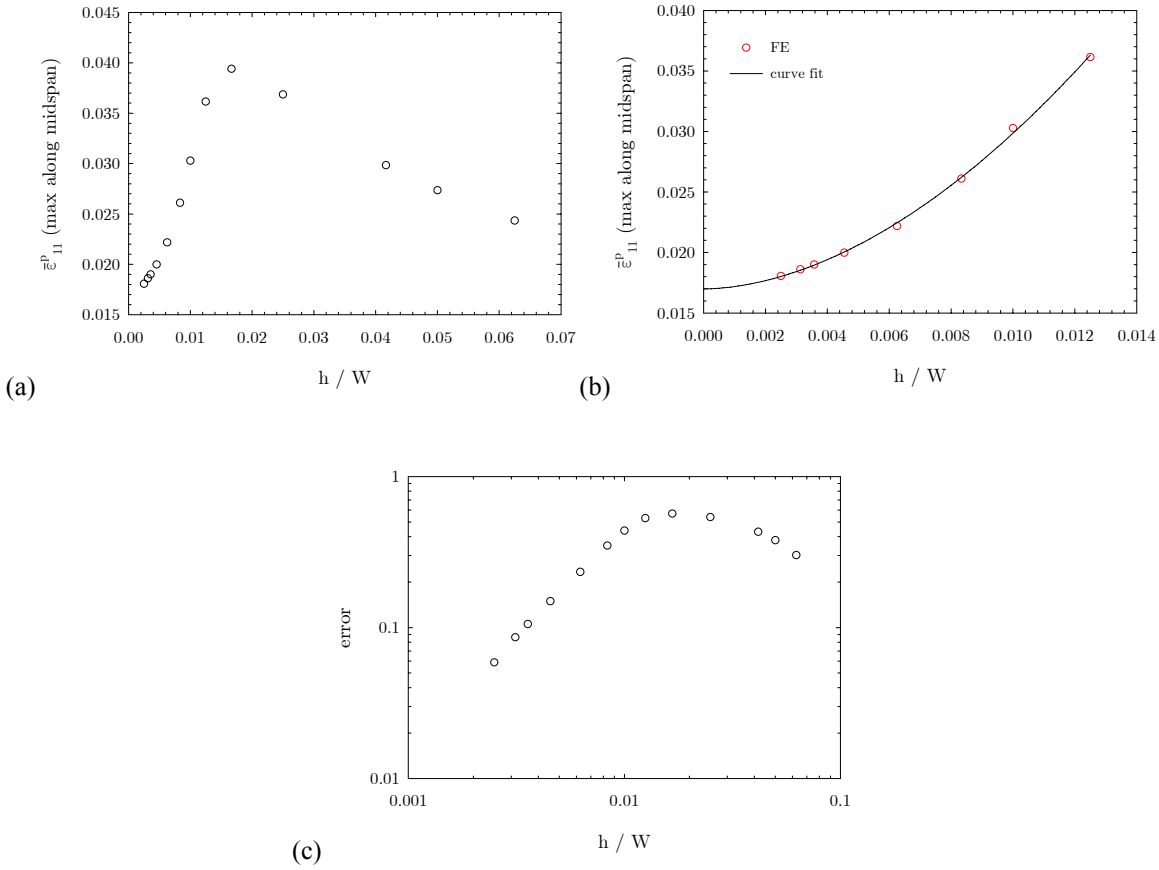

Figure 4.19: Local response and error analysis for the strain-softening plate obtained using the micropolar constitutive model (a) maximum value of $\bar{\varepsilon}^{p}_{11}$ along the midspan plotted versus normalized element size, (b) extrapolated solution for maximum value of $\bar{\varepsilon}^{p}_{11}$ along the midspan as determined from converging FE results and (c) error in FE simulations calculated with respect to the extrapolated solution.

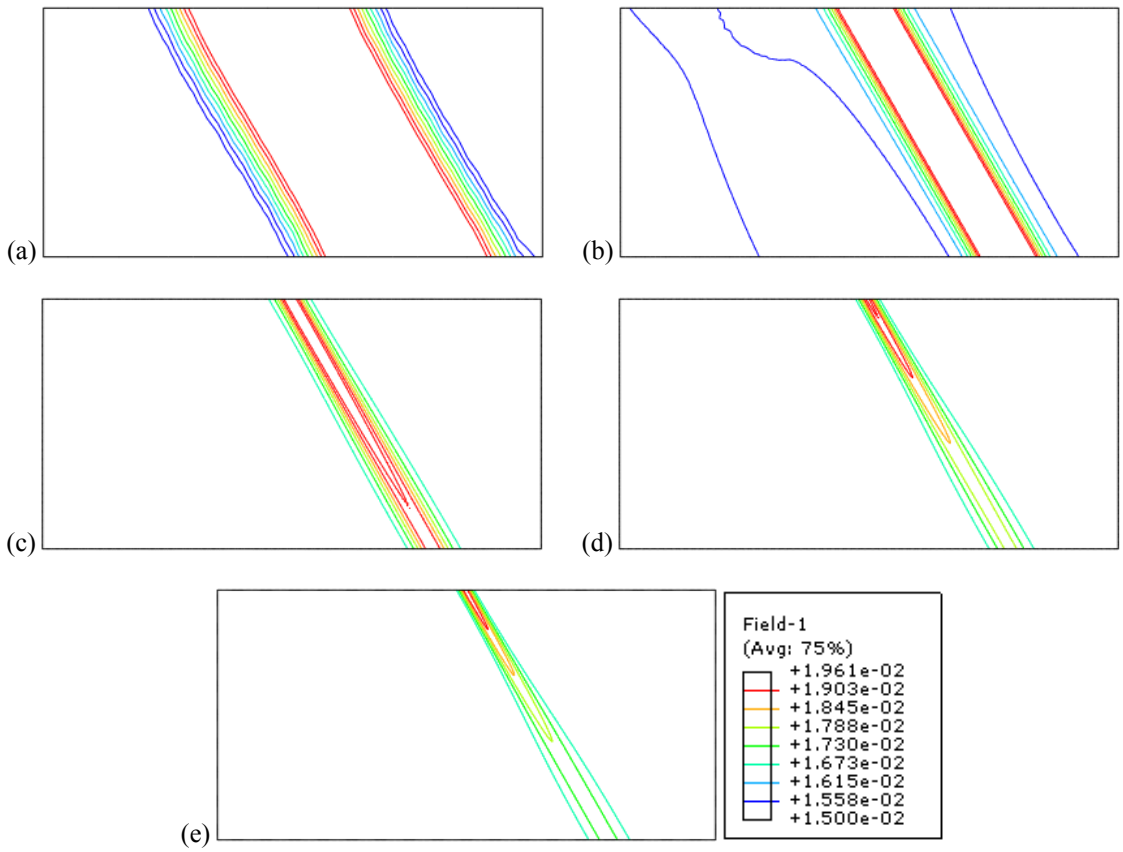

Figure 4.20: Contours of $\bar{\varepsilon}_{11}^{p}$ for the strain-softening plate obtained using the micropolar crystal plasticity model for select FE discretizations: (a) Mesh 20, (b) Mesh 100, (c) Mesh 220, (d) Mesh 320 and (e) Mesh 400.

4.4 Summary

This chapter has presented the development, implementation, and validation of a 2-D plane strain FE formulation of the micropolar single crystal plasticity theory given in Chapter 3. The governing equations for both bilinear quadrilateral (Q4) and linear triangle (LT) elements have been derived and discussed. A rate-tangent modulus integration scheme appropriate for the constitutive models introduced in Chapter 3 has been developed for both single and multicriterion flow criteria. The element-level equations have been implemented in the commercial FE software Abaqus/Standard [146] as a UEL subroutine, and the numerical implementation has been verified through a series of benchmarks and validation procedures

to ensure that the element performs as intended. The validation process has demonstrated that the element is functioning properly, and provides confidence in the results obtained for more complex initial-boundary value problems in the remainder of the research.

CHAPTER 5

NUMERICAL SIMULATIONS: SINGLE CRYSTALS

5.1 Introduction

This chapter presents an application of the micropolar single crystal elastic-viscoplastic constitutive formulations given in Chapter 3 to solve several prototypical initial-boundary value problems that frequently appear in the generalized continuum literature. Specifically, the problems to be considered are: (i) simple shearing of constrained thin films (ii) pure bending of thin films and (iii) simple shearing of metal matrix composite with stiff elastic inclusions. These particular initial-boundary value problems are appealing because there is a relatively large body of literature concerning their solution using both nonlocal continuum theories as well as discrete dislocation dynamics. As such, these related works give insight into the characteristics of the expected material response and provide valuable comparison points for the developed models. The chapter begins with an exploratory exercise in which various aspects of the different multi- and single criterion flow theories are compared and contrasted via the solution to the constrained shear problem. The intention is to gain an understanding not only of how results obtained from the two frameworks differ, but also to develop intuition as to how the non-classical material constants both qualitatively and quantitatively affect different aspects of the deformation behavior. With this knowledge in hand, the micropolar models are then calibrated to discrete dislocation dynamics simulations of equivalent initial-boundary value problems.

5.2 Constitutive Model Parametric Study and Comparison

The initial-boundary value problem of simple shearing of a constrained thin film, as considered in the numerical validation study in Chapter 4 for a purely elastic material, is studied here for an elastic-viscoplastic single crystal. The goal of this study is to systematically explore the influence of the non-

classical material parameters on the deformation behavior of the single crystal. The geometry and boundary conditions are identical to those considered in Chapter 4, and are given again in Figure 5.1 for ease of reference. The slip systems, denoted by the slip directions $\mathbf{s}^1$ and $\mathbf{s}^2$ in the figure, are separated by 60° and the crystal orientation is defined by the angle ϑ which is the angle between the x_1 axis and $\mathbf{s}^1$. The film has thickness, H, in the x_2-direction and is infinite in the x_1-direction. The bottom surface is rigidly clamped against displacements and microrotations, and a uniform displacement is applied at the top surface while the vertical displacement and microrotation are constrained. In each simulation, the films are subjected to an average macroscopic shear strain, $\Gamma = u^* / H = 0.03$, which is applied at a rate of $\dot{\Gamma} = 10^{-3}\ \mathrm{s}^{-1}$ and then unloaded back to zero strain at the same rate.

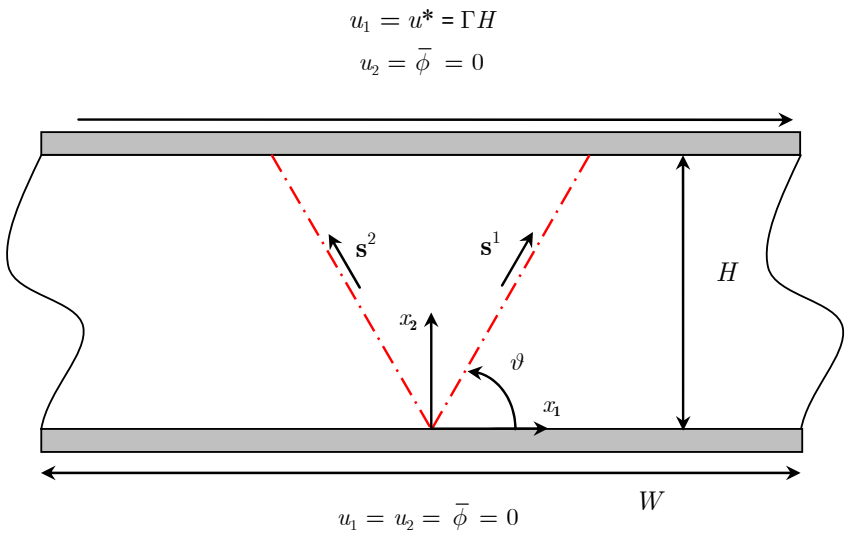

Figure 5.1: Geometry and boundary conditions for the constrained shear initial-boundary value problem.

The boundary conditions are stated as

$$u_1(x_1,0,t) = u_2(x_1,0,t) = \overline{\phi}(x_1,0,t) = 0 \tag{5.1}$$

$$u_1(x_1,H,t) = \Gamma(t)H \quad , \quad u_2(x_1,H,t) = \overline{\phi}(x_1,H,t) = 0 \tag{5.2}$$

$$\begin{gathered} u_1(+\tfrac{W}{2},x_2,t) = u_1(-\tfrac{W}{2},x_2,t) \quad , \quad u_2(+\tfrac{W}{2},x_2,t) = u_2(-\tfrac{W}{2},x_2,t) \\ \overline{\phi}(+\tfrac{W}{2},x_2,t) = \overline{\phi}(-\tfrac{W}{2},x_2,t) \end{gathered} \tag{5.3}$$

Due to the periodicity of the problem, a simple FE discretization is employed with 200 elements in the x_2-direction and a single element in the x_1-direction with appropriate boundary conditions applied to the x_1^+ and x_1^- faces (see Eq. (5.3)). The periodic boundary conditions are implemented in Abaqus via linear multi-point constraints.

Previous works that have studied this simple, yet illustrative initial-boundary value problem with generalized crystal plasticity models are those due to Shu et al. [160], Bittencourt et al. [23], Svendsen and Reese [161], Arsenlis et al. [78], Evers et al. [14], Sedlacek and Werner [79], Yefimov and Van der Giessen [162] Kuroda and Tvergaard [66], Roy and Acharya [95], Gurtin et al. [18], Hunter and Koslowski [163], and Limkumnerd and Van der Giessen [90]. The majority of these previous contributions have focused on comparing the nonlocal crystal plasticity simulation results to those obtained from the discrete dislocation dynamics simulations of Shu et al. [160], and such a comparison with respect to the micropolar models is presented in Section 5.3.1. Herein, the focus is on performing simulations to elucidate the various sources of material strengthening within the micropolar theory, their impact on the resulting deformation behavior, and to highlight the differences between the single and multicriterion formulations. Connections between the micropolar and alternative nonlocal crystal plasticity theories are made where possible.

Reducing the 3-D inelastic constitutive equations given in Chapter 3 to the problem at hand eliminates all terms associated with plastic torsion and therefore GN screw dislocations. As such, several of the non-standard material parameters are eliminated. As compared to an analogous classical crystal plasticity formulation, the number of additional model parameters needed to define the viscoplastic

response for the multi- and single criterion theories developed in Chapter 3 for the various strength models is summarized in Table 5.1, where the slip system superscripts have been suppressed for notational convenience and $h_{\perp}^{\alpha\beta}$ is the GND interaction matrix. It is clear from Table 5.1 that several additional material parameters are required to define the inelastic response for the multi- as compared to the single criterion model. To simplify matters, the following assumptions are made regarding the additional material parameters for the multicriterion model: $\dot{\varphi}_{\perp 0} = \dot{\gamma}_0$, $g_{\perp} = g$, $c_7 = c_1$, and $h_{\perp}^{\alpha\beta} = h^{\alpha\beta}$, and $n_{\perp} = m$. The remaining plastic curvature flow rule parameters, $L_{\perp}$ and $r_{\perp 0}$, are given on a case-by-case basis for each set of simulations. To facilitate comparisons with prior related studies [18, 23, 90, 160, 162], material parameters similar to those used by Shu et al. [160] have been employed. The set of fixed parameters is listed in Table 5.2 and the rest are explicitly stated during the discussion of the results, and it is noted that the interaction matrices, $h^{\alpha\beta}$, $h_{\perp}^{\alpha\beta}$, and $a^{\alpha\beta}$, are given by the second-order identity matrix, $\delta^{\alpha\beta}$. The majority of the simulations are performed with $\vartheta = 60°$ in accordance with the prior related works; however, this section concludes with a brief look at how the mechanical response changes for different crystal orientations. For ease of reference, the key features of the various multicriterion strength models are briefly recalled here (see Chapter 3 for full detail).

Multicriterion Version 1 (MCV1)

◊ Slip threshold is governed by a generalized Taylor relation, $r^{\alpha} = r_0^{\alpha} + \mu c_1 b\sqrt{\sum_{\beta} h^{\alpha\beta}(\varrho_S^{\alpha} + \varrho_G^{\alpha})}$.

◊ Curvature threshold is constant, $r_{\perp}^{\alpha} = r_{\perp 0}^{\alpha}$.

Multicriterion Version 2 (MCV2)

◊ Slip threshold is goverened by a generalized Taylor relation, $r^{\alpha} = r_0^{\alpha} + \mu c_1 b\sqrt{\sum_{\beta} h^{\alpha\beta}(\varrho_S^{\alpha} + \varrho_G^{\alpha})}$.

◊ Curvature threshold is governed by the GND density, $r_{\perp}^{\alpha} = r_{\perp 0}^{\alpha} + \mu c_7 b\sqrt{\sum_{\beta} h_{\perp}^{\alpha\beta}\left|\varrho_{G,\perp}^{\beta}\right|}$.

Multicriterion Version 3 (MCV3)

◊ Slip threshold is goverened by a generalized Taylor relation, $r^{\alpha} = r_0^{\alpha} + \mu c_1 b\sqrt{\sum_{\beta} h^{\alpha\beta}\varrho_S^{\alpha}}$.

◊ Curvature threshold is governed by the GND density, $r_{\perp}^{\alpha} = r_{\perp 0}^{\alpha} + \mu c_7 b\sqrt{\sum_{\beta} h_{\perp}^{\alpha\beta}\left|\varrho_{G,\perp}^{\beta}\right|}$.

Table 5.1: Nonlocal inelastic constitutive parameters that are required for the various micropolar models in addition to those that are needed to define an analogous local model.

Model	Nonlocal Inelastic Constitutive Parameters
Multicriterion Version 1	$L_{\perp}$, $\dot{\varphi}_{\perp 0}$, $r_{\perp 0}$, $g_{\perp}$, $n_{\perp}$
Multicriterion Versions 2 & 3	$L_{\perp}$, $\dot{\varphi}_{\perp 0}$, $r_{\perp 0}$, c_7, $h_{\perp}^{\alpha\beta}$, $g_{\perp}$, $n_{\perp}$
Single Criterion Model	$L_{\perp}$

Table 5.2: Fixed material parameters used in the parametric study of the constrained shear simulations for an elastic-viscoplastic single crystal.

Parameter	Symbol	Magnitude	Unit
Shear modulus	μ	26.3	GPa
Poisson's ratio	ν	0.33	-
Coupling parameter	N_c	0.95	-
Reference slip threshold stress	r_0	0	MPa
Threshold stress strength coefficients	c_1, c_7	0.5	-
Burgers vector magnitude	b	0.3	nm
Dislocation interaction coefficients	$h^{\alpha\beta}, h_{\perp}^{\alpha\beta}$	$\delta^{\alpha\beta}$	-
Initial SSD density	ϱ_{S0}	10.5	μm^{-2}
Dislocation immobilization coefficients	$a^{\alpha\beta}$	$\delta^{\alpha\beta}$	-
Dislocation capture radius	y_c	0	nm
Reference slip and curvature rates	$\dot{\gamma}_0, \dot{\varphi}_{\perp 0}$	10^{-3}	s^{-1}
Slip and curvature drag stresses	$g, g_{\perp}$	5	MPa
Inverse rate sensitivity exponents	$m, n_{\perp}$	20	-

The following series of simulations are performed in a sequential and selective manner to individually highlight the different sources of material strengthening. In order to restrict the nonlinear stress-strain response to that caused by the influence of GNDs, the dynamic recovery term in the SSD evolution equation has been suppressed ($y_c = 0$). The results are quantified by the average shear stress-strain response as well as the local distributions of shear strain ($u_{1,2}$) and GND density as functions of normalized film depth. The stress-strain response is characterized by the normalized surface traction, T / τ_0, (calculated from the nodal reaction forces) where $\tau_0 = 50$ MPa is the nucleation source strength used in the discrete dislocation simulations [160] and the applied shear strain, Γ . From this point forward, the notational substitution $L_p \equiv L_\perp$ is made, and all single criterion results shown are for an effective stress exponent $p = 2$.

Linear Gradient-Induced Kinematic Hardening $\{\ell_e \geq 0,\ K = 0\}$

Figure 5.2 shows the average shear stress-strain response and shear strain distributions as functions of normalized film depth, respectively, for a material where only linear kinematic hardening is active and the film thickness is taken to be $H = 1$ μm. This strengthening description is achieved by suppressing slip threshold hardening and plastic-torsion curvature effects. The plastic torsion-curvature is suppressed within the multicriterion framework by specifying an infinite initial plastic curvature threshold ($r_{\perp 0} = \infty$), and alternatively within the single criterion framework by specifying a large value of L_p / ℓ_e, i.e., $L_p / \ell_e = 1000$. The multi- and single criterion models yield the same deformation behavior under these conditions, and all of the material hardening is due to the elastic curvature effects entering via the back stress term. Increasing the elastic length scale leads to an increased hardening rate with the tangent modulus scaling linearly with ℓ_e^2. When $\ell_e = 0$ the stress-strain response is elastic-perfectly plastic since this choice suppresses the curvature-induced back stress. The elastic-plastic transition in both forward and reverse loading is quite sharp for all of the cases considered, and is due to the absence of slip threshold hardening. As shown in Figure 5.2(b), when $\ell_e > 0$, the strain profiles at the maximum applied strain are

parabolic and although the average stress-strain responses vary quite substantially, there is little discernable difference in their shapes and peak magnitudes. Upon unloading, all of the shear strain distributions for non-zero elastic length scales are tightly centered about zero, which is to be contrasted with the case of $\ell_e = 0$, where locally negative shear strains on the order of 7.5×10^{-3} are present in the near boundary regions. This type of kinematic hardening is analogous to the so-called "energetic-gradient hardening" of the Gurtin-type models; however, it is noted that in the absence of such hardening ($\ell_e = 0$) the micropolar theory does not predict a uniform distribution of strain as does theirs, as shown in Gurtin et al. [18] (see Figure 5.3). The simulation results presented from the work of Gurtin et al. [18] were carried out using different sets of material parameters, so attention is focused on the trends in behavior as opposed the actual magnitudes of the response variables.

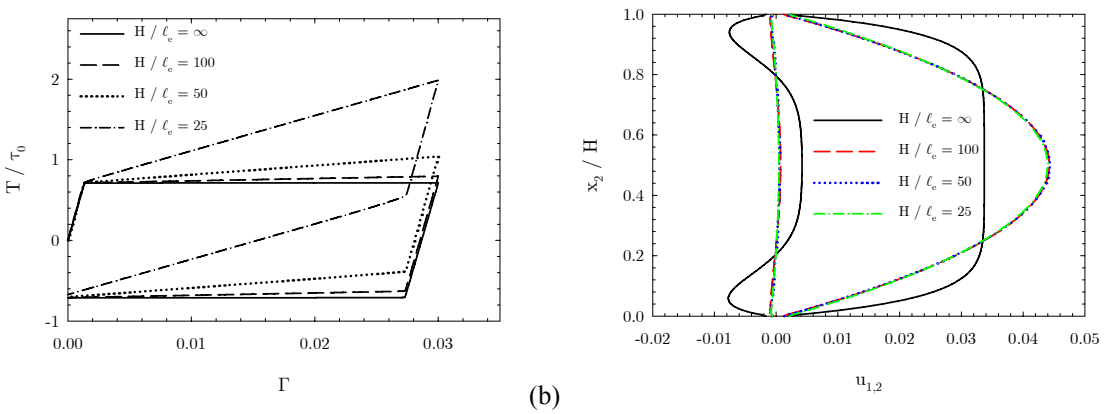

Figure 5.2: (a) Average stress-strain response and (b) shear strain distributions at $\Gamma = 0.03$ and after unloading for different values of the elastic length scale. Slip threshold hardening and plastic curvature are suppressed.

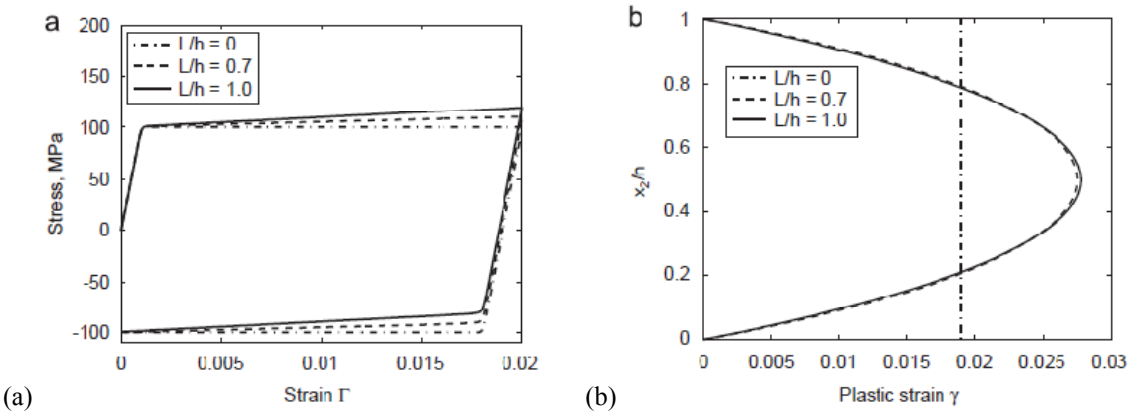

Figure 5.3: (a) Average shear stress-strain curves and (b) plastic shear strain distribution at $\Gamma = 0.02$ with "energetic-gradient" hardening, but not "dissipative-gradient" strengthening or slip resistance hardening as reported by Gurtin et al. [18].

<u>Linear Slip Threshold Hardening</u> $\{\ell_e = 0,\ K \geq 0\}$

Figure 5.4 shows the average shear stress-strain response and shear strain distributions as a function of normalized film depth, respectively, for a material with only linear slip threshold hardening active. This hardening description is achieved by suppressing the elastic length scale effects ($\ell_e = 0$) and the plastic curvature evolution. As in the case of linear kinematic hardening, the multi- and single criterion models give the same deformation behavior under these conditions, and the rate of linear hardening is quantified by the parameter, $A = c_1\mu / 2K$. Distinct from the stress-strain response for the linear kinematic hardening material, the elastic-plastic transition upon reverse yielding for a linear slip threshold hardening material is more gradual and becomes more pronounced with increases in the hardening rate. This difference in behavior is due to the differential yielding of the film upon reverse loading, and was previously pointed out by Kuroda and Tvergaard [13] but from the perspective of slip gradient-based models of crystal plasticity. Figure 5.4(b) shows that the strain profiles become more blunted and the boundary layer width decreases with increases in the hardening rate. The narrowing of the boundary layer is also apparent from inspection of the profiles at zero applied strain where the "jets" of locally negative strains become more compressed as the rate of hardening increases. As noted by Kuroda and Tvergaard [13], the decrease of the boundary layer width with increasing hardening rates is the result of a more

uniform distribution of effective film strength. The imposition of the microhard boundary conditions leads to the boundary regions being significantly more resistant to deformation than the bulk (as evidenced by the shear strain distributions), but as the slip threshold hardening rate is increased, the disparity between the bulk and boundary layer region diminishes leading to more uniform plastic flow. Similar trends are observed within the Gurtin-type framework [23] for changes in the slip threshold hardening (see Figure 5.5).

To this point, the two sources of linear material hardening within the micropolar framework have been demonstrated. As with any type of constitutive model featuring combined isotropic and kinematic hardening, information concerning other aspects of the deformation behavior in addition to the unidirectional loading response is needed to properly calibrate the model. For example, consider the stress-strain curves in Figure 5.6(a) which are identical under forward loading. The material constants have been specified for two different scenarios - one in which kinematic hardening dominates ($H / \ell_e = 50$; $A / \tau_0 = 2.5$) and the other where slip threshold hardening ($H / \ell_e = 200$; $A / \tau_0 = 8$) is dominant. This illustrative example underscores the importance of considering multiple aspects of the deformation fields, including unloading behavior, when determining the material parameters for the micropolar and other types of generalized crystal plasticity theories.

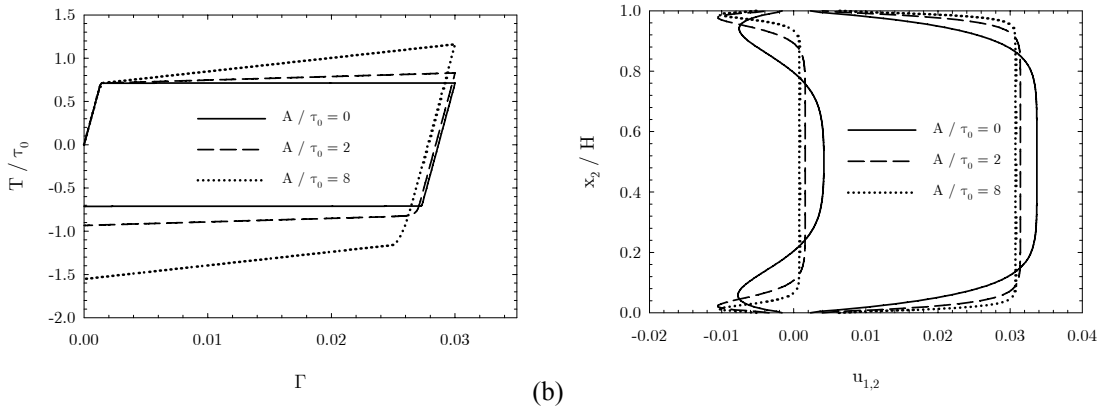

Figure 5.4: (a) Average shear stress-strain response and (b) shear strain distributions at $\Gamma = 0.03$ and after unloading for different linear slip threshold hardening coefficients. Elastic length scale hardening and plastic curvature are suppressed.

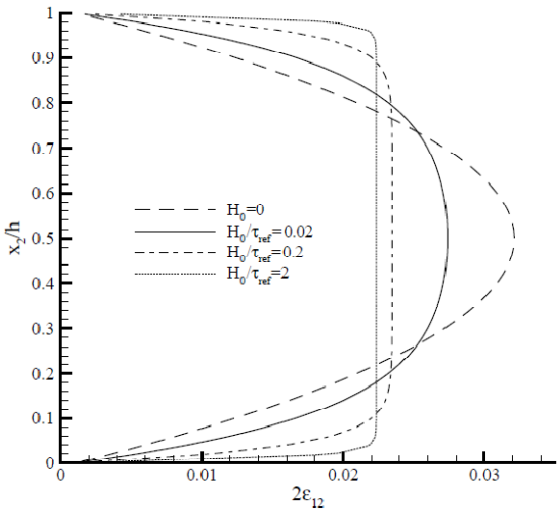

Figure 5.5: Shear strain distributions at $\Gamma = 0.0218$ for various values of linear slip resistance hardening, H_0 / τ_{ref}, as reported by Bittencourt et al. [23].

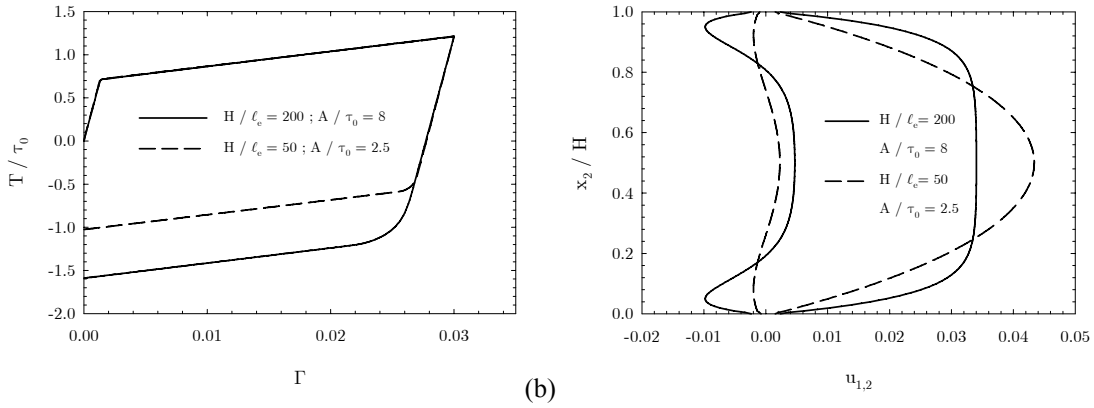

(a) (b)

Figure 5.6: (a) Average shear stress-strain response and (b) shear strain distributions at $\Gamma = 0.03$ and after unloading for two combinations of material properties that give identical stress-strain responses up to the point of reverse yielding. Plastic curvature is suppressed.

<u>Nonlinear Gradient-Induced Kinematic Hardening</u> $\{\ell_e > 0, 5 \leq L_p / \ell_e \leq 20,\ K = 0\}$

As discussed in Chapter 3, when plastic curvature is activated a gradient-induced nonlinear kinematic hardening effect results and is mainly controlled by the elastic and plastic length scale

parameters, although in the case of the multicriterion model the additional viscoplastic torsion-curvature parameters will also have an influence, especially the torsion-curvature threshold stresses. The nonlinear kinematic hardening response is controlled by two main material parameters: the effective film thickness, H / ℓ_e, and the ratio of plastic to elastic length scale, L_p / ℓ_e. The magnitude of the elastic length scale, ℓ_e, dictates the initial kinematic hardening modulus, and the ratio L_p / ℓ_e determines the transient response. The multi- and single criterion models behave differently when plastic torsion-curvature is activated; this is due to the fundamental difference in which they are formulated. Namely, the multicriterion model employs separate kinetic equations for slip and plastic torsion-curvature, whereas the single criterion model is defined in terms of single kinetic equation. To illustrate the differences between the two models and to highlight the influence of the controlling material parameters, two sets of simulations are considered. In the first set, a fixed value of $L_p / \ell_e = 5$ is considered for different relative film thicknesses, and the second examines a material with fixed relative film thickness, $H / \ell_e = 20$, for different ratios of the plastic to elastic length scale. Slip and curvature threshold hardening is suppressed in both sets of simulations. This constitutive description is achieved within the multicriterion framework by using strength model version 3 and by setting $c_2 = 0$.

The stress-strain response for the first set of simulations is shown in Figure 5.7(a) for both the multi-(black) and single (red) criterion models for three different values of the elastic length scale. Since there is no distinction between the threshold for plastic slip and torsion-curvature in the single criterion model, the plastic curvature threshold stress for the multicriterion model has been chosen such that plastic curvature initiates simultaneously with slip to make the comparison between the two models meaningful. As such, different plastic curvature thresholds are used for each elastic length scale considered and are given as $r_{\perp 0} =$ 0, 2.25, and 2.9 MPa, respectively, for $H/\ell_e =$ 1000, 20, and 10. The stress-strain curves show that the hardening response saturates more quickly for the multi- as compared to the single criterion model, and that the differences between the two become more pronounced for larger elastic length scales. This type of hardening is similar to, although not strictly analogous to, the "dissipative-gradient strengthening" in the model of Gurtin et al. [18] in that it results in increases in the (offset) yield strength

for larger values of the elastic length scale. The distinction between the two strengthening effects is that there is a change in the initial *offset* yield strength that arises due to the elastic length scale kinematic hardening in the micropolar model, whereas in the model of Gurtin et al. [18], as shown in Figure 5.8, there is a change in the proportional limit.

Further differences between the two model results are seen in the shear strain and GND density distributions, as shown in Figure 5.7 (b) and (c), respectively. The strain profiles for the multicriterion model are nearly identical for the two length scales shown and are characterized by largely uniform strain distributions with a narrow boundary layer on the order of approximately $0.08\,H$. On the other hand, the strain profiles predicted by the single criterion model have a parabolic shape with a boundary layer on the order of $0.02\,H$. The maximum local shear strain is observed to decrease with increases in the elastic length scale for both models, but this effect is more pronounced for the single criterion model results. It is rather surprising to see such uniform shear strain profiles predicted by the multicriterion model for a constitutive description that does not include slip threshold hardening. Given the results shown in Figure 5.2 and Figure 5.4, it was anticipated that the shear strain profiles would have a parabolic shape. Further investigation of the shear strain profiles as a function of the applied deformation obtained using the multicriterion model reveal that they do have a parabolic shape up until an applied macroscopic strain of $\Gamma = 0.01$, at which point they begin to blunt and transition into the shape shown in Figure 5.4(b). This behavior could be rationalized in some sense as a deterioration of the elastic length scale effects, as evidenced by the saturation of the stress-strain curve; however, this does not explain why a similar trend is not observed for the results of the single criterion model. The GND distributions, shown in Figure 5.4(c), are not markedly different for either choice of elastic length scale or model type. The key distinction between the GND density distributions for the multi- as compared to the single criterion model are the aforementioned differences in boundary layer width, as well as the bilinear variation of the GND density between the two boundary layers that is displayed for the single criterion model. In contrast, there is a region of zero GND density connecting the two boundary layers for the multicriterion model.

The stress-strain responses for the second set of simulations are shown for the single and multicriterion models in Figure 5.9(a) and (b), respectively for a fixed elastic length scale and three values of L_p / ℓ_e. As in the previous simulations, the plastic curvature threshold stress has been specified such

that plastic curvature initiates simultaneously with slip. In Figure 5.9, the stress-strain responses for the three selected values of L_p / ℓ_e are plotted along with the curve for linear gradient-induced kinematic hardening for comparison purposes. Increasing the plastic length scale leads to a higher saturation stress, and also to slower developing transients which increase noticeably in duration for the single criterion model. On the other hand, the transition from the initial hardening rate to the saturation stress level is rather abrupt in the responses obtained from the multicriterion model. The shear strain and GND distributions for these simulations are not shown for the sake of brevity as the individual variations for increases in L_p for each class of model are rather moderate. The general trends predicted by the single and multicriterion models for these distributions are qualitatively similar to those shown in Figure 5.7(b) and (c), respectively.

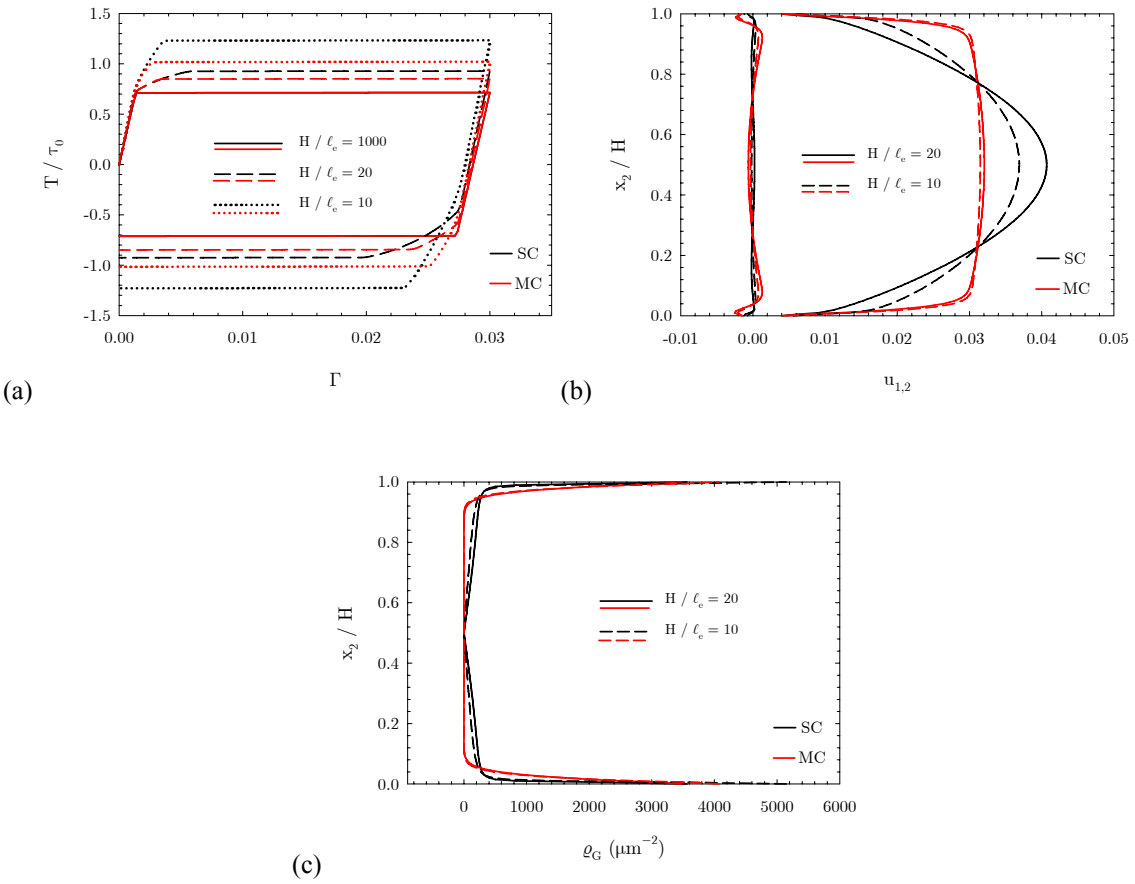

Figure 5.7: (a) Average shear stress-strain response (b) shear strain distributions at $\Gamma = 0.03$ and after unloading and (c) GND density distribution for different elastic length scales with a fixed value of $L_p \,/\, \ell_e = 5$. Slip and curvature threshold hardening is suppressed.

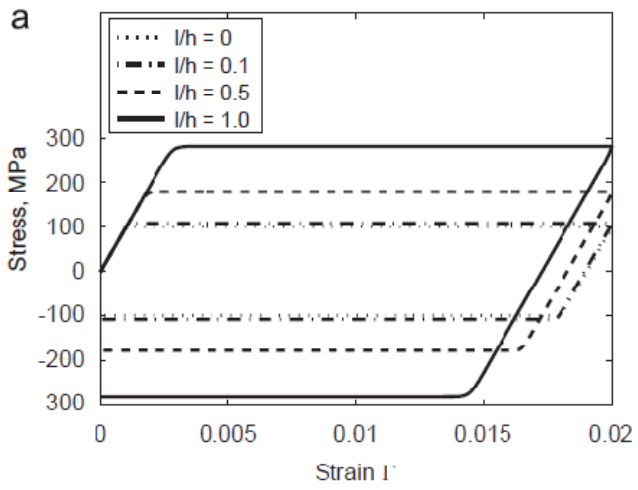

Figure 5.8: Average shear stress-strain response for the constrained shear problem at $\Gamma = 0.02$ predicted by a Gurtin type model of generalized single crystal plasticity for different values of dissipative-gradient strengthening, $l / h \geq 0$, but no energetic-gradient hardening or slip resistance hardening as reported in [18].

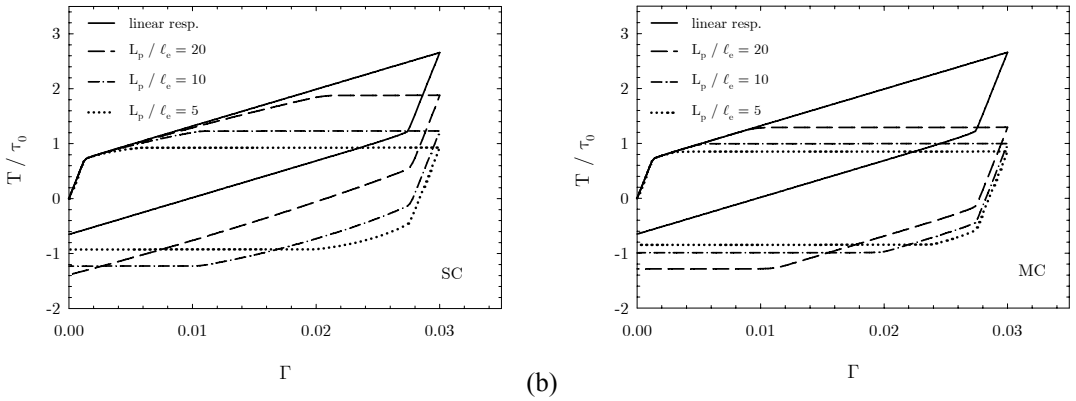

Figure 5.9: Average shear stress-strain response predicted by the (a) single and (b) multicriterion models for different values of L_p / ℓ_e for a fixed elastic length scale, $H / \ell_e = 20$. Slip and curvature threshold hardening is suppressed.

All Hardening Components Active $\{\ell_e = 20 \text{ nm},\ L_p = 100 \text{ nm},\ K = 50,\ r_{\perp 0} = 2\}$

Previously, the various material strengthening mechanisms have been isolated and examined with respect to their influence on the deformation behavior of the constrained thin film. The following set of simulations explores the full model capabilities for the single criterion model and the three versions of multicriterion model presented in Chapter 3. In the earlier studied carried out using the multicriterion model, the initial plastic curvature threshold was changed on a case-by-case basis to ensure that plastic curvature and slip initiated simultaneously; however, in these simulations a fixed value is used, $r_{\perp 0} = 2$ MPa. This value has been chosen such that the activation of plastic curvature and slip coincides for the smallest effective film thickness, $H / \ell_e = 20$, and this means that slip will precede plastic curvature for the thicker films. In comparing the models, attention is focused on the stress-strain response and the local distributions of shear strain, SSD density, and GND density. The constitutive model used for each set of results is indicated in the lower right hand corner of the plots, e.g., single criterion (SC), muli-criterion strength model version 1 (MCV1), etc.

The stress-strain curves for the various models are shown in Figure 5.10, and it is seen that model MCV1 displays the most pronounced size-dependence while the SC model exhibits the least. The most interesting stress-strain responses are obtained for the MCV1 model (see Figure 5.10(b)) and they are characterized by an extraordinary amount of slip threshold hardening that arises because of the slip threshold dependence on the GND density and the absence of curvature threshold hardening which leads to much higher GND densities as compared to the other models. The stress-strain curves for the MCV1 model display a noticeable concavity around an applied macroscopic strain of 0.003-0.006 and exhibit a softening behavior during reversed loading in the post-yield regime. This behavior is atypical as compared to that of the other constitutive models, and is be due to material instabilities caused by the lack of curvature threshold hardening. As shown in Figure 5.10(b) and (c), respectively, the stress-strain responses for the MCV2 and MCV3 models are qualitatively quite similar, and the main difference between the two is that the MCV2 leads to stiffer material behavior due to the GND contribution to slip threshold hardening. This additional slip threshold hardening for the MCV2 model also leads to a much more rounded elastic-

plastic transition as compared to the MCV3 model and is a manifestation of more pronounced differential yielding.

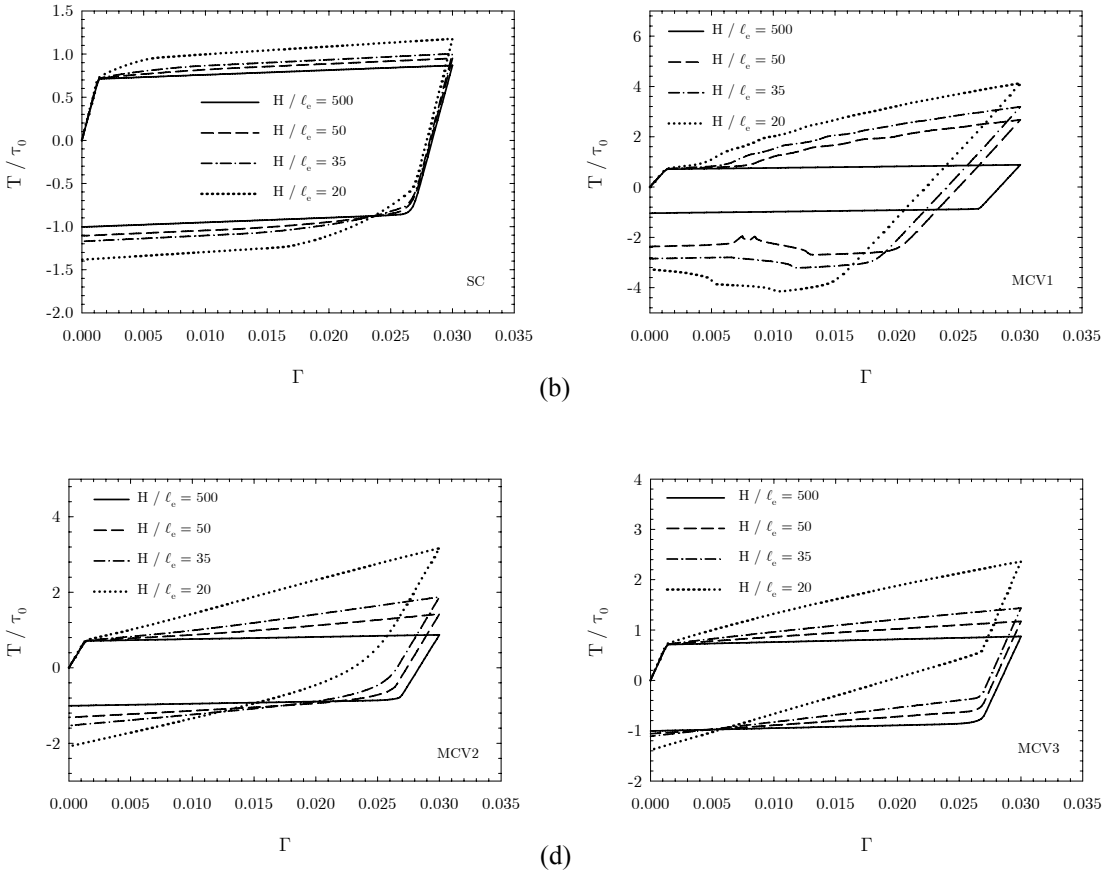

Figure 5.10: Average shear stress-strain responses predicted by the (a) single and multicriterion (b) version 1 (c) version 2 and (d) version 3 for fixed elastic length scale, $\ell_e = 20$ nm, and fixed value $L_p / \ell_e = 5$ for different film thicknesses.

The shear strain profiles are shown in Figure 5.11 for the different models at the maximum applied macroscopic strain, $\Gamma = 0.03$. As might be expected, the most interesting results are obtained for the MCV1 model which shows pointed, triangular shaped profiles for the three thinnest films. This result is to be contrasted to those of the other models, which are characterized by parabolic strain profiles. The peculiar result for the MCV1 model is again due to the combined effect of having the slip threshold stress depend on the GND density without including plastic curvature hardening which would otherwise retard the generation of GNDs. Comparing the strain fields from the MCV1 (Figure 5.11(b)) and the MCV2 (Figure 5.11(c) models, it is seen that, although the strain profiles for the MCV2 model are slightly more pointed than those for the SC and MCV3 models, the evolution into the triangular shape has been prevented by including curvature threshold hardening into the constitutive description. The shear strain profiles for the SC and MCV3 models are practically identical, and do not exhibit any unexpected or noteworthy features.

Attention is now turned to the dislocation density distributions shown in Figure 5.12 (SSD) and Figure 5.13 (GND) for the various models. Unlike the shear strain distributions, the dislocation density distributions have distinct features and trends for each model considered. In what follows, the discussion will neglect the results for the thickest film, $H / \ell_e = 500$, since all of the models are equivalent for diminishing scale effects. The SSD distributions for the SC model shown in Figure 5.12(a) have the shape of the capital Greek letter sigma, and this shape, rather than a parabolic profile, is a result of $\dot{\varrho}_S$ being defined in terms of the equivalent slip system deformation rate in the SC model. For thinner films, the maximum value of the SSD density occurs at the boundary, whereas for thicker films it occurs in the central region. Excluding the differences that are observed in the near boundary regions that are caused by the additional accumulation of SSDs due to plastic curvature, the SSD density profiles do not vary appreciably with changes in film thickness. Much like the strain profiles, the SSD density distributions for the MCV1 model are triangular in shape but contain pronounced dimples centered about the midline of the film as shown in Figure 5.12(b). These dimples are due to diminished SSD storage in the central region of the film because this region is GND density-free as shown in Figure 5.13(b), and in contrast to the SC model the SSD density profiles for the MCV1 model away from the boundaries is strong function of film thickness with thinner films being characterized by higher maximum values of SSD density (at the edge of

the dimples). Additionally, the maximum SSD densities for any given film thickness are 1.5-2 times higher for the MCV1 model as compared to the other models. In contrast to the other models, the morphology of the SSD density distributions predicted by the MCV2 model varies as a function of film thickness. As the effective film thickness, H / ℓ_e, is decreased from 50 to 35 the SSD density distribution transitions from a parabolic to a blunted shape, and the profile for the thinnest film is bimodal with off-centered twin peaks separated by a dimpled center region that is similar to but not as pronounced as that observed for the MCV1 model. The SSD density distributions obtained using the MCV3 model are parabolic in shape and do not strongly depend on the film thickness as shown Figure 5.12(d). A comparison of the SSD and GND density distributions for a given film thickness reveals that the maximum GND densities are 1-2 orders of magnitude higher than the SSD densities for all constitutive models, and it is also seen that the peak GND densities for the SC and MCV1 models are approximately an order of magnitude higher than those obtained from the MCV2 and MCV3 models.

The GND density distributions predicted by all models except for MCV1 display the same general trend: the maximum values occur at the boundary due microhard boundary condition, and then transition to zero GND density at the central region of the film. The nature of this transition is model dependent. In the case of the SC model (see Figure 5.13(a)), there is a steep gradient in GND density in the near boundary region ($\leq 0.1\,H$) which transitions to a zone characterized by milder GND density gradients that connects the boundary layer to the GND density-free zone at the midsection of the film. On the other hand, the GND density profiles for the MCV1 (see Figure 5.13(b)) model exhibit a boundary layer region also characterized by strong GND density gradients, but then maintain a nearly constant, albeit oscillatory, value of GND density between the boundary layer and midsection of the film. As discussed with regard to the earlier results, this is due to the lack of plastic curvature hardening which leads to these abrupt transitions and oscillatory behavior. The GND density profiles for the MCV2 (Figure 5.13(c)) and MCV3 (Figure 5.13(d)) models are similar in morphology to those of the SC model. The profiles for the MCV2 model are characterized by stronger transitional gradients between the boundary layer and GND density-free zone and slightly lower peak GND densities as compared to those for the MCV1 model which feature more gradual gradients and have parabolic shape.

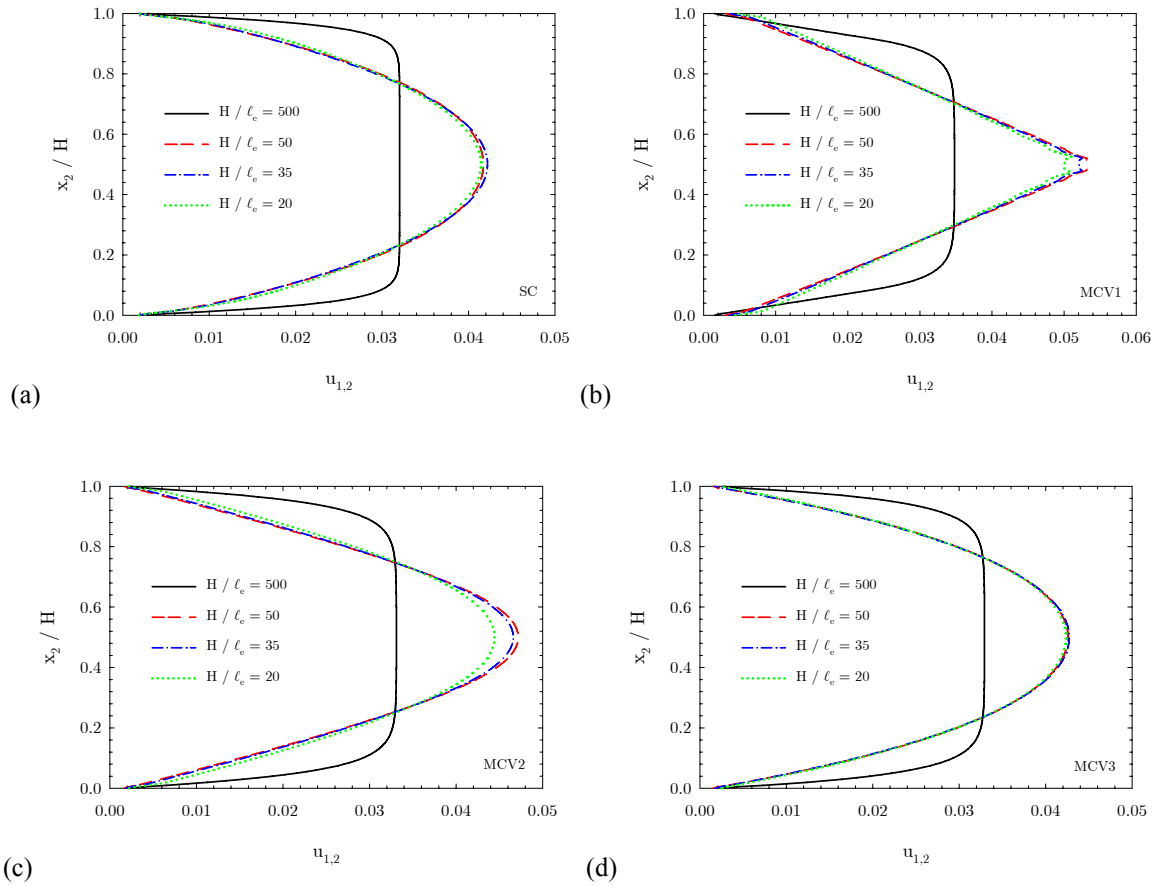

Figure 5.11: Shear strain distributions at $\Gamma = 0.03$ predicted by the (a) single and multicriterion (b) version 1 (c) version 2 and (d) version 3 for fixed elastic length scale, $\ell_e = 20$ nm, and fixed ratio $L_p \,/\, \ell_e = 5$ for different film thicknesses.

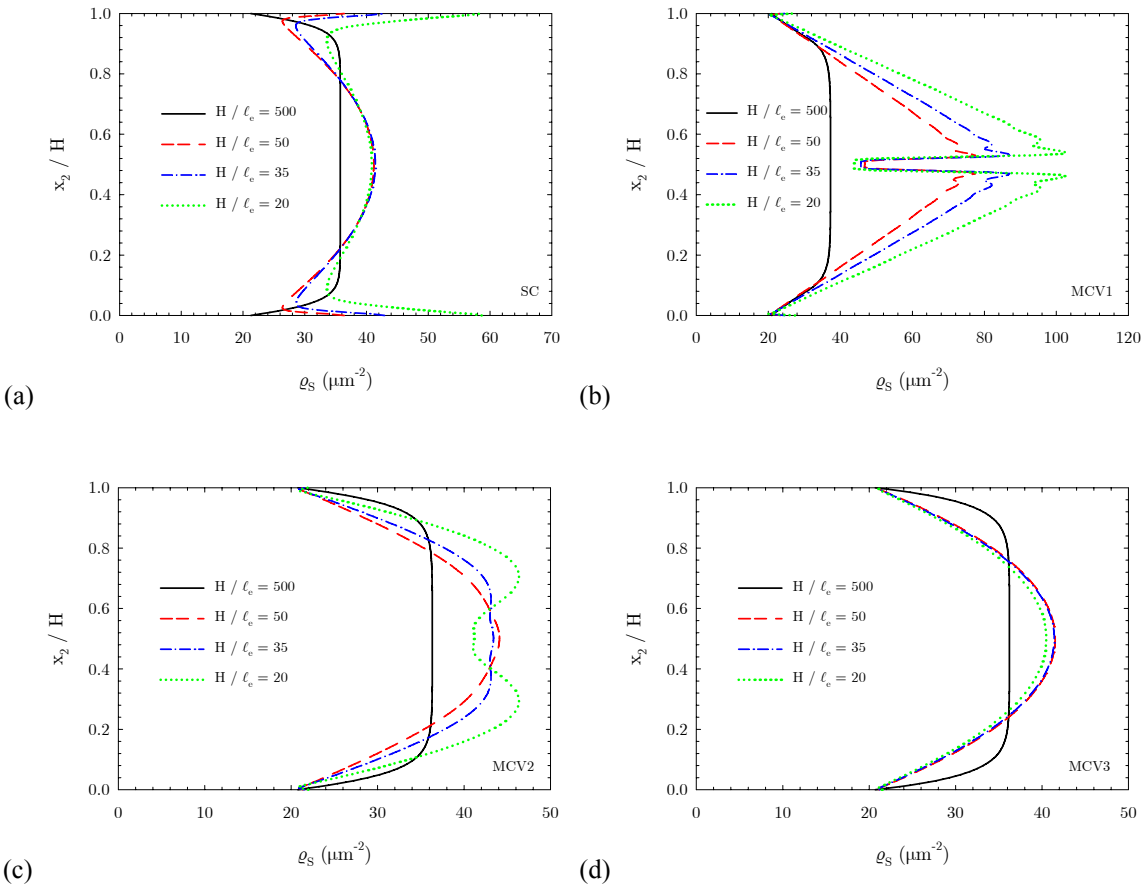

Figure 5.12: SSD density distributions at $\Gamma = 0.03$ predicted by the (a) single and multicriterion (b) version 1 (c) version 2 and (d) version 3 for fixed elastic length scale, $\ell_e = 20$ nm, and fixed ratio $L_p / \ell_e = 5$ for different film thicknesses.

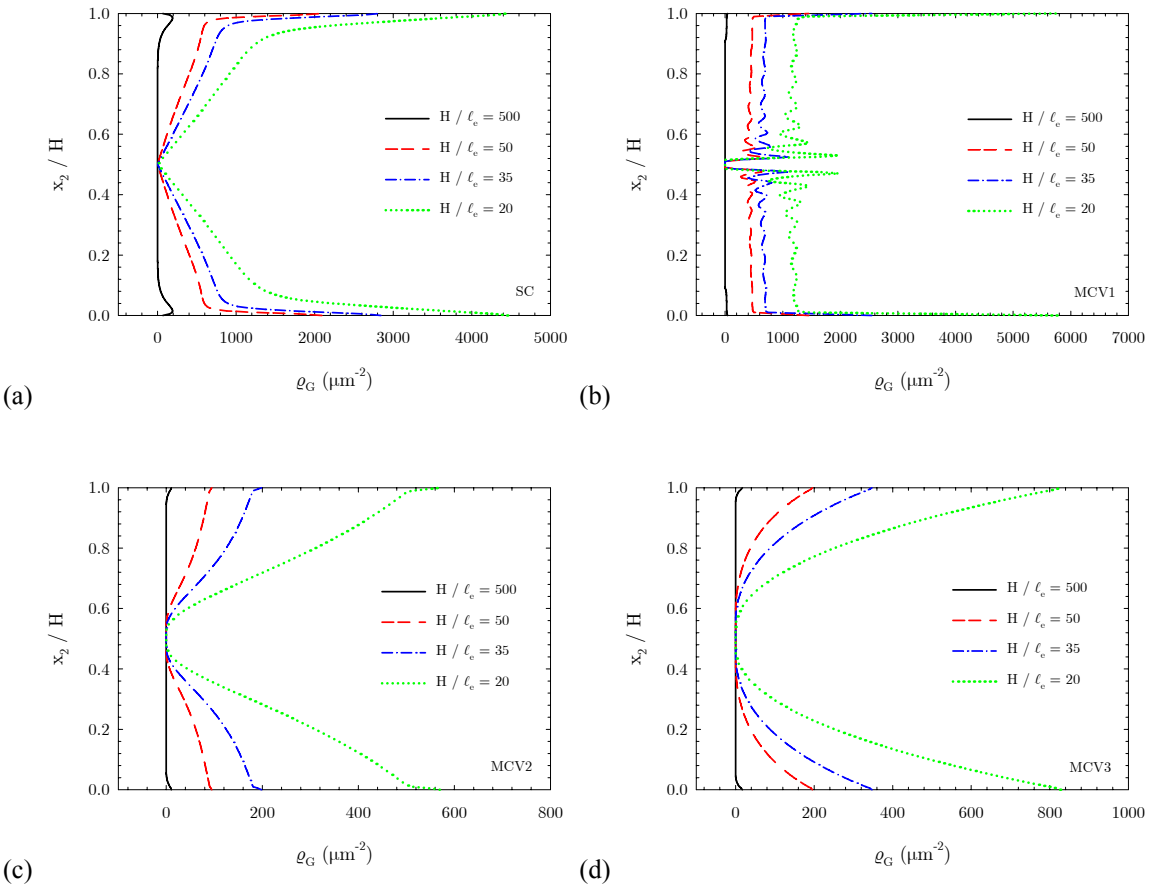

Figure 5.13: GND density distributions at $\Gamma = 0.03$ predicted by the (a) single and multicriterion (b) version 1 (c) version 2 and (d) version 3 for fixed elastic length scale, $\ell_e = 20$ nm, and fixed ratio $L_p / \ell_e = 5$ for different film thicknesses.

To conclude this section, the dependence of the mechanical response on crystal orientation is investigated using the SC model and the same material parameters as in the previous study. In related works that give solutions to the constrained shear problem [14, 18, 23, 90, 160, 162], the orientation dependence of the mechanical response is largely neglected. Typically, attention is focused solely on the 60° orientation because this is the configuration for which discrete dislocation dynamics results are readily available. These simulations are intended to demonstrate that: (i) for a given film thickness the stress-strain curves for different crystal orientations have different characteristic features and (ii) the magnitude of the size-dependent behavior is a function of the crystal orientation.

The shear stress-strain curves for a 400 nm thick film are shown below in Figure 5.14 for five different slip system orientations (see Figure 5.1) spanning the range from symmetrically aligned about the x_1-axis ($\vartheta = $-30°) to symmetrically aligned about the x_2-axis ($\vartheta = 60°$), and the corresponding shear strain, SSD and GND density distributions are given in Figure 5.15. In addition to the variations in initial yield strength which are due to having more favorably aligned slip systems with higher Schmid factors for certain orientations, it is seen that the shapes of the stress-strain curves also vary with orientation. For example, for $\vartheta =$ -30° and 15° the elastic-plastic transition is abrupt indicating that there is not a large component of gradient-induced kinematic hardening for these orientations. This is further confirmed through inspection of the GND density distributions for these orientations shown in Figure 5.15(c) which are much smaller in magnitude than for the 37.5° and 60° orientations. For these orientations, a strong nonlinearity is observed after initial yield due to gradient-induced back stresses. A somewhat unexpected result is observed for the $\vartheta =$ -7.5° orientation, where the stress-strain curve shows some mild nonlinearity just after initial yield, yet the GND density is negligible and this is out of character with what would be anticipated in light of such behavior. At first, it was unclear as to what caused this transitional region since the current mechanistic understanding of the model could not be used to explain the relationship between the distributions of the local deformation fields and the stress-strain response for this orientation. Recognizing that the shear strain profile is distinctly different for this orientation as compared to the others, there was a motivation to look more in-depth at the deformation fields which revealed that for this orientation the film is deforming predominantly via single slip. This explains the observed stress-strain behavior as single slip is a type of constrained deformation mode which leads to an apparent strengthening

effect due to the incompatibility of the slip system orientation with respect to the direction of the applied displacement.

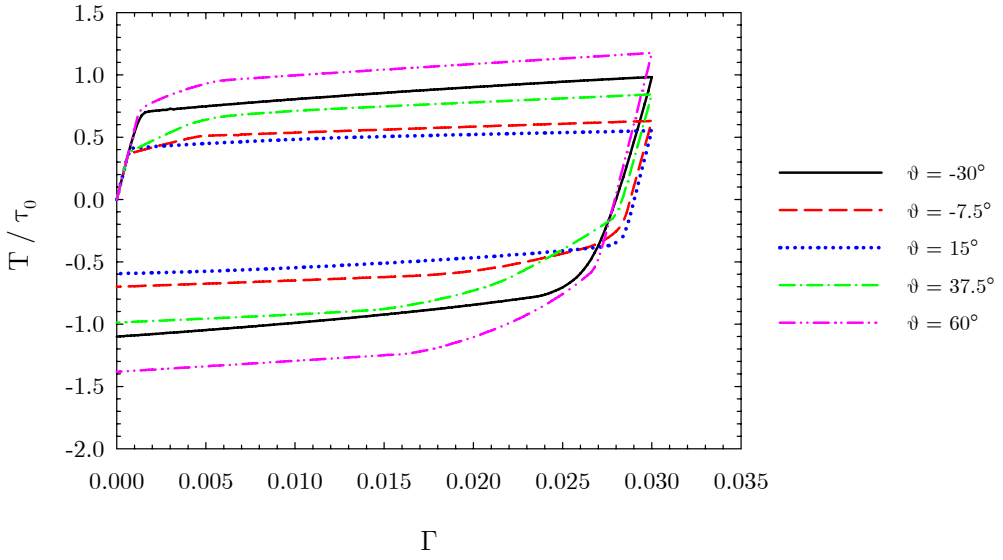

Figure 5.14: Average shear stress-strain responses predicted by the SC model for different crystal orientations for a 400 nm thick film.

To demonstrate that the magnitude of the mechanical size effect is a function of crystal orientation, the stress-strain curves for three different film thicknesses with non-negligible material length scales have been plotted in Figure 5.16 for the five previously considered orientations. It is clear from the figure that orientations $\vartheta =$ 15°, 37.5°, and 60° have more pronounced size effects than the other orientations. This is not unexpected since, as shown in Figure 5.15(c), there are higher GND densities for these orientations for a given film thickness. The fact that the mechanical size effect is dependent on the crystal orientation is not unexpected since the strength of the gradients in the deformation fields obviously varies with crystal orientation. This limited set of simulations investigating the interrelationship between crystal orientation and gradient-dependent deformation is not intended to explore the full range of ramifications for all of the constitutive models; rather, it is intended to set the stage for subsequent

discussions that arise later in the work regarding the orientation dependence of certain inelastic constitutive parameters related to the defect substructure evolution and by proxy the mechanical response.

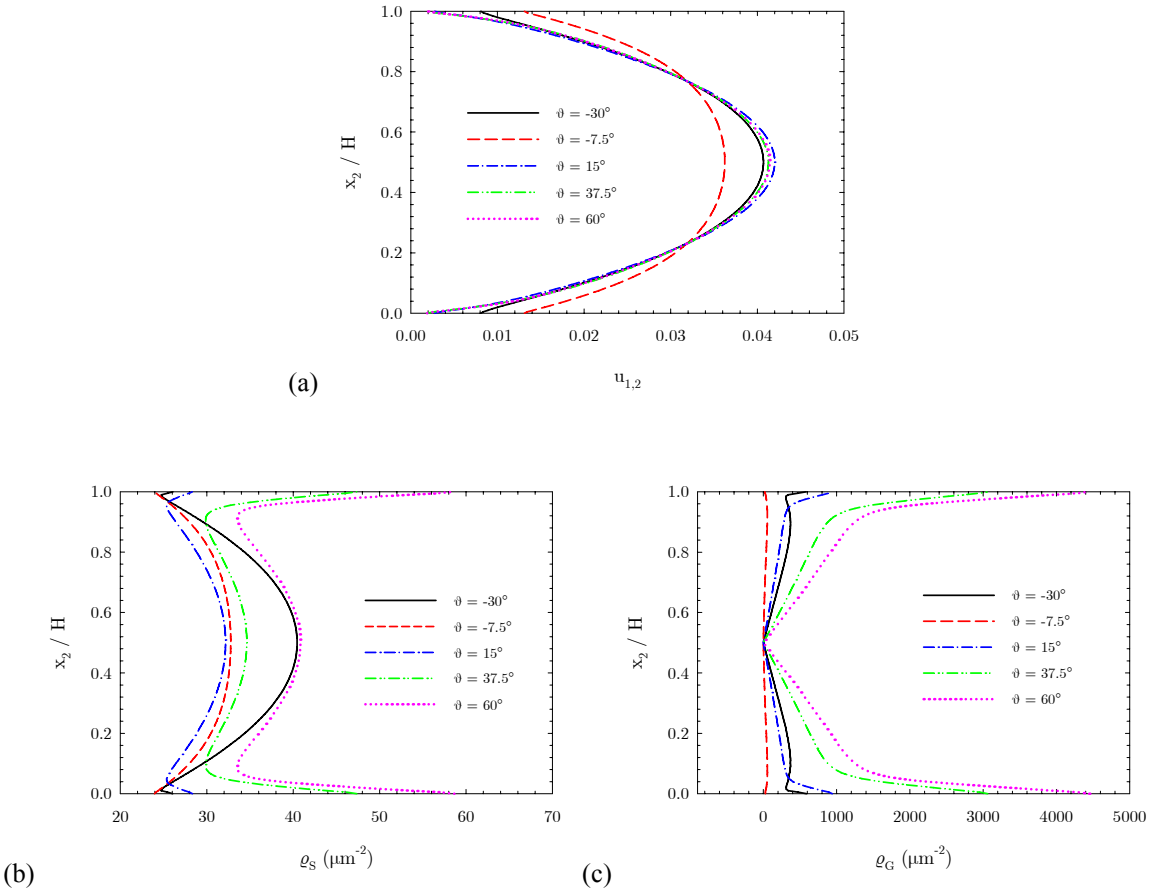

Figure 5.15: (a) Shear strain (b) SSD density and (c) GND density distributions for a 400 nm thick film at $\Gamma = 0.03$ for various crystal orientations.

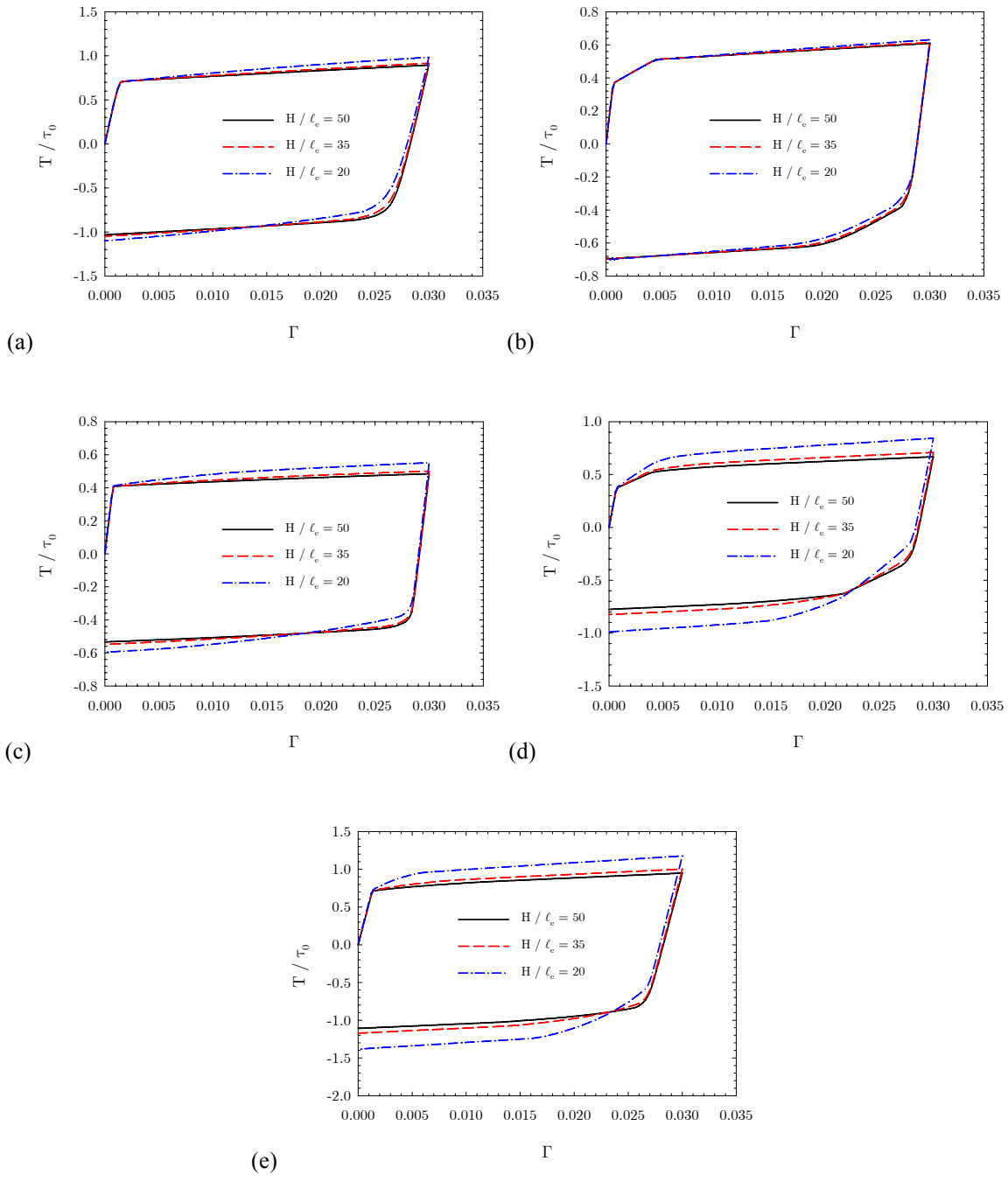

Figure 5.16: Average shear stress-strain response as predicted by the single criterion model for different film thicknesses (a) ϑ = -30° (b) ϑ = -7.5° (c) ϑ = 15° (d) ϑ = 37.5° and (e) ϑ = 60°.

5.3 Comparison to Discrete Dislocation Dynamics Simulations

The remainder of this chapter presents the solutions to three initial-boundary value problems that have been obtained using the micropolar single crystal plasticity models and discrete dislocation dynamics. The three initial boundary value problems are: (i) the previously examined constrained shearing of a thin layer, (ii) thin films subjected to pure bending, and (iii) simple shearing of a metal matrix composite. The discrete dislocation simulation results have been taken from the literature and are based on the Van der Giessen and Needleman [57] model, as reviewed in Chapter 2. The pertinent references for the discrete dislocation results are given in the appropriate subsections.

5.3.1 Simple Shear of Constrained Thin Films

The geometry and boundary conditions for the constrained shear initial-boundary value problem have been shown in Figure 5.1 and outlined in Section 5.2 and are not repeated here. A mesh density of 200 uniformly sized elements have been chosen for the discretization of the strip in the x_2-direction. This density has been chosen as a balance between an effective resolution of the deformation fields and the computational cost, as a large number of simulations have been run to calibrate and tune the model to the discrete dislocation results. As has been shown in Section 4.3.3, the mesh required to obtain a converged solution in terms of local extrema in field variables can be computationally prohibitive for certain boundary value problems. The discrete dislocation results shown in the following figures are from the work of Shu et al. [160] and have been extracted using the DataThief III software [164]. The micropolar models are calibrated to the discrete dislocation simulations for a 1 μm thick film since this is the only height for which all of the relevant deformation fields are available. For this film thickness, the macroscopic stress-strain response, shear strain profiles at different levels of applied strain, and the GND density profiles are known, whereas only the stress-strain response is given for other film thicknesses. It is noted that as demonstrated in Section 5.2 and also in the subsequent results, knowledge of only the stress-strain behavior is insufficient for obtaining an unambiguous calibration of the micropolar models. Nevertheless, the material parameters determined from best-fits to the discrete dislocation data for $H = 1$ μm will be used to

simulate the mechanical response of films of varying thickness to assess scale-dependence of the flow stress and strain-hardening rate.

The discrete dislocation simulations are carried out for a material that is initially dislocation-free and contains a random spatial distribution of dislocation sources which have varying dislocation source strengths. The dislocation source strengths are assumed to have a Gaussian distribution with a mean nucleation strength, τ_0, equal to 50 MPa with a standard deviation of 10 MPa. For a given source, the strength is determined by randomly sampling this distribution and as a result the initial yield strengths observed in the discrete dislocation simulations are going to have some statistical variance related to the number and position of the weaker sources. In the related study of Yefimov and Van der Giessen [162] as much as 20% variation in the initial yield strengths have been observed for different realizations of source distributions for a fixed film thickness. The fact that the source strengths are statistically distributed also leads to the serrated nature of the stress-strain response which reflects the load drops that occur when different sources are activated. The dislocation distribution that emerges in the discrete dislocation simulations is characterized by intense boundary layers of like-signed dislocations that pile up at the rigid boundaries as shown in Figure 5.17. The central region of the film is relatively free of dislocations and the top and bottom boundary layers are densely populated with negatively and positively signed dislocations, respectively. It is often argued that this type of slip constraint is similar to the situation that arises at grain boundaries in polycrystals. Shu et al. [160] have reported that the boundary layers are roughly $0.2H$ thick and that they increase in size with deformation. The boundary layer thickening corresponds with the lengthening of the dislocation pile-ups emanating from the impenetrable boundaries.

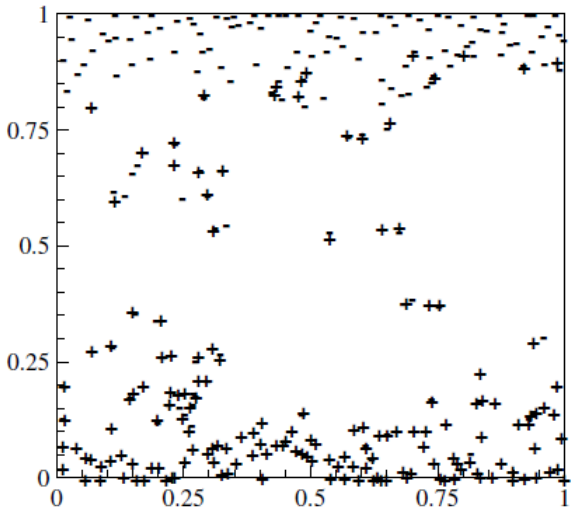

Figure 5.17: Dislocation distribution at $\Gamma = 0.015$ for a 1 μm thick film from a discrete dislocation dynamics simulation [162]. Positive dislocations are denoted by "+" and negative ones by "-".

The procedural logic used to fit the micropolar models to the discrete dislocation simulation results is now briefly described. The initial yield point was chosen, as in Shu et al. [160], to coincide with the back-extrapolated flow stress that was determined from a linear best fit of the post-yield stress-strain curve of the discrete dislocation data. Given a fixed initial yield point, approximate upper bounds can be established for ℓ_e and K by considering in succession material strengthening due solely to linear gradient-induced kinematic hardening and linear slip threshold hardening. For example, given a target stress-strain curve the value the maximum value of ℓ_e can be determined by assuming that all of the material hardening is due to the gradient-induced back stresses, whereas the maximum value of K is determined by assuming that all of the material hardening is due to isotropic slip threshold hardening. In reality the material strengthening for the constrained shear initial-boundary value problem will have both isotropic and kinematic hardening components. As discussed in Section 5.2, either the unloading behavior or the shape of the strain distributions can be used to determine the relative proportions of each hardening mode. Since unloading data is unavailable, the strain-profiles are achieve this goal by recalling that blunted profiles are associated with more prevalent slip threshold hardening whereas parabolic profiles indicate the gradient-induced kinematic hardening is more dominant. Finally, the plastic length scale is determined by fitting the

GND density distributions. It has previously been demonstrated that the ratio of the plastic to elastic length scales influences the nonlinear stress strain behavior, but it also dictates the maximum values of the GND density fields. For a fixed value of L_p / ℓ_e, the peak GND density at the rigid boundary will remain approximately the same as ℓ_e is varied.

The calibrated material parameters are listed in Table 5.3 and have been specified in accordance with the discrete dislocation simulations performed by Shu et al. [160]. In accordance with this previous work and also the related work of Bittencourt et al. [23] only linear slip threshold hardening has been considered ($y_c = 0$), and the interaction matrices only account for self-hardening, i.e., $h^{\alpha\beta} = h_{\perp}^{\alpha\beta} = a^{\alpha\beta} = \delta^{\alpha\beta}$. The initial flow strength is specified in terms of a reference slip threshold stress, r_0, rather than an initial SSD density, ϱ_{S0}, because the material is assumed to be initially dislocation free in the discrete dislocation simulations. However, to avoid null SSD density evolution a negligibly small but nonzero (10^{-6} μm^{-2}) value of initial SSD density has been specified for each slip system. The curvature viscoplastic flow parameters for the multicriterion models, i.e., the reference curvature rate, strength coefficient, threshold stress, drag stress, and inverse rate sensitivity exponent are taken to be equal to their plastic slip counterparts. For each constitutive model considered, the results of prospective best-fits are presented for multiple values of the elastic and plastic length scales to demonstrate how the results are affected by slight changes in the material length scale parameters in the vicinity of the optimum choice.

Table 5.3: Fixed material parameters for the constrained shear simulations for an elastic-viscoplastic single crystal.

Parameter	Symbol	Magnitude	Unit
Shear modulus	μ	26.3	GPa
Poisson's ratio	ν	0.33	-
Coupling parameter	N_c	0.95	-
Reference slip threshold stress	r_0	12.78	MPa
Slip threshold stress strength coefficient	c_1	0.5	-
Burgers vector magnitude	b	0.25	nm
Dislocation interaction coefficients	$h^{\alpha\beta}$	$\delta^{\alpha\beta}$	-
Initial SSD density	ϱ_{S0}	10^{-6}	μm^{-2}
Dislocation immobilization coefficients	$a^{\alpha\beta}$	$\delta^{\alpha\beta}$	-
Dislocation segment length constant	K	20	-
Dislocation capture radius	y_c	0	nm
Reference slip rate	$\dot{\gamma}_0$	10^{-3}	s^{-1}
Slip drag stress	g	5	MPa
Inverse rate sensitivity exponent for slip	m	20	-
Reference curvature threshold stress	$r_{\perp 0}$	12.78	MPa
Curvature threshold strength coefficient	c_7	0.5	-
Dislocation interaction coefficients	$h_{\perp}^{\alpha\beta}$	$\delta^{\alpha\beta}$	-
Reference rotational rate	$\dot{\varphi}_{\perp 0}$	10^{-3}	s^{-1}
Curvature drag stress	$g_{\perp}$	5	MPa
Inverse rate sensitivity exponent for curvature	$n_{\perp}$	20	-

Single Criterion Model (SC)

The stress-strain curves for four different values of the elastic length scale ranging from 5-20 nm (colored lines) are plotted against the discrete dislocation stress-strain curve in Figure 5.18, and judging solely on this response variable it could be argued that each curve represents a good approximation to the discrete dislocation data. To further discern the quality of the fits, the local shear strain distributions for each parameter set are given in Figure 5.19 for several different levels of applied strain. These distributions indicate that for $\ell_e = 5$ nm that there is too much slip threshold hardening, whereas for $\ell_e = 20$ nm the gradient-induced kinematic hardening is slightly over pronounced. The shear strain distributions for $\ell_e = 10$ nm and 15 nm both give quality fits to the discrete dislocation data, with the distributions for the

former displaying some minor blunting indicating that slip threshold hardening is still making a significant contribution to the total strengthening behavior.

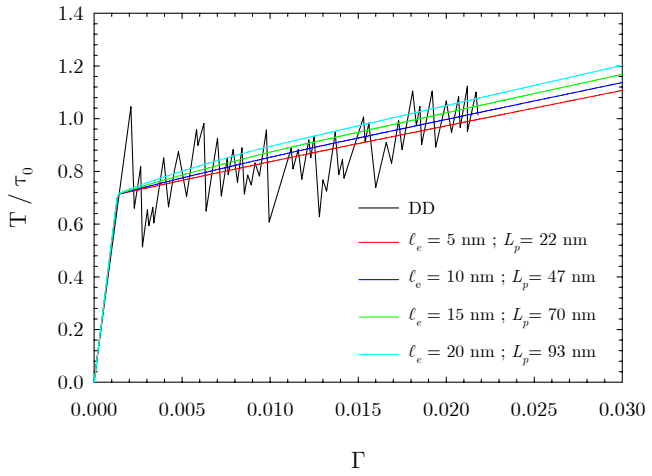

Figure 5.18: Average stress-strain response for the calibrated single criterion model for different elastic length scales with $L_p / \ell_e \approx 4.5$ plotted against the discrete dislocation (DD) results [160]. $H = 1$ μm.

The signed GND density distributions for each set of simulations are shown in Figure 5.20 and it is noted that the plastic to elastic length scale ratio determined to provide the best correlation with the discrete dislocation data is $L_p / \ell_e \approx 4.5$. In Figure 5.20(a), the micropolar results are plotted against the discrete dislocation results at $\Gamma = 0.0068$, and in Figure 5.20(b) they are plotted against the statistical dislocation model of Limkumnerd and Van der Giessen [90] at $\Gamma = 0.0218$. The signed GND density distributions for both $\ell_e = 10$ nm and 15 nm agree reasonably well with both the discrete dislocation and statistical dislocation model results. The statistical dislocation model of Limkumnerd and Van der Giessen [90] is a type of non-work-conjugate higher-order theory discussed in Section 2.3.4 that couples the standard crystal plasticity mechanical boundary value problem with the dislocation transport problem. It may seem odd that the micropolar model is being compared to another type of nonlocal continuum model

as part of a model parameter validation; however, these types of statistical crystal plasticity models are very similar to discrete dislocation dynamics models in that they explicitly model the transport and annihilation of dislocations, and it has been demonstrated that they are able to capture the dislocation substructure evolution exceptionally well for a wide-range of initial-boundary value problems [74, 90, 162, 165-168]. Because of this and due to the limited amount of discrete dislocation dynamics data available, it is beneficial and justified to use this additional data as a model cross-check. It is emphasized that the micropolar models are *fit* to the discrete dislocations simulations and only *compared* to the statistical crystal plasticity model. The SSD and total dislocation density distributions are plotted for the single criterion model in Figure 5.21(a) and (b), respectively, and it is shown that the SSDs are negligible as compared to the GNDs with the maximum SSD density ranging from approximately 5-9 μm^{-2} for the different values of the elastic length scale, whereas the maximum GND density is on the order of 1000 μm^{-2}.

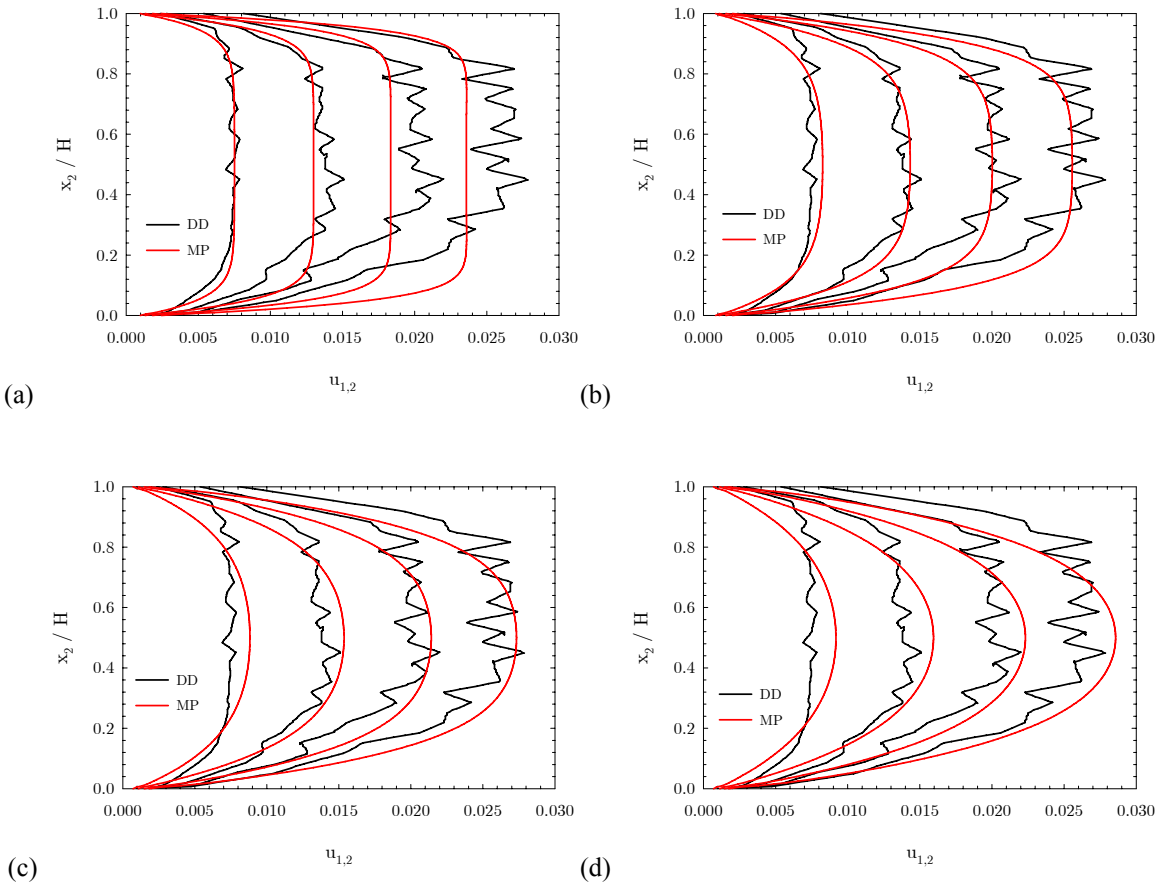

Figure 5.19: Shear strain distributions at $\Gamma = 0.0068$, 0.0118, 0.0168, and 0.0218 for the calibrated single criterion model (MP) with (a) $\ell_e = 5$ nm (b) $\ell_e = 10$ nm (c) $\ell_e = 15$ nm and (d) $\ell_e = 20$ nm with $L_p / \ell_e \approx 4.5$ plotted versus discrete dislocation dynamics results [160]. $H = 1$ μm.

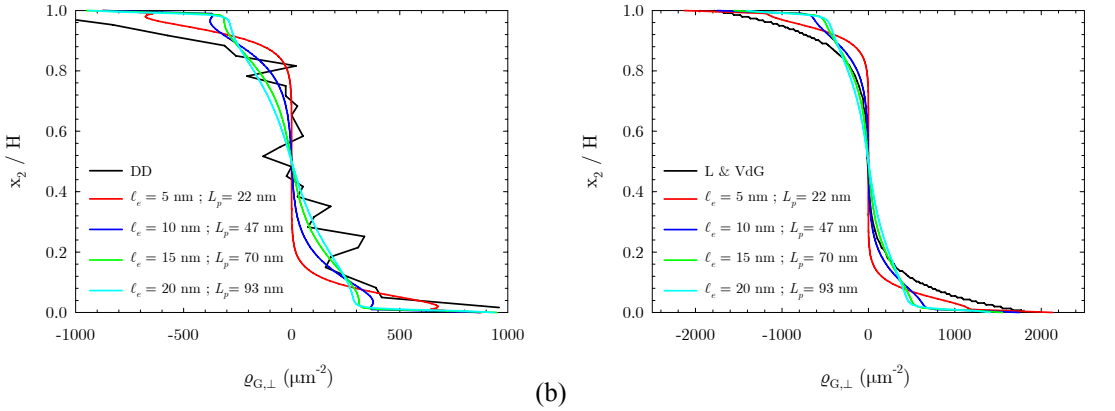

Figure 5.20: Signed GND density distributions for the calibrated single criterion model for different elastic length scales with $L_p \,/\, \ell_e \approx 4.5$ (a) at $\Gamma = 0.0168$ as compared to the discrete dislocation results [160] and (b) at $\Gamma = 0.0218$ as compared to the statistical dislocation model of Limkumnerd and Van der Giessen [90]. $H = 1$ μm.

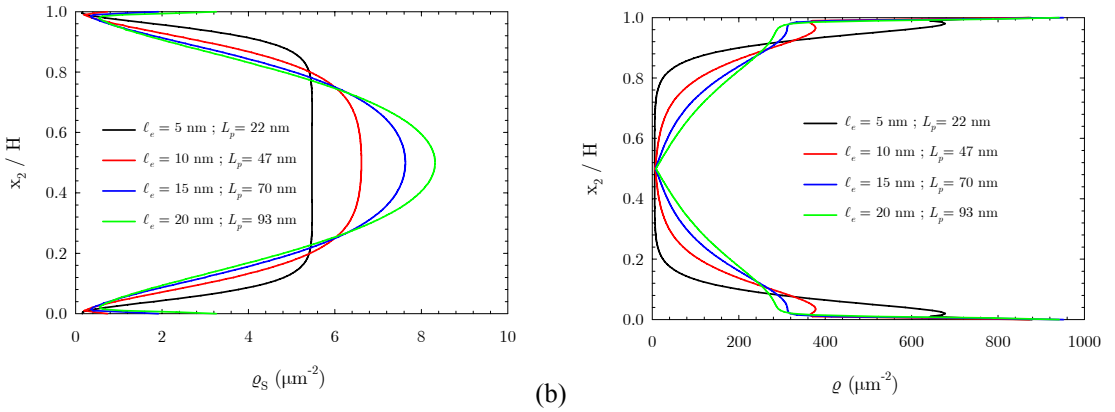

Figure 5.21: (a) SSD and (b) total dislocation density distributions at $\Gamma = 0.0168$ for the calibrated single criterion model for different elastic length scales with $L_p \,/\, \ell_e \approx 4.5$. $H = 1$ μm.

Multicriterion Model Version 1 (MCV1)

The stress-strain curves for various sets of length scale parameters are given in Figure 5.22 for the MCV1 model. The deformation responses for three different elastic length scales, $\ell_e = 5$, 10, and 15 nm, have been simulated and none of the simulations are able to adequately capture the relevant aspects of all deformation fields. Just considering the stress-strain response and the shear strain distributions shown in Figure 5.22 and Figure 5.23, respectively, it seems that the simulations performed with $\ell_e = 5$ nm provide the best correlation with the discrete dislocation data; however, the signed GND density distributions shown for this set of material parameters shown in Figure 5.24(a) are completely at odds with the discrete dislocation simulation results. In fact, there is at least an order of magnitude difference between the signed GND density distributions predicted by the micropolar model for all sets of material constants considered and the discrete dislocation results. For this reason, the discrete dislocation results have not been included in the GND density plots shown in Figure 5.24(a) as they totally obscure the results of the micropolar simulations. In contrast to the last set of simulations, different values of L_p / ℓ_e have been employed for each elastic length scale, and that as anticipated the peak magnitude of the GND densities at the boundaries varies from one set of simulations to another with smaller values of L_p / ℓ_e being associated with larger magnitudes. One might be inclined to think that L_p / ℓ_e should be further decreased to bring the micropolar model results into better agreement with the discrete dislocation results; however, doing so would lead to a significant increase in strain hardening similar to what is seen in Figure 5.10(b), thereby introducing disagreement between the micropolar and discrete dislocation stress-strain responses. For the sake of completeness, the SSD and total dislocation density distributions are given in Figure 5.24(b) and (c), respectively. In addition to the disagreement between the MCV1 and discrete dislocation models with respect to the magnitude of the GND and total dislocation density distributions, the general shapes of the distributions are at odds with discrete dislocation results as well (see Figure 5.20(a)).

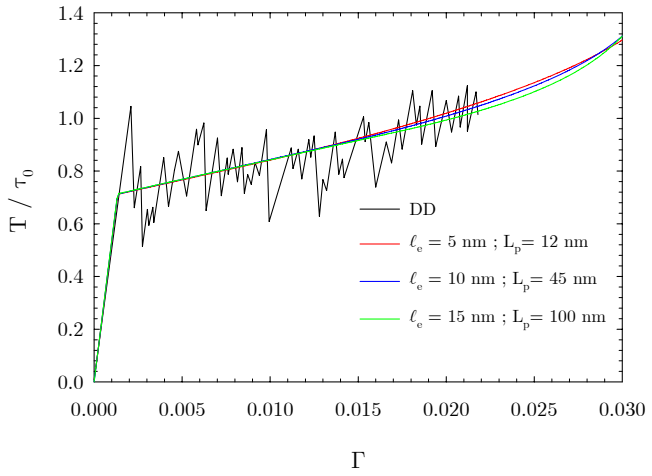

Figure 5.22: Average stress-strain response for the calibrated multicriterion model (version 1) for different elastic and plastic length scales plotted against the discrete dislocation (DD) results [160]. $H = 1$ **μm.**

The inability to establish a material parameter set that captures the essential features of all relevant deformation fields indicates that the MCV1 model is inadequate. This does not come as a surprise as concerns over the model's stability and fidelity with respect to physical reality have previously been raised in the parametric study performed in Section 5.2. The recognition of these limitations is important since this type of model has been used rather extensively to simulate mechanical size effects [34, 37, 40, 41, 128]. Such a model has also been advocated by the present authors [169], and in fact these revelations provided the impetus for pursuing multicriterion models that incorporate curvature threshold hardening.

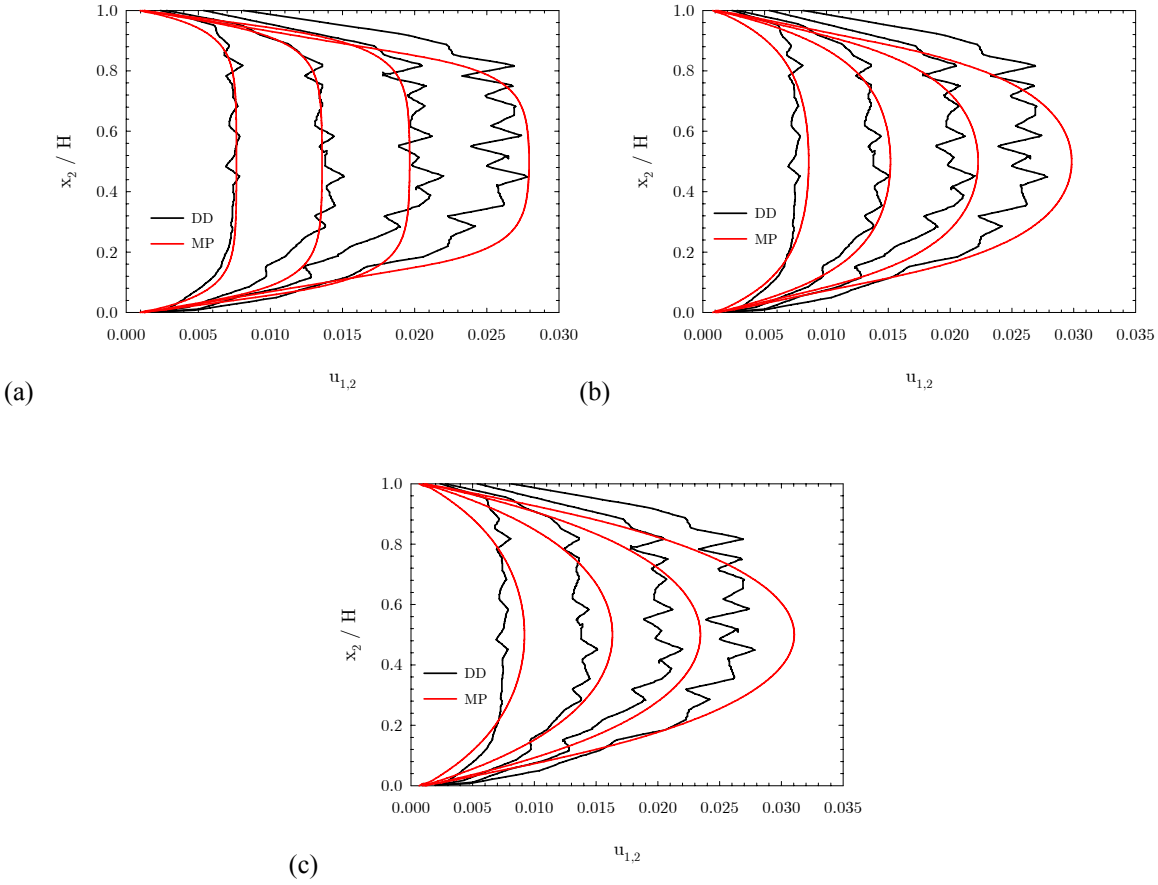

Figure 5.23: Shear strain distributions at $\Gamma = 0.0068$, 0.0118, 0.0168, and 0.0218 for the calibrated multicriterion model (version 1) with (a) $\ell_e = 5$ nm (b) $\ell_e = 10$ nm and (c) $\ell_e = 15$ nm plotted versus discrete dislocation dynamics results [160]. $H = 1$ μm.

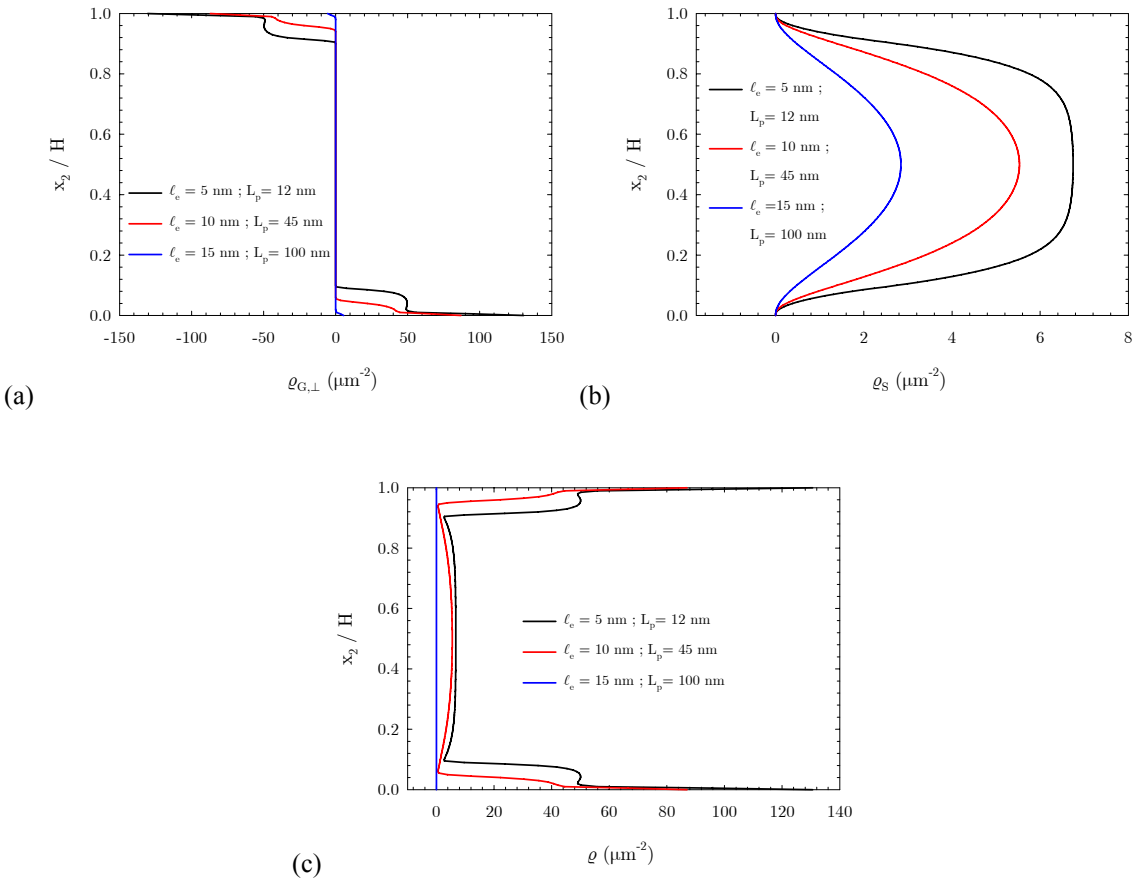

Figure 5.24: (a) Signed GND (b) SSD and (c) total dislocation densities at $\Gamma = 0.0168$ for the calibrated multicriterion model (version 1) for different elastic and plastic length scales. $H = 1$ μm.

<u>Multicriterion Model Version 2 (MCV2)</u>

The stress-strain curves and local shear strain distributions from simulations using the MCV2 model are plotted against the discrete dislocation simulation results in Figure 5.25 and Figure 5.26, respectively, for two sets of material length scale parameters. Two different values of L_p / ℓ_e have been considered; $L_p / \ell_e = 1$ for $\ell_e = 5$ nm and $L_p / \ell_e = 4$ for $\ell_e = 15$ nm. While the stress-strain curves obtained from the MCV2 model compare quite well with the discrete dislocation result, the shear strain profiles do not. During earlier stages of the deformation ($\Gamma = 0.0068$ and 0.0118), there is good agreement between the two simulation results; however, as the deformation progresses and the effects of slip threshold

hardening due to GNDs becomes more pronounced, the shear profiles predicted by the MCV2 model began to narrow and grow in intensity more rapidly that in the discrete dislocation simulation. This behavior is more pronounced for the simulation with $\ell_e = 5$ nm since $L_p / \ell_e = 1$ since, as previously discussed, a lower value of this ratio leads to an increase in the magnitude of the GND density field. This fact is verified in Figure 5.27(a) which shows the signed GND density distributions for both simulations, and the maximum GND density when $L_p / \ell_e = 1$ is approximately 50 μm^{-2} and 10 μm^{-2} when $L_p / \ell_e = 4$.

As in the case of the MCV1 model, the MCV2 model also underpredicts the magnitude of the GND density field by an order of magnitude (again see Figure 5.20(a)). In order to get a GND density field whose magnitude is within the range of that predicted by the discrete dislocation simulations, a ratio $L_p / \ell_e < 1$ must be used. However, when a plastic to elastic length scale ratio of less than unity is employed in conjunction with the MCV2 model, there is an artificially pronounced increase in the strain hardening response that is similar to that displayed by the MCV1 model in Figure 5.10(b). Furthermore, it has already been shown in Figure 5.26(a) that using a plastic to elastic length scale ratio of one ($L_p / \ell_e = 1$) already leads to poor agreement between the micropolar and discrete dislocation strain profiles due to the GND contribution to the slip threshold stress. Therefore, decreasing L_p / ℓ_e to increase the magnitude of the GND density field will have the adverse effect of introducing significant error into the correlation between the micropolar and discrete dislocation stress-strain curves and shear strain distributions. As before with the MCV1 model, this implies that the MCV2 model cannot capture all of the relevant trends in the deformation fields for a single set of material parameters and is therefore inadequate.

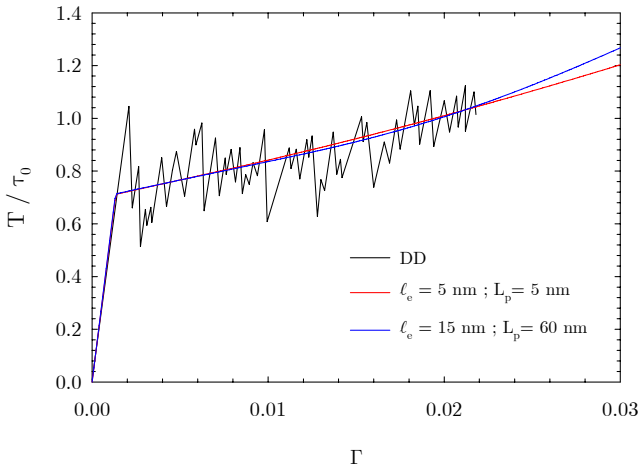

Figure 5.25: Average stress-strain response for the calibrated multicriterion model (version 2) for different elastic and plastic length scales plotted against the discrete dislocation results [160]. $H = 1$ **μm.**

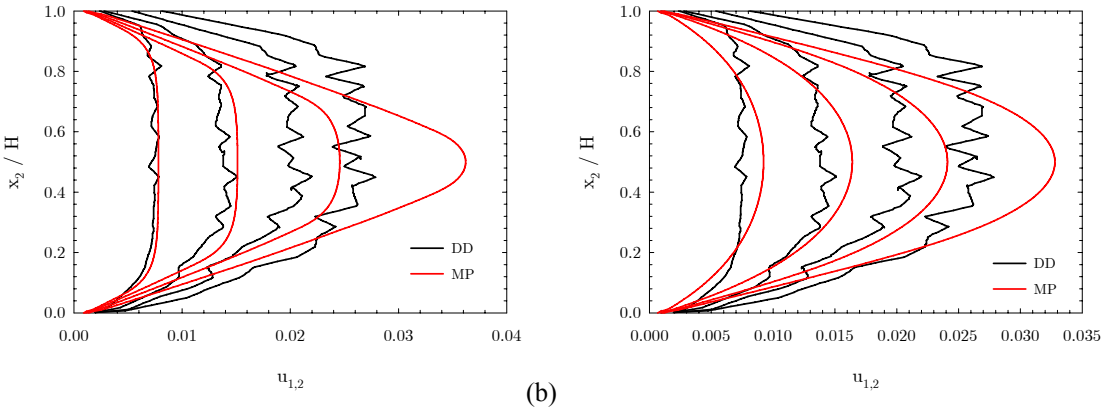

Figure 5.26: Shear strain distributions at $\Gamma = 0.0068$**, 0.0118, 0.0168, and 0.0218 for the calibrated multicriterion model (version 2) with (a)** $\ell_e = 5$ **nm and (b)** $\ell_e = 15$ **nm plotted versus discrete dislocation dynamics results [160].** $H = 1$ **μm.**

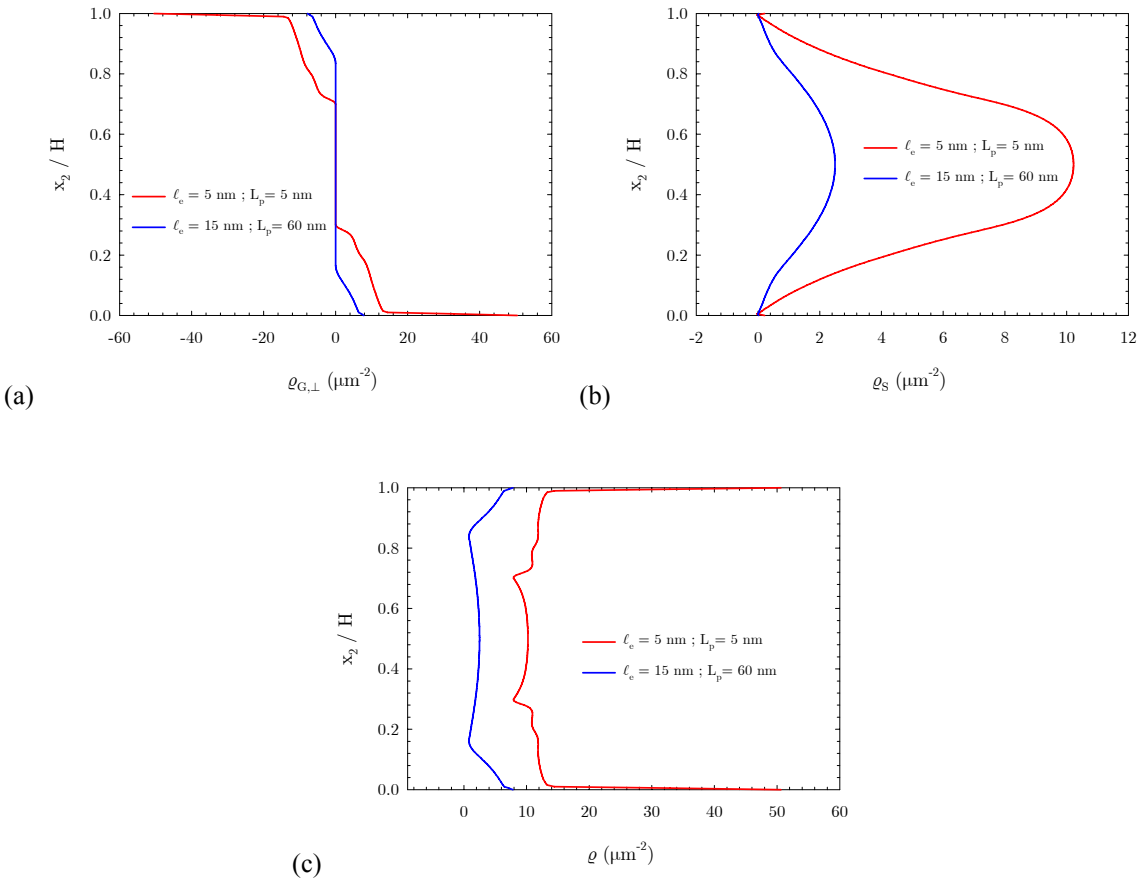

Figure 5.27: (a) Signed GND (b) SSD and (c) total dislocation densities at $\Gamma =$ 0.0168 for the calibrated multicriterion model (version 2) for different elastic and plastic length scales. $H =$ 1 μm.

Multicriterion Model Version 3 (MCV3)

The stress-strain curves for the MCV3 model are plotted against the discrete dislocation results in Figure 5.28 for two different sets of material length scale parameters and are shown to compare favorably. The distinction between the two results is rather obvious in that for $\ell_e = 20$ nm, the stress-strain curve is rather noticeably nonlinear due to the smaller value of L_p / ℓ_e that has been used, leading to a reduction of the gradient-induced back stress, whereas for $\ell_e = 10$ nm the response is only slightly nonlinear. Figure 5.29 shows the local shear strain distributions for each simulation and the results again compare favorably

with the discrete dislocation simulations and are nearly indistinguishable from one another. Turning attention now to the signed GND density plots shown in Figure 5.30(a) against the discrete dislocation result at $\Gamma = 0.0068$ and in Figure 5.30(b) against the statistical dislocation crystal plasticity model results of Limkumnerd and Van der Giessen [90] at $\Gamma = 0.0218$, it is shown that the MCV3 model is in good qualitative and quantitative agreement with each result for both sets of material parameters. However, the signed GND density predicted by the MCV3 model with $\ell_e = 20$ nm more closely coincides with both the discrete and statistical dislocation models. The SSD and total dislocation density distributions are given in Figure 5.31(a) and (b), respectively, for the MCV3 model. The maximum SSD density at the center of the film for the MCV3 model with $\ell_e = 10$ nm is 6.8 μm^{-2} as compared to 3.8 μm^{-2} when $\ell_e = 20$ nm, and in both cases the SSD densities are negligible as compared to the GND densities as evidenced by the total dislocation density distributions shown in Figure 5.31(b).

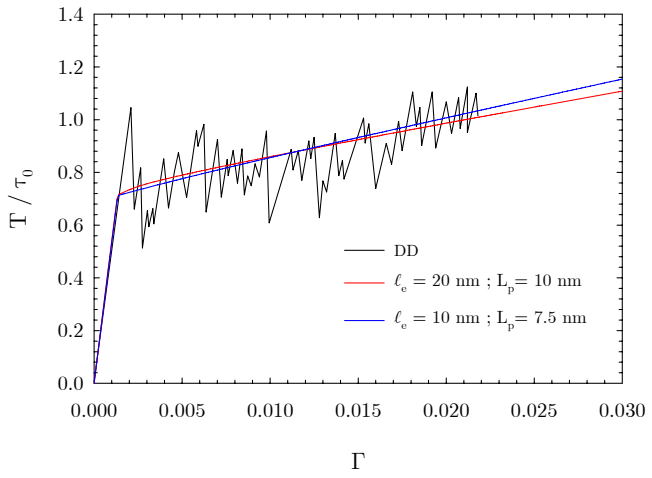

Figure 5.28: Average stress-strain response for the calibrated multicriterion model (version 3) for different elastic and plastic length scales plotted against the discrete dislocation results [160]. $H = 1$ μm.

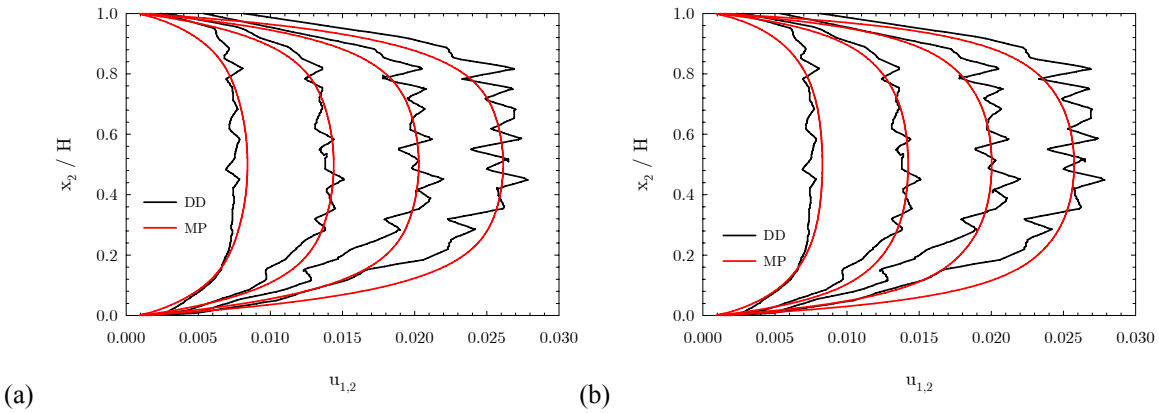

Figure 5.29: Shear strain distributions at $\Gamma = 0.0068$, 0.0118, 0.0168, and 0.0218 for the calibrated multicriterion model (version 3) with (a) $\ell_e = 20$ nm and (b) $\ell_e = 10$ nm plotted versus discrete dislocation dynamics results [160]. $H = 1$ µm.

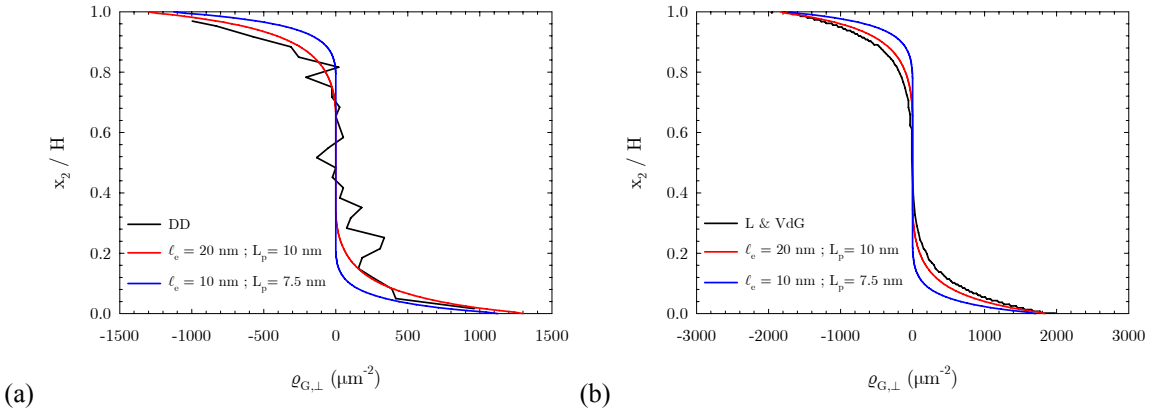

Figure 5.30: Signed GND density distributions for the calibrated multicriterion model (version 3) for different elastic and plastic length scales (a) at $\Gamma = 0.0168$ as compared to the discrete dislocation results [160] and (b) at $\Gamma = 0.0218$ as compared to the statistical dislocation model of Limkumnerd and Van der Giessen [90]. $H = 1$ µm.

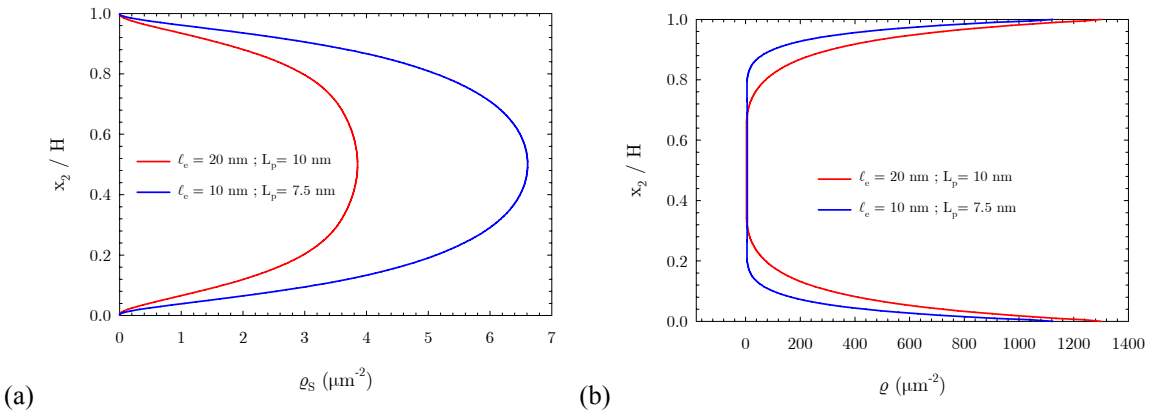

Figure 5.31: (a) SSD and (b) total dislocation densities at $\Gamma = 0.0168$ for the calibrated multicriterion model (version 3) for different elastic and plastic length scales. $H = 1$ μm.

In contrast to the prior two versions of the multicriterion model, version 3 has demonstrated the ability to accurately and simultaneously reproduce the stress-strain response, the shear strain distribution, and the GND density distribution from the discrete dislocation simulations. Accordingly, the MCV3 model will be exclusively employed when the multicriterion model is applied in future segments of this work. To assess the models' predictive capabilities, a series of simulations have been performed using the optimum free fitting parameters for the SC and MCV3 models, which are listed in Table 5.4, for various film thicknesses and the resulting stress-strain responses are compared to the discrete dislocation results as shown in Figure 5.32. The initial slip threshold has been kept the same for $H = 500$ nm ($r_0 = 12.78$ MPa), but has been modified for $H = 2$ μm to $r_0 = 9.5$ MPa to capture the statistical variation in the initial yield strength observed in the discrete dislocation simulation. Both the SC and MCV3 model results are in fairly good agreement with the discrete dislocation simulations, although there is some variation in the strain hardening response observed for the two larger film thicknesses where the single criterion model predicts slightly higher hardening rates.

Table 5.4: Optimum single criterion (SC) and multicriterion (MCV3) free model parameters for the constrained shear simulations for an elastic-viscoplastic single crystal as determined by fitting to discrete dislocation results for $H = 1$ μm.

Parameter	Symbol	Magnitude	Unit
SC Model			
Elastic length scale	ℓ_e	10	nm
Plastic length scale	L_p	47	nm
MCV3 Model			
Elastic length scale	ℓ_e	20	nm
Plastic length scale	L_p	10	nm

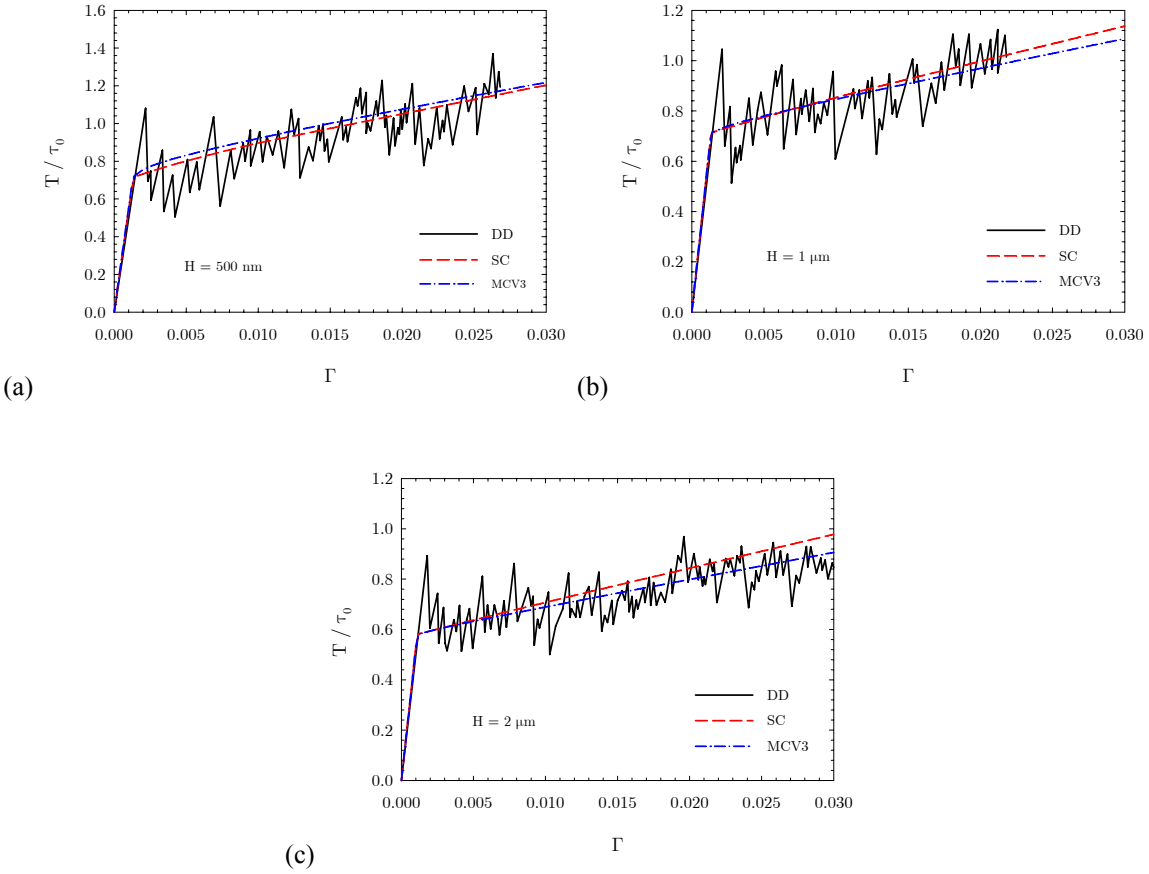

Figure 5.32: Average stress-strain response for the calibrated single and multicriteiron (version 3) models using the optimum values of the free fitting parameters for different film thicknesses plotted against the discrete dislocation results [160] (a) $H = 500$ nm (b) $H = 1$ μm and (c) $H = 2$ μm.

The SSD and GND densities are plotted for both models as a function of normalized position in Figure 5.33 at $\Gamma = 0.03$ for all three film thicknesses to demonstrate the size-dependence of the relative SSD and GND contributions. Discrete dislocation results are not available for $H = 500$ nm and 2 μm. These plots show that GND fraction of the total dislocation density dominates regardless of film thickness, as the peak GND density values are approximately two orders of magnitude larger than the peak SSD densities. However, as expected, as the film thickness is increased the SSD density profiles bcome more blunted and the boundary layer width decreases. A comparison of Figure 5.33(a) to Figure 5.33(c), shows that this behavior is more pronounced for the SC model as compared to the MCV3 model since the maximum difference in peak SSD density is approximately 9 μm^{-2} for the SC model and 2.5 μm^{-2} for the MCV3 model. The GND density profiles for the various film thicknesses, as shown in Figure 5.33(b) and (d) are quite similar for both models in terms of peak magnitude at the boundaries and also in terms of shape and boundary layer width, especially for the 1 μm and 2 μm thick films. However, the change in the GND density as a function of normalized position for the 500 nm thick film is much more rapid for the SC model as compared to the MCV3 model; a fact that is underscored by the development of a boundary layer of the entire film thickness for the SC model, whereas a finite boundary layer is observed for the MCV3 model.

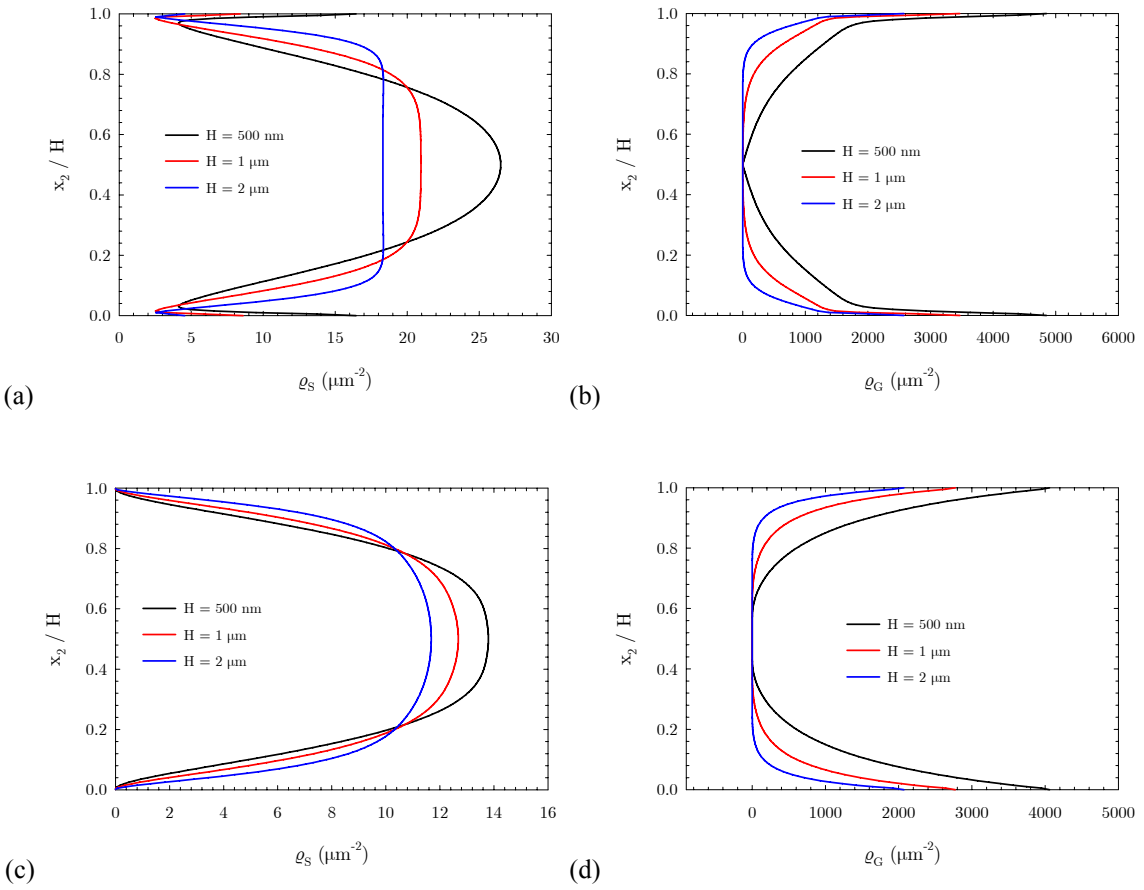

Figure 5.33: (a) & (c) SSD density and (b) & (d) GND densities at $\Gamma = 0.03$ for the calibrated single criterion (top) and multicriterion (MCV3) (bottom) models using the optimum free fitting parameters.

5.3.2 Pure Bending of Thin Films

This section presents the calibration of the micropolar models to discrete dislocation dynamics simulations of unpassivated single crystal thin films subjected to pure bending. Strain gradients naturally arise in bending modes of deformation and the generation of polar dislocation densities is required to accommodate the imposed deformation in plastically bent crystals. For this reason, pure bending is a popular initial-boundary value problem used for experimentally measuring [4, 170] and studying via numeral simulation [4, 102, 162, 168, 171-182] plasticity size effects. In the present work, attention is focused on the discrete dislocation simulations of bending performed by Yefimov et al. [168] and Yefimov

and Van der Giessen [162]. These studies examine both single and double slip configurations. The advantage of studying the single slip configuration is that it enables the constitutive models to be evaluated when there are no slip system interactions. Results are presented for the single and multicriterion (MCV3) models for the single slip configuration, and for the single criterion model for the double slip configuration. Naturally, the single slip configuration is examined first.

A 2-D thin film of width, W, and thickness, H, is subjected to pure bending in a state of plane strain as sketched in Figure 5.34. The $x_1 - x_2$ plane is taken as the bending plane and a coordinate system is attached to the midpoint of the film. The deformation is defined through the edge rotation angle, Θ, and is prescribed through a linear variation of the x_1 displacement component as a function of distance from the neutral axis as

$$u_1(\pm\tfrac{W}{2}, x_2, t) = \pm\Theta(t)x_2 \tag{5.4}$$

A constant macroscopic rotation rate, $\dot{\Theta} = 10^{-3}$ s^{-1}, is imposed until the final rotation angle is achieved, and the top and bottom surfaces of the beam are prescribed to be traction-free. As shown in Figure 5.34, a single slip system is oriented at an angle ϑ with respect to the x_1-axis, and slip is constrained to occur within are interior to the angled black lines. This restriction has been imposed in the discrete dislocation simulations in order to avoid the complication of having dislocations exit the crystal through the lateral faces where the displacement boundary conditions are prescribed. For the single slip configuration, two different film thicknesses are considered, $H = 2$ and 4 μm, and the films are taken to have the same width-to-thickness ratio, $W / H = 3$. Slip system orientations of 30° and 60° are studied and will be referred to ϑ_{30} and ϑ_{60} in the following. The average macroscopic response is quantified by the bending moment, M, work-conjugate to Θ which is given by

$$M = \int_{-H/2}^{H/2} \sigma_{11}(\pm\tfrac{W}{2}, x_2)x_2 dx_2 \tag{5.5}$$

A thickness-independent measure of the macroscopic response is given by the normalized bending moment, M / M_{ref}, with the reference bending moment, M_{ref}, defined as

$$M_{ref} = \frac{2}{H}\int_{-H/2}^{H/2} \bar{\tau}_{nuc} x_2^2 dx_2 = \frac{2}{3}\bar{\tau}_{nuc}\left(\frac{H}{2}\right)^2 \tag{5.6}$$

where $\bar{\tau}_{nuc} = 50$ MPa is the mean critical nucleation stress used in the discrete dislocation simulations. The reference moment is that which would induce a linear stress distribution over the height of the beam equal to $\bar{\tau}_{nuc} x_2 / (H / 2)$. Uniform finite element meshes of bilinear quadrilateral elements are used in each simulation with mesh densities of 66 × 38 for ϑ_{30} and 155 × 30 for ϑ_{60}.

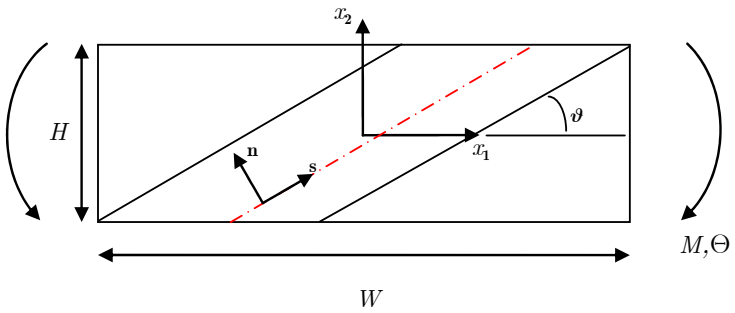

Figure 5.34: Schematic of the geometry and boundary conditions for the single slip bending simulations as used in Yefimov et al. [168].

The set of fixed material parameters is listed in Table 5.5 and have been specified in accordance with the discrete dislocation simulations and prior discussions. The initial material state in the discrete dislocation simulations is assumed to be free of obstacles and dislocations, and as a result all of the dislocations stored in the material are geometrically necessary. Dislocations of both signs are nucleated from the distributed point sources, but those that are not required to accommodate the imposed deformation exit the crystal through the free surfaces. This occurs because there are no point obstacles or dislocations lying on intersecting slip planes to otherwise impede their flow. The resulting dislocation configurations at $\Theta = 0.015$ from the discrete simulations for the two slip system orientations are shown in Figure 5.35. Since all of the dislocations in the single slip configuration are geometrically necessary, the constants

related to the generation of SSDs are taken to be zero. In the present context, the slip system threshold stress is defined solely by r_0 which is related to the source strength in the discrete dislocation simulations, and should not necessarily be treated as an absolute material constant due to the statistical variations in the source strength and placement used in the discrete dislocation simulations. The initial yield point in the discrete simulations will significantly depend on the availability of weak sources near the top and bottom surfaces of the film where the stresses are higher. This indicates that the stochastic component of the initial yield scale-dependence in the discrete simulations may be even more pronounced in bending than for the constrained shear problem. The free fitting parameters are $\{r_0, \ell_e, L_\perp\}$ for the single criterion model and $\{r_0, r_{\perp 0}, g_\perp, \ell_e, L_\perp\}$ for the multicriterion model, and are given along with subsequent discussion of results.

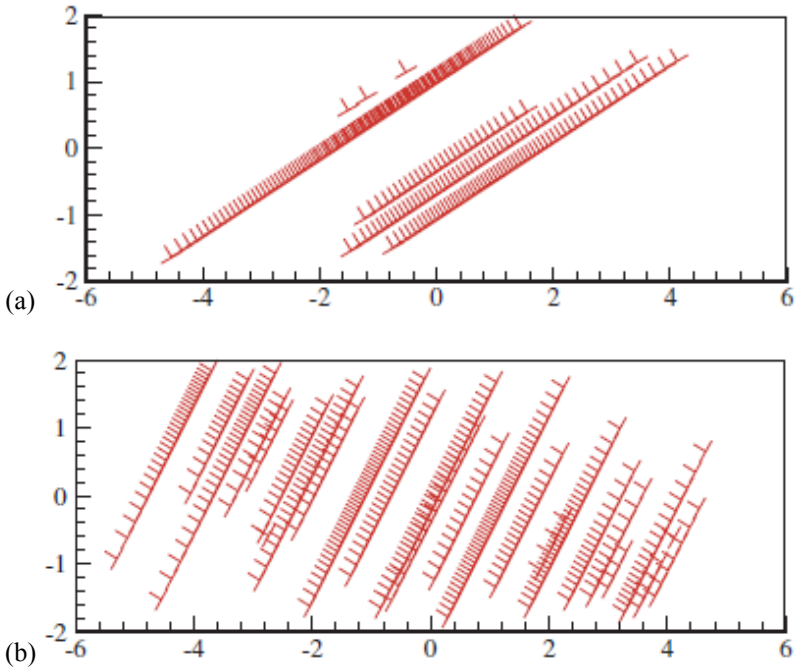

Figure 5.35: Dislocation distributions at $\Theta = 0.015$ for the 4 μm thick films for (a) $\vartheta = 30°$ and (b) $\vartheta = 60°$ as obtained from the discrete dislocation simulations [168].

Table 5.5: Fixed material parameters used in the single slip pure bending simulations for an elastic-viscoplastic single crystal.

Parameter	Symbol	Magnitude	Unit
Shear modulus	μ	26.3	GPa
Poisson's ratio	ν	0.33	-
Coupling parameter	N_c	0.95	-
Slip threshold stress strength coefficient	c_1	N/A	-
Burgers vector magnitude	b	0.25	nm
Dislocation interaction coefficients	$h^{\alpha\beta}$	N/A	-
Initial SSD density	ϱ_{S0}	N/A	μm^{-2}
Dislocation immobilization coefficients	$a^{\alpha\beta}$	N/A	-
Dislocation segment length constant	K	N/A	-
Dislocation capture radius	y_c	N/A	nm
Reference slip rate	$\dot{\gamma}_0$	10^{-3}	s^{-1}
Slip drag stress	g	5	MPa
Inverse rate sensitivity exponent for slip	m	20	-
Curvature threshold strength coefficient	c_7	0.5	-
Dislocation interaction coefficients	$h_{\perp}^{11}$	1	-
Reference rotational rate	$\dot{\varphi}_{\perp 0}$	10^{-3}	s^{-1}
Inverse rate sensitivity exponent for curvature	$n_{\perp}$	20	-

Single Criterion Model (SC)

The calibrated normalized moment-rotation plots for both slip system orientations and thicknesses are plotted in Figure 5.36 for the SC model, and they are in reasonably good agreement with the discrete dislocation results with respect to both the orientation and scale-dependence. The calibrated values of the free fitting parameters for this set of results are given in Table 5.6, and it is noted that the same values of reference slip threshold stress and elastic length scale have been used for both orientations. Except for the 2 μm thick film for ϑ_{60}, the SC model results are in good quantitative agreement with the initial yield strengths predicted by the discrete dislocation model. According to the discrete dislocation model, the yield strength for the 2 μm thick film for ϑ_{60} is actually lower than that of the 4 μm film, and this is due to the stochastic variation in the dislocation source strengths. The inherent differences between the discrete and nonlocal continuum formulations forces one to calibrate the continuum model to either the initial yield

or a best-fit of the total response as both aspects of the deformation cannot be simultaneously captured. The results in Figure 5.36(a) conform to the former strategy instead of the latter.

Table 5.6: Calibrated SC free model parameters used in the single slip pure bending simulations for an elastic-viscoplastic single crystal.

Parameter	Symbol	Magnitude	Unit
Reference slip threshold stress	τ_0	10	MPa
Elastic length scale	ℓ_e	125	nm
Plastic length scale ($\vartheta = 30°$)	L_p	562	nm
Plastic length scale ($\vartheta = 60°$)	L_p	250	nm

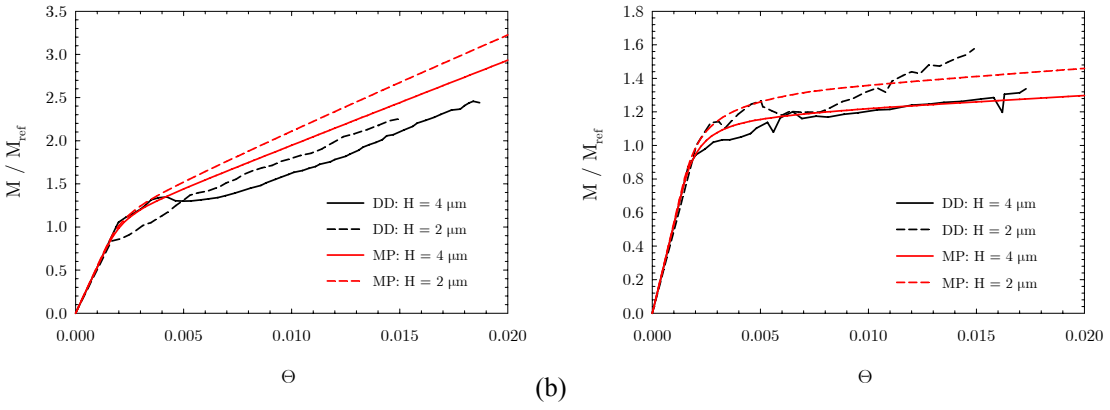

Figure 5.36: Normalized moment-rotation response for the calibrated single criterion model (MP) for both film thicknesses plotted against the discrete dislocation dynamics results [168] for (a) $\vartheta = 30°$ and (b) $\vartheta = 60°$.

The discrete simulations display an approximately linear hardening rate that increases with decreasing film thickness, and the micropolar model shows similar trends although the rate is somewhat underestimated for the 2 μm thick film with ϑ_{60}. There is a much higher hardening rate regardless of the specimen size for ϑ_{30} as compared to ϑ_{60} as shown in Figure 5.36(c); this is not a by-product of the

constitutive model, but rather reflective of the way the boundary value problem is constructed with distinct elastic and plastic zones. In these simulations, the films are composite elastic-plastic materials and the plastic zone size is much smaller for ϑ_{30}. Therefore, the outer elastic regions contribute significantly to the substantially higher apparent hardening rates due to the increased effective film stiffness for this orientation. In fact, a traditional (local) model of crystal plasticity with an elastic-perfectly plastic slip system level response would yield an apparent hardening rate comparable to, albeit lower than that shown in Figure 5.36(a). Clearly, there is also a contribution to the differences in the apparent hardening rates for the two orientations that arises due to the relative misalignment of the slip direction and the direction of the imposed deformation, i.e., the x_1 direction. This portion is that attributed to the orientation dependent GND distributions that develop. To more clearly sort out the GND component of hardening for the different orientations, a set of simulations should be performed in which the total area fractions of the elastic and plastic zones are equal.

The cumulative plastic slip distributions are shown for the SC model in Figure 5.37 and Figure 5.38 for ϑ_{30} and ϑ_{60}, respectively, at $\Theta = 0.015$. In both cases the maximum values of cumulative slip occur at the free surface, but distinct differences in the overall slip morphologies are readily apparent. For ϑ_{30} the region of high intensity slip is highly concentrated and extends from the free surface in a linear fashion and parallel to the elastic-plastic interface. In contrast, the crystal with ϑ_{60} is characterized by smooth semi-circular lobes of high intensity slip that are more evenly distributed along the free surfaces. Because slip is more evenly distributed in the crystal with ϑ_{60}, the maximum values of cumulative slop are lower for this orientation as compared to ϑ_{30}. For both orientations there are only minor, almost unperceivable, changes in the field contours with film thickness. The localized, high intensity contour regions are slightly more pronounced for the *thicker* films in both cases with maximum values of cumulative slip equal to 0.037 and 0.035 for the 4 μm and 2 μm thick films, respectively, for ϑ_{30} and equal to 0.025 and 0.024 for the 4 μm and 2 μm thick films, respectively, for ϑ_{60}.

(a)

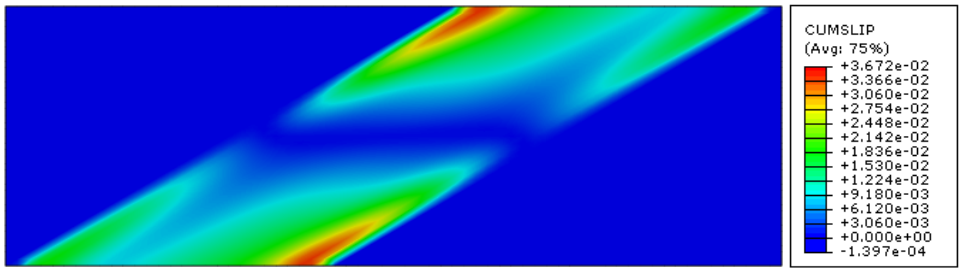

(b)

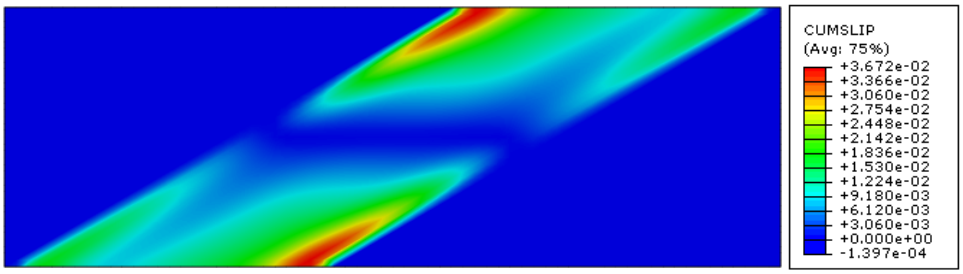

Figure 5.37: Contours of cumulative plastic slip for the calibrated single criterion model at $\Theta = 0.015$ for $\vartheta = 30°$ (a) $H = 2$ μm and (b) $H = 4$ μm.

(a)

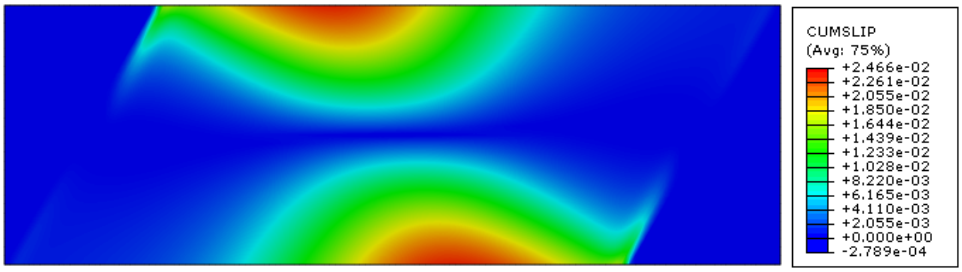

(b)

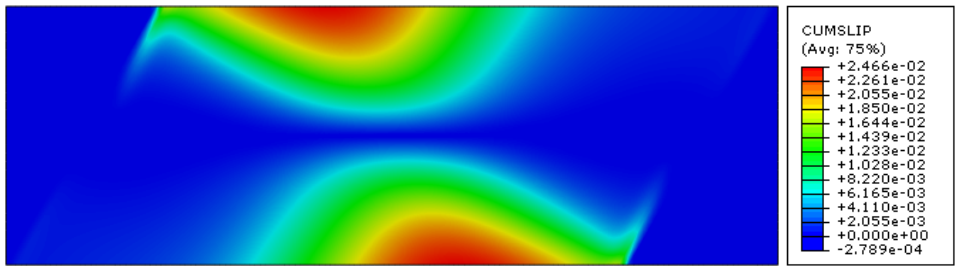

Figure 5.38: Contours of cumulative plastic slip for the calibrated single criterion model at $\Theta = 0.015$ for $\vartheta = 60°$ (a) $H = 2$ μm and (b) $H = 4$ μm.

The dislocation configurations predicted by the discrete dislocation simulations consist of a few populated slip planes in which large numbers of like-signed dislocations are arranged in long pile-up configurations as shown in Figure 5.35. As previously discussed, dislocations of both signs are emitted from the sources, but those not required for compatibility exit through the free surfaces. Therefore, the total dislocation density coincides with the GND density ($\varrho_S = 0$); an observation that is consistent with the predictions of the statistical dislocation crystal plasticity model of Yefimov et al. [168] (henceforth YVG). The dislocation density contour plot for both film thicknesses are shown in Figure 5.39 for ϑ_{30} at an $\Theta = 0.015$. The 2 μm thick film has a maximum local dislocation density of 39.8 μm^{-2} and the 4 μm thick film has a maximum value of 22.6 μm^{-2}, and both films exhibit clear dislocation-free zones along the neutral axis. The thickness of the dislocation-free region is approximately 3-4 times larger for the 4 μm thick film. It is also noted that the highly slipped regions for this crystal orientation, as shown in Figure 5.37, overlap with the regions of high dislocation density as shown in Figure 5.39 even though there is no slip-induced SSD generation for the single slip configuration.

Figure 5.40 shows the contour plots of the total dislocation density distribution at $\Theta = 0.015$ for the 4 μm thick film with ϑ_{30} as predicted by the model of YVG and the SC model, and good qualitative agreement is found with respect to the morphology of the distribution. The maximum local dislocation density predicted by YVG is approximately 68 μm^{-2}, which is three times larger than the 23 μm^{-2} predicted by the SC model. Although the peak local densities predicted by the micropolar model are substantially lower, it is demonstrated subsequently that the evolution of the total dislocation density computed over the entire film is captured quite well by the SC model as compared to the discrete dislocation results. These two observations imply that the dislocation distribution is more homogeneously distributed for the micropolar material; a fact that is underscored in the uncropped dislocation density plot in given in Figure 5.40(c). In addition to the heavily dislocated triangular-shaped lobes located on either side of the neutral axis, there are also mild dislocation distributions spread throughout the rest of plastic zone which are not present in the results of the YVG model. Figure 5.40 also shows that the YVG model develops distinct dislocation-free regions near the free surfaces, whereas the micropolar model does not. In fact, the micropolar model yields a rather high dislocation density at the free surfaces near the elastic-plastic

interfaces which are generated because of the strong rotational gradients that arise due to the compliance mismatch. The dislocation-free zones are seen in both the discrete dislocation and YVG nonlocal continuum models for this orientation, and are evidently a manifestation of an image force effect that naturally emerges in these theories. In fact, the lack of the image force effect in the micropolar model could potentially explain the lower dislocation density values that are observed. The image forces conceivably would force the dislocations contained in the outer layers of the foils towards the center of the film thereby increasing the maximum local density in the triangular lobe regions. Additionally, the image forces would serve to decrease the thickness of the dislocation-free zone predicted by the micropolar model which is seen to be 4-5 times thicker than that predicted by the YVG model. It is possible that such an image force effect might be achievable within the micropolar framework through an appropriately specified couple traction along the free surfaces; however, it is not apparent at this time as to how this would be accomplished.

(a)

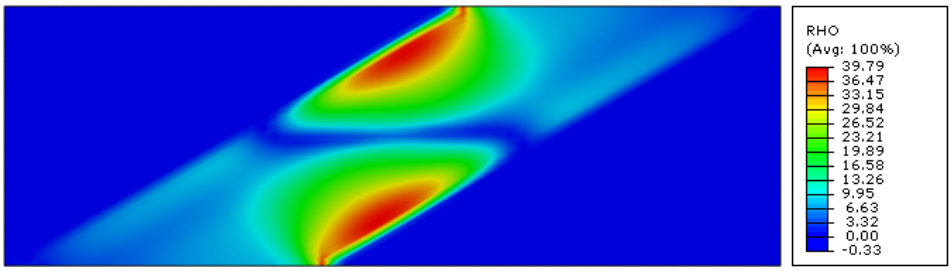

(b)

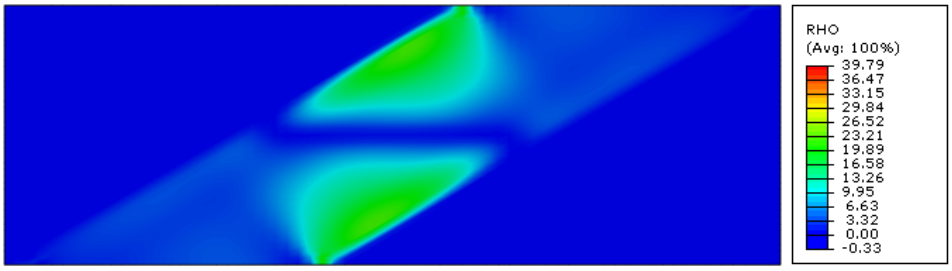

Figure 5.39: Contours of total dislocation density for the calibrated single criterion model at $\Theta = 0.015$ for $\vartheta = 30°$ (a) $H = 2$ μm and (b) $H = 4$ μm. Dislocation density is reported in units of μm^{-2}.

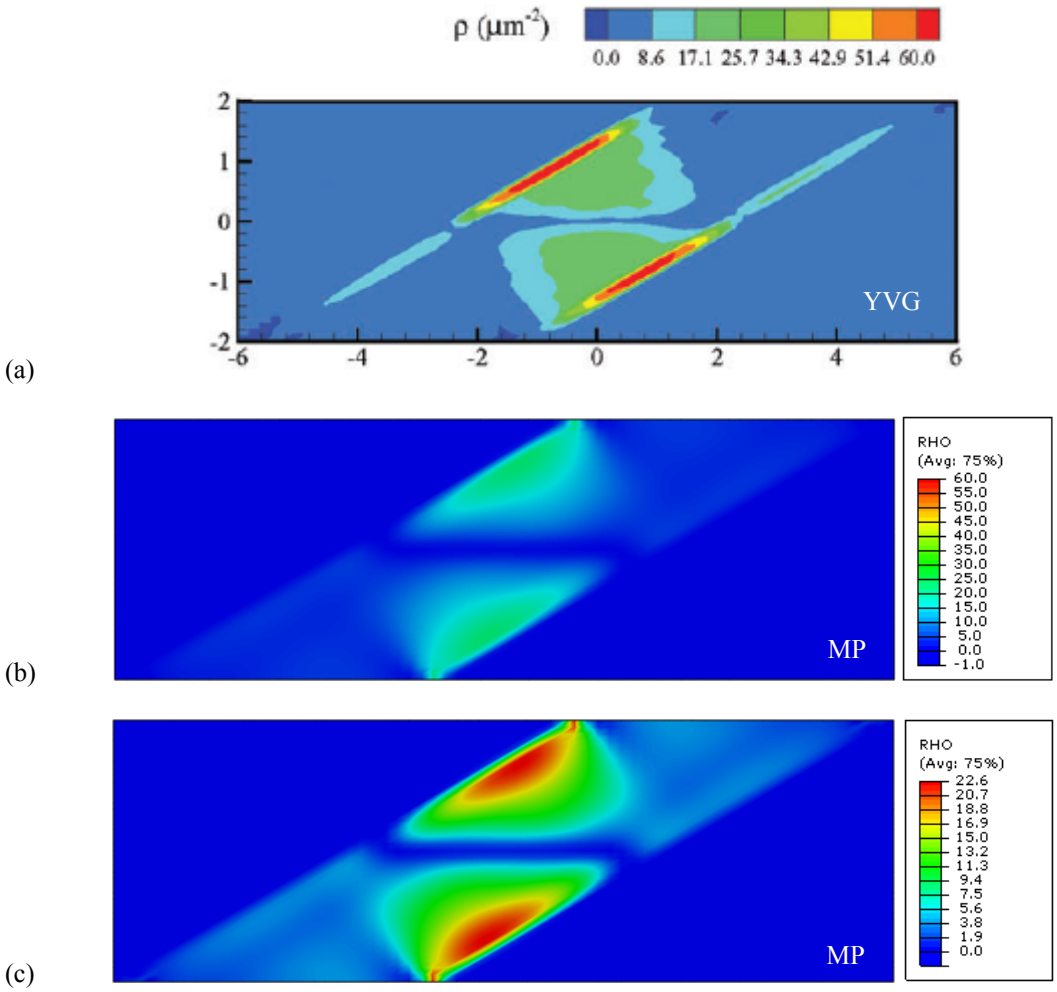

Figure 5.40: Contours of total dislocation density for $\vartheta = 30°$ at $\Theta = 0.015$ for the 4 μm thick film according to the (a) statistical dislocation dynamics model (YVG) [168] and (b) and (c) for the calibrated single criterion model (MP). Dislocation density is reported in units of μm^{-2}.

The total dislocation density contour plots for the ϑ_{60} films at $\Theta = 0.015$ are given for the SC model in Figure 5.41. The morphology of the dislocation density distribution for this crystal orientation is much different than that observed for the ϑ_{30} films, and can be characterized as ellipsoidal-shaped lobes that originate at the free surface corner of the elastic-plastic interface and extend (major axis of the ellipsoid) towards the neutral axis in the direction perpendicular to the elastic-plastic interface. The maximum dislocation density at this applied level of deformation is 160.3 μm^{-2} and 98.3 μm^{-2} for the 2 μm

and 4 μm thick films, respectively, and occurs at the free surface. This is in contrast to the films with ϑ_{30} where the maximum value of the dislocation density occurs in the center of the subsurface high intensity zone (see Figure 5.40(c)). It is also seen in Figure 5.41(a) that there is no dislocation-free zone adjacent to the neutral axis for the 2 μm thick film. Whereas the cumulative slip and dislocation density contours were quite similar in shape and hot-spot distribution for the ϑ_{30} films, the same cannot be said for the ϑ_{60} films whose corresponding distributions are markedly dissimilar as seen by comparing Figure 5.38 and Figure 5.41.

(a)

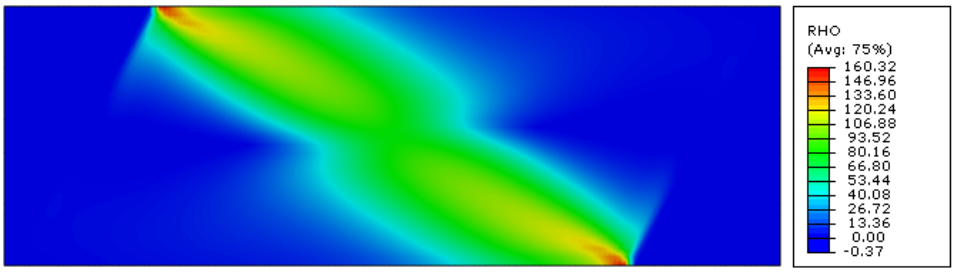

(b)

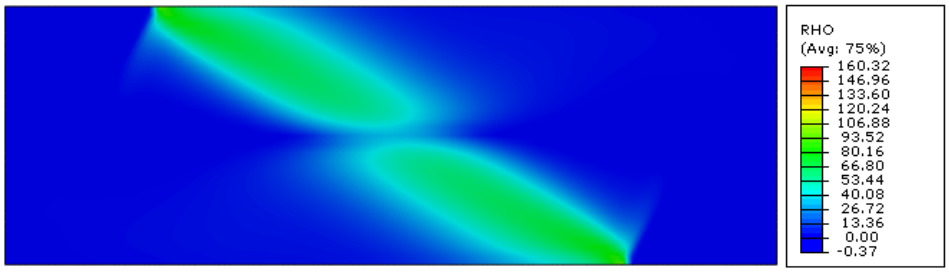

Figure 5.41: Contours of total dislocation density for the calibrated single criterion model at $\Theta = 0.015$ for $\vartheta = 60°$ (a) $H = 2$ μm and (b) $H = 4$ μm. Dislocation density is reported in units of μm^{-2}.

For comparison purposes, the dislocation density contours for the ϑ_{60} films are now plotted along with those obtained from the YVG model at $\Theta = 0.01$ as shown in Figure 5.42. As in the simulations with ϑ_{30}, the peak local values of the distribution predicted by the micropolar model are slightly lower than those obtained by the YVG model. The maximum values of dislocation density predicted by the

micropolar model are 50 μm^{-2} and 74 μm^{-2}, respectively, for the 4 μm and 2 μm thick films. The maximum local values of obtained by the YVG model are approximately 100 μm^{-2} for both film thicknesses, but for the 2 μm thick film there are several more hot spots located throughout the plastic zone as compared to the thicker film. Both models predict a broadening of the dislocation distribution (along the minor axis of the ellipsoid) and a reduction in the thickness of the dislocation-free zone with a decrease in the film thickness. The fields from the YVG model display a certain amount of discreteness as evidenced by the slip bands of alternating intensity, whereas the micropolar model gives much smoother dislocation fields. Unlike the situation for the films with ϑ_{30}, there does not appear to be a clearly defined dislocation-free region near the free surfaces predicted by the YVG model; however, the micropolar model still shows higher dislocation density contour levels along the free surface in comparison. Again, this is believed to be due to the lack of image force effects that are present in the YVG model, and according to the previous argument explains the discrepancies between the maximum local values of dislocation density obtained from the two models.

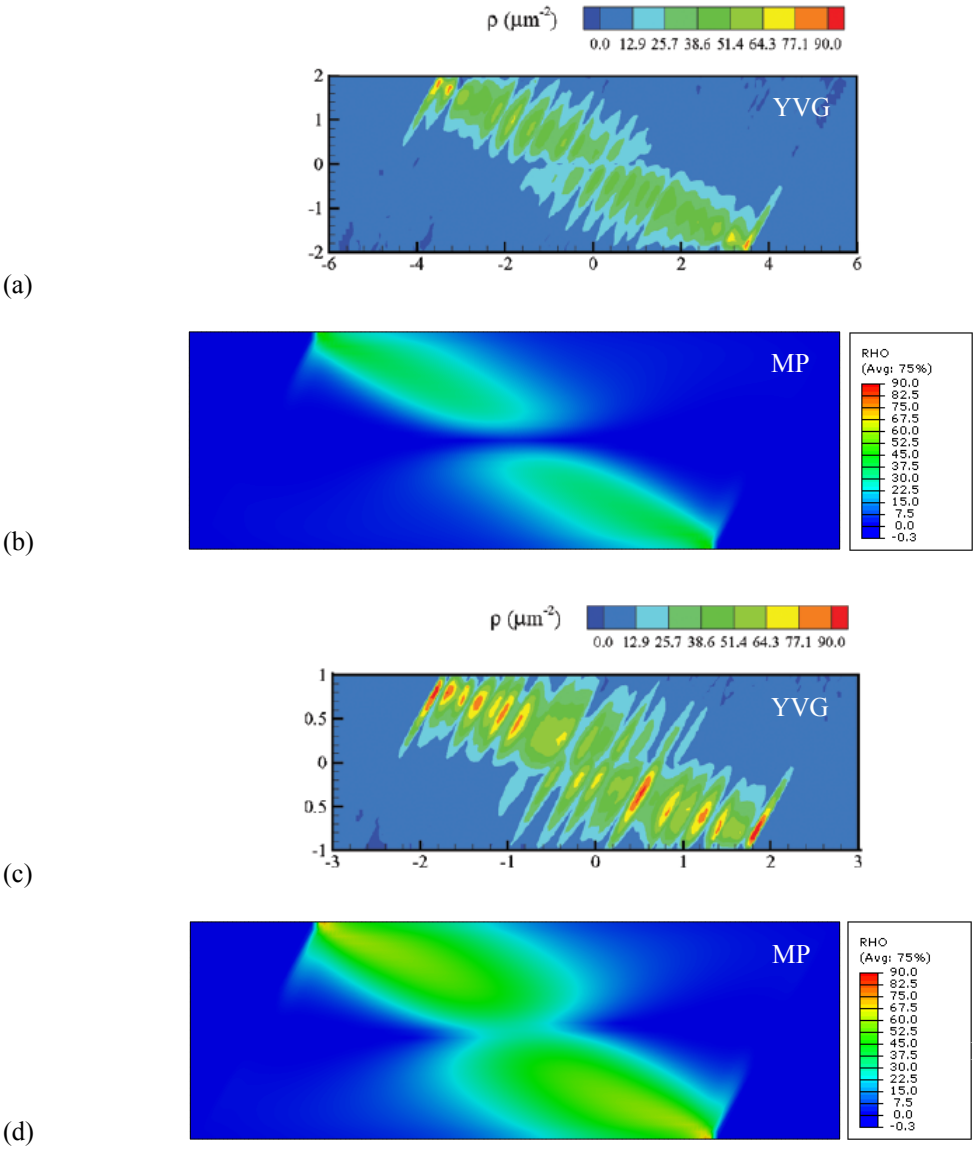

Figure 5.42: Contours of total dislocation density for $\vartheta = 60°$ at $\Theta = 0.01$ according to the statistical dislocation dynamics model (YVG) [168] for the (a) 4 μm and (c) 2 μm thick films and for the calibrated single criterion model (MP) for the (b) 4 μm and (d) 2μm thick films. Dislocation density is reported in units of μm^{-2}.

It has been demonstrated in Figure 5.40 and Figure 5.42, that the SC micropolar model generally underestimates the peak local values of dislocation density calculated using the YVG model by about a factor of 2-3. However, as shown in Figure 5.43, the micropolar model accurately captures the evolution of the total (computed over the entire volume) dislocation density as function of the imposed deformation.

The evolution of the total dislocation density is plotted for the 4 μm thick film for both crystal orientations as a function the rotation angle in Figure 5.439(a) and as a function of the macroscopic plastic curvature, K^{p}, in Figure 5.43(b). As shown by Nye [70] and Ashby [11] the theoretical GND density required for accommodating an imposed bending angle, Θ, can be calculated from knowledge of the average macroscopic plastic curvature which is defined as [172]

$$\mathrm{K}^{\mathrm{p}} = \frac{2\Theta}{W} - \frac{M}{EI} \tag{5.7}$$

where the plane strain bending stiffness is $EI = \mu H^3 / 6(1-\nu)$. The theoretical GND density is then defined as

$$\hat{\varrho}_G = \frac{\mathrm{K}^{\mathrm{p}}}{b_1} \tag{5.8}$$

where $b_1 = b\cos\vartheta$ is the magnitude of the x_1-component of the Burgers vector. The macroscopic plastic curvatures in Figure 5.43(b) have been calculated via Eq. (5.7) and the dislocation densities have been computed by volume averaging the centroidal element values over the FE mesh. It is seen in Figure 5.43(b) that in agreement with Eq. (5.8), the dislocation density increases in an approximately linear fashion with respect to the plastic curvature for both sets of simulations. Also, as expected from Eq. (5.8), the dislocation density at a given level of plastic curvature is higher for the ϑ_{60} film. Since the component of the Burgers vector along the axis of deformation is smaller for this orientation, more dislocations are needed to accommodate the deformation. Different ratios of L_p / ℓ_e have been used for each orientation to achieve good agreement with the discrete dislocation results shown in Figure 5.43. Recall that this ratio is directly related to the total dislocation density in the film with smaller values being associated with larger total densities. Changing either the elastic or plastic length scale while keeping their ratio fixed does not alter the total dislocation density of the film; therefore, using a fixed ratio for both orientations would lead to a disagreement between the micropolar and discrete dislocation results for one of the crystal orientations.

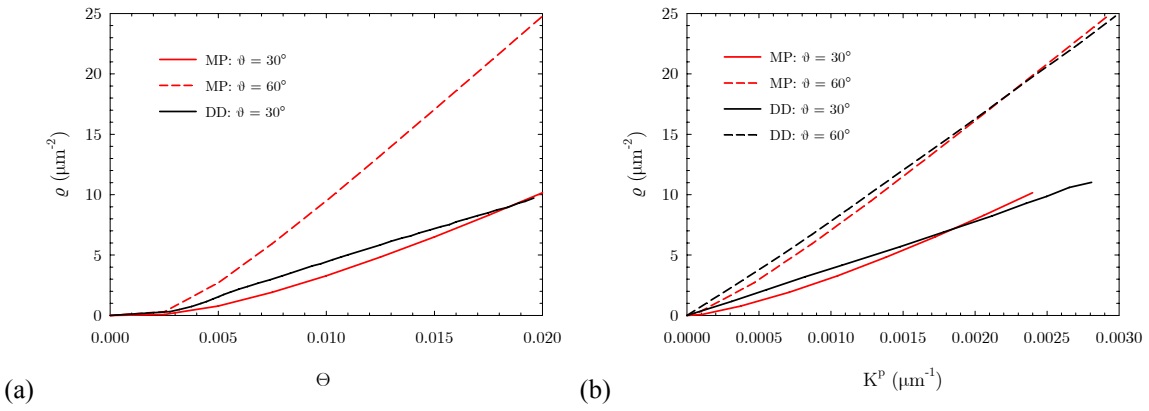

Figure 5.43: Evolution of the total dislocation density versus (a) imposed rotation angle (DD data are not available for $\vartheta = 60°$) and (b) macroscopic plastic curvature predicted by the calibrated single criterion (MP) and discrete dislocation (DD) [168] models for the 4 μm thick film.

Multicriterion Version 3 (MCV3)

The results of the calibrated multicriterion model (MCV3) are briefly presented prior to moving on to the study of the double slip configuration. An abbreviated discussion is warranted because there are only minor differences between the results of the SC and MCV3 micropolar models, and attention is focused on highlighting these differences as well as demonstrating their agreement with the discrete dislocation results. The adjustable model parameters for the MCV3 model are given in Table 5.7, and all of the parameters except for the plastic lengths scale are the same for both orientations. The initial curvature threshold and drag stresses have been chosen such that plastic curvature activates simultaneously with slip for the 4 μm thick film with ϑ_{60}, and such that the ratio of threshold stress to drag stress for slip and curvature are equal, i.e., $r_0 / g = r_{\perp 0} / g_{\perp}$. Figure 5.44 shows the normalized moment-rotation responses for the MCV3 model plotted against the discrete dislocation results and good agreement is demonstrated. The results are nearly identical to those of the SC model, but there is a higher hardening rate for the ϑ_{60} films for the MCV3 model.

Table 5.7: Calibrated MCV3 free model parameters used in the single slip pure bending simulations for an elastic-viscoplastic single crystal.

Parameter	Symbol	Magnitude	Unit
Reference slip threshold stress	r_0	10	MPa
Elastic length scale	ℓ_e	125	nm
Reference curvature threshold stress	$r_{\perp 0}$	1.4	MPa
Curvature drag stress	$g_{\perp}$	0.7	MPa
Plastic length scale ($\vartheta = 30°$)	L_p	150	nm
Plastic length scale ($\vartheta = 60°$)	L_p	70	nm

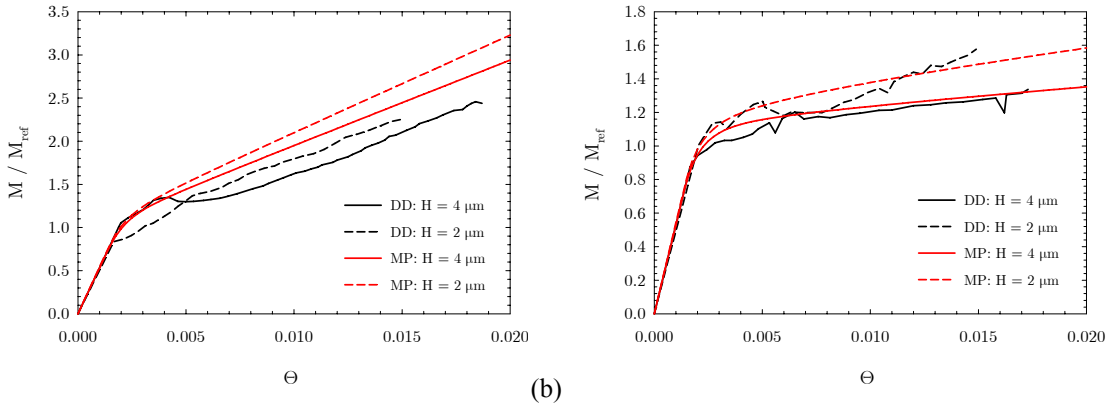

Figure 5.44: Normalized moment-rotation response for the calibrated mulit-criterion (MP) model for both film thicknesses plotted against the discrete dislocation dynamics results [168] for (a) $\vartheta = 30°$ and (b) $\vartheta = 60°$.

The cumulative slip fields for the MCV3 model are not shown as they are identical to those for the SC model shown in Figure 5.37 and Figure 5.38. Figure 5.45 gives the total dislocation density contour plots for the MCV3 model for the ϑ_{30} films at $\Theta = 0.015$, and are to be compared with the analogous contour plots for the SC model that are given in Figure 5.39. The dislocation density contours for the MCV3 model for both film thicknesses are contiguous across the neutral axis and therefore do not exhibit a dislocation-free zone at this level of deformation. Although the maximum local values of dislocation density are similar to that predicted by the SC model, 41 μm^{-2} and 28.3 μm^{-2} for the 2 and 4 μm thick films,

respectively, the contour hot spots have delocalized from a narrow band along the elastic-plastic interface and have begun to merge as demonstrated in Figure 5.45(a) for the 2 μm thick film. In contrast to the SC model, the maximum dislocation density values for the MCV3 model occur at the intersection of the elastic-plastic interface with the free surface. As compared to the dislocation density contour plot from the YVG model for the ϑ_{30} film that is shown in Figure 5.40(a), the SC model is seen to be in better agreement with this result.

(a)

(b)

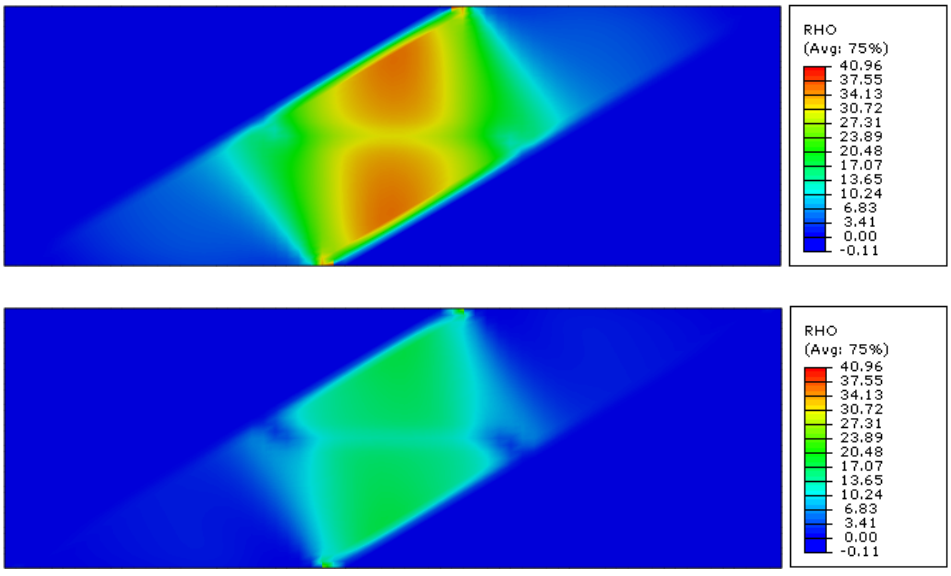

Figure 5.45: Contours of total dislocation density for the calibrated multicriterion model at $\Theta = 0.015$ for $\vartheta = 30°$ (a) $H = 2$ μm and (b) $H = 4$ μm. Dislocation density is reported in units of μm^{-2}.

In Figure 5.46, the dislocation density contours for the ϑ_{60} films at $\Theta = 0.01$ are shown for both the YVG and MCV3 models and they are seen to be in good agreement. The maximum dislocation densities, which occur at the intersection of the elastic-plastic interface with the free surface, are larger than those predicted by the SC model and are 95.8 μm^{-2} for the 2 μm thick film and 59.1 μm^{-2} for the 4 μm thick film. As was the case for the ϑ_{30} films, there is a negligible or non-existent dislocation-free zone adjacent

to the neutral axis for the MCV3 model, and as shown in Figure 5.46 is in good agreement with the result from the YVG model.

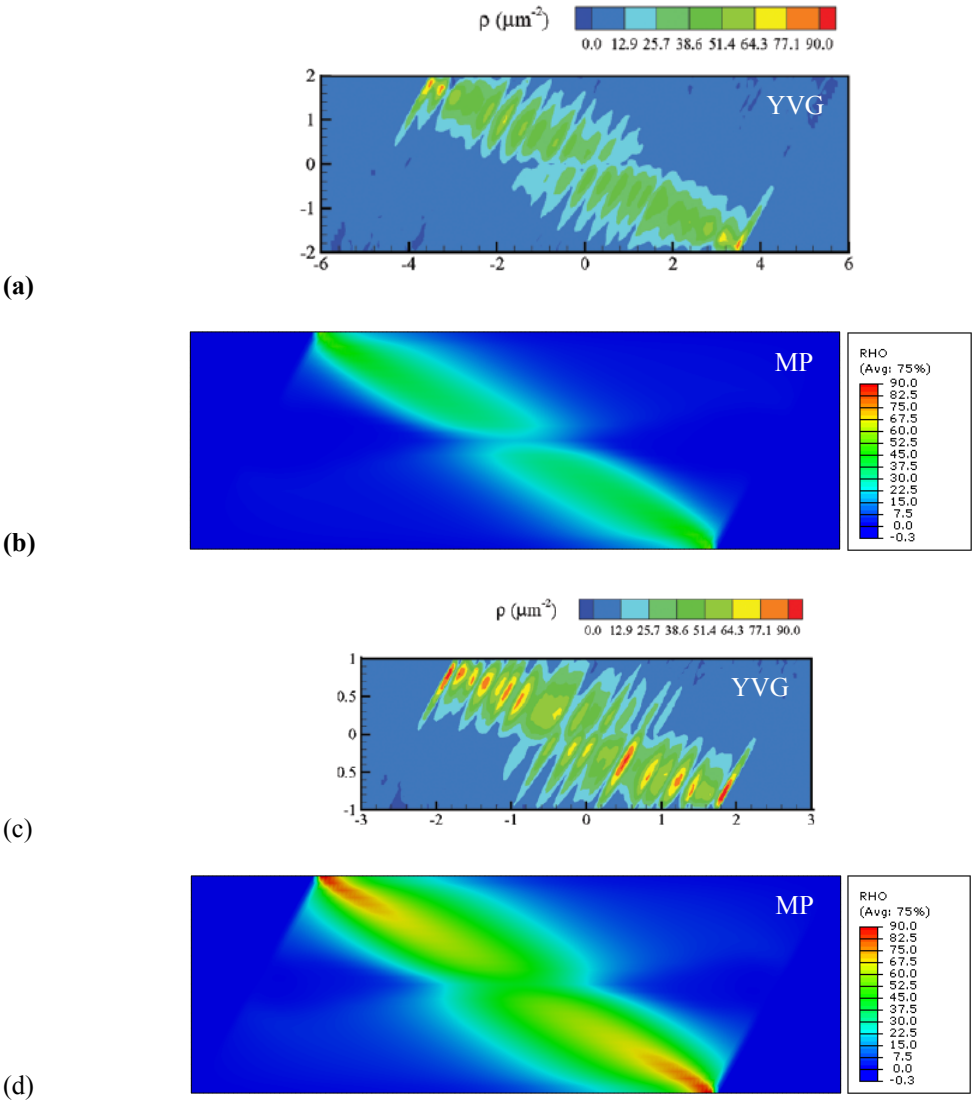

(a)

(b)

(c)

(d)

Figure 5.46: Contours of total dislocation density for $\vartheta = 60°$ at $\Theta =$ 0.01 according to the statistical dislocation dynamics model (YVG) [168] for the (a) 4 μm and (c) 2 μm thick films and for the calibrated multicriterion (MP) model for the (b) 4 μm and (d) 2μm thick films. Dislocation density is reported in units of μm^{-2}.

Finally, the evolution of the total film dislocation density calculated by both the discrete dislocation and MCV3 models is plotted as function of the imposed rotation and macroscopic plastic curvature for the 4 μm thick film as shown in Figure 5.47. The results from the MCV3 model are in good agreement with those available from the discrete dislocation simulations. It has been demonstrated that both the SC and MCV3 micropolar models are able to accurately reproduce the general deformation behavior, in terms of both the macroscopic response and the dislocation evolution density evolution. While there are subtle differences between the deformation fields predicted by the two micropolar models, there does not seem to be a distinct advantage of one versus the other than the fact that the single criterion model requires fewer model parameters and is therefore easier to calibrate. That being said, a scenario could arise such that the increased flexibility of the multicriterion is necessary and/or desirable. This type of situation has not been encountered this research and the single criterion model will be exclusively employed for the remainder of this work unless otherwise noted.

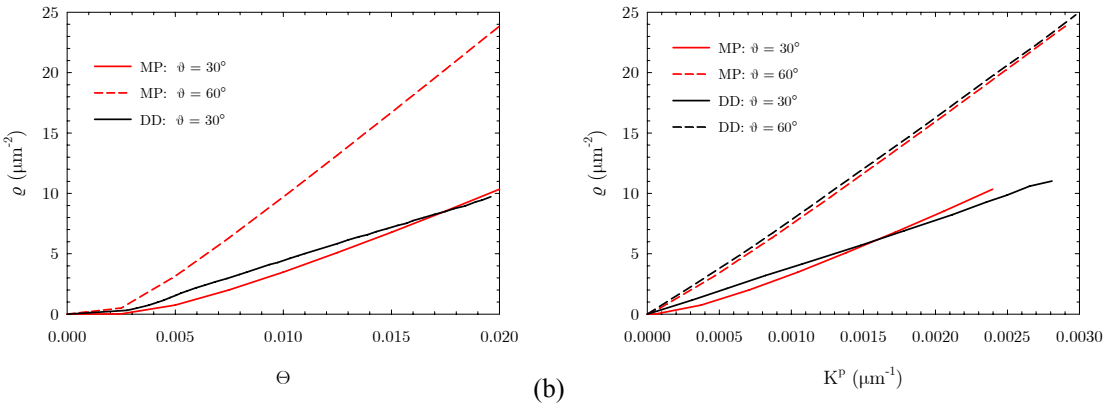

Figure 5.47: Evolution of the total dislocation density versus (a) imposed rotation angle (DD data is not available for $\vartheta = 60°$) and (b) macroscopic plastic curvature predicted by the calibrated multicriterion (MP) and discrete dislocation (DD) [168] models for the 4 μm thick film.

Attention is now turned to the double slip configuration shown in Figure 5.48 As in the single slip case, two orientations are considered, ϑ_{30} and ϑ_{60} where the orientation angle is defined as before as the

angle between the x_1-axis and the slip direction for slip system 1. For each orientation, the second slip system is symmetrically aligned with respect to the x_2-axis, and the angle between the x_1-direction and the slip direction for the second system is 150° for ϑ_{30} and 120° for ϑ_{60}. The films have been partitioned into distinct elastic and plastic zones as before and in analogy to the discrete dislocation and statistical dislocation crystal plasticity simulations performed by Yefimov and Van der Giessen [162] (henceforth YV). The elastic zones are the triangular regions located at the top, bottom, left, and right ends of the film as shown in Figure 5.48, and each slip system is active in the diagonal strip of material parallel to the slip direction as also indicated in the Figure. For slip system 1, this diagonal strip extends from the lower left hand corner to the upper right hand corner of the film, and for slip system 2 the diagonal strip extends from the upper left hand corner to the bottom right hand corner. The plastic zone can be divided into five regions: four single slip regions (two for each slip system) that are the outermost regions of the diagonal strips and a double slip region located at the intersection of the two diagonal strips which is indicated by the blue dotted lines in Figure 5.48. The boundary conditions, analysis methods, and FE meshes are the same as for the single slip configuration. Two different film thicknesses are simulated, $H = 4$ μm and 8 μm, with the ratio $W / H = 3$ fixed.

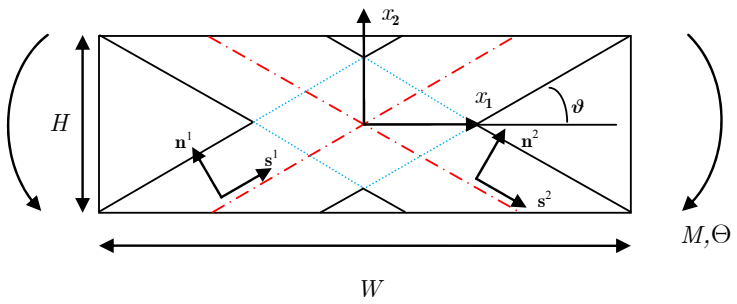

Figure 5.48: Schematic of the geometry and slip system configuration for the double slip bending simulations as used in Yefimov and Van der Giessen [162].

Distinct from the simulations performed for the single slip configuration and because of the potential for slip system interaction in the double slip configuration, slip system hardening due to SSD evolution cannot be ignored. The interaction of dislocations on intersecting slip planes is clearly evident in the dislocation distributions obtained from discrete simulations and shown for both orientations in Figure 5.49. This presents an additional complexity as compared to the single slip configuration as the material parameters governing the SSD generation, annihilation, and contribution to slip threshold hardening must be determined in addition to the usual free parameters for the single criterion model, i.e., $\{ r_0, \ell_e, L_\perp \}$. The additional material parameters that must specified are: c_1, $h^{\alpha\beta}$, ϱ_{S0}, $a^{\alpha\beta}$, K, and y_c. Most of these material parameters are known and/or can be specified with confidence based on typical values used in the literature. Accordingly, the dislocation segment length constant, K, is taken to be the only additional fitting parameter. The fixed material parameters for the double slip configuration micropolar simulations are listed in Table 5.8, and the calibrated free parameters are given with along with the discussion of results. The dislocation interaction and immobilization coefficients are assumed to be isotropic, i.e., $h^{\alpha\beta} = a^{\alpha\beta} = 1$. All simulation results for the double slip configuration have been obtained with the single criterion model.

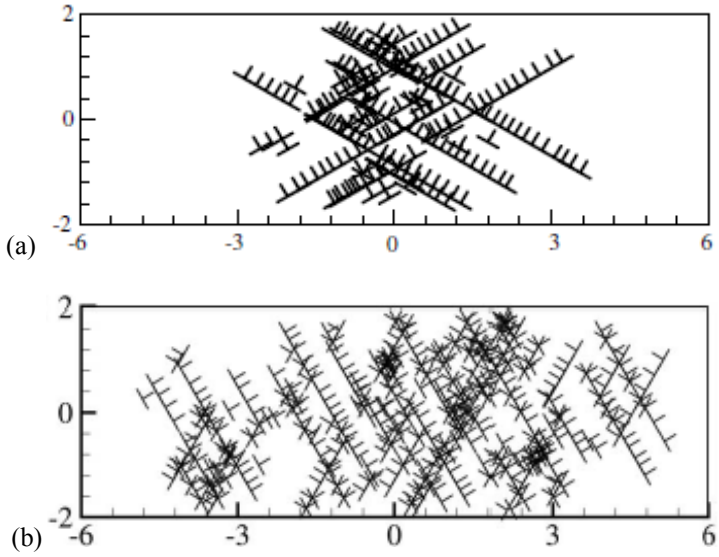

Figure 5.49: Dislocation distributions at $\Theta = 0.015$ for the 4 μm thick films for (a) $\vartheta = 30°$ and (b) $\vartheta = 60°$ as obtained from the discrete dislocation simulations [162].

Table 5.8: Fixed SC model parameters used in the double slip pure bending simulations for an elastic-viscoplastic single crystal.

Parameter	Symbol	Magnitude	Unit
Shear modulus	μ	26.3	GPa
Poisson's ratio	ν	0.33	-
Coupling parameter	N_c	0.95	-
Threshold stress strength coefficient	c_1	0.5	-
Burgers vector magnitude	b	0.25	nm
Dislocation interaction coefficients	$h^{\alpha\beta}$	1.0	-
Initial SSD density	ϱ_{S0}	10^{-6}	μm^{-2}
Dislocation immobilization coefficients	$a^{\alpha\beta}$	1.0	-
Dislocation capture radius	y_c	1.5	nm
Reference slip rate	$\dot{\gamma}_0$	10^{-3}	s^{-1}
Drag stress	g	5	MPa
Inverse rate sensitivity exponent	m	20	-

The calibrated normalized moment-rotation responses for both film thicknesses and both orientations are shown in Figure 5.50 for the micropolar and discrete dislocation models. The calibrated free fitting parameters are listed in Table 5.9, and in contrast to the single slip bending simulations different

elastic length scales have been specified for each orientation. Different dislocation segment length constants, i.e., those that govern SSD production, have been used for each orientation as well. It is noted that the micropolar model has been fitted to the average post-yield behavior instead of the initial yield point. The response in terms of both the initial yield point and hardening rate is similar for both orientations unlike the single slip configuration, where the hardening rate was much higher for the ϑ_{30} films due to larger effective film thickness resulting from the dominant influence of the elastic regions. The scale-dependence of the macroscopic behavior is more pronounced for the ϑ_{60} films as demonstrated in Figure 5.50(b).

Table 5.9: Calibrated SC free model parameters used in the double slip pure bending simulations for an elastic-viscoplastic single crystal.

Parameter	Symbol	Magnitude	Unit
Reference slip threshold stress	r_0	10	MPa
Elastic length scale ($\vartheta = 30°$)	ℓ_e	300	nm
Elastic length scale ($\vartheta = 60°$)	ℓ_e	600	
Dislocation segment length constant ($\vartheta = 30°$)	K	160	
Dislocation segment length constant ($\vartheta = 60°$)	K	26	
Plastic length scale ($\vartheta = 30°$)	L_p	750	nm
Plastic length scale ($\vartheta = 60°$)	L_p	700	nm

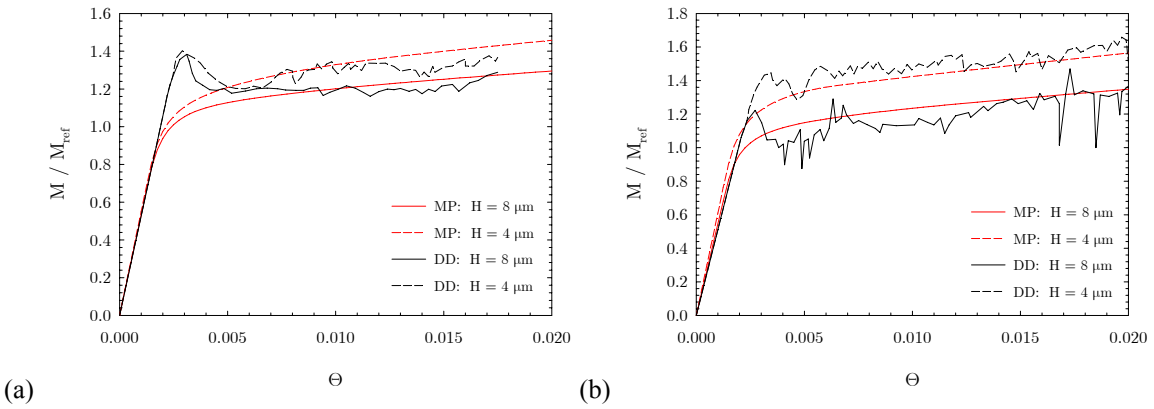

Figure 5.50: Normalized moment-rotation response for the calibrated single criterion model (MP) for both film thicknesses plotted against the discrete dislocation dynamics (DD) results [162] for (a) $\vartheta = 30°$ and (b) $\vartheta = 60°$.

Contours of the SSD density fields for the ϑ_{30} films are given in Figure 5.51 as obtained from the micropolar model at $\Theta = 0.02$. The contours show maximums in the SSD density located along the free surfaces in the outer quadrants where single slip is taking place, and the majority of the SSD density is seen to be stored in these quadrants as opposed to the central region of the film where slip system interaction should be the strongest. There is almost negligible scale-dependence of the SSD density distribution with the only noticeable difference being the slight increase in intensity of the circular nodules located at the top and bottom corners of the diamond-shaped double slip region for the 4 μm thick film. The maximum SSD densities are 0.069 μm^{-2} and 0.066 μm^{-2} for the 4 μm and 8 μm thick films, respectively.

(a)

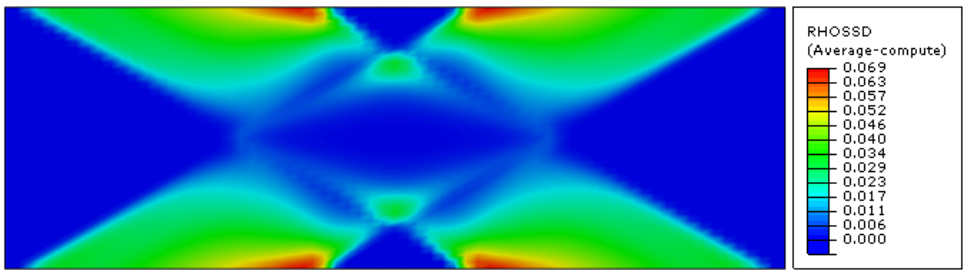

(b)

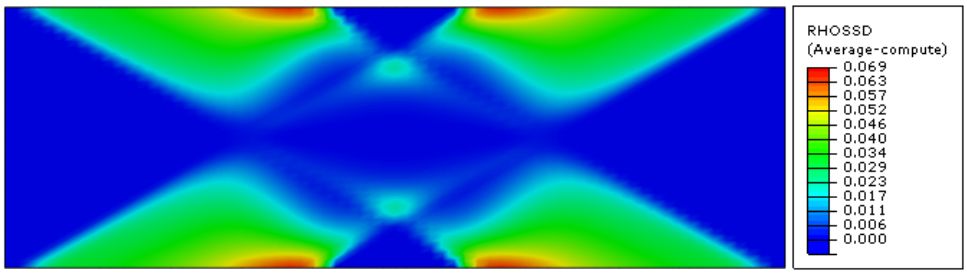

Figure 5.51: Contours of SSD density for the calibrated single criterion model at $\Theta = 0.02$ for $\vartheta = 30°$ (a) $H = 4$ μm and (b) $H = 8$ μm. Dislocation density is reported in units of μm^{-2}.

Figure 5.52 shows the total dislocation density contour plots for the ϑ_{30} films at $\Theta = 0.02$, and it is revealed that the magnitude of the total dislocation density field is approximately three orders of magnitude larger than that of the SSD density field indicating that the total density field is predominantly geometrically necessary. The peaks in total density occur at the free surfaces near the centrally located elastic-plastic interfaces for both film thicknesses, and the maximum values are 57.7 μm^{-2} and 32.3 μm^{-2} for the 4 μm and 8 μm thick films, respectively. In the case of the 8 mm thick film, there is dislocation-limited region (not dislocation-free) adjacent to the neutral axis in between the regions of higher dislocation density, whereas the high intensity regions have merged and become interconnected for the 4 μm thick film. Recall that the dislocation density fields that develop for the single slip configuration, as shown in Figure 5.39, have maximum dislocation density values in the subsurface region and high intensity zones of dislocation density that grow parallel to and alongside the elastic-plastic interface. On the other hand, the maximum dislocation density values for the double slip configuration occur at the free surfaces, as shown in Figure 5.52(a), and there are bands of dislocations of slightly lower intensity that grow inward and nearly perpendicular to the slip direction for any given quadrant.

(a)

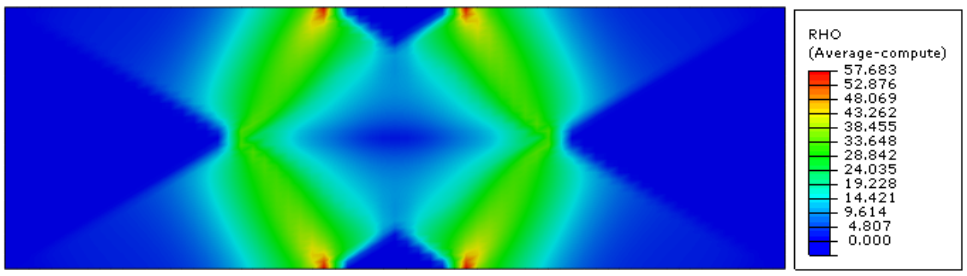

(b)

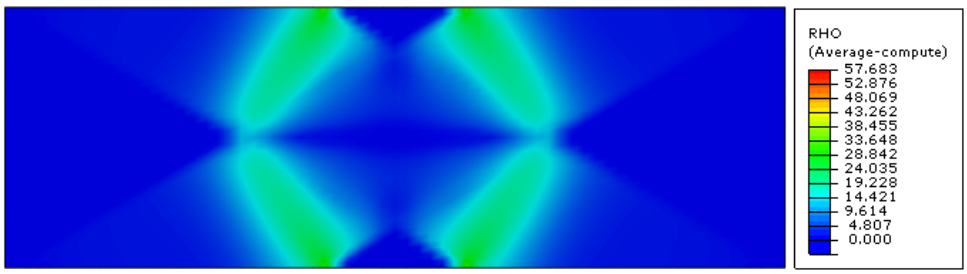

Figure 5.52: Contours of total dislocation density for the calibrated single criterion model at $\Theta = 0.02$ for $\vartheta = 30°$ (a) $H = 4$ μm and (b) $H = 8$ μm. Dislocation density is reported in units of μm^{-2}.

In Figure 5.53 the total and GND density fields on slip system 1 are plotted for both the micropolar and YV models at $\Theta = 0.015$ for the 4 μm thick film. Once again, the micropolar model underestimates the maximum local values of both the total and GND density, and recall that this is believed to be due to the lack of an image force effect in the micropolar framework. As in the single slip configuration, there are significant dislocation-free regions near the free surfaces in the results of YV as shown in Figure 5.53(a) and (c), but the micropolar model, as most clearly shown in Figure 5.53(b) yields a more uniform distribution of the dislocation density from the bottom to the top of the film. Although it is hard to see from the figure, since the micropolar results have been plotted on the same contour scale as the YV results, the morphologies of the total dislocation density distributions are in good agreement as can be inferred from comparing the uncropped total dislocation density contour plot given in Figure 5.52(a) to that given for the YV model in Figure 5.53(a). The general shape of the GND density distribution and the location of hot spots for the micropolar model are also found to be in general agreement with that shown in Figure 5.53(c). The most notable difference between the dislocation density fields (both total and GND) predicted by both models is that the micropolar model does not capture the appropriate relative intensity of

the dislocation density bands parallel to the slip direction and located in the central, double slip zone. This would be rectified through the image force effect which would serve to concentrate the dislocation density fields in more central regions of the film.

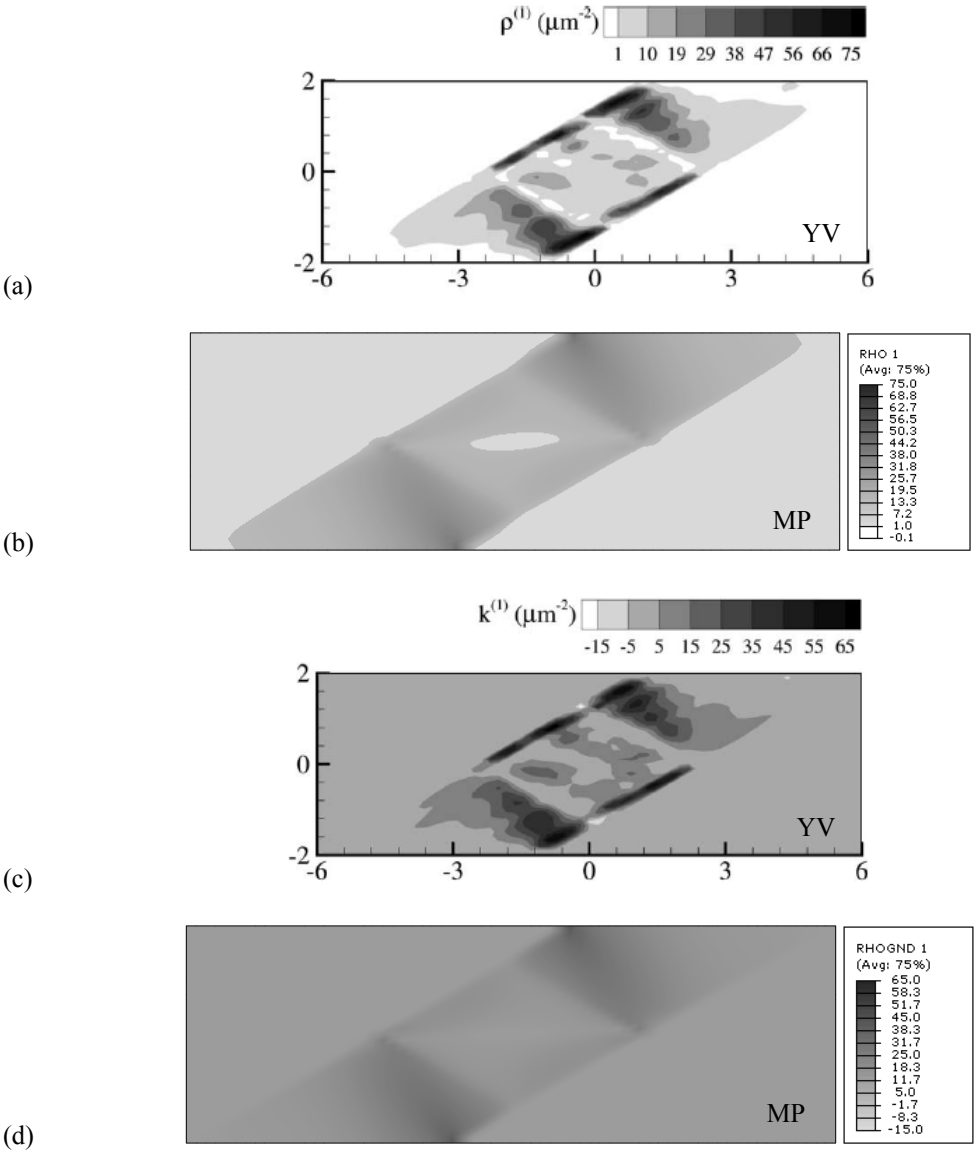

Figure 5.53: Contours of dislocation density on slip system 1 at $\Theta = 0.015$ for the 4 μm thick film: (a) total dislocation density for the statistical dislocation dynamics model (YV) [162] (b) total dislocation density for the calibrated single criterion model (MP) (c) GND density for the statistical dislocation dynamics model and (d) GND dislocation density for the calibrated single criterion model.

The micropolar model SSD density fields are plotted for the ϑ_{60} films at $\Theta = 0.02$ in Figure 5.54. The maximum values of the SSD density, which occur at the free surfaces and are relatively size-independent, are 2.38 μm^{-2} and 2.28 μm^{-2} for the 4 μm and 8 μm thick films, respectively. While the maximum SSD density values do not vary much with changes in film thickness, Figure 5.54 shows that the localized corner regions of high density in the 8 μm thick film transition into a more uniformly distributed high intensity band spreading across the top and bottom surfaces of the 4 μm thick film. In contrast to the films with ϑ_{30}, there are large, pronounced SSD density-free zones located at the center of the ϑ_{60} films. It is also noted that the magnitude of the SSD density field is larger for the ϑ_{60} oriented crystals, but this is expected since a smaller value of K (more SSD generation) has been used for this orientation.

(a)

(b)

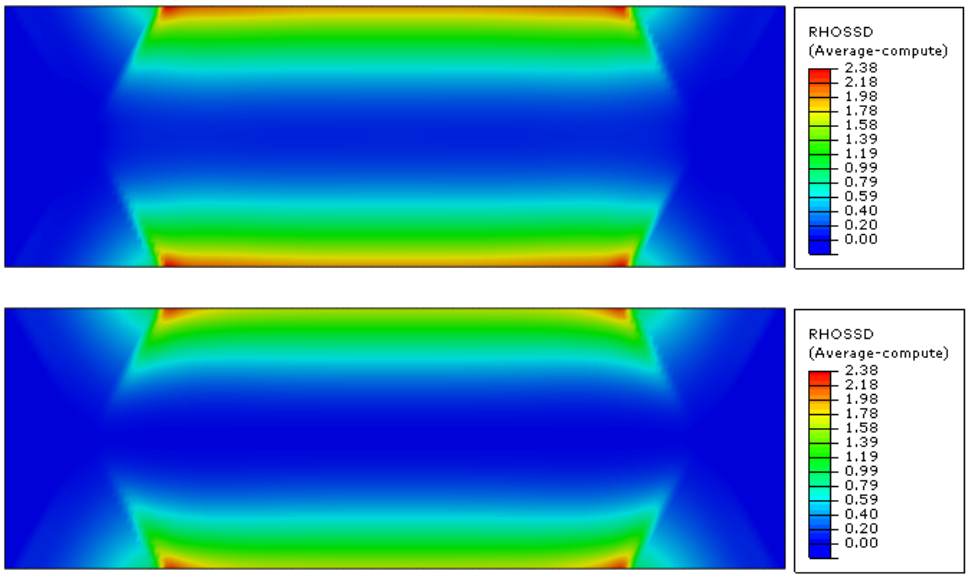

Figure 5.54: Contours of SSD density for the calibrated single criterion model at $\Theta = 0.02$ for $\vartheta = 60°$ (a) $H = 4$ μm and (b) $H = 8$ μm. Dislocation density is reported in units of μm^{-2}.

The total dislocation density fields for the ϑ_{60} oriented films are plotted for the micropolar model at $\Theta = 0.02$ in Figure 5.55, and for the YV and micropolar models $\Theta = 0.015$ in Figure 5.56. As

evidenced by the magnitude of the total dislocation density, it is again concluded that the overwhelming majority of the density field is geometrically necessary. The maximum total dislocation density values occur at the free surfaces for both film thicknesses and are given as 53.9 μm^{-2} and 22.9 μm^{-2} for the 4 μm and 8 μm thick films, respectively. The geometrical configuration of the elastic and plastic phases for the ϑ_{60} oriented crystal is such that there is no centrally located elastic zone. Therefore, as shown in Figure 5.54 and Figure 5.55, the dislocation density fields are continuous and smooth, whereas for the ϑ_{30} orientation the dislocation density contours have a checkered type of pattern. As shown in Figure 5.54, there is a narrow dislocation-free zone adjacent to the neutral axis for the 8 μm thick film; however, no such region exists for the 4 μm thick film. Figure 5.56 demonstrates that the total dislocation density field predicted by the micropolar model for the ϑ_{60} oriented crystal is good general agreement with the YV model for the 4 μm thick film, although the by now usual discrepancies between the two models results are present. Namely, there is no image force effect and associated dislocation stand-off distance near the free surfaces in the micropolar model, and therefore the maximum local values of dislocation density are underestimated. Additionally, the YV model results show a slight decrease in the intensity of the dislocation density along the neutral axis of the film as seen in Figure 5.56(a) that is not present in the micropolar model results.

(a)

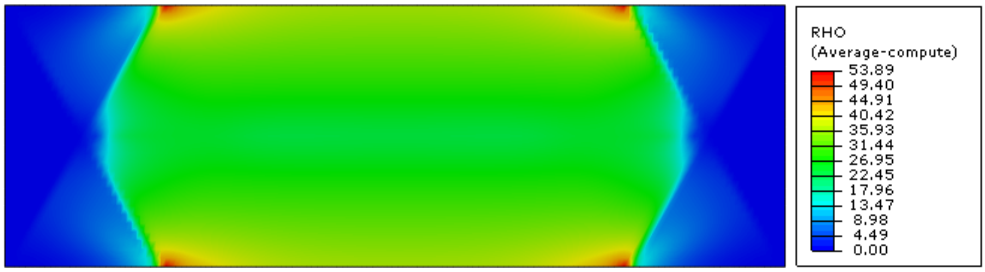

(b)

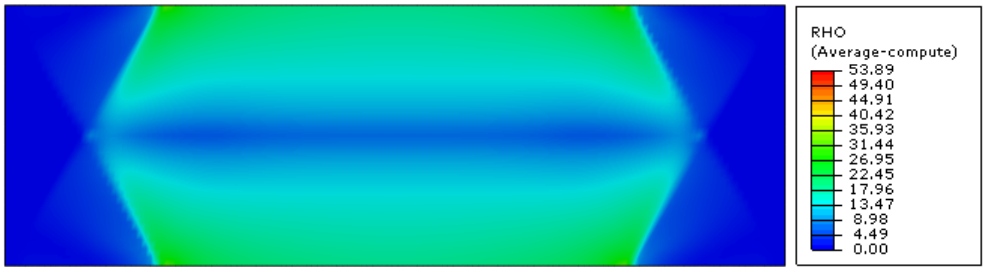

Figure 5.55: Contours of total dislocation density for the calibrated single criterion model at $\Theta = 0.02$ for $\vartheta = 60°$ (a) $H = 4$ μm and (b) $H = 8$ μm. Dislocation density is reported in units of μm^{-2}.

(a)

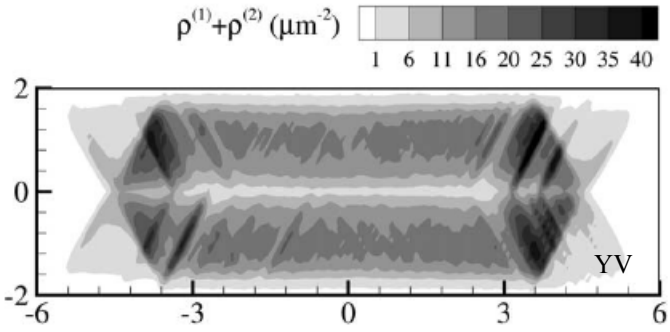

(b)

Figure 5.56: Contours of total dislocation density on both slip systems at $\Theta = 0.015$ for the 4 μm thick film for (a) the statistical dislocation dynamics model (YV) [162] and (b) calibrated single criterion model (MP).

The evolution of the total film dislocation density is plotted for both film orientations and thicknesses versus the macroscopic plastic curvature in Figure 5.57(a) and (b), respectively, and the total versus the applied rotation for the 4 μm thick film in Figure 5.57(c). In general, the micropolar results compare favorably to the discrete dislocation results, but slightly underestimate the total dislocation densities. The micropolar model is able to capture the change in slope of the dislocation density-plastic curvature plot with the change in thickness for the ϑ_{30} oriented films (see Figure 5.57(a)), but not for the ϑ_{60} oriented films (see Figure 5.57(b)). The dislocation density-plastic curvature plots obtained from the micropolar model for the ϑ_{60} oriented films overlap, whereas the discrete dislocation curve for the 8 μm thick film shows an increase in slope with increasing macroscopic plastic curvature, while the slope for the 4 μm remains essentially constant. It is unclear as to why the micropolar model does not predict a similar trend for this orientation. The evolution of the total film dislocation density as a function of the applied rotation angle for the 4 μm thick film according to the micropolar model and discrete dislocation model is given in Figure 5.57(c), and the micropolar model demonstrates excellent agreement with discrete dislocation result for the ϑ_{30} oriented film. No discrete dislocation data are available for the ϑ_{60} oriented film.

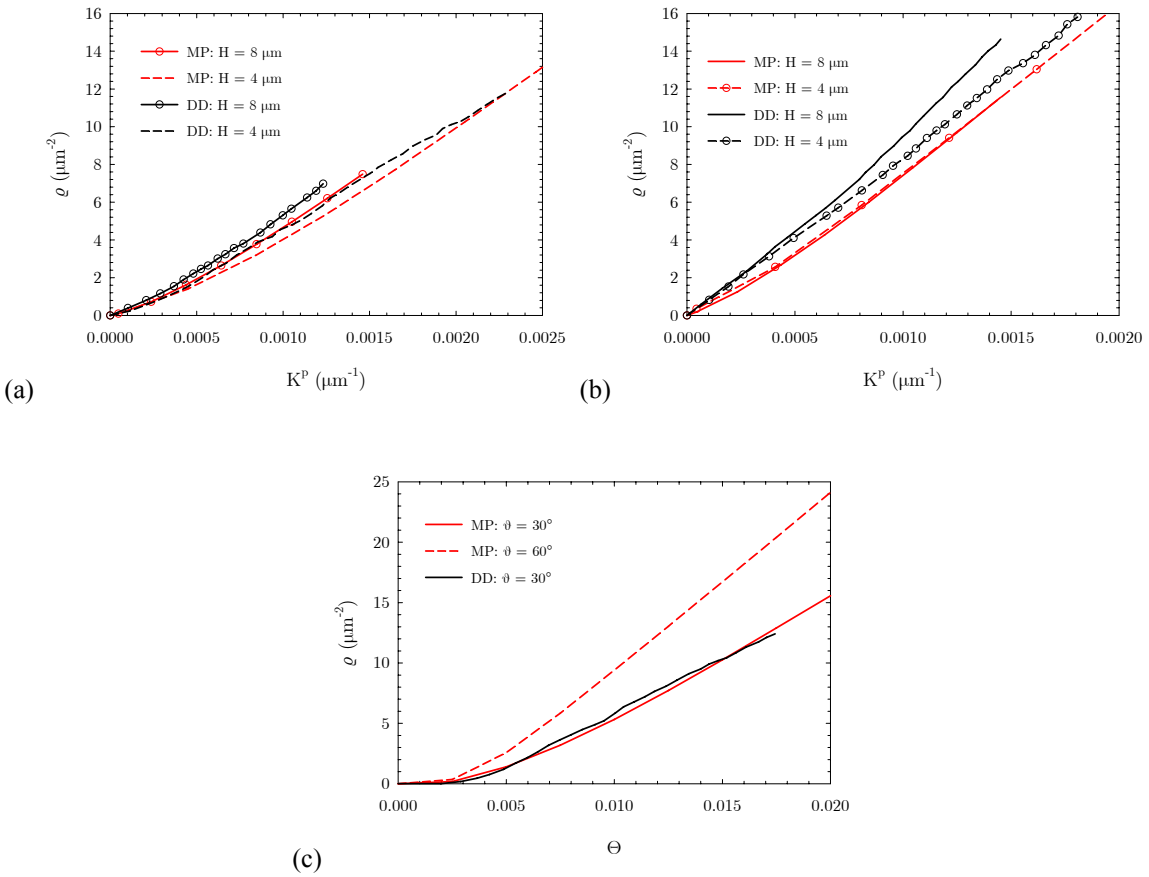

Figure 5.57: Evolution of the total film dislocation density versus macroscopic plastic curvature as predicted by the calibrated single criterion (MP) and discrete dislocation (DD) [162] models (a) $\vartheta = 30°$ and (b) $\vartheta = 60°$ and (c) versus the imposed rotation angle (DD data are not available for $\vartheta = 60°$). $H = 4$ μm.

5.3.3 Simple Shear of a Metal Matrix Composite

This section presents a comparison of the micropolar model to discrete dislocation simulations of particle strengthening in metal matrix composites. An idealized material system is considered as shown in Figure 5.58, and consists of an elastic-plastic matrix phase (white) with a single slip system parallel to the x_1-direction that is reinforced by a periodic distribution of elastic particles (gray). Due to the periodicity of the microstructure, a unit cell of dimensions $2W \times 2H$ ($W = H\sqrt{3}$) is modeled and the particles have

dimensions of $2W_f \times 2H_f$. Two distinct particle morphologies with different aspect ratios but the same area fraction, $A_f = 0.2$, are studied:

I. Square particles where $W_f = H_f = 0.416\,H$.

II. Rectangular particles where $H_f = 2\,W_f = 0.588\,H$

The key distinction between the two morphologies is that there is an unobstructed vein of matrix material that extends from one side of the unit cell to the other for Material I, whereas no such clear path exists for Material II (as demonstrated in Figure 5.58). Therefore, any differences in material strengthening that are observed for the two materials are due to heterogeneous deformation (phase morphology) and not phase volume fraction effects. In the analysis, the unit cells are subjected to simple shear through horizontal displacements applied to top and bottom surfaces and periodic conditions are enforced in the x_1-direction. This initial-boundary value problem was initially posed and analyzed via discrete dislocation dynamics by Cleveringa et al. [183, 184]. Subsequent works devoted to the comparison of various nonlocal crystal plasticity solutions to the discrete dislocation results have been carried out by Bassani et al.[185], Bittencourt et al. [23], and Yefimov et al. [74]. Related numerical studies of sub-micron scale crystal plasticity and mechanical size-effects for two-phase elastic-plastic composites have been carried out by Shenoy et al. [186], Needleman and Van der Giessen [187], Forest and Sedlacek [39], Schwarz et al. [188], Yassar et al. [189], and Taupin et al. [190]. The current analysis is carried out in accord with and to be compared to the discrete dislocation simulations of Yefimov et al. [74].

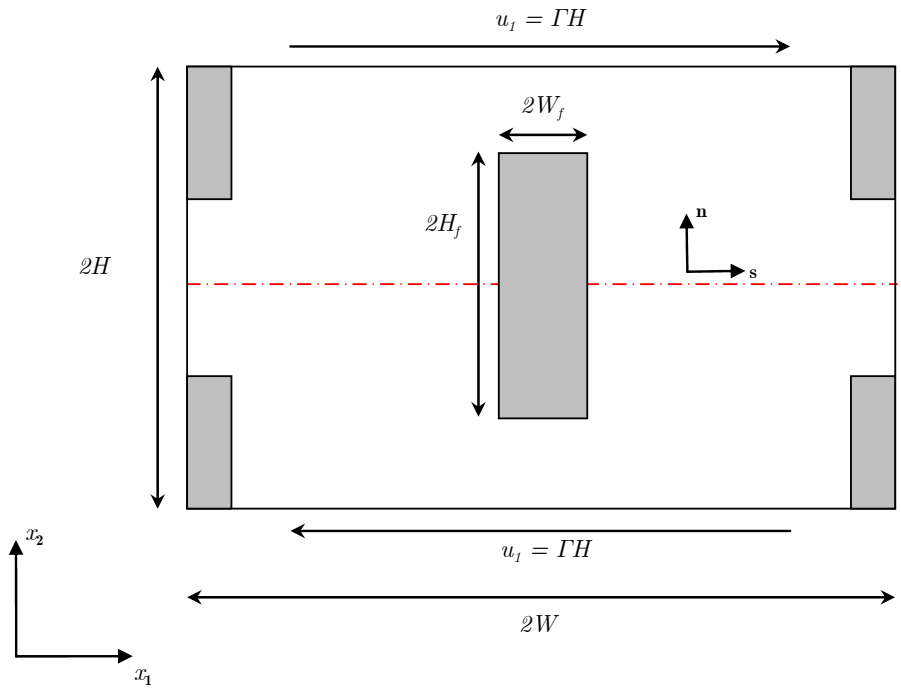

Figure 5.58: Schematic of the geometry and slip system configuration for the metal matrix composition initial-boundary value problem as outlined in Yefimov et al. [74].

The 2-D unit cell is deformed in plane strain simple shear which is prescribed through displacements applied in the x_1-direction to the top and bottom surfaces. The unit cell is subjected to macroscopic shear strain of $\Gamma = 0.01$ which is applied at a rate of $\dot{\Gamma} = 10^{-3}$ s^{-1} and then unloaded back to zero strain. The top and bottom surfaces are restrained against vertical displacements and periodic conditions are applied on the lateral faces. The boundary conditions are stated as

$$u_1(x_1, \pm H, t) = \pm\Gamma(t)H \quad , \quad u_2(x_1, \pm H, t) = 0 \tag{5.9}$$

$$\begin{gathered} u_1(-W, x_2, t) = u_1(W, x_2, t) \quad , \quad u_2(-W, x_2, t) = u_2(W, x_2, t) \\ \bar{\phi}(-W, x_2, t) = \bar{\phi}(W, x_2, t) \end{gathered} \tag{5.10}$$

Baseline simulations are performed for Materials I and II with a unit cell half-height of $H = C = 4000\,b$, and additional simulations are performed for Material II with $H = 0.5\,C$ and $H = 2\,C$ to study the size-

dependence of the mechanical response. Results from simulations of Material I for different unit cell sizes are not shown because they do not elicit scale dependence due to the geometrical configuration of the particles. The FE mesh consists of 106×61 bilinear quadrilateral elements, and all simulations have been performed with the single criterion micropolar model. The material parameters used in the simulations are given in Table 5.10, and are representative of silicon carbide particles embedded in an aluminum matrix [184].

Table 5.10: Material parameters used in the metal matrix composite simulations for an elastic-viscoplastic single crystal matrix phase.

Parameter	Symbol	Magnitude	Unit
Shear modulus	μ	26.3	GPa
Poisson's ratio	ν	0.33	-
Coupling parameter	N_c	0.95	-
Elastic length scale	ℓ_e	125	nm
Plastic length scale	L_p	125	nm
Threshold stress	r_0	21	MPa
Threshold stress strength coefficients	c_1	N/A	-
Burgers vector magnitude	b	0.25	nm
Dislocation interaction coefficients	$h^{\alpha\beta}$	N/A	-
Initial SSD density	ϱ_{S0}	N/A	μm^{-2}
Dislocation immobilization coefficients	$a^{\alpha\beta}$	N/A	-
Dislocation segment length constant	K	N/A	
Dislocation capture radius	y_c	N/A	nm
Reference slip rate	$\dot{\gamma}_0$	10^{-3}	s^{-1}
Drag stress	g	5	MPa
Inverse rate sensitivity exponent	m	20	-

The discrete dislocation simulations of Yefimov et al. [74] have been carried out for a matrix material that is initially free of dislocations and point obstacles. Therefore, the yield strength is governed by the dislocation source characteristics and material strengthening is due solely to dislocation-dislocation and dislocation-particle interactions. The dislocation sources are randomly distributed with a uniform source density and the source strengths are randomly chosen from a Gaussian distribution with mean and

standard deviation of 50 MPa and 10 MPa, respectively. The average stress-strain responses predicted by the discrete simulations are markedly different for the two morphologies. An essentially elastic-perfectly plastic response is observed for Material I, whereas Material II displays an approximately linear hardening rate. These differences in behavior are due to the fact that Material I contains an unblocked matrix channel. Dislocations nucleated in this channel are highly mobile and able to traverse the entire unit cell, and as a result only a small number of dislocations are needed to accommodate the imposed deformation. On the other hand, mobile dislocations in Material II are obstructed and form pileups originating at the matrix-particle interface, and these pileups generate strong back stresses which lead to the observed material strengthening for this particle morphology. The validity of this analysis is confirmed upon inspection of the dislocation distributions for the two particle morphologies shown in Figure 5.59 at an applied strain of 0.6% and also the unloading behavior as shown in Figure 5.60(c). Figure 5.59shows an extremely low dislocation density for Material I, and a much higher density for Material II with many dislocations located at the matrix-particle interfaces. The dislocation arrangement for Material II is characterized by tilt wall type configurations on the lateral faces of the central particle which form to maintain compatibility between the matrix and the inclusion as argued by Ashby [11], and also by extended pileups which are clearly seen in the outermost quadrants of the unit cell. The unloading curves offer further evidence that material strengthening is governed by the development of GND induced back stresses since a strong Bauschinger effect is observed for Material II while unloading is essentially elastic for Material I.

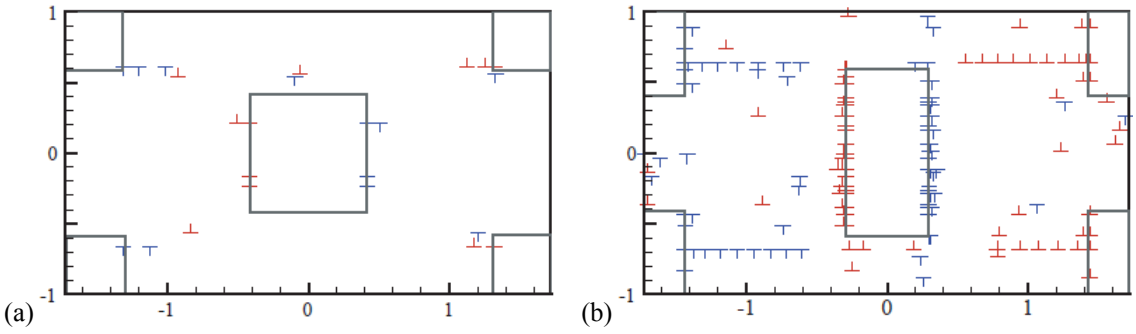

Figure 5.59: Dislocation density distributions at $\Gamma = 0.006$ from the discrete dislocation simulations [74] for (a) Material I and (b) Material II.

It is noted (see Table 5.10) that guided by the analysis of the discrete dislocation results that terms associated with the SSD strengthening and evolution have been suppressed. Recall that the same assumption has been made in the single slip configuration bending simulations presented in Section 5.3.2 because there, as in the current case, were no short-range obstacles to slip (point obstacles or intersecting slip planes). The calibrated material parameters have been determined by fitting the micropolar model to the discrete dislocation results with $H = C$. Given that SSD density evolution is neglected, there are three free fitting parameters: r_0, ℓ_e, and L_p. The initial threshold stress, r_0, is determined by fitting stress-strain response for Material I, and the elastic and plastic length scales have been determined by fitting to the hardening behavior and dislocation density evolution of Material II. The average shear stress-strain responses from the micropolar and discrete dislocation simulations for Material I and II with $H = C$ are shown in Figure 5.60(a). The micropolar stress-strain curves are in good agreement with the discrete dislocation results for both Materials I and II during forward loading; however, the Bauschinger effect observed for Material II during unloading is significantly underestimated by the micropolar model.

Figure 5.60(b) shows the stress-strain curves for Material II for three different unit cell sizes as obtained from the micropolar model using the calibrated set of material parameters. There micropolar model results display a clear "smaller is stronger" trend with respect to the observed hardening slope, but in contrast to the discrete simulations there is no difference in the initial yield strengths among the three specimens considered. The strong variation in initial yield strength seen in the discrete simulations is governed by the statistics of the dislocation sources, and cannot be captured in a continuum model that treats all (matrix) material points as equally potent sources for initiating plastic flow. If the initial threshold stress is treated as an additional fitting parameter for each unit cell size, reflecting the statistical variations in the source strengths, then excellent agreement between the micropolar and discrete dislocation stress-strain curves is obtained as shown in Figure 5.60(c). The modified threshold stresses used in these simulations are 13 MPa and 30 MPa for $H = 2C$ and $H = 0.5C$, respectively.

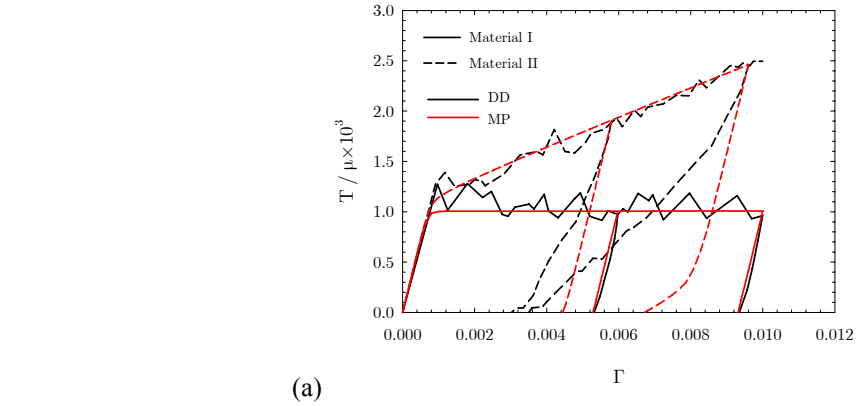

(a)

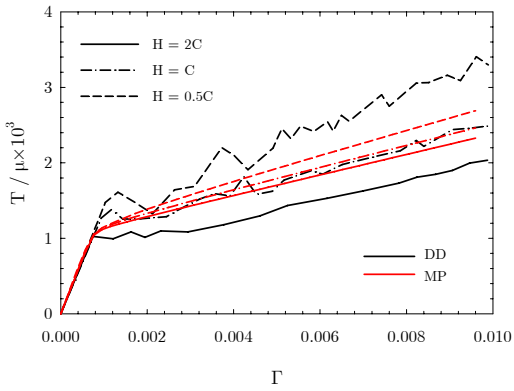

(b)

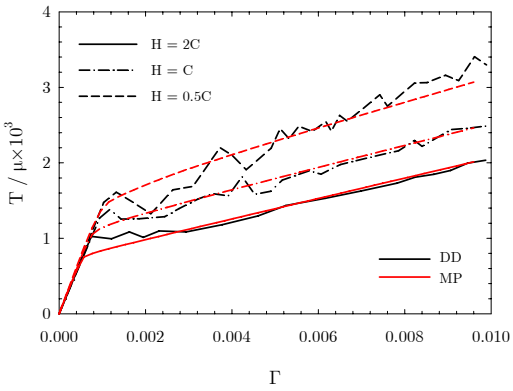

(c)

Figure 5.60: Average stress-strain response for (a) both Material I and II with $H = C$ (b) Material II for different specimen heights with fixed initial slip threshold (c) and Material II with variable slip threshold.

The cumulative plastic slip distribution for Material I with $H = C$ at $\Gamma = 0.006$ as predicted by the micropolar model and the statistical dislocation dynamics model of Yefimov et al. [74] is shown in Figure 5.61. Both models yield cumulative slip fields that are similar in morphology and magnitude, that are characterized by the intense localization of plasticity in the unreinforced veins of matrix material. It is noted that the localized zones of slip are symmetric for the micropolar model, whereas there is an obvious asymmetry for the statistical dislocation dynamics model owing to the distribution of source strengths. The maximum values of cumulative slip are 0.037 and 0.04 for the micropolar and YGV models, respectively.

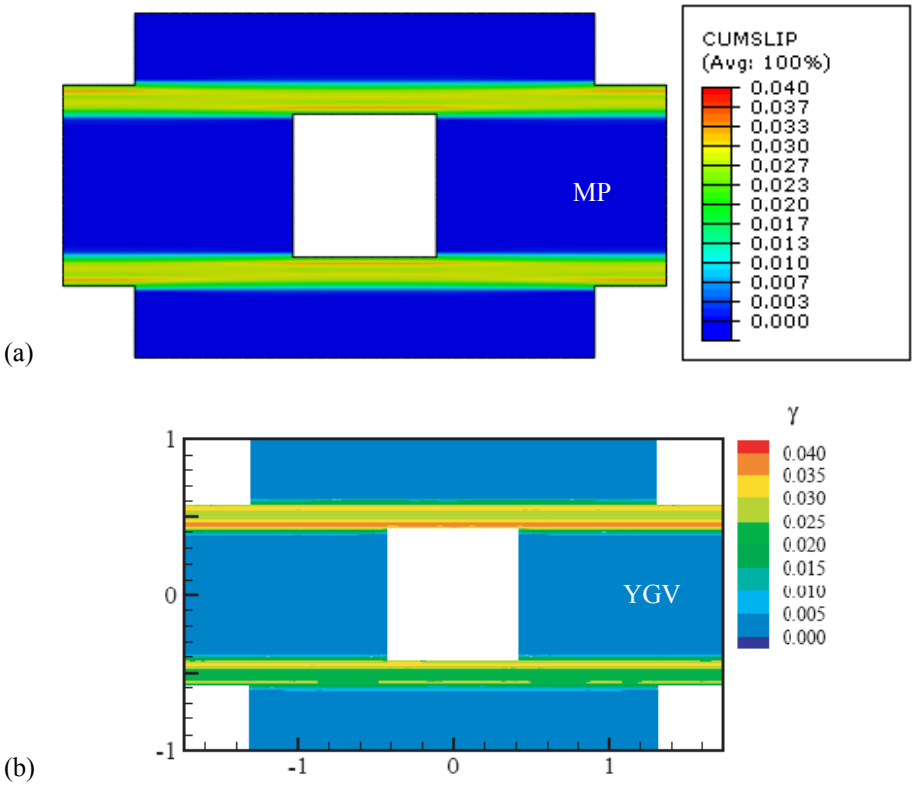

Figure 5.61: Contours of cumulative slip at $\Gamma = 0.006$ for Material I (a) calibrated single criterion micropolar model (MP) and (b) statistical dislocation dynamics model (YGV) [74]. $H = C$ **.**

Contours of the total dislocation (GND) density fields are shown in Figure 5.62 for Material I at $\Gamma = 0.006$ for the micropolar and YGV model, and it is seen that both models predict maximum local values of dislocation density at the corners of the central particle. It is noted that the maximum value of dislocation density is approximately 13 times higher for the YGV model as compared to the micropolar model, and because of this difference in magnitude the results have been plotted on separate contour scales. The exact nature of this discrepancy is unclear, but it could be related to the fact that there is no SSD production in the micropolar model. Even though there is no SSD (or any) hardening for Material I, as indicated in the discrete dislocation stress-strain curve shown in Figure 5.60(a), there will still be some amount of statistically stored dislocations, e.g., dipolar configurations, within the matrix. This is an aspect of the discrete simulations that the YGV model will inherently pickup, whereas the micropolar model will not (due to the a priori zero SSD assumption). Dislocation-based continuum crystal plasticity formulations

(either local or nonlocal) describe material strengthening through the evolution of the dislocation density, and in the absence of material strengthening there is rarely a "need" to track the dislocation density evolution. To remedy this discrepancy, a non-null evolution of SSDs could be specified while ignoring their contribution to strengthening, but this is typically not done because this is in fact how the effect of SSDs on material response is quantified. Continuum theories which treat the dislocation dynamics sub-problem explicitly, such as the YGV model, do not suffer from these same limitations because of the way the SSD and GND density evolution is naturally coupled through the dislocation conservation equations.

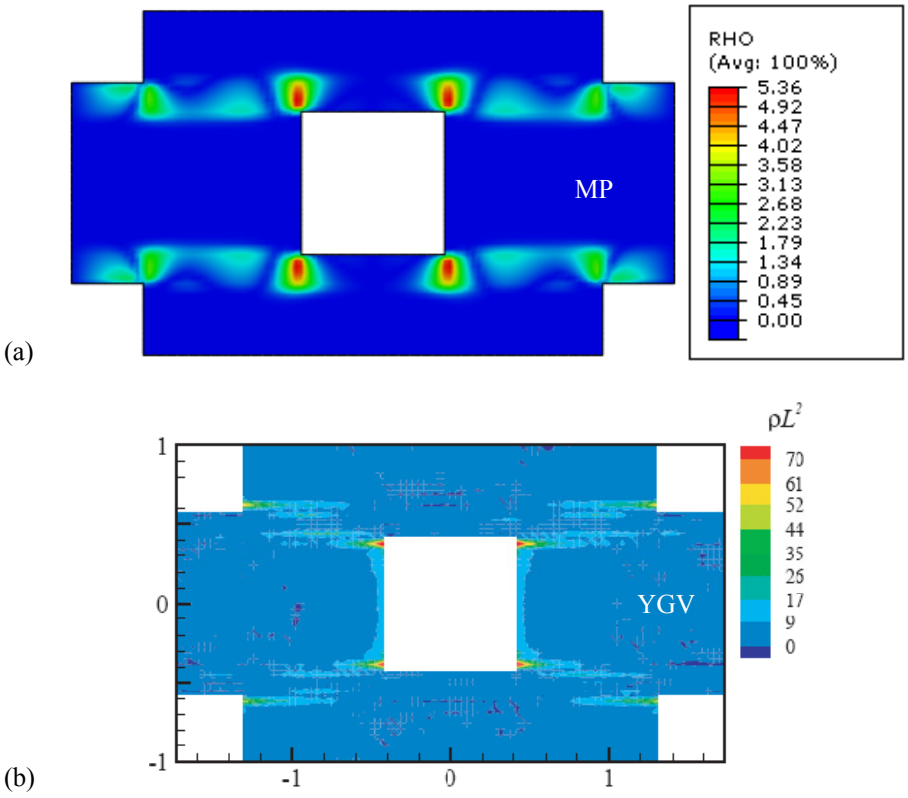

Figure 5.62: Contours of dislocation density at $\Gamma = 0.006$ for Material I (a) calibrated single criterion micropolar model (MP) and (b) statistical dislocation dynamics model (YGV) [74]. $H = C$.

The cumulative slip contours for Material II at $\Gamma = 0.006$ are shown in Figure 5.63 for the micropolar and YGV models, and there is good agreement between the morphologies of the two distributions. The morphologies are characterized by highly localized slip bands that form along the top and bottom faces of the particles, but do not extend across the full width of the unit cell due the obstruction provided by the particle overlap. It is significant that the cumulative slip distribution for the micropolar model is qualitatively similar to that of the YGV model, as it has been pointed out [74] that the nonlocal theories of Bassani et al. [185] and Bittencourt et al. [23] do not capture the appropriate trends. This is demonstrated in Figure 5.64 which shows cumulative slip contours at $\Gamma = 0.0096$ for the Gurtin-type model [23] for (a) a local crystal plasticity model and for (b) the nonlocal model with microclamped (zero plastic strain) boundary conditions imposed at the matrix-particle interface. In addition to the localized slip bands parallel to the direction of shearing, both the local and nonlocal theories display a significant amount slip at the matrix-particle interface. The slip contours shown in Bassani et al. [185] display similar trends, and these results are inconsistent with the discrete dislocation simulations which show almost no slip near the vertical faces of the particles. It is also important to note that the model used in Bassani et al. [185] is a low-order type of nonlocal theory, whereas the results presented in Bittencourt et al. [23] are for a Gurtin-type work-conjugate higher-order theory. In other words, the limitations of these two models with respect to capturing the cumulative slip distributions cannot solely be attributed one type of nonlocal formulation versus the other. It was argued by Yefimov et al. [74] that this limitation is due to the fact that dislocation nucleation is assumed to be instantaneous and unlimited in these types of theories. However, the micropolar model is able to capture the same cumulative slip morphology without explicitly treating dislocation nucleation and its statistical variance, so there must be an alternative and/or supplemental explanation for this behavior. Although the micropolar model is in good agreement with the YGV model in terms of the overall cumulative slip distribution, it is pointed out that the intensity of slip bands is noticeably higher for the micropolar model as seen in Figure 5.63(a). To facilitate comparison of the two results the contour bar for the micropolar cumulative slip plot has been clipped such that any value greater than 0.025 is shown as red. It seen that the overwhelming majority of plastic deformation is accommodated by the slip bands for the micropolar model, whereas the slip is more evenly distributed for the YGV model.

The maximum value of cumulative slip predicted by the micropolar model is 0.053 which is approximately twice the value reported for the YGV model.

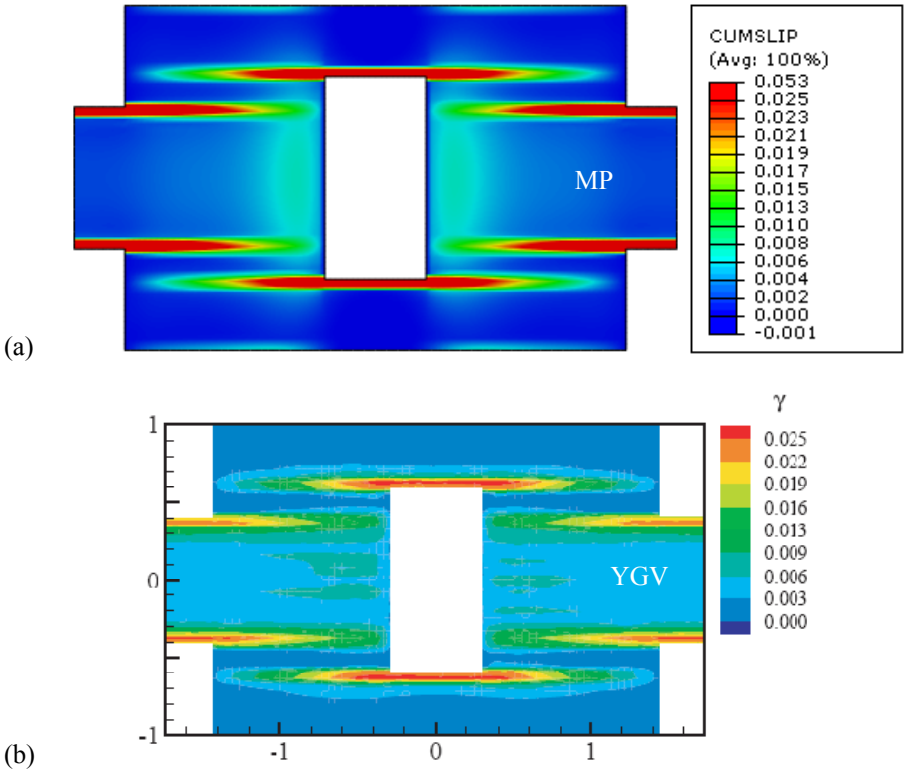

Figure 5.63: Contours of cumulative slip at $\Gamma = 0.006$ for Material II (a) calibrated single criterion micropolar model (MP) and (b) statistical dislocation dynamics model (YGV) [74]. $H = C$.

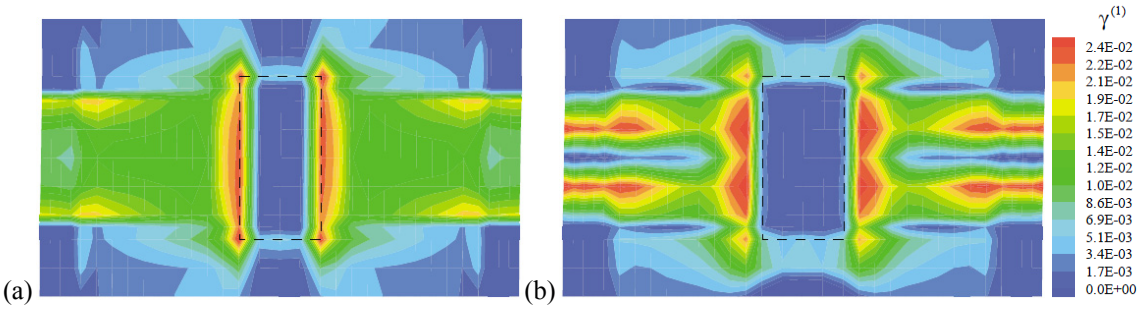

Figure 5.64: Contours of cumulative slip at $\Gamma = 0.0096$ for Material II (a) local theory and (b) Gurtin-type nonlocal theory with microclamped interfacial boundary conditions according to Bittencourt et al. [23].

The total dislocation density contour plots for Material II at $\Gamma = 0.006$ are given in Figure 5.65 for both the micropolar and YGV models. In agreement with the discrete dislocation simulations, both models show large numbers of dislocations along the vertical faces of the matrix-particle interface and very few dislocations distributed throughout the matrix. These interfacial dislocations are geometrically necessary and are generated to accommodate the rotational gradients that develop. In contrast to the bending simulations where the micropolar models consistently underestimated the maximum local values of dislocation density observed in YGV model results, the magnitude of the dislocation density fields are much more congruent for this initial-boundary value problem. This is not unexpected since it has previously been demonstrated for the constrained shear problem, i.e., another problem with microrigid boundary conditions, that the micropolar model is capable of capturing the peak dislocation density magnitude. One feature of the dislocation distribution that is seen in the discrete dislocation (see Figure 5.59(b)) and YGV model results, but not for the micropolar model is the dislocation pileups emanating from the particles. The lack of this characteristic feature in the micropolar simulations can be related back to the prior discussion of the dislocation configuration observed in Material I, where it was argued that the disagreement between the micropolar and YGV models is related to a certain amount of dislocation density that exists within the actively slipped regions that does not have a significant impact on the material strengthening behavior. The situation is slightly different here since the previous arguments made in reference to Material I revolved around an unaccounted for SSD density, whereas the "missing"

dislocations in the current scenario are arranged in pileups and are by definition GNDs. These subtle but important differences aside, the limiting feature and cause of the discrepancy between the micropolar and YGV models for both Materials I and II is the same; namely, that the unaccounted for dislocation density in the micropolar is due to the assumption that there is no dislocation generation (either SSDs or phenomenological GNDs) associated with slip. This argument is supported by the observation, as in the case for Material I, that these dislocation pileups are found to be collinear with the intensely sheared slip bands as can be seen by comparing Figure 5.63(b) and Figure 5.65(b). As previously discussed, the YGV model is able to pick up these features of the dislocation distribution that are observed in the discrete dislocation simulations because it treats the dislocation dynamics sub-problem explicitly. As such, the dislocation pileups at interfaces naturally emerge due to the direct treatment and impedance of dislocation flux.

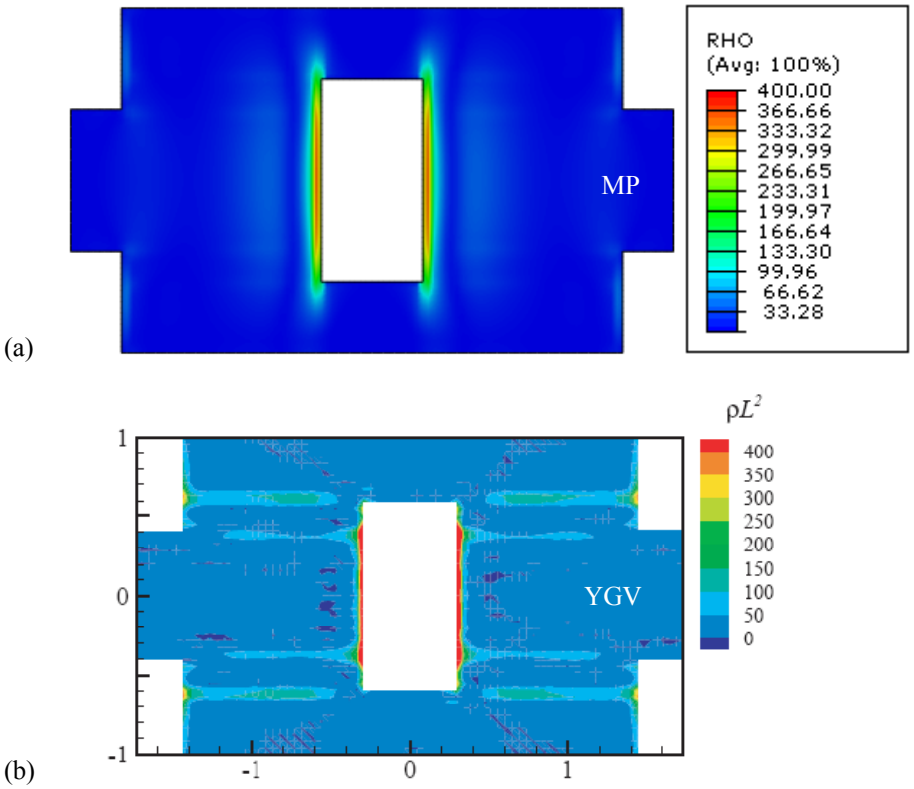

Figure 5.65: Contours of total dislocation density at $\Gamma = 0.006$ for Material II (a) calibrated single criterion micropolar model (MP) and (b) statistical dislocation dynamics model (YGV) [74]. $H = C$.

The size-dependence of the dislocation distribution and evolution is demonstrated in Figure 5.66 and Figure 5.67, respectively. Figure 5.66 gives the total dislocation density contour plots for Material II at $\Gamma = 0.006$ for the three different unit cell sizes. There is nothing particularly interesting about the individual plots as they all have the same morphology, and as expected the magnitude of the dislocation density increases with decreasing unit cell size. The maximum local dislocation density values predicted by the micropolar model at this applied strain level are 417 μm^{-2}, 363.1 μm^{-2}, and 259.6 μm^{-2} for $H = 0.5C$, $H = C$, and $H = 2C$, respectively. The total dislocation density in the matrix is plotted as a function of applied shear strain for both the micropolar and discrete dislocation models for the three unit cell sizes in Figure 5.67. The micropolar model results are in good agreement with the discrete dislocation simulations for the two largest unit cell sizes, but there is a rather modest discrepancy for the smallest unit

cell size. It is noted that the material parameters have been determined by fitting to the discrete dislocation results for the middle unit cell size, $H = C$, and then held fixed for the other simulations. Consequently, the micropolar and discrete dislocation results for this unit cell size are the most closely aligned. Interestingly, the micropolar model overestimates the total dislocation density for the largest unit cell size and underestimates it for the smallest one. The lack of a consistent trend with respect to the variation of dislocation density evolution as a function of unit cell size might indicate that different material length scale parameters need to be used for each simulation. This would be in contrast to the pure bending simulations where different material length scale parameters are required for different crystal orientations, but not for different film thicknesses. The justification for using different material length scale parameters for varying crystal orientations is rather straight-forward since the nature of the dislocation configuration changes as a function of crystal orientation. However, it is unclear as to what the physical justification would be for varying the material length scale parameters as function of specimen thickness since the orientational nature of the dislocation distribution does not change. It is conceivable that some other non-orientational aspect of the dislocation distribution necessitates such specimen size-dependent material length scale parameters, but it is impossible to draw any definitive conclusions in this regard with the limited amount of discrete dislocation simulation data that are available.

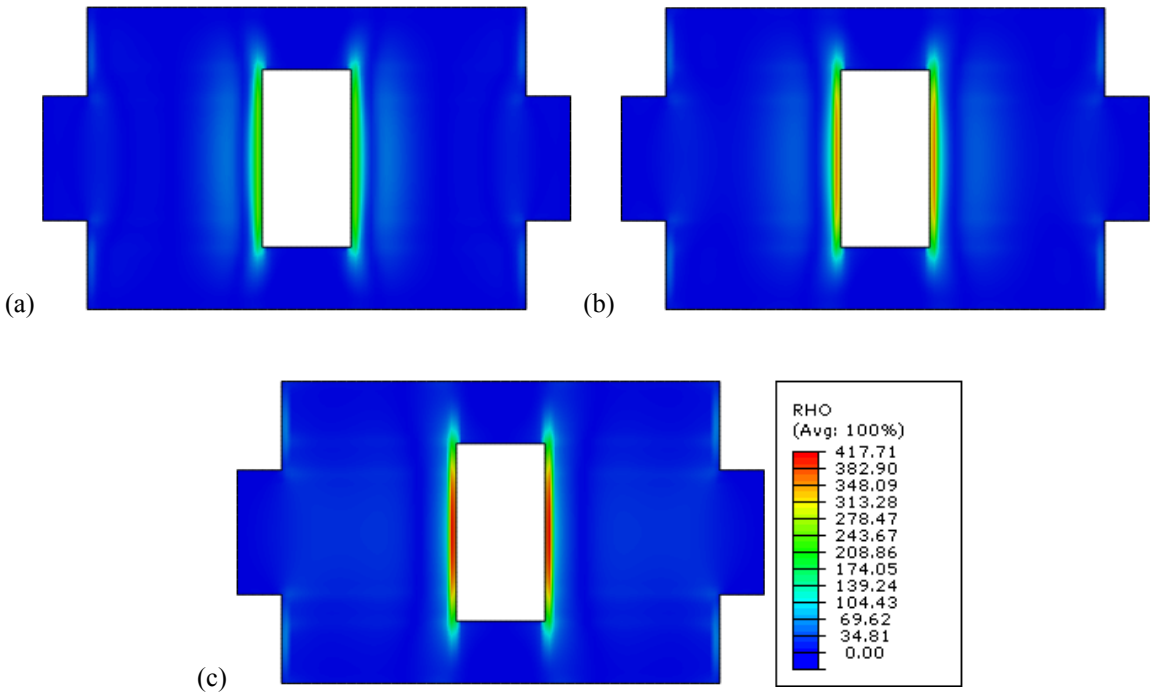

Figure 5.66: Contours of total dislocation density for Material II at $\Gamma = 0.006$ for the calibrated single criterion model (a) $H = 2C$ (b) $H = C$, and (c) $H = 0.5C$.

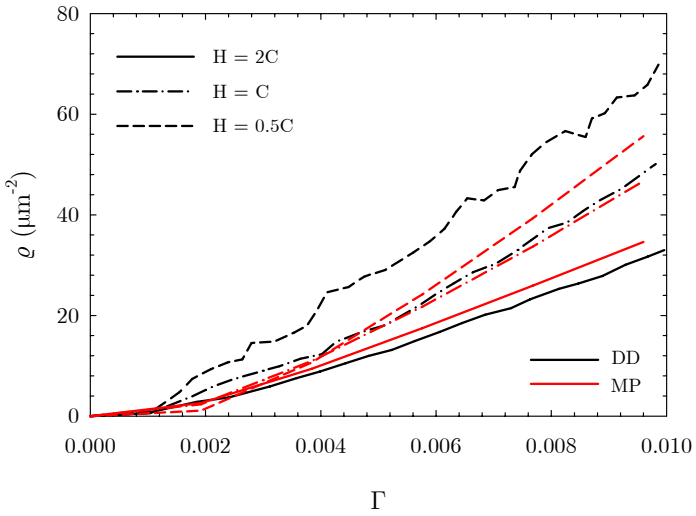

Figure 5.67: Evolution of total matrix dislocation density versus applied strain as predicted by the calibrated single criterion model (MP) and discrete dislocation dynamics (DD) [74] for various unit cell sizes.

5.4 Summary

This chapter presents the results of single crystal simulations performed using the micropolar crystal plasticity models developed in Chapter 3. The first part of the chapter was devoted to a parametric study of the various models in order to gain an understanding as to how the non-classical material parameters influence different aspects of the deformation behavior, and also to assess the variation in model predictions for a common and well-understood initial-boundary value problem. The second part of the chapter used the insight gained during the parametric study to then calibrate the micropolar model to discrete dislocation dynamics simulations of three equivalent initial-boundary value problems. Specifically, the initial-boundary value problems that have been studied are: (i) constrained shearing of thin films, (ii) pure bending films, and (iii) simple shearing of a metal matrix composite. It has been demonstrated that the micropolar models are in general agreement with the discrete dislocation simulations, and are capable of reproducing many of the their characteristic features. Attention has also been called to the limitations of the theory. Notable among these are the limitations of strength model versions 1 (MCV1) and 2 (MCV2) proposed for the multicriterion theory. These strengthening descriptions have proven incapable of capturing all relevant aspects of the discrete dislocation simulations simultaneously with a single set of material parameters. As such, these models have been deemed physically invalid, and have been discarded as viable material descriptions.

CHAPTER 6

NUMERICAL SIMULATIONS: POLYCRYSTALS

6.1 Introduction

This chapter presents a study of polycrystalline deformation via numerical simulations employing the micropolar single crystal plasticity constitutive models developed in Chapter 3. A primary motivation for the development of single crystal plasticity constitutive models is the desire to compute mechanical response of polycrystals as the aggregate behavior of an ensemble of single crystals, and this is a relatively more daunting task for discrete dislocation models. Simulations of this kind allow the connection between local microstructural arrangement and polycrystalline deformation behavior to be studied. Typical quantities of interest in such analyses are the homogenized stress-strain response, the evolution of texture, the development and distribution of microplasticity, shear localization, etc. There has been a recent interest in applying nonlocal crystal plasticity models to study the scale-dependent behavior of polycrystals. In particular, the scaling behavior of the flow stress with grain size is sought. It is well known that the flow strength in polycrystals scales as a power of the inverse grain size with a scaling exponent typically reported to be in the range $0.3 \leq n \leq 1$ [191] where $n = 0.5$ corresponds to the classical Hall-Petch exponent [1, 2]. While modeling the grain size dependence of yield strength and flow stress in polycrystalline metals is often cited as a motivation for developing nonlocal crystal plasticity theories, there are relatively few computational studies devoted to direct numerical simulation of explicitly rendered (i.e., non-homogenized) polycrystals using such theories [15, 34, 41, 104, 106, 111, 192-198]. The simulations performed in the sequel are not exhaustive, and are only intended to demonstrate the general range and nature of scale effects that can be achieved with the micropolar crystal plasticity models.

6.2 Polycrystal Representation and FE Model

In the following, two different polycrystalline representations are considered. One representation, which will be termed "traditional", makes no distinction between the grain interior and grain boundary regions and employs the micropolar crystal plasticity model up the grain boundaries, and the other treats the polycrystal as being comprised of core (grain interior) and mantle (grain boundary) regions. The former approach is typical of how polycrystals have traditionally been modeled with single crystal plasticity, and the core-mantle representation is a more recent trend that has been used invoked as a means of describing scale-dependent behavior. The rationale behind the core-mantle description is based on the notion that there is a grain boundary affected zone where the material properties (i.e., slip behavior) will differ from those in the interior of the grain. In core-mantle models based on local constitutive theories, the grain boundaries, being sites of high GND density, are usually specified a constitutive character that is stiffer (higher yield strength and strain hardening rates) than the grain interiors such that as the volume fraction of GBs changes the material the material elicits a size dependent response due to the composite nature of the material model. The core-mantle methodology is not often used in conjunction with nonlocal constitutive theories as a natural scale-dependence and delineation between grain interiors and boundary regions will emerge due to the concentration of strain gradients in the vicinity of GBs. This is precisely what happens when the micropolar theory is used in a traditional polycrystalline model.

The core-mantle methodology is used here in a different context and is motivated by the desire to draw an analogy between the micropolar and higher-order slip gradient-based polycrystal simulations. It has previously been discussed with respect to the higher-order slip gradient-based crystal plasticity theories that while they admit the specification of arbitrary interfacial boundary conditions in general, only two types of conditions (microfree and microclamped) have been used in practice. The microfree condition is used to model free surfaces and grain boundaries are almost exclusively modeled with the microrigid condition [15, 197]. Several works have discussed various types of intermediate micro boundary conditions from a theoretical perspective [78, 93, 114, 199], but very little has been done in this regard in terms of applications and numerical simulations. The microrigid condition enforces a zero plastic deformation constraint, thereby creating thin boundary layer (mantle) of essentially elastic material

adjacent to the grain boundary. As an analog to this, a core-mantle model is developed where the grain core's constitutive response is described by micropolar crystal viscoplasticity and the mantle region is described by micropolar elasticity. Similar studies of scale-dependent mechanical behavior have been carried out at the single crystal level using micropolar and micromorphic crystal plasticity by Forest and Sedlacek [39], Forest [38], and Cordero et al. [33] through the analysis of two-phase laminates. In their works, a simplified unit cell with a single slip system oriented perpendicular to the phase interface is analyzed. The core-mantle polycrystal simulations in this thesis represent a generalization and extension of these earlier contributions.

In the following simulations, the mechanical response of a small statistical volume element (SVE) containing 30 randomly oriented grains is investigated for remote uniaxial loading conditions. As shown in Figure 6.1, the grains are modeled as regular hexagons and the grain boundary regions are specified to be $0.025\,d$ thick, where d is the grain diameter. The same FE discretization is used for both the traditional and core-mantle representations of the polycrystal. A mapped mesh comprised of 72 (3×6 in each quadrant) bilinear quadrilateral elements is used for the grain interiors and the grain boundary regions have three elements through the thickness. Polycrystals with four different grain sizes are simulated, $d \in \{250, 500, 1000, 10000\}$ nm, and three SVE instantiations with different orientation distributions are studied for each grain size. Periodic displacement and rotation boundary conditions are applied in both the x_1- and x_2-directions of the SVE and the remote tension applied through a displacement boundary condition on control node D in the vertical direction as indicated in Figure 6.2 The periodic boundary conditions have been implemented via linear multi-point constraints according to the developments in van der Sluis et al. [200]. The boundary conditions are stated as

$$\begin{aligned} u_1(0,H,t) = 0 \quad &, \quad u_2(0,H,t) = U(t) \\ \mathbf{u}(0,0,t) = \mathbf{0} \quad &, \\ u_2(W,0,t) = 0 \quad & \end{aligned} \tag{6.1}$$

and the periodicity constraints are

$$\mathbf{u}(0,0<x_2<H,t)-\mathbf{u}(0,0,t)=\mathbf{u}(W,0<x_2<H,t)-\mathbf{u}(W,0,t)$$

$$\mathbf{u}(0<x_1<W,0,t)-\mathbf{u}(0,0,t)=\mathbf{u}(0<x_1<W,0,t)-\mathbf{u}(0,H,t)\ , \tag{6.2}$$

$$\mathbf{u}(0,H,t)-\mathbf{u}(0,0,t)=\mathbf{u}(W,H,t)-\mathbf{u}(W,0,t)$$

for the displacements and

$$\begin{aligned}\overline{\phi}(0,0\le x_2\le H,t)&=\overline{\phi}(W,0\le x_2\le H,t)\\ \overline{\phi}(0\le x_1\le W,0,t)&=\overline{\phi}(0\le x_1\le W,H,t)\end{aligned} \tag{6.3}$$

for the rotations. In each simulation, the SVE is subjected to an average true strain of 0.05 that is applied at a rate of 10^{-3} s^{-1} where the SVE nominal uniaxial strain is defined as $\varepsilon_{22}=u_2(0,H,t)\ /\ H$. The single criterion theory is used in all of the polycrystal simulations, and the material parameters used in the simulations are given in Table 6.1. It has been demonstrated in Chapter 5 that the micropolar material parameters required for reproducing the behavior of single crystal discrete dislocation dynamics simulations are orientation and initial-boundary value problem dependent. Therefore, it is reasonable to assume that the material parameters for each grain should be a function of its orientation and also the orientation of its nearest neighbors since this will define the local boundary conditions for each grain. On the other hand, there is no way to determine what the grain-by-grain material parameters should be *a priori*; therefore, all of the grains are assumed to have identical material properties. In this regard, the following studies are intended only to highlight general trends in the deformation behavior and not to corroborate with experimental or finer scale simulation results as there is insufficient data available for this purpose. It is to be understood that the list of material parameters given in Table 6.1 apply to the grain cores only. The micropolar elastic material parameters used for the grain boundary regions in the core-mantle simulations is covered in more detail during the discussion of those results.

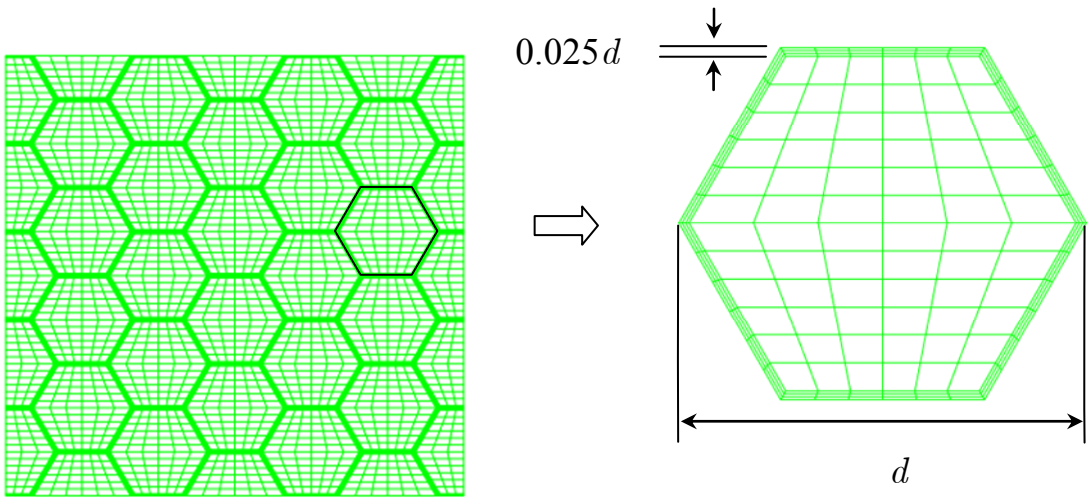

Figure 6.1: Finite element discretization used for polycrystalline simulations. Entire SVE (left) and individual grain (right).

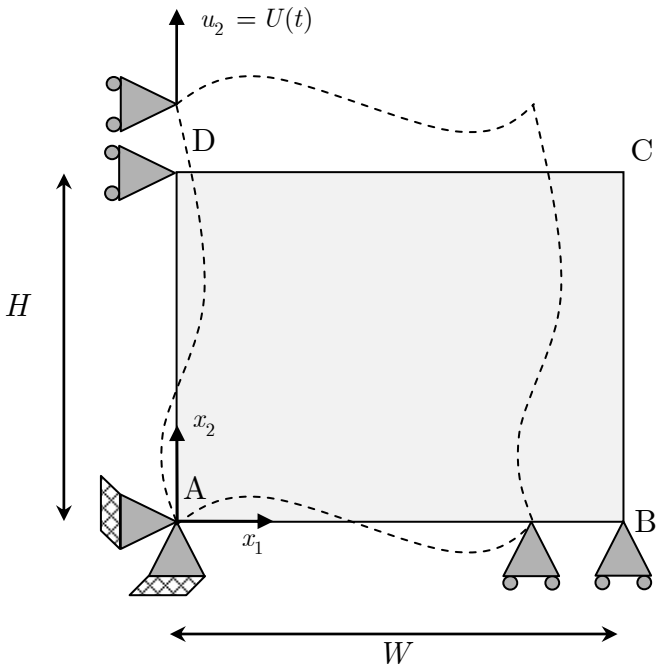

Figure 6.2: Schematic of geometry and periodic boundary conditions for the SVE polycrystal simulations.

Table 6.1: Single crystal elastic-viscoplastic material parameters used in the polycrystalline simulations.

Parameter	Symbol	Magnitude	Unit
Shear modulus	μ	26.3	GPa
Poisson's ratio	ν	0.33	-
Coupling parameter	N_c	0.95	-
Plastic-elastic length scale ratio	$L_p \ / \ \ell_e$	4.5	-
Threshold stress	r_0	12.8	MPa
Threshold stress strength coefficients	c_1	0.5	-
Burgers vector magnitude	b	0.25	nm
Dislocation interaction coefficients	$h^{\alpha\beta}$	1.0	-
Initial SSD density	ϱ_{S0}	10^{-6}	μm^{-2}
Dislocation immobilization coefficients	$a^{\alpha\beta}$	0.1	-
Dislocation segment length constant	K	40	
Dislocation capture radius	y_c	1.5	nm
Reference slip rate	$\dot{\gamma}_0$	10^{-3}	s^{-1}
Drag stress	g	5	MPa
Inverse rate sensitivity exponent	m	20	-

6.3 Results and Discussion

Three different sets of results are presented in the following discussion. Two values of the elastic length scale parameter $\ell_e \in \{10, 250\}$ nm are used in the simulations with the traditional polycrystalline representation and a single elastic length scale, $\ell_e = 10$ nm is considered for the core-mantle simulations. In the following analysis, attention is focused on the macroscopic stress-strain behavior, the scaling of flow stress with (inverse) grain size and the distributions of the lattice rotation, SSD, GND and cumulative slip fields. The cumulative slip fields are defined for each slip system as

$$\tilde{\gamma}^{\alpha} = \int \left| \dot{\gamma}^{\alpha} \right| dt \tag{6.4}$$

The macroscopic uniaxial true stress-strain response is calculated from the previously given definition of nominal SVE strain, i.e., $e_{22} = U(t) \ / \ H$, and the SVE nominal stress which is defined in terms of the

vertical component of the reaction force, r_2^f, at control node D as $s_{22} = r_2^f(D) / W$ where unit thickness has been assumed in the out-of-plane direction. The scaling of macroscopic flow stress as a function of grain size is defined in terms of an extended Hall-Petch [1, 2, 201] relation, i.e.,

$$\sigma(\varepsilon) = \sigma_0(\varepsilon) + k_{HP}(\varepsilon) d^{-n(\varepsilon)} \tag{6.5}$$

where σ is the macroscopic flow stress, σ_0 is a constant reference flow stress, k_{HP} is a proportionality constant, d is the grain size, and n is the scaling exponent. The explicit dependence of the arguments on the applied strain is included to underscore that the scaling behavior will be studied at multiple points in the deformation history. The reference flow stress is defined as the corresponding macroscopic stress at vanishing length scale effects, i.e., the flow stress that would be obtained from an identical simulation using a classical (local) theory of crystal plasticity. In the following analysis, the reference stress-strain response is taken to be that of a polycrystal with $d / \ell_e = 1000$. In order to keep the number of figures to a minimum in the following presentation of results, the deformation field contour plots are given for a single SVE instantiation (SVE2). While the local fields vary from one SVE to another, the general trends observed for a single SVE will apply to the others as well. To facilitate discussion of certain aspects of the deformation fields, a grain identification scheme is shown along with the grain orientations in Figure 6.3. The grain orientation is depicted by a pair of intersecting red lines that are parallel to the slip directions.

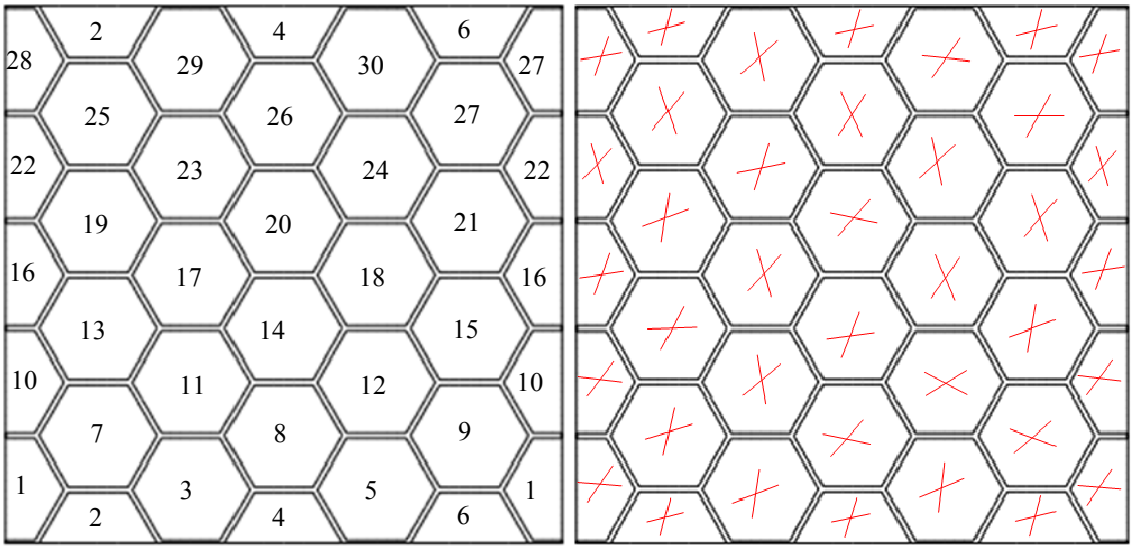

Figure 6.3: Grain numbering scheme (left) and slip system orientation (right) for the SVE2 model polycrystal.

6.3.1 Traditional Polycrystal Representation

The macroscopic stress-strain curves from the simulations employing the traditional polycrystal representation with $\ell_e = 250$ nm are shown for each SVE and grain size in Figure 6.4, and it is clear that there is a pronounced scale-dependence on the material response. Each set of stress-strain curves have been plotted using the same scale along the stress axis, and a moderate amount of variability in the magnitude and scope of the size effect is demonstrated for the different SVE instantiations. The trends in the stress-strain behavior are quantitatively similar for SVE1 and SVE3, whereas the size effects for SVE2 are much smaller in comparison. The marked increase in flow stress with decreasing grain size for this series of simulations is not surprising since a large value of the elastic length scale has been used corresponding to effective grain sizes of $d / \ell_e \in \{1,2,4,400\}$. Recall that the elastic length scales determined by calibrating the micropolar model to single crystal discrete dislocation simulations yielded effective material thicknesses in the range $15 \leq H / \ell_e \leq 100$ where H is the critical dimension of the single crystal. The magnitude of the flow stress size effect is quantified by determining the extended Hall-

Petch parameters for three levels of applied strain $\varepsilon \in \{0.01, 0.03, 0.05\}$. The extended Hall-Petch parameters are determined from a least-squares regression analysis of the average SVE response. The results are shown in Figure 6.5 where the filled markers represent the mean SVE value and the error bars indicate the maximum and minimum values among the three SVEs considered. The scaling exponents for the three strain levels, as indicated in the figure, are $n = 0.20$, 0.31, and 0.45. It is noted that the data points for $d = 10$ μm have not been included in the fitting procedure since the scale effects have significantly diminished for this effective grain size ($d / \ell_e = 400$) and the data is inconsistent with the trend exhibited by the other grain sizes. The scaling exponent is an increasing function of strain and this can be rationalized by the fact that lattice torsion-curvature (strain gradients) becomes more pronounced with continued deformation.

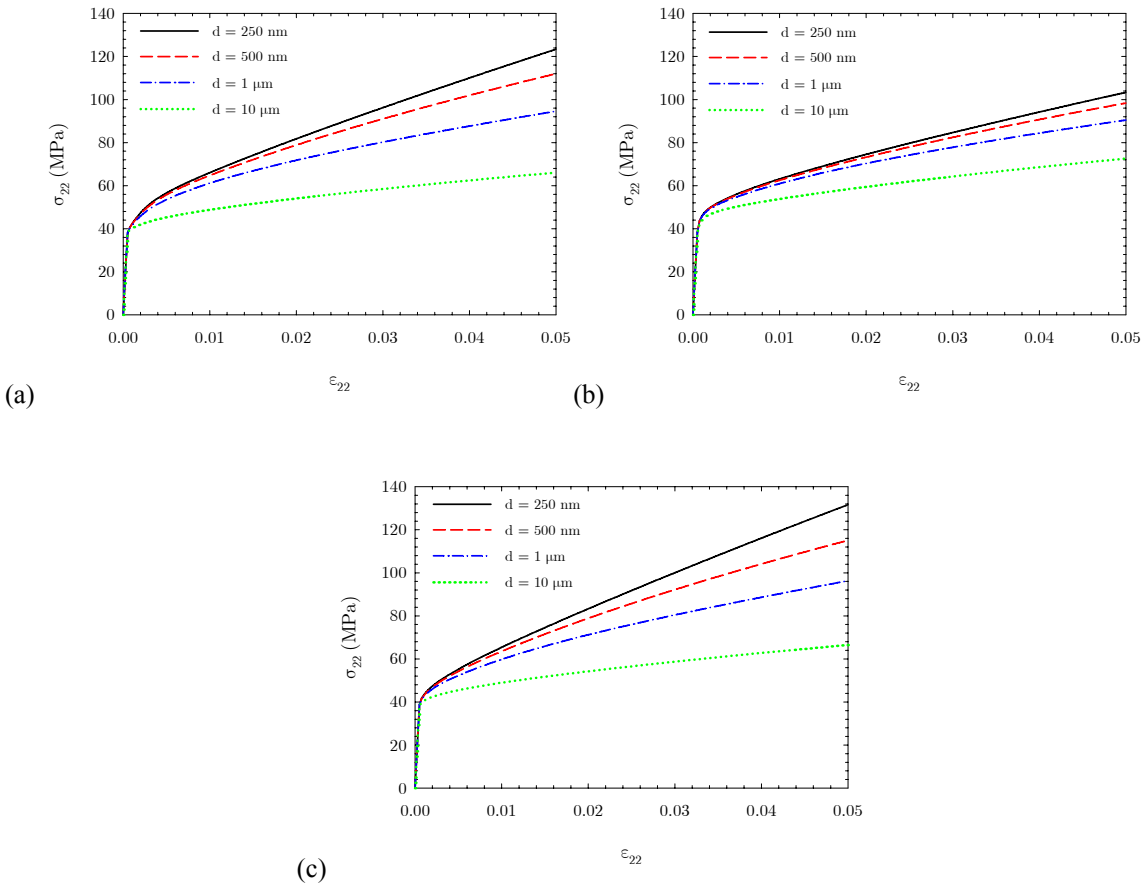

Figure 6.4: Macroscopic true uniaxial stress-strain curves for the traditional polycrystal model with $\ell_e = 250$ nm. (a) SVE1, (b) SVE2, and (c) SVE3.

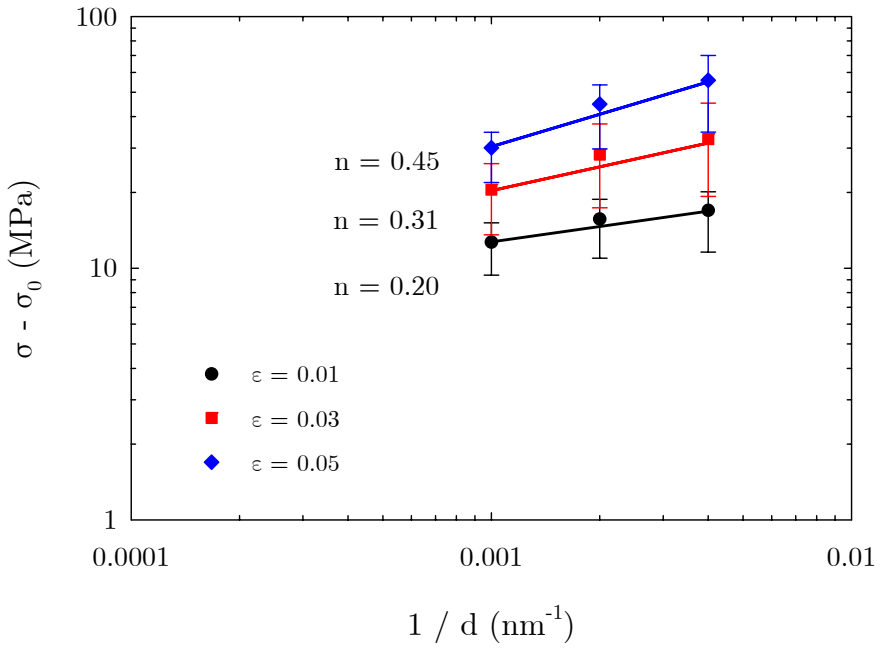

Figure 6.5: Scaling of macroscopic flow stress as a function of grain size for the traditional polycrystal representation with $\ell_e = 250$ nm.

Next, the change in GND density fields as a function of grain size is examined. It is anticipated according to physical intuition that the peak magnitude and overall intensity of the GND density distribution should increase with decreasing grain size as discussed in the works of Ashby [11] and Fleck et al. [5], amongst others, and that they should be concentrated near the grain boundaries. Figure 6.6 shows the GND density contour plots for SVE2 for each grain size on a fixed contour scale that has been clipped such that values $\geq 4\times10^{8}$ mm^{-2} are colored red to assist visualization of the field variations. Counter to expectations, the intensity of the GND density field is observed to *increase* with increasing grain size with maximum local values of 1.55×10^{8}, 4.99×10^{8}, 1.59×10^{9}, and 2.90×10^{9} mm^{-2} for grain sizes of 250, 500, 1000, and 10,000 nm, respectively. This unexpected behavior mandates a more in-depth look at the deformation fields in search of an explanation for this phenomenon, and it was found that the polycrystals are exceedingly rotationally stiff due to the large effective grain sizes considered. In support of this assertion, the lattice rotation fields for SVE2 are shown for each grain size in Figure 6.7. Each contour plot

has been given along with its own unique legend in order to clearly illustrate to full range of the lattice rotations for each grain size. Attention is drawn to the overall uniformity of the lattice rotation fields for the three smallest grain sizes as compared to that of the largest. The range of the former is approximately $3° \leq \bar{\phi} \leq 5°$, whereas a much wider range of lattice rotations, $-0.2° \leq \bar{\phi} \leq 7.5°$, develop for the polycrystal with $d = 10$ μm. The uniformity of the intergranular lattice rotation fields for the smaller grain sizes means that the individual grains are constrained against deforming independently, and instead must act in a cooperative manner, thereby leading to the pronounced strengthening evidenced in stress-strain curves shown in Figure 6.4. Additionally, a more uniform lattice rotation field results in diminished lattice curvature and, therefore, less GNDs. This explains the counterintuitive trend displayed in Figure 6.6.

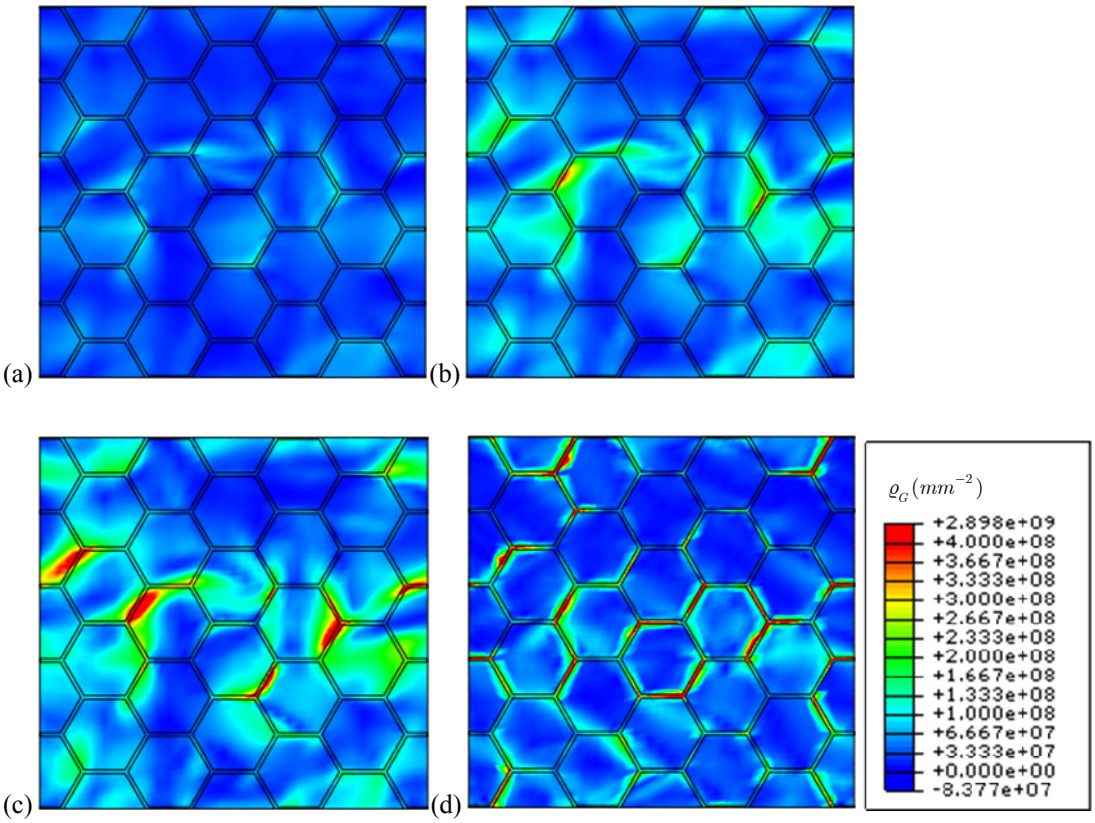

Figure 6.6: GND density distributions at $\varepsilon_{22} = 0.05$ for the traditional polycrystal representation (SVE2) with $\ell_e = 250$ nm (a) $d = 250$ nm (b) $d = 500$ nm (c) $d = 1$ μm and (d) $d = 10$ μm.

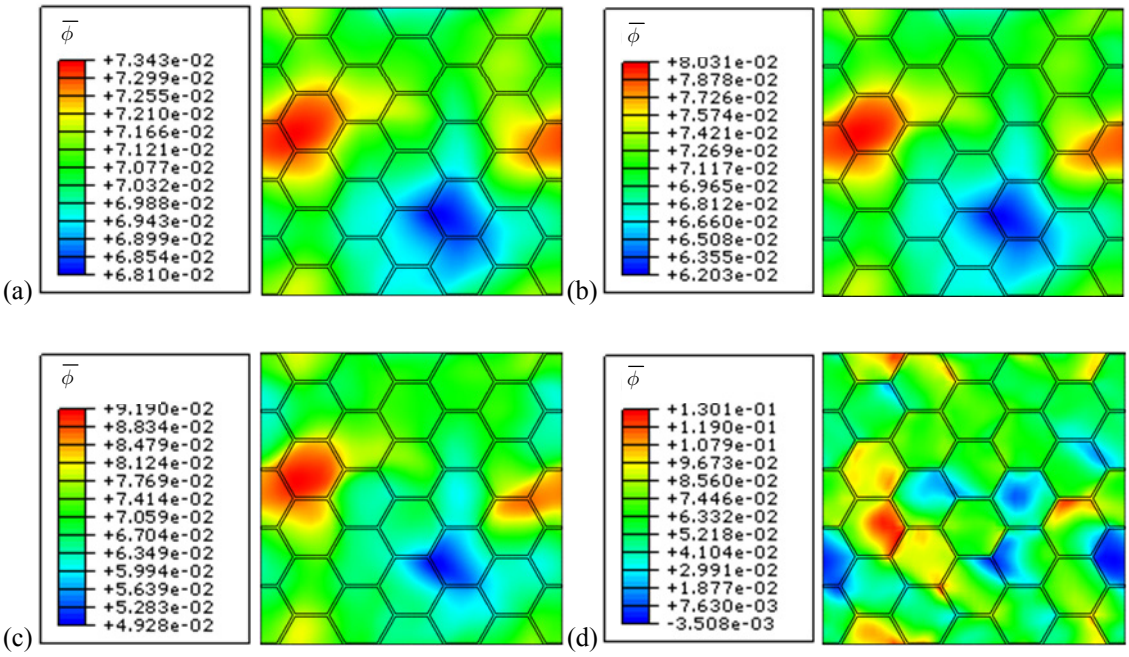

Figure 6.7: Lattice rotation distributions at $\varepsilon_{22} = 0.05$ for the traditional polycrystal representation (SVE2) with $\ell_e = 250$ nm (a) $d = 250$ nm (b) $d = 500$ nm (c) $d = 1$ μm and (d) $d = 10$ μm.

Although this anomalous behavior, i.e., GND density increasing with increasing grain size, was not anticipated prior to performing the simulations, it is not totally unexpected. As previously discussed, the three smallest effective grain sizes used in this study, i.e., $d / \ell_e = 1$, 2 and 4 are much smaller than what was required to reproduce the results of the single crystal discrete dislocation simulations presented in Chapter 5. However, since the initial-boundary value problems studied in the single crystal simulations involved either microfree (bending) or microrigid (constrained shear and matrix-inclusion) boundary conditions, it was expected that larger effective grain thicknesses would be admissible due to the intermediate nature of the intergranular constraints in the traditional representation of the polycrystal without causing unphysical behavior. In fact, additional simulations that are not shown here have been performed for a much smaller model polycrystal in an effort to establish a lower bound for the effective grain size above which this contradictory behavior is not observed. The lower bound was determined to be $d / \ell_e \approx 5$, and above this value the appropriate trend between the grain size and the intensity of the GND

density field is maintained. In light of the physically questionable results obtained for the traditional representation of the polycrystal with $\ell_e = 250$ nm, further examination of the cumulative slip and SSD density fields for this material description is not pursued. Instead, the analysis of the traditional polycrystal representation is continued for a material description that employs a more realistic value of the elastic length scale parameter.

The stress-strain curves for the traditional polycrystal with $\ell_e = 10$ nm are shown in Figure 6.8 for each of the three SVEs, and it is noted the magnitude of the size effect on flow stress has significantly diminished as compared to the previously considered material description. The maximum difference in the macroscopic stress at $\varepsilon_{22} = 0.05$ between the polycrystals with the largest and smallest grain sizes amongst all SVEs is only 8 MPa for the material description with $\ell_e = 10$ nm as compared to 65 MPa when $\ell_e = 250$ nm. The flow stress scaling behavior is shown in Figure 6.9, and the scaling exponents have been determined to be $n = 1.02$, 1.09, and 1.12 for the three increasing levels of applied strain. These results indicate that the flow stress scales approximately with the inverse grain size, and the flow exponent increases with deformation although by a much smaller amount than the previously considered case where a increase by factor of two was observed. Therefore, both the magnitude and evolution of the flow stress scaling behavior is a function of effective grain thickness, d / ℓ_e, for the traditional polycrystal representation.

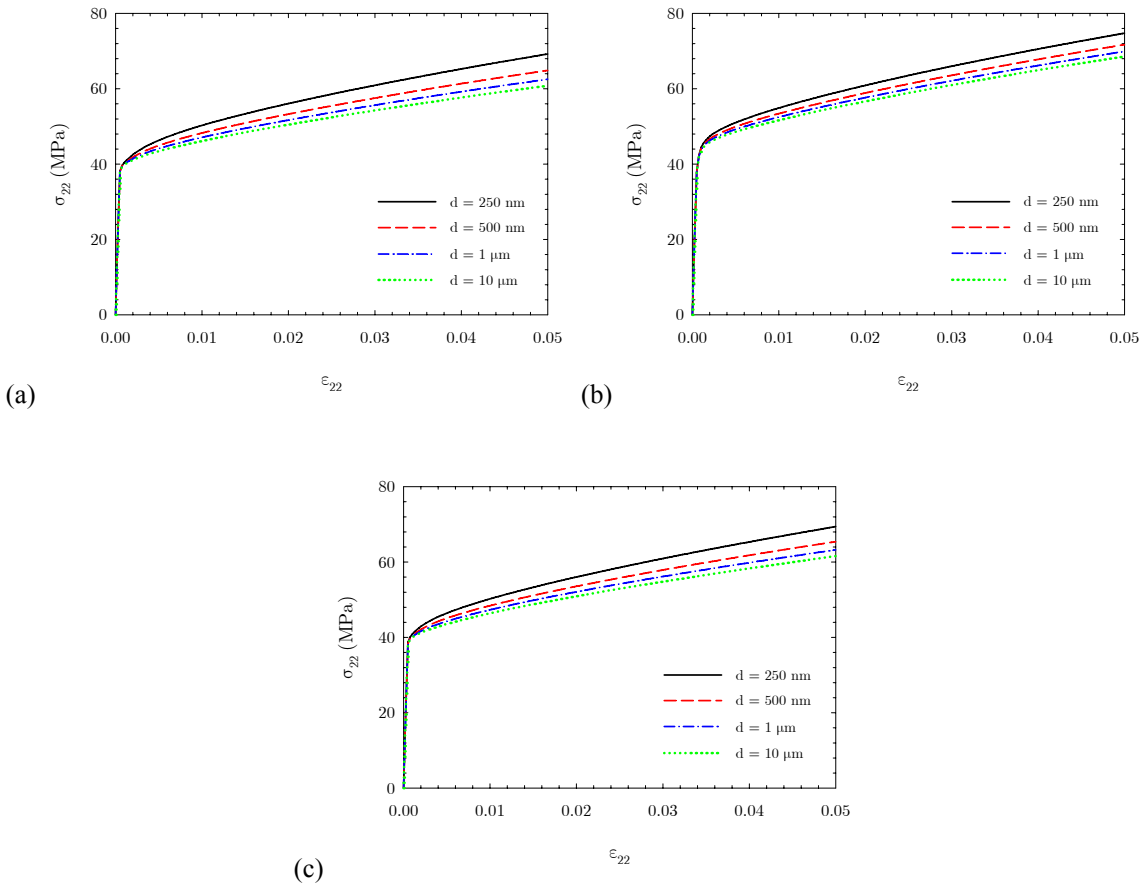

Figure 6.8: Macroscopic true uniaxial stress-strain curves for the traditional polycrystal model with $\ell_e = 10$ nm. (a) SVE1, (b) SVE2, and (c) SVE3.

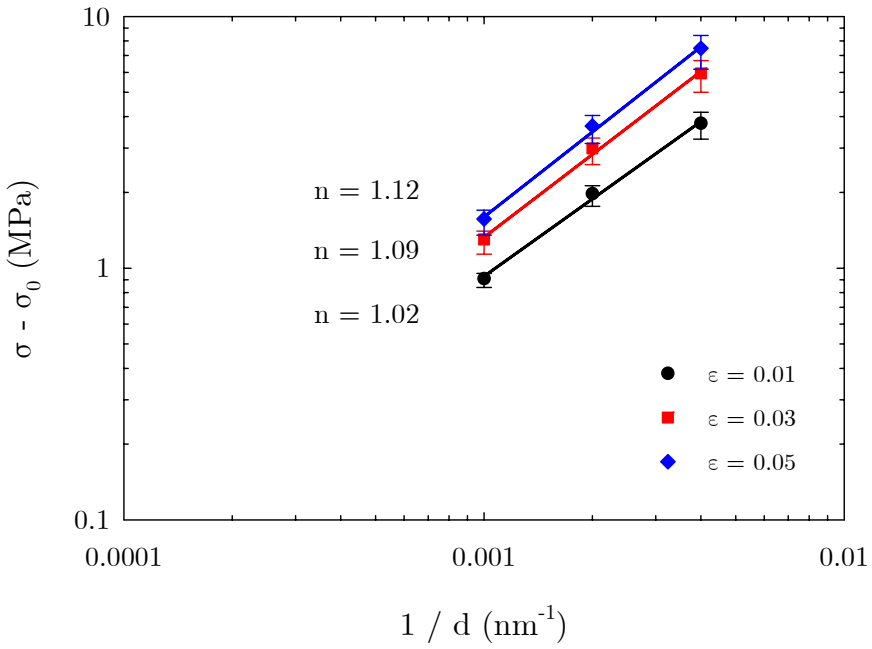

Figure 6.9: Scaling of macroscopic flow stress as a function of grain size for the traditional polycrystal representation with ℓ_e = 10 nm.

The cumulative slip field contour plots for both slip systems at $\varepsilon_{22} = 0.05$ are shown for SVE2 with grain sizes of 250 nm and 10 μm in Figure 6.10. Contour plots for the other two grain sizes have not been included in the figure because they do not reveal any additional insight as to how the fields vary with diminishing microstructural length scales. The contours have been cropped such that cumulative slip values greater than 0.25 appear as red to assist the visualization of the local field variations. The maximum local values of cumulative slip are relatively insensitive to changes in grain size, and are given as $\tilde{\gamma}^1_{\max} = 0.58$ and $\tilde{\gamma}^2_{\max} = 0.34$ for $d = 250$ nm and $\tilde{\gamma}^1_{\max} = 0.59$ and $\tilde{\gamma}^2_{\max} = 0.32$ for $d = 10$ μm. Furthermore, there is no general tendency for the local slip fields to increase/decrease in intensity with changes in grain size. Rather, it is seen that decreasing the grain size leads to an increase in the local cumulative slip magnitudes in some grains and decreases in others. This is reflective of the orientation-dependent gradient induced strengthening effects which tend to preferentially promote slip in grains with

weaker size-dependent strengthening. Gaining an in-depth understanding of this type of scale-dependent cooperative grain deformation could prove useful to those concerned with tailoring local microstructural arrangements and grain orientation/misorienation to achieve maximum flow resistance near critical component features. Lastly, attention is called to the fact that about half of the grains are deforming primarily by single slip, and that a large fraction of the actively deforming grains have rather uniform cumulative slip distributions as there are only a few grains that exhibit hot spots. It is also worth pointing out that the few observed hot spots all emanate from the grain boundary regions.

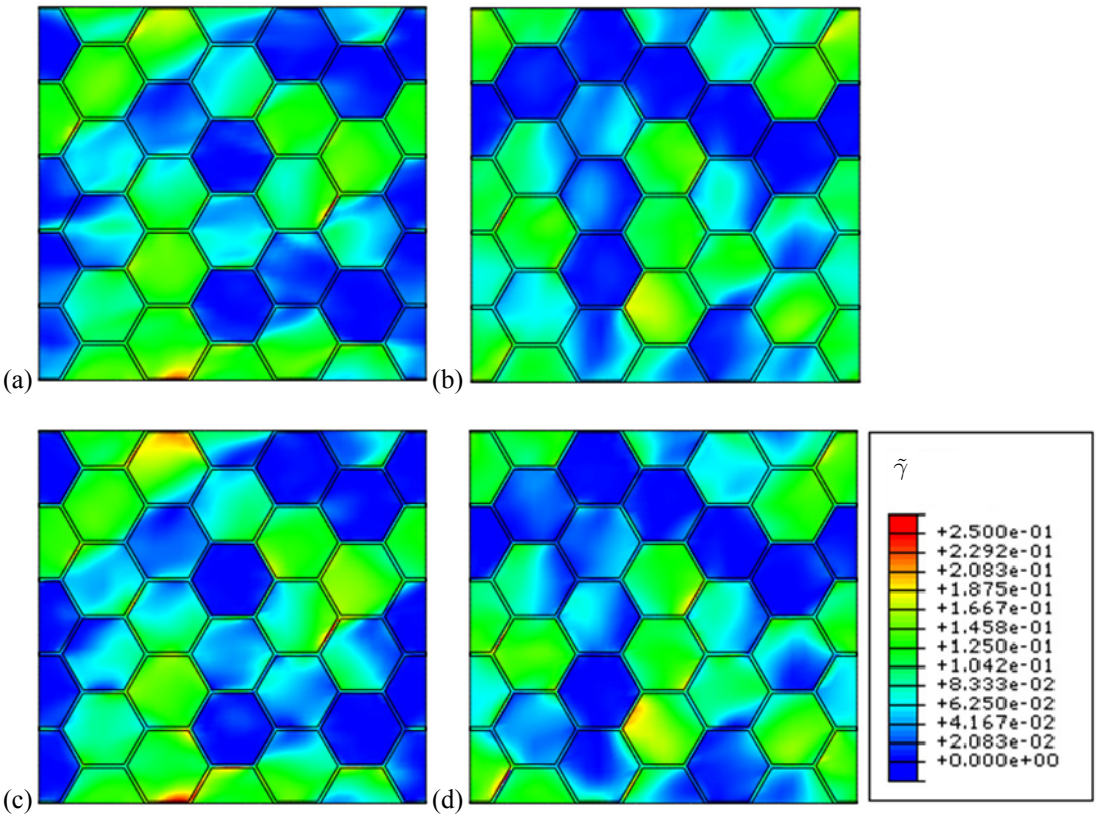

Figure 6.10: Cumulative slip distributions at $\varepsilon_{22} = 0.05$ for the traditional polycrystal representation (SVE2) with $\ell_e = 10$ nm (a) $d = 250$ nm slip system 1 (b) $d = 250$ nm slip system 2 (c) $d = 10$ μm slip system 1 and (d) $d = 10$ μm slip system 2.

The SSD and GND density contour plots are for SVE2 at $\varepsilon_{22} = 0.05$ are shown for all four grain sizes in Figure 6.11 and Figure 6.12, respectively. The contour plots have been cropped such that values above 1×10^8 mm^{-2} appear as red, and the maximum local values of SSD density are 2.58×10^8 mm^{-2} ($d =$ 250 nm), 2.40×10^8 mm^{-2} ($d = 500$ nm), 1.86×10^8 mm^{-2} ($d = 1$ μm), and 1.45×10^8 mm^{-2} ($d = 10$ μm). The SSD density fields essentially follow the same trends with respect to changes in grain size as the cumulative slip fields, although there are some subtle differences due to the fact that the SSD density evolution equation is defined as a function of the effective inelastic slip system deformation rate instead of the magnitude of the slip rate. Most notably, there is a higher propensity for the SSD density to concentrate in grain boundary regions with decreasing grain size. This is most readily apparent for the 250 nm and 500 nm grain sizes which are shown in Figure 6.11(a) and (b). While the intensity of the SSD density fields is relatively scale insensitive, it is demonstrated in Figure 6.12 that the GND density fields are substantially enhanced as the grain size is decreased. The GND density contours have been cropped such that values greater than 9×10^9 mm^{-2} appear red in the Figure, and the maximum local values are 9.45×10^{10} mm^{-2} ($d = 250$ nm), 6.68×10^{10} mm^{-2} ($d = 500$ nm), 4.73×10^{10} mm^{-2} ($d = 1$ μm), and 7.31×10^9 mm^{-2} ($d = 10$ μm). Not only do the peak GND densities increase with decreasing grain size, but there is also a notable increase in the GND density boundary layer width. This is most evident for the 250 nm grain size where in a few instances the boundary layer has extended well into or entirely over the interior region of the grain.

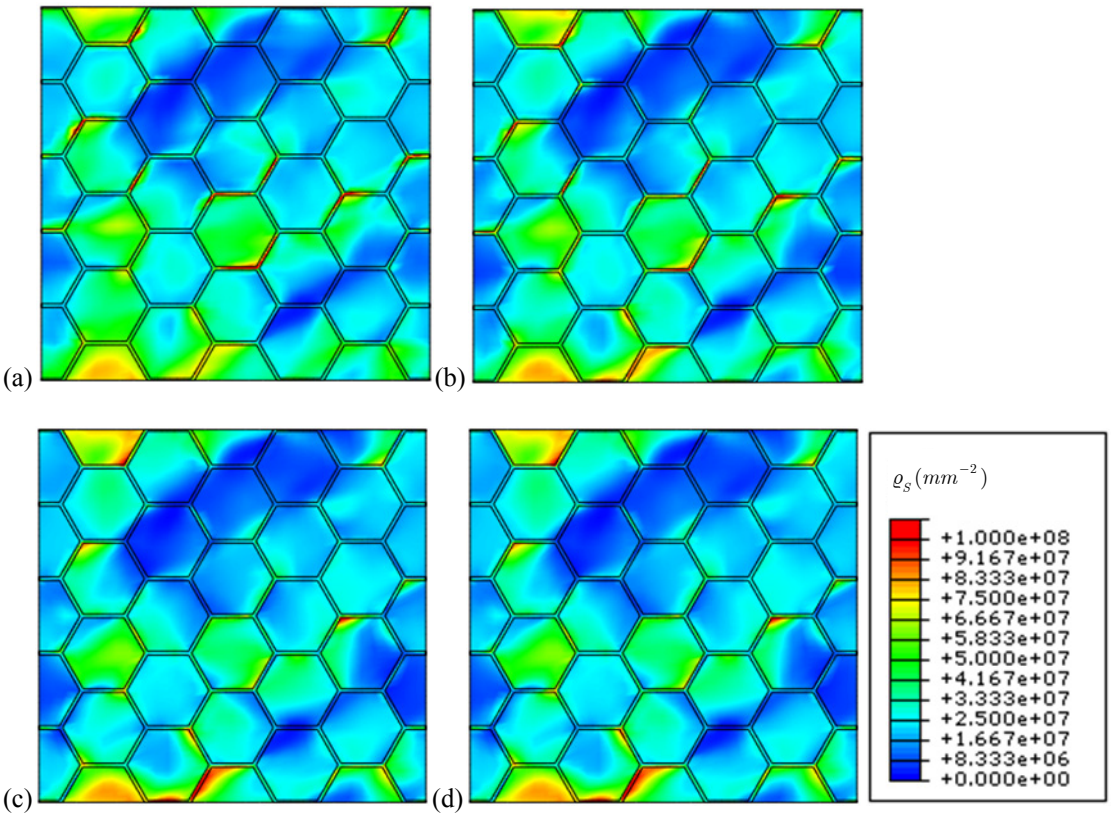

Figure 6.11: SSD density distributions at $\varepsilon_{22} = 0.05$ for the traditional polycrystal representation (SVE2) with $\ell_e = 10$ nm (a) $d = 250$ nm (b) $d = 500$ nm (c) $d = 1$ μm and (d) $d = 10$ μm.

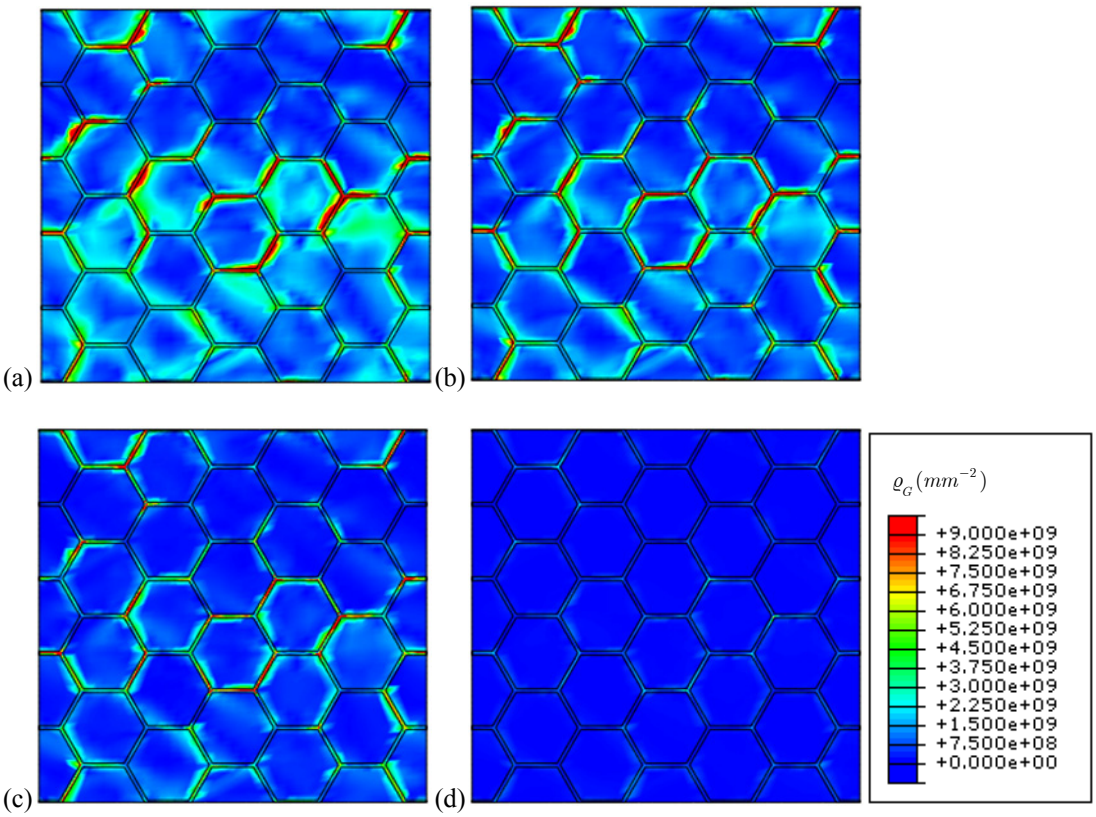

Figure 6.12: GND density distributions at $\varepsilon_{22} = 0.05$ for the traditional polycrystal representation (SVE2) with $\ell_e = 10$ nm (a) $d = 250$ nm (b) $d = 500$ nm (c) $d = 1$ μm and (d) $d = 10$ μm.

6.3.2 Core-Mantle Polycrystal Representation

Recall that the core-mantle model developed in this work has been motivated by the periodic single crystal two-phase laminate studies of Sedlacek and Forest [202], Forest and Sedlacek [39], Forest [38], and Cordero et al. [33]. In their works, they have primarily considered a single crystal wedged between two elastic adherends with a single slip system aligned perpendicular to the material interface. The material system is then subjected to a macroscopic simple shear and the size-dependent mechanical behavior is studied by varying the length of the single crystal phase. This initial-boundary value problem is similar to the constrained shear problem that has been solved in Chapters 4 and 5; however, the distinction here is that intermediate types of interfacial conditions can be explored instead of assuming a completely microrigid interface. The compliance of the interface is determined by the mismatch in the non-traditional

micropolar elastic constants, ℓ_e and μ_c, between the core and mantle region. However, the simulations performed in this section will only consider a mismatch of the micropolar coupling modulus, μ_c. Physically, the coupling modulus mismatch between phases can be understood in terms of how easily the couple stresses that arise at the interface can be mitigated. The couple stresses will remain concentrated at the interface for equal values of the coupling modulus, but will be diffused through the elastic phase when the mantle coupling modulus is lower than that of the core. It is noted that in addition to the geometrical simplifications made in the two-phase laminate analysis discussed above; the constitutive description has also been simplified as compared to the following polycrystal analysis. Those analyses considered a micropolar material description with no plastic curvature and no slip threshold hardening. In other words, all of the scale-dependent strengthening effects reported in those works are due to the linear form of gradient induced kinematic hardening.

The material properties for the grain cores used in these simulations are given in Table 6.1, and the elastic length scale is specified to be the same for both the grain and core phases as $\ell_e = 10$ nm. This value has been chosen so that the results of the current study can be compared to those obtained for the traditional polycrystal representation presented in the previous section. The coupling modulus mismatch is chosen to be $\mu_c^C / \mu_c^M = 10^4$ where the "C" and "M" superscripts refer to the core and mantle, respectively. This coupling modulus mismatch value was chosen in an effort to keep the scale effects from what we consider to be too extreme. The effect of the coupling modulus mismatch on the macroscopic stress-strain response is demonstrated in Figure 6.13 for SVE1 with $d = 250$ nm.

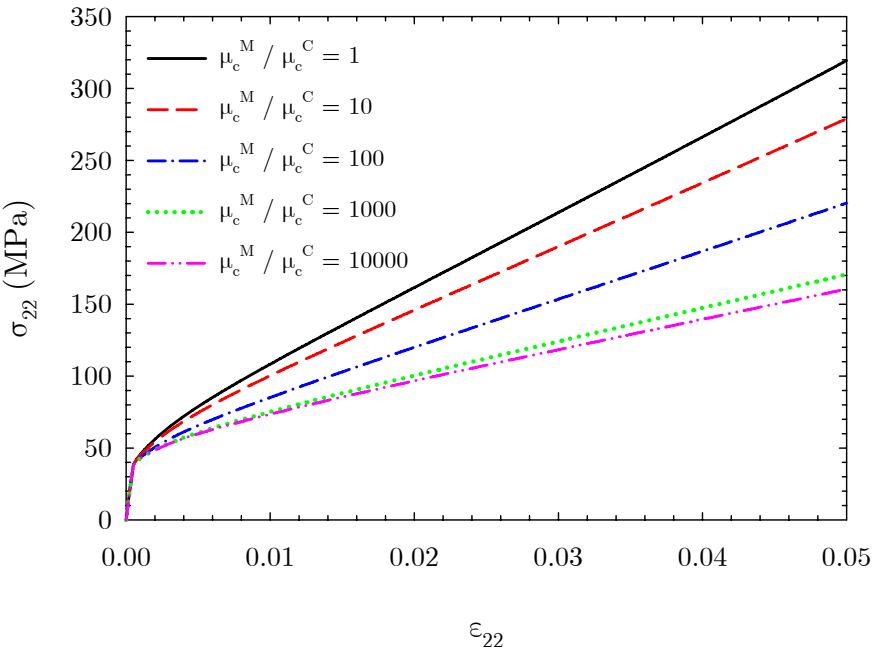

Figure 6.13: Macroscopic true uniaxial stress-strain curves for the core-mantle polycrystal model (SVE1) with $d = 250$ nm and $\ell_e = 10$ nm for various values of the coupling modulus mismatch.

The macroscopic uniaxial true stress-strain curves for the core-mantle polycrystal representation are given for each SVE in Figure 6.14. As compared to the stress-strain responses obtained from the analysis of the traditional polycrystal model, the core-mantle model results show very little variability between the individual SVE responses and also exhibit a significantly higher hardening rate. In fact, the core-mantle stress strain curves even have a hardening rate greater than that of the traditional model with $\ell_e = 250$ nm. Of course, this is due to the fact that the mantle is not allowed to plastically deform, and this represents a much more rigid constraint, even with a relaxed couple modulus, than is present in the traditional polycrystal simulations. The scaling behavior of the macroscopic flow stress is shown in Figure 6.15, and the scaling exponents for the three increasing strain levels are determined to be $n = 0.79$, 0.84, and 0.96. These values are intermediate to those obtained in the analysis of the traditional polycrystal

model with $\ell_e = 10$ nm and 250 nm, yet in agreement with the previous analyses it is seen that the scaling exponent is larger for higher levels of applied strain.

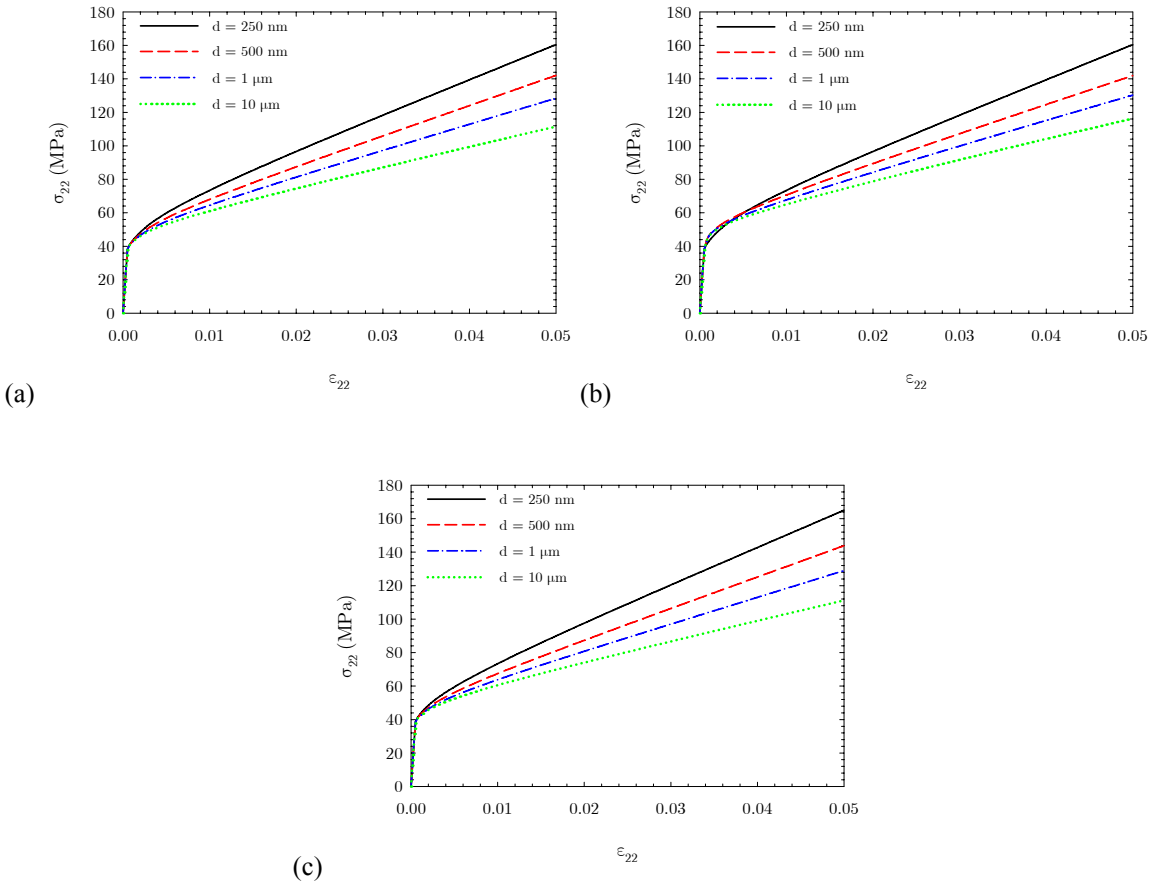

Figure 6.14: Macroscopic true uniaxial stress-strain curves for the core-mantle polycrystal model with $\ell_e = 10$ nm. (a) SVE1, (b) SVE2, and (c) SVE3.

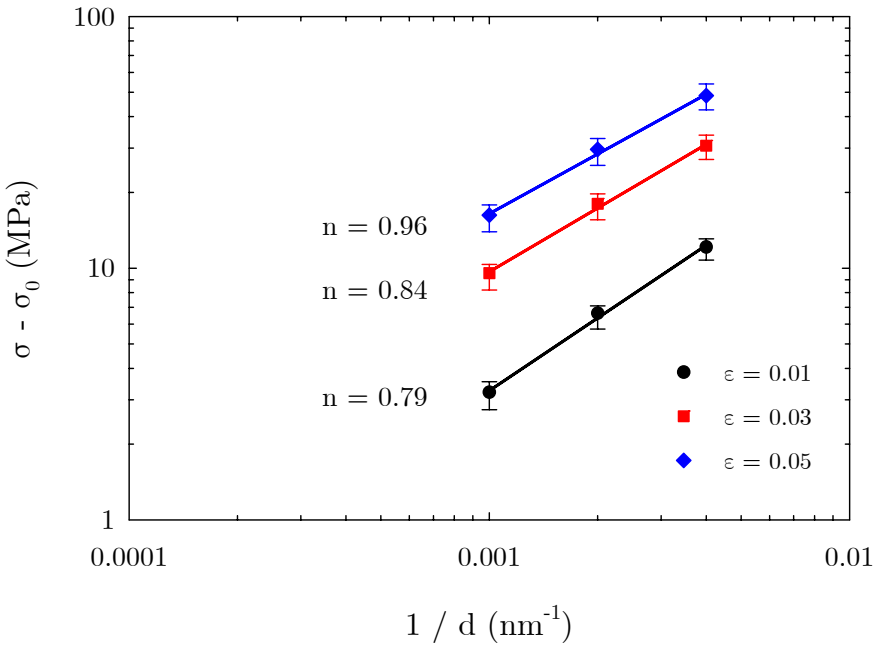

Figure 6.15: Scaling of macroscopic flow stress as a function of grain size for the core-mantle polycrystal representation with $\ell_e = 10$ nm.

Contour plots of the cumulative slip fields for both slip systems at $\varepsilon_{22} = 0.05$ for SVE2 with grain sizes of 250 nm and 10 μm are shown in Figure 6.16. The contour plots have been cropped such that values of cumulative slip greater that 0.25 are shown as red and the maximum local values are $\tilde{\gamma}^1_{\max} = 0.296$ and $\tilde{\gamma}^2_{\max} = 0.243$ for $d = 250$ nm and $\tilde{\gamma}^1_{\max} = 0.228$ and $\tilde{\gamma}^2_{\max} = 0.228$ for $d = 10$ μm. In accord with the earlier observations, there is no general size-dependent trend with respect to the deviations in the cumulative slip fields; some grains exhibit more intense shearing when the grain diameter is decreased whereas others are less prone to plastically deform. As compared to the traditional polycrystal simulations, the maximum cumulative slip values in the core-mantle simulations are significantly lower. This is explained by noting that the peaks in the cumulative slip fields occur exclusively in the grain boundary regions for the traditional polycrystal representation, while they remain elastic in the current material description. Thus, plastic slip is prevented from localizing into these areas leading to a more

uniform distribution of slip throughout the grain interiors and lower peak intensity cumulative slip hot spots. The inability of the grain boundaries to plastically deform also leads to additional slip system activity. For example, several of the grains that primarily deform via single slip in the traditional polycrystal model, show increased levels of slip on the secondary slip system in the core-mantle model.

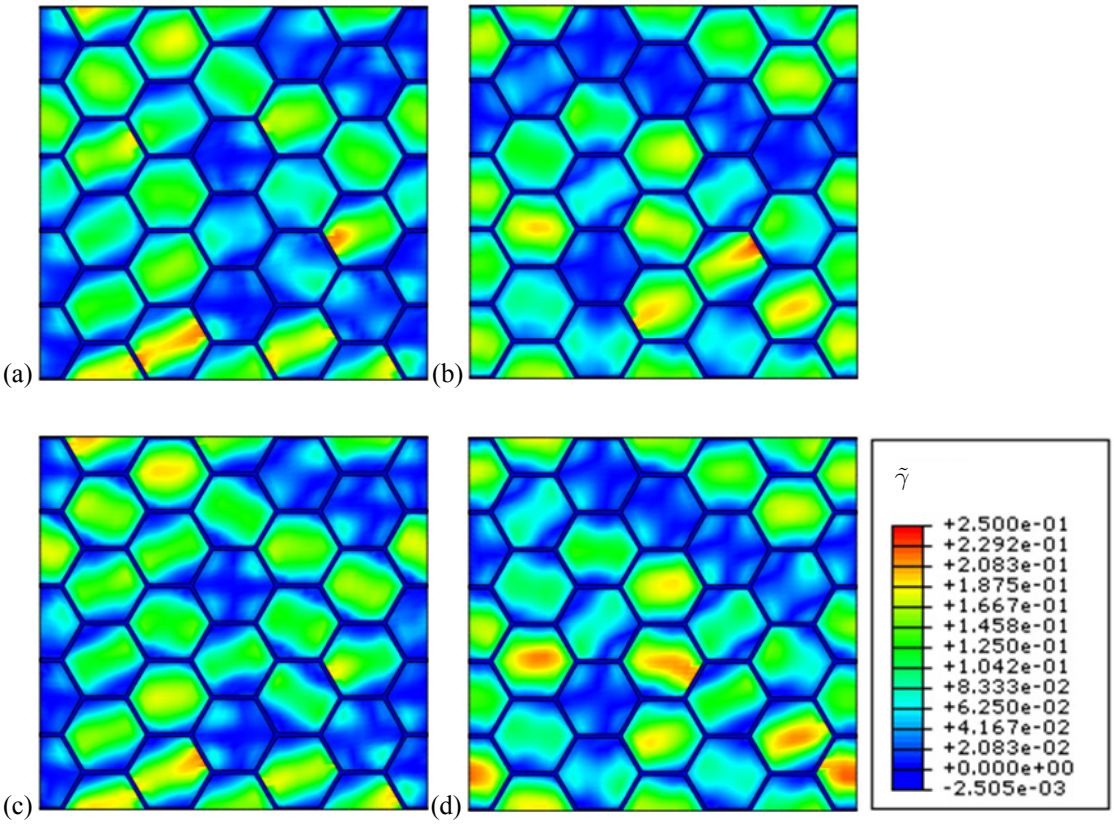

Figure 6.16: Cumulative slip distributions at $\varepsilon_{22} = 0.05$ for the core-mantle polycrystal representation (SVE2) with $\ell_e = 10$ nm (a) $d = 250$ nm slip system 1 (b) $d = 250$ nm slip system 2 (c) $d = 10$ μm slip system 1 and (d) $d = 10$ μm slip system 2.

SSD and GND density contour plots are shown for SVE2 for all grain sizes in Figure 6.17 and Figure 6.18, respectively. The SSD density fields exhibit limited sensitivity to changes in grain size and the maximum values span a much narrower spectrum, 1.23×10^8 mm^{-2} ($d = 250$ nm) - 1.32×10^8 mm^{-2}

($d = 10$ μm), as compared to the traditional polycrystal representation. Again, this is due to the no slip restriction in the grain boundary regions. For the most part, the SSD density is concentrated within the grain interiors with decreasing field intensity as the grain boundaries are approached; however, a few grains contain tear-shaped hot spots that originate at the core-mantle interface and extend into the core region. Figure 6.18 demonstrates that the magnitude of the GND density distribution depends strongly on the grain size, and this sensitivity is more pronounced for the core-mantle as compared to the traditional polycrystal representation. The contour plots have been cropped such that values greater than 9×10^{9} mm^{-2} are shown in red and the maximum values are 1.48×10^{10} mm^{-2} ($d = 250$ nm), 8.33×10^{9} mm^{-2} ($d = 500$ nm), 4.14×10^{9} mm^{-2} ($d = 1$ μm), and 4.68×10^{8} mm^{-2} ($d = 10$ μm). As expected, the GND density fields are concentrated near the core-mantle interface, and the development of well-defined boundary layers is clearly evident. The boundary layers tend to have a preferential alignment where parallel regions of higher GND density are separated by a relatively low GND density zone, but the boundary layers in some of the grains are multi-directional leaving only a small globular core of low GND density in the grain interior. It is also pointed out that the hot spots of GND density (see Figure 6.18(a)) do not always occur at the core-mantle interface, and there are in fact far more instances where the intragranular GND density peaks occur at points slightly offset from the interfaces.

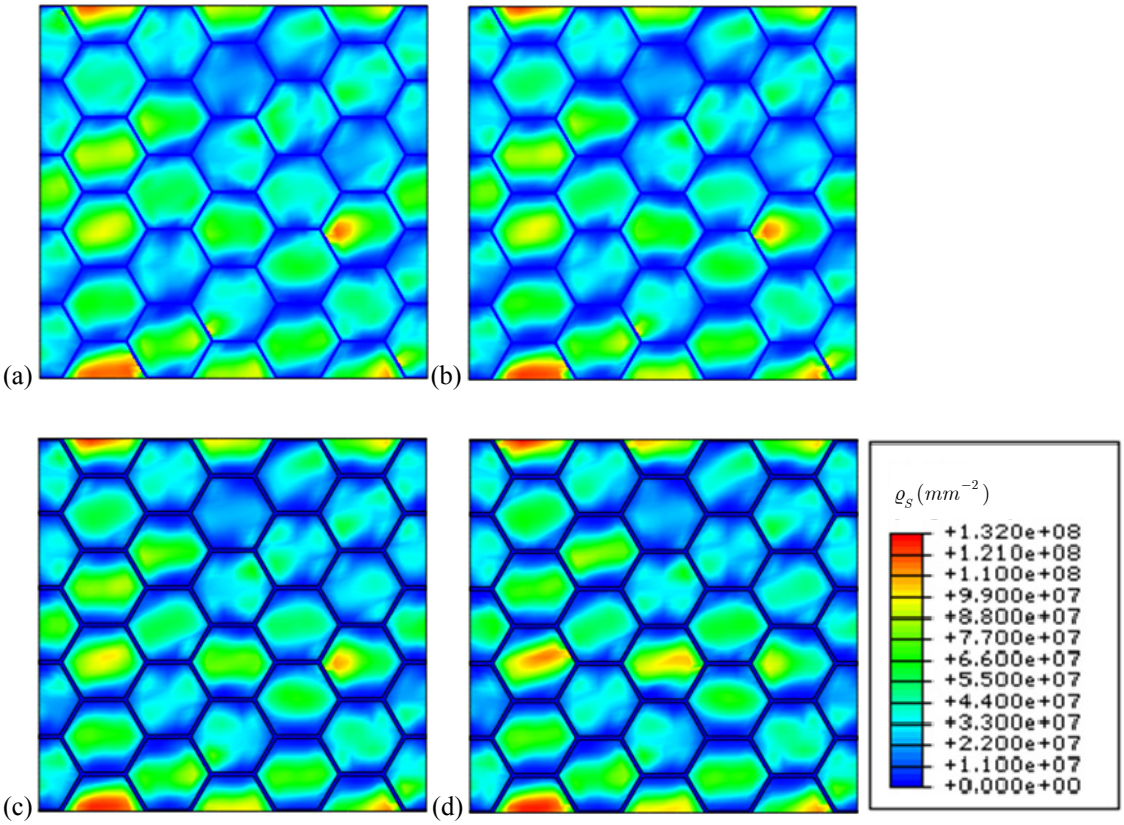

Figure 6.17: SSD density distributions at $\varepsilon_{22} = 0.05$ for the core-mantle polycrystal representation (SVE2) with $\ell_e = 10$ nm (a) $d = 250$ nm (b) $d = 500$ nm (c) $d = 1$ μm and (d) $d = 10$ μm.

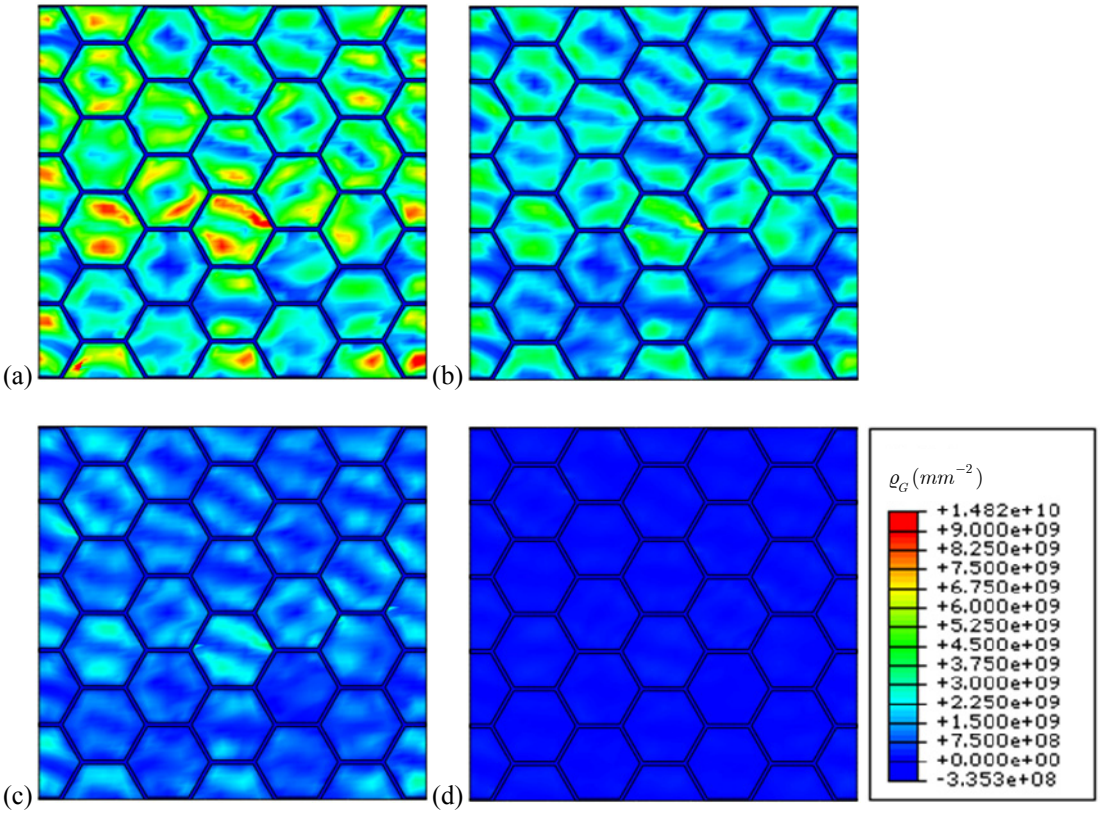

Figure 6.18: GND density distributions at $\varepsilon_{22} = 0.05$ for the core-mantle polycrystal representation (SVE2) with $\ell_e = 10$ nm (a) $d = 250$ nm (b) $d = 500$ nm (c) $d = 1$ μm and (d) $d = 10$ μm.

Finally, this subsection is concluded with side-by-side deformation field contour plots for both the traditional and core-mantle polycrystal representations at $\varepsilon_{22} = 0.05$ for SVE2 with $d = 250$ nm and $\ell_e = 10$ nm as shown in Figure 6.19. All of the plots have been previously shown and the various trends have been discussed, but they are given here on the same contour scale to offer a more direct comparison. Since many the similarities and differences between the two sets of polycrystalline results have already been discussed in detail, the previous commentary is only briefly reviewed. The cumulative slip fields in the traditional polycrystal tend to localize in the grain boundary regions leading to larger maximum local peaks as compared to the core mantle model. As a result of the additional deformation constraints imposed by the elastic grain boundary mantle, more slip activity is observed on secondary slip systems in the core-mantle model. Similar trends are also seen with respect to the SSD density field as they tend to localize

into the grain boundary regions in the traditional model, whereas the peak intensities primarily occur in the grain interiors in the core-mantle model. The GND density fields for the traditional model are much more highly localized near the grain boundaries (thinner boundary layers) than for the core-mantle model, and as a result the peak GND density values are consistently higher for this polycrystal description. While only a few grains exhibit local GND density hot spots in the traditional model, a higher percentage of grains display significant GND accumulation in the core-mantle model. This occurs because the GNDs cannot localize into the grain boundary regions in the core-mantle model, and therefore other grains must develop appreciable GND density fields in order to accommodate the imposed deformation. Finally, the lattice rotation fields are observed to be more uniform for the traditional model, a fact that is not surprising. By decreasing the couple modulus of the mantle region with respect to the grain core, the intergranular rotational constraints have been relaxed for the core-mantle model which gives the individual grains more freedom to deform independently and leads to the greater variations in lattice rotation. On the other hand, the intergranular rotations are tightly coupled in the traditional model and the result is a less heterogeneous lattice rotation field.

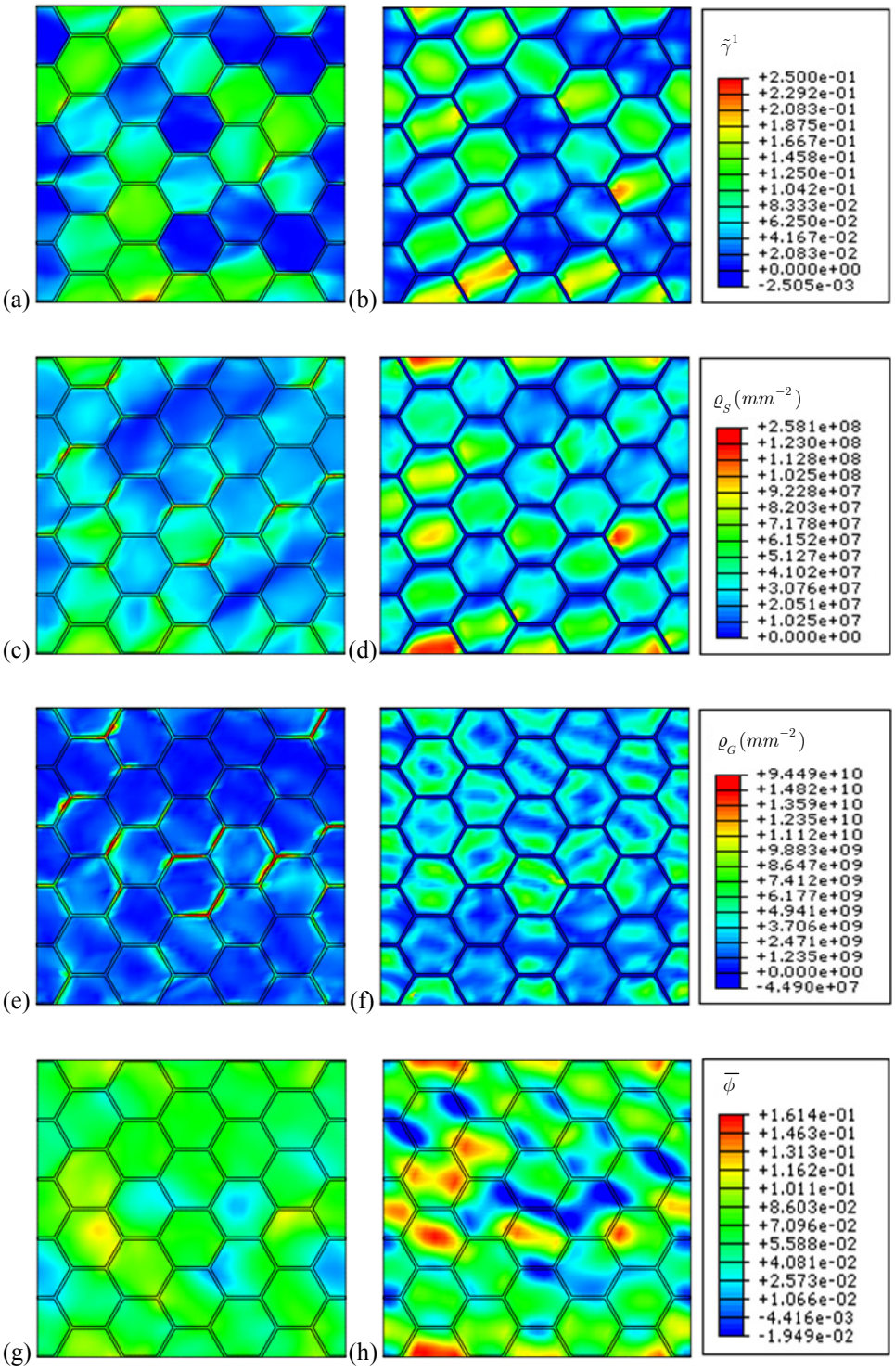

Figure 6.19: Comparison of deformation fields for traditional (left column) and core-mantle (right column) polycrystal representations for $d\ /\ \ell_e = 25$ at $\varepsilon_{22} = 0.05$. (a) and (b) cumulative slip on slip system 1 (c) and (d) SSD density (e) and (f) GND density and (g) and (h) lattice rotation.

6.4 Summary

This chapter has presented a study of the scale-dependent mechanical response of small polycrystalline ensembles using the micropolar crystal plasticity theory developed in Chapter 3. Two different representations of the polycrystal have been studied: a traditional model and a core-mantle model. The traditional polycrystal representation does not delineate the grain interior from the grain boundary region, whereas the core-mantle model does. Each grain is treated as a micropolar elastic-viscoplastic constituent in the former type of model where the intergranular responses are coupled through shared lattice rotational degrees-of-freedom at the grain boundaries. The core-mantle description treats the polycrystal as a collection of micropolar elastic-viscoplastic grains (cores) embedded in a micropolar elastic matrix (mantle). In the core-mantle model, the size-dependent response of the polycrystal is governed by the mismatch in the micropolar couple modulus between the core and mantle phases. The relative couple modulus mismatch determines how the couple stresses are diffused at the core-mantle interface. When the couple modulus is equal in the two phases, the couple stresses remain concentrated and give a very strong size-dependent response. As the couple modulus of the mantle is lowered with respect to the core, the couple stresses become more diffuse and the size-effect becomes less pronounced. A limited number of simulations have been performed to highlight the general features of the deformation fields for the two polycrystal representations, and the scaling of the mechanical response with grain size has been both qualitatively and quantitatively discussed.

CHAPTER 7

SUMMARY AND CONCLUSIONS

7.1 Summary

This research is concerned with the development of models of micropolar single crystal plasticity as an alternative to the more common slip gradient-based models of generalized single crystal plasticity. A micropolar continuum is a type of higher-order work-conjugate continuum that has the desired model features stated at the outset of the work, i.e., the model:

- ◊ maintains the standard treatment of elastic-plastic thermodynamics,
- ◊ avoids treating the plastic slips as generalized displacements,
- ◊ admits higher-order (non-standard) boundary conditions, and
- ◊ offers a simpler and more efficient numerical implementation as compared to the slip gradient-based approaches

The three main objectives of this work are to:

- ◊ Develop physically-based models of micropolar single crystal elasto-viscoplasticity.
- ◊ Implement the constitutive models in a finite element code.
- ◊ Apply the models to simulate the scale-dependent mechanical response of single and polycrystalline metals, benchmark against discrete dislocation simulations, and conduct parametric studies to shed light on more appropriate forms of constitutive relations within the micropolar crystal plasticity construct.

In conjunction with these stated objectives, two distinct viscoplastic modeling frameworks - the so-called single- and multicriterion theories are developed. Dislocation-based strength models are proposed for each theory are developed which enables clear connections between the micropolar theory and various aspects of slip gradient-based generalized crystal plasticity theories to be established. The dislocation-based strength models provide a physically-based description of scale-dependent strengthening and make the framework amenable for comparing to finer scale simulation results more directly. The development of the single-criterion flow rule has been motivated by related earlier works in phenomenological macroscopic micropolar elastoplasticity, and also by the desire to minimize the number of non-standard constitutive parameters. This work represents the first attempt of employing a single-criterion flow rule within a theory of micropolar single crystal plasticity. Several variations of the dislocation-based strength models appropriate for each theory have been proposed and evaluated via direct numerical simulation. It has been demonstrated that strength models in which the slip threshold is given by a generalized Taylor relation (dependence on the summed SSD and GND densities) are incapable of accurately capturing the deformation behavior observed in discrete dislocation simulations of an equivalent initial-boundary value problem. This is an important observation since generalized crystal plasticity models typically include this type of isotropic hardening description, and our results show that, at least for the micropolar framework, this is a physically questionable assumption.

Two-dimensional versions of the constitutive theories have been numerically implemented via a user element (UEL) subroutine in the implicit commercial finite element code Abaqus/Standard. The element performance is validated through the solution of elastic initial-boundary value problems with closed-form solutions, and the convergence behavior is also demonstrated for an elastic-plastic initial-boundary value problem exhibiting strain localization thereby verifying the mesh regularizing features of the nonlocal formulation. Convergence has been demonstrated both in terms of the global, e.g., the stress-strain behavior, and local response, and it has been observed that the rate of convergence for the global response is much higher than for local behavior.

The constitutive models are then employed to solve several standard initial-boundary value problems for heterogeneously deforming single crystals including: simple shearing of a constrained thin film, pure bending of thin films, and simple shearing of a metal matrix composite with elastic inclusions.

First, the general performance of the constitutive models is demonstrated via solution of the constrained shear problem in order to gain an understanding of how the non-classical inelastic material constants affect the mechanical response and the resulting deformation fields. It is seen that the elastic length scale governs the gradient induced kinematica hardening response where larger values of the elastic length scale lead to higher rates of kinematic hardening. Additionally, the ratio of plastic-to-elastic length scale dictates the accumulation of GND density and the transient nonlinear kinematic harderning response. Smaller ratios of plastic-to-elastic length scale are associated with larger accumulated GND densities and more rapid saturation of the kinematic hardening, whereas larger ratios lead to converse behavior.

This information is then used to guide calibration of the micropolar models to results of equivalent initial-boundary value problems solved using discrete dislocation dynamics. The deformation behavior predicted by the calibrated micropolar models is then compared to results obtained from both discrete dislocation dynamics simulations as well as alternative generalized crystal plasticity theories. Comparison and calibration with respect to the former provides guidance in the specification of non-traditional material intrinsic length scale parameters, and demonstrates the developed models' ability to capture the relevant heterogeneous deformation fields and size-dependent mechanical behavior predicted by a finer scale constitutive description. Comparison to results obtained using other generalized crystal plasticity theories has demonstrated that the deformation behavior predicted by these alternative theories can be qualitatively and quantitatively reproduced by the micropolar theory. A few notable results have emerged from the single crystal studies and the comparison to discrete dislocation dynamics simulations. It has been demonstrated that all substructure evolution parameters - not just the length scales - are sensitive to the specific boundary value problem being solved. The micropolar theory has demonstrated that it can accurately describe the dislocation substructure evolution in the presence of microrigid boundaries; however, as observed in the pure bending simulations, there is a deficiency in modeling microfree surfaces due to the lack of an image force effect. Finally, it has been observed in the metal matrix composite simulations that the micropolar theory accurately captures the development of compatibility maintaining dislocation structures, e.g., tilt walls, but does not predict other types of non-redundant dislocation structures, e.g., dislocation pileups, that may develop. These findings suggest that the micropolar model needs to be improved in an effort to represent these additional long-range interaction fields due to the

presence of free surfaces and the development of dislocation structures that are not accounted for in the current formulation.

Finally, the models are applied to simulate the deformation behavior of small polycrystalline ensembles. Due to the previously outlined model limitations that have emerged out of the single crystal simulations, only a limited number of polycrystal simulations have been peformed. These limitations should be addressed within the single crystal constitutive description prior to performing more extensive polycrystal simulations. Two different polycrystal representations are considered: a traditional representation in which the micropolar model is employed up to the grain boundary and a core-mantle representation in which the grain boundary regions are treated as elastic. Direct numerical simulations are performed for a range of grain sizes using both polycrystal representations in order to evaluate the aggregate mechanical response, and the scale-dependent deformation behavior is subsequently analyzed. For the limited cases studied in this work, it has been observed that the flow stress scales exponentially with the inverse grain size with scaling exponents in the range $0.2 \leq n \leq 1.1$ and the scaling exponent increases with deformation. It has also been determined that there is a critical limiting effective grain size, $d / \ell_e = 5$, for the traditional representation below which the simulations yield aphysical results. This is due to the polycrystal being overly stiff with respect to the development of lattice curvature for effective grain sizes smaller than this.

7.2 Novel Contributions

The unique contributions of this dissertation as summarized as follows:

Constitutive Model Development

- Two new physically-based theories of micropolar single crystal plasticity have been developed.
  - A multicriterion flow theory with a dislocation-based strength model has been proposed and is an extension of the phenomenological strength model of Forest et al. [34]. The replacement of the phenomenological strength model with a dislocation-based model is a necessary step for relating

the current developments to existing physically-based models, and also for making direct comparisons to finer scale simulations, i.e., discrete dislocation dynamics.

- A novel single-criterion flow theory with a dislocation-based strength model has also been proposed. Single-criterion flow rules are commonly used in other types of higher-order nonlocal crystal plasticity theories, and are advantageous because they significantly reduce the number of non-standard material constants as compared to multicriterion theories.

- Several variations of the dislocation-based strength models have been proposed and their performance has been evaluated via direct numerical simulation. It has been demonstrated that some of the strength models do not produce deformation behavior consistent with observations from finer scale discrete dislocation simulations.

❖ The relationship between the developed models and the more common slip gradient-based theories has been established.

- A focused effort has been made to relate the models to the prominent and highly cited model due to Gurtin [17], which is a significant contribution since the proposed models offer a simpler numerical implementation than the former. This has important implications in the practical application of the model in 3-D numerical simulations.

Numerical Simulations

❖ A numerical implementation of the model has been developed and incorporated into the commercial finite element code Abaqus/Standard as a user element subroutine.

❖ The numerical implementation has been validated through the solution of boundary value problems with known analytical solutions, and the convergence behavior for an inelastic problem featuring strain localization has been studied and the mesh regularization properties have been demonstrated.

❖ The role of the model length scale parameters has been clearly defined in terms of their effect on the mechanical response and the development of heterogeneous deformation fields. This understanding is critical to ascribing physical significance to the nonlocal material parameters.

❖ The viability of the models has been established through a comparison to discrete dislocation dynamics simulations of equivalent initial-boundary value problems. This not only demonstrates that the models are capable of capturing the physics of lower length scale deformation processes in meaningful way, but also suggests they could be incorporated as part of a multi-scale modeling framework.

- A pathway and methodology for calibrating the micropolar model parameters to discrete dislocation dynamics simulations has been established. Knowledge of how the nonlocal material parameters relate to various aspects of the finer scale simulations lends confidence that the calibrated values are physically meaningful.

7.3 Conclusions

The following conclusions are drawn from the work presented in this dissertation:

- The developed micropolar models are capable of accurately modeling the size-dependent mechanical response exhibited by fine scale discrete dislocation dynamics simulations.

- The size-effects in the model are related to the development of gradients in lattice rotation, i.e., lattice torsion curvature. As a result, there is minimal scale-dependence in the initial yield point. This, however, should not be viewed as a limitation as there is a growing amount of evidence that scale-dependence of initial yield strength is a source-controlled phenomenon which should be incorporate in the model through variations in the initial slip system threshold stress.

- The strength models based on an additive superposition of the SSD and GND densities in the slip threshold stress yield results inconsistent with discrete dislocation dynamics simulations. Namely, they overestimate the amount of isotropic hardening.

- The multicriterion strength model based on a constant curvature threshold stress leads to material instability and excessive isotropic hardening due to the unlimited generation of GNDs.

- The single-criterion model has proven capable of describing the full range of material behavior as the multicriterion model with significantly fewer nonlocal material parameters.

- The single crystal simulations calibrated to discrete dislocation dynamics results have demonstrated that the both model length scale parameters and the dislocation substructure evolution constants depend not only on the boundary value problem being considered, but also on the crystal orientation. This suggests that using uniform length scale and dislocation substructure

parameters for each grain in a polycrystal analysis is not justified, since the orientations and local boundary conditions at each grain boundary will vary from one grain to another.

- The model length scale parameters control transients in the gradient induced kinematic hardening.
  - In the absence of plastic curvature, a linear kinematic hardening response that is proportional to the square of the elastic length scale is obtained.
  - The magnitude of the scale-dependent linear kinematic hardening modulus depends on the orientation of the crystal, because the crystal orientation will dictate the strength of the curvatures that develop.
  - When plastic curvature is non-negligible, a nonlinear kinematic hardening response is obtained. Larger ratios L_p / ℓ_e lead to slower developing transients, where as lower ratios lead to faster saturation behavior.
- The ratio L_p / ℓ_e dictates the total accumulated GND density in the continuum.
- The mesh regularization properties of the micropolar model have been demonstrated for the initial-boundary value problem of strain localization in a strain softening material. The macroscopic (force-deflection) behavior converges much more rapidly than the peak local field values.
- The micropolar model has been shown to have striking similarities to the Gurtin-type slip gradient-based single crystal plasticity model.
- The micropolar model has demonstrated good agreement with discrete dislocation simulations that feature microrigid boundary conditions; however, as the problems of pure bending have shown, there seems to be a deficiency in modeling the microfree boundary condition. The image force effect is not accurately reflected in the micropolar model, and significant GND density is seen to accumulate at the free surface.
- The micropolar theory does an adequate job of predicting the development compatibility maintaining dislocation structures, i.e., those do to pure bending or those that gather in a tilt wall configuration in the metal matrix composite problem, but are unable to predict other types of non-

redundant dislocation structures such as dislocation pileups that develop simply due to slip obstruction. This is due to the inherent decoupling of the plastic slip and curvature responses within the micropolar theory. In fact, the underestimation of the Bauschinger effect for the metal matrix composite problem is believed to be partially due to the unaccounted back stresses caused by these neglected pileup configurations.

- The scaling behavior of the polycrystalline flow stress has been quantified for two polycrystalline representations.

  - The flow stress scaling exponents were in the range of $0.2 \leq n \leq 1.1$ and increase with increase with applied deformation.

  - A critical limiting value of the effective grain size, $d / \ell_e \approx 5$, was determined for the traditional polycrystal representation. Using smaller values of effective grain size lead to enhanced size-effects, but also the unphysical situation of increasing GND density with increasing grain size.

  - The traditional polycrystal representation tends to feature both SSD and GND densities which localize into the grain boundary regions, whereas in the core-mantle representation the SSDs tend to be more centrally located in the grain interiors and the GNDs primarily form directional boundary layers that grow with decreasing grain size.

  - The cumulative slip and SSD density fields are relatively insensitive to changes in grain size as compared to the GND density distributions.

7.4 Recommendations for Future Work

This research has focused on the development, implementation, and application of a micropolar model of single crystal plasticity as a more computationally efficient alternative to slip gradient-based models of generalized crystal plasticity. Furthermore, a clear connection between the two approaches has been put forth both theoretically in terms of model structure, and also computationally in terms of the way

various model components affect different aspects of the deformation fields and macroscopic response during heterogeneous deformation. However, there is still one fundamental difference between the two classes of higher-order theories; namely, the disparity between the types of micro boundary conditions that can be applied. In slip gradient-based higher-order theories, the admissible types of micro boundary conditions are either in terms of slip and higher-order microcouple tractions (work conjugate) or slip and GND density (non-work conjugate), while the micro boundary conditions in the micropolar model are in terms of lattice rotations or couple tractions. The relationship between the two types of micro boundary conditions has only been qualitatively discussed in the present work, and it may be fruitful to try and establish a more rigorous connection between them, if such a direct connection exists. In particular, this knowledge could be potentially used to apply an appropriate constraint or couple traction on the free surface in bending to create the image force effect that is present in the discrete and statistical dislocation simulations, but is absent in the micropolar simulations. Furthermore, it is envisioned that an understanding of the interrelationship between the two sets of micro boundary conditions is essential to prescribing conditions at grain boundaries that are intermediate to the microfree and microrigid constraints. These intermediate boundary conditions presumably would reflect partial slip transfer and slip blockage at the boundaries, but would ultimately be doing so in an indirect manner. This disconnect between the physics of slip transfer and the micro boundary conditions is a weakness of the micropolar theory, but it is also this aspect that makes the framework more computationally tractable.

It has been demonstrated that the micropolar models are able to reproduce both the macroscopic mechanical response and dislocation substructure evolution predicted by discrete dislocation dynamics simulations quite well. On the other hand, it has been seen that the micropolar length scale parameters must be changed from one boundary value problem to the next, and also for solutions to the same boundary value problem when the crystal orientation is changed. Further study of the interrelationship between the type of boundary value problem, the crystal orientation, and the length scale parameters required to reproduce discrete dislocation dynamics results would be highly beneficial. In particular, it would be interesting to extend the developed micropolar theories to include thermal strains, and to compare to the thermal cycling experiments of passivated thin films bonded to rigid substrates performed by Nicola et al. [6]. It would be especially significant if enough insight could be gained such that the micropolar

parameters could be estimated prior to performing the discrete dislocation simulations. Such knowledge would then imbue the micropolar models with true predictive capability.

Finally, several model enhancements are recommended in order of increasing difficulty and/or utility. It is suggested that the model should be extended to

- include an additional kinematic hardening component to account for the back stress contributions due to dislocation pileups,
- three dimensions, and
- finite deformation.

The first suggested enhancement addresses to the inability of the current version of the micropolar model to capture the back stress contribution due to dislocation pileups as illustrated in the composite shear initial-boundary value problem. Typically, the only nonlocal back stress component incorporated in nonlocal crystal plasticity models is that due to the compatibility induced GNDs; however, the current research suggests that this assumption is insufficient in certain situations. The importance of an additional contribution to back stress due to highly ordered dislocation structures (e.g., stacks of dislocation pileups) has been noted by Roy et al. [203], Mesarovic et al. [204], and Baskaran et al. [205]. The extension of the model to 3-D should be relatively straight-forward, and will enable the model to be more closely compared with experimental observations as well as a more diverse set of computational studies. For example, an extension to 3-D will facilitate a comparison to the more advanced 3-D discrete dislocation dynamics frameworks (e.g., Zbib et al. [59], Ghoniem et al. [54], and Weygand et al. [58]), and will also allow for the effects of GN screw dislocations to be studied. Lastly, the extension of the model to account for finite deformations, while theoretically challenging, will enable to model to be applied to problems such as metal forming where large lattice rotations are observed. A study of texture evolution predicted by a 3-D finite deformation micropolar crystal plasticity model has not been done to date, and it would be informative to evaluate the micropolar model predictions with respect to experimental observations and results from a classical crystal plasticity theory. As an intermediate step to implementing a full finite deformation theory with both elastic-plastic strain and torsion-curvature, a theory with only elastic torsion-curvature could be

pursued thereby avoiding issues associated with the elastic-plastic decomposition of the finite lattice torsion-curvature. In fact, recently Forest [38] and Cordero et al. [33] have advocated micropolar approaches neglecting plastic torsion-curvature within an infinitesimal deformation framework. This approach was not pursued in this research because it results in a linear gradient-induced kinematic hardening and a more general description was favored; however, this methodology should be sufficient for initial studies of finite deformation micropolar crystal plasticity.

REFERENCES

[1] E.O. Hall, The Deformation and Ageing of Mild Steel .3. Discussion of Results, Proceedings of the Physical Society of London Section B, 64 (1951) 747-753.

[2] N.J. Petch, The Cleavage Strength of Polycrystals, Journal of the Iron and Steel Institute, 174 (1953) 25-28.

[3] Q. Ma, D.R. Clarke, Size-dependent hardness of single crystals, J. Mater. Res., 10 (1995) 853-863.

[4] J.S. Stolken, A.G. Evans, A microbend test method for measuring the plasticity length scale, Acta Mater., 46 (1998) 5109-5115.

[5] N.A. Fleck, G.M. Muller, M.F. Ashby, J.W. Hutchinson, Strain gradient plasticity: Theory and experiment, Acta Metall. Mater., 42 (1994) 475-487.

[6] L. Nicola, Y. Xiang, J.J. Vlassak, E. Van der Giessen, A. Needleman, Plastic deformation of freestanding thin films: Experiments and modeling, J. Mech. Phys. Solids, 54 (2006) 2089-2110.

[7] R.P. Vinci, J.J. Vlassak, Mechanical behavior of thin films, Annu. Rev. Mater. Sci., 26 (1996) 431-462.

[8] R.J. Asaro, J.R. Rice, Strain localization in ductile single crystals, J. Mech. Phys. Solids, 25 (1977) 309-338.

[9] J.L. Bassani, Plastic flow of crystals, in: Advances in Applied Mechanics, Vol 30, 1994, pp. 191-258.

[10] J.R. Rice, Inelastic constitutive relations for solids: An internal-variable theory and its application to metal plasticity, J. Mech. Phys. Solids, 19 (1971) 433-455.

[11] M.F. Ashby, Deformation of plastically non-homogeneous materials, Philos. Mag., 21 (1970) 399-424.

[12] Z.P. Bazant, M. Jirasek, Nonlocal integral formulations of plasticity and damage: Survey of progress, J. Eng. Mech.-ASCE, 128 (2002) 1119-1149.

[13] M. Kuroda, V. Tvergaard, Studies of scale dependent crystal viscoplasticity models, J. Mech. Phys. Solids, 54 (2006) 1789-1810.

[14] L.P. Evers, W.A.M. Brekelmans, M.G.D. Geers, Non-local crystal plasticity model with intrinsic SSD and GND effects, J. Mech. Phys. Solids, 52 (2004) 2379-2401.

[15] L.P. Evers, W.A.M. Brekelmans, M.G.D. Geers, Scale dependent crystal plasticity framework with dislocation density and grain boundary effects, Int. J. Solids Struct., 41 (2004) 5209-5230.

[16] M.E. Gurtin, On the plasticity of single crystals: free energy, microforces, plastic-strain gradients, J. Mech. Phys. Solids, 48 (2000) 989-1036.

[17] M.E. Gurtin, A gradient theory of single-crystal viscoplasticity that accounts for geometrically necessary dislocations, J. Mech. Phys. Solids, 50 (2002) 5-32.

[18] M.E. Gurtin, L. Anand, S.P. Lele, Gradient single-crystal plasticity with free energy dependent on dislocation densities, J. Mech. Phys. Solids, 55 (2007) 1853-1878.

[19] A. Ma, F. Roters, D. Raabe, A dislocation density based constitutive model for crystal plasticity FEM including geometrically necessary dislocations, Acta Mater., 54 (2006) 2169-2179.

[20] A. Ma, F. Roters, D. Raabe, On the consideration of interactions between dislocations and grain boundaries in crystal plasticity finite element modeling - Theory, experiments, and simulations, Acta Mater., 54 (2006) 2181-2194.

[21] C.S. Han, A.X. Ma, F. Roters, D. Raabe, A finite element approach with patch projection for strain gradient plasticity formulations, Int. J. Plast., 23 (2007) 690-710.

[22] F.T. Meissonnier, E.P. Busso, N.P. O'Dowd, Finite element implementation of a generalised non-local rate-dependent crystallographic formulation for finite strains, Int. J. Plast., 17 (2001) 601-640.

[23] E. Bittencourt, A. Needleman, M.E. Gurtin, E. Van der Giessen, A comparison of nonlocal continuum and discrete dislocation plasticity predictions, J. Mech. Phys. Solids, 51 (2003) 281-310.

[24] U. Borg, C.F. Niordson, J.W. Kysar, Size effects on void growth in single crystals with distributed voids, Int. J. Plast., 24 (2008) 688-701.

[25] J.Y. Shu, W.E. King, N.A. Fleck, Finite elements for materials with strain gradient effects, Int. J. Numer. Methods Eng., 44 (1999) 373-391.

[26] V.P. Smyshlyaev, N.A. Fleck, The role of strain gradients in the grain size effect for polycrystals, J. Mech. Phys. Solids, 44 (1996) 465-495.

[27] J.Y. Shu, N.A. Fleck, Strain gradient crystal plasticity: Size-dependent deformation of bicrystals, J. Mech. Phys. Solids, 47 (1999) 297-324.

[28] H.K. Kim, S.I. Oh, Finite element analysis of grain-by-grain deformation by crystal plasticity with couple stress, Int. J. Plast., 19 (2003) 1245-1270.

[29] P.M. Naghdi, A.R. Srinivasa, A dynamical theory of structured solids I: Basic developments, Philos. Trans. R. Soc. Lond. Ser. A, 345 (1993) 425-458.

[30] P.M. Naghdi, A.R. Srinivasa, Characterization of Dislocations and Their Influence on Plastic-Deformation in Single-Crystals, Int. J. Eng. Sci., 32 (1994) 1157-1182.

[31] K.C. Le, H. Stumpf, A model of elastoplastic bodies with continuously distributed dislocations, Int. J. Plast., 12 (1996) 611-627.

[32] K.C. Le, H. Stumpf, Nonlinear continuum theory of dislocations, Int. J. Eng. Sci., 34 (1996) 339-358.

[33] N.M. Cordero, A. Gaubert, S. Forest, E.P. Busso, F. Gallerneau, S. Kruch, Size effects in generalised continuum crystal plasticity for two-phase laminates, J. Mech. Phys. Solids, In Press, Corrected Proof.

[34] S. Forest, F. Barbe, G. Cailletaud, Cosserat modelling of size effects in the mechanical behaviour of polycrystals and multi-phase materials, International Journal of Solids and Structures, 37 (2000) 7105-7126.

[35] S. Forest, G. Cailletaud, R.W. Sievert, A Cosserat theory for elastoviscoplastic single crystals at finite deformation, Arch. Mech., 49 (1997) 705-736.

[36] J.D. Clayton, D.L. McDowell, D.J. Bammann, Modeling dislocations and disclinations with finite micropolar elastoplasticity, Int. J. Plast., 22 (2006) 210-256.

[37] S. Forest, Modeling slip, kink and shear banding in classical and generalized single crystal plasticity, Acta Mater., 46 (1998) 3265-3281.

[38] S. Forest, Some links between Cosserat, strain gradient crystal plasticity and the statistical theory of dislocations, Philos. Mag., 88 (2008) 3549-3563.

[39] S. Forest, R. Sedlacek, Plastic slip distribution in two-phase laminate microstructures: dislocation-based versus generalized continuum approaches, Philos. Mag., 83 (2003) 245-276.

[40] R. Sievert, S. Forest, R. Trostel, Finite deformation Cosserat-type modelling of dissipative solids and its application to crystal plasticity, J. Phys. IV, 8 (1998) 357-364.

[41] A. Zeghadi, S. Forest, A.-F. Gourgues, O. Bouaziz, Cosserat continuum modelling of grain size effects in metal polycrystals, Proc. Appl. Math. Mech., 5 (2005) 79-82.

[42] A.C. Eringen, E.S. Suhubi, Nonlinear theory of simple micro-elastic solids, Int. J. Eng. Sci., 2 (1964) 189-203.

[43] E. Cosserat, F. Cosserat, Theorie des corps deformables, Librairie Scientifique A. Hermann et Fils, Paris, 1909.

[44] D. Besdo, Some remarks on material laws of plastomechanics of Cosserat continua, Z. Angew. Math. Mech., 54 (1974) T70-T71.

[45] H. Lippmann, A Cosserat theory of plastic flow, Acta Mech., 8 (1969) 255-284.

[46] A. Sawczuk, On yielding of Cosserat continua, Archiwum Mechaniki Stosowanej, 19 (1967) 471-480.

[47] R. de Borst, A generalization of J_2-flow theory for polar continua, Comput. Meth. Appl. Mech. Eng., 103 (1993) 347-362.

[48] P. Steinmann, A micropolar theory of finite deformation and finite rotation multiplicative elastoplasticity, Int. J. Solids Struct., 31 (1994) 1063-1084.

[49] P. Grammenoudis, C. Tsakmakis, Hardening rules for finite deformation micropolar plasticity: Restrictions imposed by the second law of thermodynamics and the postulate of Il'iushin, Continuum Mech. Thermodyn., 13 (2001) 325-363.

[50] P. Neff, A finite-strain elastic-plastic Cosserat theory for polycrystals with grain rotations, Int. J. Eng. Sci., 44 (2006) 574-594.

[51] Abaqus/Standard, Version 6.7, Simulia Corp., 2007.

[52] D. Peirce, C.F. Shih, A. Needleman, A tangent modulus method for rate dependent solids, Comput. Struct., 18 (1984) 875-887.

[53] B. Devincre, L.P. Kubin, Mesoscopic simulations of dislocations and plasticity, Materials Science and Engineering A, 234 (1997) 8-14.

[54] N.M. Ghoniem, S.H. Tong, L.Z. Sun, Parametric dislocation dynamics: A thermodynamics-based approach to investigations of mesoscopic plastic deformation, Phys. Rev. B, 61 (2000) 913-927.

[55] K.W. Schwarz, Simulation of dislocations on the mesoscopic scale. I. Methods and examples, J. Appl. Phys., 85 (1999) 108-119.

[56] V.B. Shenoy, R.V. Kukta, R. Phillips, Mesoscopic analysis of structure and strength of dislocation junctions in fcc metals, Phys. Rev. Lett., 84 (2000) 1491-1494.

[57] E. Van der Giessen, A. Needleman, Discrete dislocation plasticity: A simple planar model, Model. Simul. Mater. Sci. Eng., 3 (1995) 689-735.

[58] D. Weygand, L.H. Friedman, E. van der Giessen, A. Needleman, Discrete dislocation modeling in three-dimensional confined volumes, Materials Science and Engineering a-Structural Materials Properties Microstructure and Processing, 309 (2001) 420-424.

[59] H.M. Zbib, M. Rhee, J.P. Hirth, On plastic deformation and the dynamics of 3D dislocations, Int. J. Mech. Sci., 40 (1998) 113-127.

[60] V.A. Lubarda, J.A. Blume, A. Needleman, An analysis of equilibrium dislocation distributions, Acta Metall. Mater., 41 (1993) 625-642.

[61] B.D. Coleman, M.E. Gurtin, Thermodynamics with internal state variables, J. Chem. Phys., 47 (1967) 597-613.

[62] H. Mecking, U.F. Kocks, Kinetics of flow and strain-hardening, Acta Metall., 29 (1981) 1865-1875.

[63] P. Franciosi, A. Zaoui, Multislip in fcc crystals a theoretical approach compared with experimental data, Acta Metall., 30 (1982) 1627-1637.

[64] P.J. Armstrong, C.O. Frederick, A mathematical representation of the multiaxial Bauschinger effect, in: Report RD/B/N 731, C.E.G.B.

[65] D. Hull, D.J. Bacon, Introduction to Dislocations, Fourth ed., Butterworth-Heinemann, Oxford, 2001.

[66] M. Kuroda, V. Tvergaard, On the formulations of higher-order strain gradient crystal plasticity models, J. Mech. Phys. Solids, 56 (2008) 1591-1608.

[67] K. Kondo, On the analytical and physical foundations of the theory of dislocations and yielding by the differential geometry of continua, Int. J. Eng. Sci., 2 (1964) 219-252.

[68] B.A. Bilby, R. Bullough, E. Smith, Continuous distributions of dislocations: A new application of the methods of non-Riemannian geometry, Proceedings of the Royal Society of London Series A: Mathematical and Physical Sciences, 231 (1955) 263-273.

[69] E. Kroner, Allgemeine kontinuumstheorie der versetzungen und eigenspannungen, Archive for Rational Mechanics and Analysis, 4 (1960) 273-334.

[70] J.F. Nye, Some geometrical relations in dislocated crystals, Acta Metall., 1 (1953) 153-162.

[71] H. Mughrabi, On the role of strain gradients and long-range internal stresses in the composite model of crystal plasticity, Mater. Sci. Eng. A, 317 (2001) 171-180.

[72] C.J. Bayley, W.A.M. Brekelmans, M.G.D. Geers, A comparison of dislocation induced back stress formulations in strain gradient crystal plasticity, Int. J. Solids Struct., 43 (2006) 7268-7286.

[73] J.M. Gerken, P.R. Dawson, A crystal plasticity model that incorporates stresses and strains due to slip gradients, J. Mech. Phys. Solids, 56 (2008) 1651-1672.

[74] S. Yefimov, I. Groma, E. van der Giessen, A comparison of a statistical-mechanics based plasticity model with discrete dislocation plasticity calculations, J. Mech. Phys. Solids, 52 (2004) 279-300.

[75] A. Acharya, J.L. Bassani, Lattice incompatibility and a gradient theory of crystal plasticity, J. Mech. Phys. Solids, 48 (2000) 1565-1595.

[76] A. Acharya, A model of crystal plasticity based on the theory of continuously distributed dislocations, J. Mech. Phys. Solids, 49 (2001) 761-784.

[77] M. Kuroda, V. Tvergaard, A finite deformation theory of higher-order gradient crystal plasticity, J. Mech. Phys. Solids, 56 (2008) 2573-2584.

[78] A. Arsenlis, D.M. Parks, R. Becker, V.V. Bulatov, On the evolution of crystallographic dislocation density in non-homogeneously deforming crystals, J. Mech. Phys. Solids, 52 (2004) 1213-1246.

[79] R. Sedlacek, E. Werner, Constrained shearing of a thin crystalline strip: Application of a continuum dislocation-based model, Phys. Rev. B, 69 (2004) 1-12.

[80] K. Shizawa, H.M. Zbib, A thermodynamical theory of gradient elastoplasticity with dislocation density tensor. I: Fundamentals, Int. J. Plast., 15 (1999) 899-938.

[81] B. Svendsen, Continuum thermodynamic models for crystal plasticity including the effects of geometrically-necessary dislocations, J. Mech. Phys. Solids, 50 (2002) 1297-1329.

[82] A. Arsenlis, D.M. Parks, Crystallographic aspects of geometrically-necessary and statistically-stored dislocation density, Acta Mater., 47 (1999) 1597-1611.

[83] E. Kroner, Initial studies of plasticity theory based upon statistical mechanics, in: M.F. Kanninen, W.F. Adler, A.R. Rosenfield, R.I. Jaffee (Eds.) Inelastic Behavior of Solids, McGraw-Hill, New York, 1969, pp. 137-147.

[84] S. Sun, B.L. Adams, C. Shet, S. Saigal, W. King, Mesoscale investigation of the deformation field of an aluminum bicrystal, Scripta Materialia, 39 (1998) 501-508.

[85] S. Sun, B.L. Adams, W.E. King, Observations of lattice curvature near the interface of a deformed aluminium bicrystal, Philos. Mag. A, 80 (2000) 9-25.

[86] J.W. Kysar, Y.X. Gan, T.L. Morse, X. Chen, M.E. Jones, High strain gradient plasticity associated with wedge indentation into face-centered cubic single crystals: Geometrically necessary dislocation densities, J. Mech. Phys. Solids, 55 (2007) 1554-1573.

[87] B.C. Larson, A. El-Azab, W.G. Yang, J.Z. Tischler, W.J. Liu, G.E. Ice, Experimental characterization of the mesoscale dislocation density tensor, Philos. Mag., 87 (2007) 1327-1347.

[88] B.C. Larson, J.Z. Tischler, A. El-Azab, W.J. Liu, Dislocation density tensor characterization of deformation using 3D X-ray microscopy, J. Eng. Mater. Technol., 130 (2008) 1-10.

[89] M.G.D. Geers, W.A.M. Brekelmans, C.J. Bayley, Second-order crystal plasticity: internal stress effects and cyclic loading, Model. Simul. Mater. Sci. Eng., 15 (2007) S133-S145.

[90] S. Limkumnerd, E. Van der Giessen, Study of size effects in thin films by means of a crystal plasticity theory based on DiFT, J. Mech. Phys. Solids, 56 (2008) 3304-3314.

[91] A. Acharya, Driving forces and boundary conditions in continuum dislocation mechanics, Proceedings of the Royal Society of London Series a-Mathematical Physical and Engineering Sciences, 459 (2003) 1343-1363.

[92] A. Acharya, Constitutive analysis of finite deformation field dislocation mechanics, J. Mech. Phys. Solids, 52 (2004) 301-316.

[93] A. Acharya, Jump condition for GND evolution as a constraint on slip transmission at grain boundaries, Philos. Mag., 87 (2007) 1349-1359.

[94] A. Acharya, A. Beaudoin, R. Miller, New perspectives in plasticity theory: Dislocation nucleation, waves, and partial continuity of plastic strain rate, Mathematics and Mechanics of Solids, 13 (2008) 292-315.

[95] A. Acharya, A. Roy, Size effects and idealized dislocation microstructure at small scales: Predictions of a Phenomenological model of Mesoscopic Field Dislocation Mechanics: Part I, J. Mech. Phys. Solids, 54 (2006) 1687-1710.

[96] A. Acharya, A. Roy, A. Sawant, Continuum theory and methods for coarse-grained, mesoscopic plasticity, Scripta Materialia, 54 (2006) 705-710.

[97] A. Roy, A. Acharya, Finite element approximation of field dislocation mechanics, J. Mech. Phys. Solids, 53 (2005) 143-170.

[98] A. Roy, A. Acharya, Size effects and idealized dislocation microstructure at small scales: Predictions of a Phenomenological model of Mesoscopic Field Dislocation Mechanics: Part II, J. Mech. Phys. Solids, 54 (2006) 1711-1743.

[99] S.N. Varadhan, A.J. Beaudoin, A. Acharya, C. Fressengeas, Dislocation transport using an explicit Galerkin/least-squares formulation, Modelling and Simulation in Materials Science and Engineering, 14 (2006) 1245-1270.

[100] J.D. Clayton, D.L. McDowell, A multiscale multiplicative decomposition for elastoplasticity of polycrystals, Int. J. Plast., 19 (2003) 1401-1444.

[101] J.D. Clayton, D.L. McDowell, D.J. Bammann, A multiscale gradient theory for single crystalline elastoviscoplasticity, Int. J. Eng. Sci., 42 (2004) 427-457.

[102] J.M. Gerken, P.R. Dawson, A finite element formulation to solve a non-local constitutive model with stresses and strains due to slip gradients, Comput. Meth. Appl. Mech. Eng., 197 (2008) 1343-1361.

[103] W.M. Ashmawi, M.A. Zikry, Effects of grain boundaries and dislocation density evolution on large strain deformation modes in fcc crystalline materials, J. Comput-Aided Mater. Des., 7 (2000) 55-62.

[104] W.M. Ashmawi, M.A. Zikry, Prediction of grain-boundary interfacial mechanisms in polycrystalline materials, J. Eng. Mater. Technol., 124 (2002) 88-96.

[105] W.M. Ashmawi, M.A. Zikry, Grain boundary effects and void porosity evolution, Mech. Mater., 35 (2003) 537-552.

[106] W.M. Ashmawi, M.A. Zikry, Single void morphological and grain-boundary effects on overall failure in FCC polycrystalline systems, Materials Science & Engineering A, 343 (2003) 126-142.

[107] D. Walgraef, E.C. Aifantis, Dislocation patterning in fatigued metals as a result of dynamical instabilities, J. Appl. Phys., 58 (1985) 688-691.

[108] I. Groma, Link between the microscopic and mesoscopic length-scale description of the collective behavior of dislocations, Phys. Rev. B, 56 (1997) 5807-5813.

[109] L. Nicola, E. Van der Giessen, M.E. Gurtin, Effect of defect energy on strain-gradient predictions of confined single-crystal plasticity, J. Mech. Phys. Solids, 53 (2005) 1280-1294.

[110] L. Bardella, A deformation theory of strain gradient crystal plasticity that accounts for geometrically necessary dislocations, J. Mech. Phys. Solids, 54 (2006) 128-160.

[111] U. Borg, A strain gradient crystal plasticity analysis of grain size effects in polycrystals, Eur. J. Mech. A-Solids, 26 (2007) 313-324.

[112] P.M. Naghdi, A.R. Srinivasa, A Dynamical Theory of Structured Solids .2. Special Constitutive-Equations and Special Cases of the Theory, Philosophical Transactions of the Royal Society of London Series a-Mathematical Physical and Engineering Sciences, 345 (1993) 459-476.

[113] G.A. Maugin, Method of virtual power in continuum-mechanics: Application to coupled fields, Acta Mech., 35 (1980) 1-70.

[114] M.E. Gurtin, A. Needleman, Boundary conditions in small-deformation, single-crystal plasticity that account for the Burgers vector, J. Mech. Phys. Solids, 53 (2005) 1-31.

[115] M.E. Gurtin, A finite-deformation, gradient theory of single-crystal plasticity with free energy dependent on densities of geometrically necessary dislocations, Int. J. Plast., 24 (2008) 702-725.

[116] U. Borg, J.W. Kysar, Strain gradient crystal plasticity analysis of a single crystal containing a cylindrical void, Int. J. Solids Struct., 44 (2007) 6382-6397.

[117] R. Deborst, Numerical modeling of bifurcation and localization in cohesive-frictional materials, Pure Appl. Geophys., 137 (1991) 367-390.

[118] R. Deborst, A generalization of J_2-flow theory for polar continua, Comput. Meth. Appl. Mech. Eng., 103 (1993) 347-362.

[119] P. Steinmann, An improved FE expansion for micropolar localization analysis, Commun. Numer. Methods Eng., 10 (1994) 1005-1012.

[120] P. Steinmann, Theory of finite micropolar elastoplasticity, Z. Angew. Math. Mech., 74 (1994) T245-T247.

[121] P. Steinmann, Theory and numerics of ductile micropolarelastoplastic damage, Int. J. Numer. Methods Eng., 38 (1995) 583-606.

[122] P. Grammenoudis, C. Tsakmakis, Finite element implementation of large deformation micropolar plasticity exhibiting isotropic and kinematic hardening effects, Int. J. Numer. Methods Eng., 62 (2005) 1691-1720.

[123] P. Grammenoudis, C. Tsakmakis, Predictions of microtorsional experiments by micropolar plasticity, Proc. R. Soc. London Ser. A-Math. Phys. Eng. Sci., 461 (2005) 189-205.

[124] P. Grammenoudis, C. Tsakmakis, Micropolar plasticity theories and their classical limits. Part I: Resulting model, Acta Mech., 189 (2007) 151-175.

[125] P. Neff, The Cosserat couple modulus for continuous solids is zero viz the linearized Cauchy-stress tensor is symmetric, ZAMM-Z. Angew. Math. Mech., 86 (2006) 892-912.

[126] P. Neff, K. Chelminski, Well-posedness of dynamic cosserat plasticity, Appl. Math. Optim., 56 (2007) 19-35.

[127] P. Neff, K. Chelminski, W. Muller, C. Wieners, A numerical solution method for an infinitesimal elasto-plastic cosserat model, Math. Models Meth. Appl. Sci., 17 (2007) 1211-1239.

[128] S. Forest, P. Boubidi, R. Sievert, Strain localization patterns at a crack tip in generalized single crystal plasticity, Scr. Mater., 44 (2001) 953-958.

[129] S. Forest, R. Sievert, Elastoviscoplastic constitutive frameworks for generalized continua, Acta Mech., 160 (2003) 71-111.

[130] W. Pietraszkiewicz, V.A. Eremeyev, On natural strain measures of the non-linear micropolar continuum, Int. J. Solids Struct., 46 (2009) 774-787.

[131] C. Sansour, A unified concept of elastic-viscoplastic Cosserat and micromorphic continua, J. Phys. IV, 8 (1998) 341-348.

[132] R.A. Toupin, Elastic materials with couple stresses, Archive for Rational Mechanics and Analysis, 11 (1962) 385-414.

[133] S. Kessel, Lineare elastizitatstheorie des anisotropen Cosserat-kontinuums, Abh. Braunschweig. Wiss. Ges., 16 (1964) 1-22.

[134] A.C. Eringen, Microcontinuum field theories I: Foundations and solids, Springer-Verlag New York, Inc., 1999.

[135] G.Z. Voyiadjis, M.I. Alsaleh, K.A. Alshibli, Evolving internal length scales in plastic strain localization for granular materials, International Journal of Plasticity, 21 (2005) 2000-2024.

[136] J. Weertman, Anomalous work hardening, non-redundant screw dislocations in a circular bar deformed in torsion, and non-redundant edge dislocations in a bent foil, Acta Mater., 50 (2002) 673-689.

[137] H. Mughrabi, On the current understanding of strain gradient plasticity, Mater. Sci. Eng. A, 387-389 (2004) 209-213.

[138] S.C. Cowin, Stress functions in Cosserat elasticity, Int. J. Solids Struct., 6 (1970) 389-398.

[139] C.S. Hartley, A method for linking thermally activated dislocation mechanisms of yielding with continuum plasticity theory, Philos. Mag., 83 (2003) 3783-3808.

[140] C.J. Bayley, W.A.M. Brekelmans, M.G.D. Geers, A three-dimensional dislocation field crystal plasticity approach applied to miniaturized structures, Philos. Mag., 87 (2007) 1361-1378.

[141] E. Kroner, On the physical reality of torque stresses in continuum mechanics, Int. J. Eng. Sci., 1 (1963) 261-278.

[142] K. Garikipati, Couple stresses in crystalline solids: Origins from plastic slip gradients, dislocation core distortions, and three-body interatomic potentials, J. Mech. Phys. Solids, 51 (2003) 1189-1214.

[143] M. Zhou, D.L. McDowell, Equivalent continuum for dynamically deforming atomistic particle systems, Philos. Mag. A, 82 (2002) 2547-2574.

[144] T. Belytschko, Nonlinear finite elements for continua and structures, John Wiley, Chichester ;, 2000.

[145] T.J.R. Hughes, The finite element method : linear static and dynamic finite element analysis, Prentice-Hall, Englewood Cliffs, N.J. :, 1987.

[146] Abaqus/Standard, Version 6.7, Simulia Corp., 2007.

[147] K.-J.r. Bathe, Finite element procedures, Prentice Hall, Englewood Cliffs, N.J. :, 1996.

[148] D. Peirce, R.J. Asaro, A. Needleman, Material rate dependence and localized deformation in crystalline solids, Acta Metall., 31 (1983) 1951-1976.

[149] S. Diebels, H. Steeb, The size effect in foams and its theoretical and numerical investigation, Proc. R. Soc. London Ser. A-Math. Phys. Eng. Sci., 458 (2002) 2869-2883.

[150] P. Neff, I. Munch, Simple shear in nonlinear Cosserat elasticity: bifurcation and induced microstructure, Continuum Mech. Thermodyn., 21 (2009) 195-221.

[151] D.J. Luscher, A hierarchical framework for the multiscale modeling of microstructure evolution in heterogeneous materials, in: Mechanical Engineering, Georgia Institute of Technology, Atlanta, GA, 2009.

[152] L. Li, S.S. Xie, Finite element method for linear micropolar elasticity and numerical study of some scale effects phenomena in MEMS, Int. J. Mech. Sci., 46 (2004) 1571-1587.

[153] S. Nakamura, R.S. Lakes, Finite-Element Analysis of Stress-Concentration around a Blunt Crack in a Cosserat Elastic Solid, Comput. Meth. Appl. Mech. Eng., 66 (1988) 257-266.

[154] E. Providas, M.A. Kattis, Finite element method in plane Cosserat elasticity, Comput. Struct., 80 (2002) 2059-2069.

[155] E. Sharbati, R. Naghdabadi, Computational aspects of the Cosserat finite element analysis of localization phenomena, Comput. Mater. Sci., 38 (2006) 303-315.

[156] H.W. Zhang, H. Wang, G.Z. Liu, Quadrilateral isoparametric finite elements for plane elastic Cosserat bodies, Acta Mech. Sin., 21 (2005) 388-394.

[157] P.N. Kaloni, T. Ariman, Stress concentration effects in micropolar elasticity, Z. Angew. Math. Phys., 18 (1967) 136-&.

[158] R. de Borst, Numerical modeling of bifurcation and localization in cohesive-frictional materials, Pure Appl. Geophys., 137 (1991) 367-390.

[159] R. de Borst, L.J. Sluys, Localization in a Cosserat continuum under static and dynamic loading conditions, Comput. Meth. Appl. Mech. Eng., 90 (1991) 805-827.

[160] J.Y. Shu, N.A. Fleck, E. Van der Giessen, A. Needleman, Boundary layers in constrained plastic flow: Comparison of nonlocal and discrete dislocation plasticity, J. Mech. Phys. Solids, 49 (2001) 1361-1395.

[161] B. Svendsen, S. Reese, Continuum thermodynamic modeling and simulation of additional hardening due to deformation incompatibility, in: C. Miehe (Ed.) Solid Mechanics and its Applications, Kluwer Academic Publishers, Dordrecht, 2003, pp. 141-150.

[162] S. Yefimov, E. Van der Giessen, Multiple slip in a strain-gradient plasticity model motivated by a statistical-mechanics description of dislocations, Int. J. Solids Struct., 42 (2005) 3375-3394.

[163] A. Hunter, M. Koslowski, Direct calculations of material parameters for gradient plasticity, J. Mech. Phys. Solids, 56 (2008) 3181-3190.

[164] DataThief III, version 1.5, 2008.

[165] S. Limkumnerd, E. Van der Giessen, Statistical approach to dislocation dynamics: From dislocation correlations to a multiple-slip continuum theory of plasticity, Phys. Rev. B, 77 (2008).

[166] S. Yefimov, I. Groma, E. Van der Giessen, Comparison of a statistical-mechanics based plasticity model with discrete dislocation plasticity calculations, J. Phys. IV, 11 (2001) 103-110.

[167] S. Yefimov, E. van der Giessen, Size effects in single crystal thin films: nonlocal crystal plasticity simulations, Eur. J. Mech. A-Solids, 24 (2005) 183-193.

[168] S. Yefimov, E. Van der Giessen, I. Groma, Bending of a single crystal: discrete dislocation and nonlocal crystal plasticity simulations, Model. Simul. Mater. Sci. Eng., 12 (2004) 1069-1086.

[169] J.R. Mayeur, D.L. McDowell, D.J. Bammann, Dislocation-based micropolar single crystal plasticity: Comparison of multi- and single criterion theories, J. Mech. Phys. Solids, (2010).

[170] E. Demir, D. Raabe, F. Roters, The mechanical size effect as a mean-field breakdown phenomenon: Example of microscale single crystal beam bending, Acta Mater., 58 (2010) 1876-1886.

[171] F. Akasheh, H.M. Zbib, T. Ohashi, Multiscale modelling of size effect in fcc crystals: discrete dislocation dynamics and dislocation-based gradient plasticity, Philos. Mag., 87 (2007) 1307-1326.

[172] H.H.M. Cleveringa, E. Van der Giessen, A. Needleman, A discrete dislocation analysis of bending, Int. J. Plast., 15 (1999) 837-868.

[173] C.T. Hou, Z.H. Li, M.S. Huang, C.J. Ouyang, Discrete dislocation plasticity analysis of single crystalline thin beam under combined cyclic tension and bending, Acta Mater., 56 (2008) 1435-1446.

[174] M.I. Idiart, V.S. Deshpande, N.A. Fleck, J.R. Willis, Size effects in the bending of thin foils, Int. J. Eng. Sci., 47 (2009) 1251-1264.

[175] M. Kuroda, V. Tvergaard, Effects of microscopic boundary conditions on plastic deformations of small-sized single crystals, Int. J. Solids Struct., 46 (2009) 4396-4408.

[176] M. Kuroda, V. Tvergaard, T. Ohashi, Simulations of micro-bending of thin foils using a scale dependent crystal plasticity model, Model. Simul. Mater. Sci. Eng., 15 (2007) S13-S22.

[177] C. Motz, D. Weygand, J. Senger, P. Gumbsch, Micro-bending tests: A comparison between three-dimensional discrete dislocation dynamics simulations and experiments, Acta Mater., 56 (2008) 1942-1955.

[178] S. Sandfeld, T. Hochrainer, P. Gumbsch, M. Zaiser, Numerical implementation of a 3D continuum theory of dislocation dynamics and application to micro-bending, Philos. Mag., 90 3697-3728.

[179] R. Sedlacek, Bending of thin crystalline strips: Comparison of continuum dislocation-based models, Materials Science and Engineering a-Structural Materials Properties Microstructure and Processing, 400 (2005) 439-442.

[180] R. Sedlacek, Orowan-type size effect in plastic bending of free-standing thin crystalline strips, Materials Science and Engineering a-Structural Materials Properties Microstructure and Processing, 393 (2005) 387-395.

[181] K. Suzuki, Y. Matsuki, K. Masaki, M. Sato, M. Kuroda, Tensile and microbend tests of pure aluminum foils with different thicknesses, Materials Science and Engineering a-Structural Materials Properties Microstructure and Processing, 513-14 (2009) 77-82.

[182] S. Tang, C. Zhu, Y.G. Wei, Size effects in micro-bending deformation of MEMS devices based on the discrete dislocation theory, Int. J. Nonlinear Sci. Numer. Simul., 3 (2002) 699-702.

[183] H.H.M. Cleveringa, E. Van der Giessen, A. Needleman, A discrete dislocation analysis of residual stresses in a composite material, Philos. Mag. A, 79 (1999) 893-920.

[184] H.H.M. Cleveringa, E. VanderGiessen, A. Needleman, Comparison of discrete dislocation and continuum plasticity predictions for a composite material, Acta Mater., 45 (1997) 3163-3179.

[185] J.L. Bassani, A. Needleman, E. Van der Giessen, Plastic flow in a composite: a comparison of nonlocal continuum and discrete dislocation predictions, Int. J. Solids Struct., 38 (2001) 833-853.

[186] V.B. Shenoy, H.H.M. Cleveringa, R. Phillips, E. Van der Giessen, A. Needleman, Simulated small-angle scattering patterns for a plastically deformed model composite material, Model. Simul. Mater. Sci. Eng., 8 (2000) 557-581.

[187] A. Needleman, E. Van der Giessen, Discrete dislocation and continuum descriptions of plastic flow, Materials Science and Engineering a-Structural Materials Properties Microstructure and Processing, 309 (2001) 1-13.

[188] C. Schwarz, R. Sedlacek, E. Werner, Plastic deformation of a composite and the source-shortening effect simulated by a continuum dislocation-based model, Model. Simul. Mater. Sci. Eng., 15 (2007) S37-S49.

[189] R.S. Yassar, S.D. Mesarovic, D.P. Field, Micromechanics of hardening of elastic-plastic crystals with elastic inclusions: I-Dilute concentration, Int. J. Plast., 23 (2007) 1901-1917.

[190] V. Taupin, S. Berbenni, C. Fressengeas, O. Bouaziz, On particle size effects: An internal length mean field approach using field dislocation mechanics, Acta Mater., 58 5532-5544.

[191] L.P. Evers, D.M. Parks, W.A.M. Brekelmans, M.G.D. Geers, Crystal plasticity model with enhanced hardening by geometrically necessary dislocation accumulation, J. Mech. Phys. Solids, 50 (2002) 2403-2424.

[192] Y. Aoyagi, K. Shizawa, Multiscale crystal plasticity modeling based on geometrically necessary crystal defects and simulation on fine-graining for polycrystal, Int. J. Plast., 23 (2007) 1022-1040.

[193] M. Becker, Incompatibility and instability based size effects in crystals and composites at finite elastoplastic strains, in: Institute of Mechanics (Civil Engineering), University of Stuttgart, Stuttgart, 2006.

[194] S. Bargmann, M. Ekh, K. Runesson, B. Svendsen, Modeling of polycrystals with gradient crystal plasticity: A comparison of strategies, Philos. Mag., 90 1263-1288.

[195] W.A. Counts, M.V. Braginsky, C.C. Battaile, E.A. Holm, Polycrystalline kinematics: An extension of single crystal kinematics that incorporates initial microstructure, Int. J. Solids Struct., 44 (2007) 5742-5751.

[196] W.A. Counts, M.V. Braginsky, C.C. Battaile, E.A. Holm, Predicting the Hall-Petch effect in fcc metals using non-local crystal plasticity, Int. J. Plast., 24 (2008) 1243-1263.

[197] M.G.D. Geers, W.A.M. Brekelmans, P.J.M. Janssen, Size effects in miniaturized polycrystalline FCC samples: Strengthening versus weakening, Int. J. Solids Struct., 43 (2006) 7304-7321.

[198] A. Ma, F. Roters, D. Raabe, Studying the effect of grain boundaries in dislocation density based crystal-plasticity finite element simulations, Int. J. Solids Struct., 43 (2006) 7287-7303.

[199] M.E. Gurtin, A theory of grain boundaries that accounts automatically for grain misorientation and grain-boundary orientation, J. Mech. Phys. Solids, 56 (2008) 640-662.

[200] O. van der Sluis, P.J.G. Schreurs, W.A.M. Brekelmans, H.E.H. Meijer, Overall behaviour of heterogeneous elastoviscoplastic materials: effect of microstructural modelling, Mech. Mater., 32 (2000) 449-462.

[201] R. Armstrong, R.M. Douthwaite, I. Codd, N.J. Petch, Plastic deformation of polycrystalline aggregates, Philos. Mag., 7 (1962) 45-&.

[202] R. Sedlacek, S. Forest, Non-local plasticity at microscale: A dislocation-based and a Cosserat model, Phys. Status Solidi B-Basic Res., 221 (2000) 583-596.

[203] A. Roy, R.H.J. Peerlings, M.G.D. Geers, Y. Kasyanyuk, Continuum modeling of dislocation interactions: Why discreteness matters?, Materials Science and Engineering a-Structural Materials Properties Microstructure and Processing, 486 (2008) 653-661.

[204] S.D. Mesarovic, R. Baskaran, A. Panchenko, Thermodynamic coarsening of dislocation mechanics and the size-dependent continuum crystal plasticity, J. Mech. Phys. Solids, 58 311-329.

[205] R. Baskaran, S. Akarapu, S.D. Mesarovic, H.M. Zbib, Energies and distributions of dislocations in stacked pile-ups, Int. J. Solids Struct., 47 1144-1153.